DISSERTATION

Study of the hot deformation behaviour of metal-based alloys under consideration of processing maps

Martina Dikovits
Institute for Materials Science and Welding

A thesis submitted for the degree
‘Doktor der technischen Wissenschaften‘
at the Faculty of Mechanical Engineering and Economic Sciences

supervised by
Ass. Prof. Dr. techn. Univ.-Doz. Cecilia Poletti

Institute for Materials Science and Welding

Graz University of Technology

The important thing in science is not so much to
obtain new facts as to discover new ways of
thinking about them.

Sir William Lawrence Bragg

Preface

This PhD thesis is submitted for the degree “Doktor der technischen Wissenschaften” at the Faculty of Mechanical Engineering and Economic Sciences at Graz University of Technology. The work was carried out between 2010 and 2013 under the supervision of Prof. Cecilia Poletti at the Institute of Materials Science and Technology (Vienna University of Technology) and at the Institute for Materials Science and Welding (Graz University of Technology). This thesis was funded by the Austrian Science Fund (FWF) through the project P22238-N22.

I declare that I have authored this thesis independently, that I have not used other than the declared sources / resources, and that I have explicitly marked all material which has been quoted either literally or by content from the used sources.

Martina Dikovits
Graz, January 2014

Acknowledgements

I would like to thank Prof. Cecilia Poletti for supervising this thesis, for her continuous support and encouragement, and for the patience and pressure in the right moments.

Prof. Hans-Peter Degischer from the Institute of Materials Science and Technology at the Vienna University of Technology, and Prof. Christof Sommitsch from the Institute for Materials Science and Welding at the Graz University of Technology were kind enough to let me use the facilities at their institutes which I highly appreciated.

Thanks to Prof. Frank Montheillet for accepting to read this work, and for the comments and suggestions to it.

I am thankful to the Austrian Science Fund (FWF) for supporting this work through the project P22238-N22, and to the Austrian Agency for International Mobility and Cooperation in Education, Science and Research (OeAD) for funding the project WTZ Indien 2011-12. In addition, thanks to Prof. Gajanan Prabhakar Chaudhari and Prof. Vivek Pancholi, I was able to work at their institute at the Indian Institute of Technology, in Roorkee, India.

Moreover, Prof. Peter Hodgson and Prof. Matthew Barnett gave me the outstanding opportunity to work in their Light Metals group at the Institute for Frontier Materials, Deakin University, Australia.

I have to say thank you to the people from USTEM and FELMI for their help regarding the EBSD measurements.

Furthermore, I am very grateful for my colleagues at the Institute for Materials Science and Welding for the good collaboration throughout this work.

Finally, I would like to express my gratitude to my parents and friends for their great support throughout my studies.

Abstract

Thermomechanical processes, such as forging, extrusion or rolling play an important role in industry all over the world. During the application of these processes, a change at macro- (reaching the desired shape) as well as at micro-scales appears due to dynamic recrystallization, dynamic recovery and twinning, for example. The microstructure is of central importance for the properties of a material e. g. a small grain size is associated with an increment of the hardness. Therefore, it would be a great benefit, if the modifications in the microstructure due to the thermomechanical processes can be predicted. There are different possibilities to model the hot deformation behaviour of metals. One of them, which is mainly investigated in this work are the so-called deformation maps. A special type of deformation maps are the processing maps which are developed by Prasad, with a further modification by Murty and Rao. These types of processing maps consist of two superimposed maps: an efficiency of power value, and an instability map. The efficiency of power value can be directly correlated to microstructural changes, (e. g. dynamic recovery, dynamic recrystallization and twinning in the material) due to its correlation with m or the stress exponent n and its relationship with diffusional processes. The instability maps used in the processing maps of Prasad and Murty and Rao cannot be related correctly to flow localization, adiabatic heating effects, shear band formation, cracking, and the formation of voids. However, they are easy to generate and thus are intensively used by scientists and industry. Furthermore, there are still on-going discussions about the physical foundation of the maps. These controversies are mainly due to the treatment of microstructural changes and heat transfer processes as two separated phenomena, only done for elastic and not for plastic deformation.

Finally, deformation maps will be a useful tool which allows to choose the correct processing window related to the temperature and strain rate for a given strain if the instability approach is revised which has been already started.

Kurzfassung

Thermomechanische Umformprozesse wie Walzen, Schmieden und Strangpressen spielen eine wichtige Rolle in der Industrie und werden weltweit angewandt.

Während dieser Prozesse kommt es einerseits zu einer Formänderung und andererseits zu einer Änderung in der Mikrostruktur durch Mechanismen wie dynamische Erholung, dynamische Rekristallisation oder Zwillingsbildung. Die Art des entstandenen Gefüges ist verantwortlich für die sich ergebenden Eigenschaften des Materials. Nun wäre es von Vorteil, wenn man die Änderung des Gefüges vorhersagen könnte. Verschiedene Modelle wurden entwickelt, wie thermomechanische Umformprozesse modelliert werden können. Eine Möglichkeit dazu, sind die sogenannten „deformation maps". Ein Spezialfall der „deformation maps" sind die sogenannten „processing maps", welche von Prasad entwickelt und von Murty und Rao erweitert wurden. „Processing maps" bestehen aus zwei überlagerten Karten: zum einen aus einer „Effizienzkarte", welche die Effizienz der Gefügeänderung (z. B. dynamische Erholung, dynamische Rekristallisation und Zwillingsbildung) angibt und zum anderen aus einer „Instabilitätskarte" welche Instabilitäten wie Risse, Poren, Fließlokalisationen oder adiabatisches Fließverhalten aufzeigt. Allerdings wurde festgestellt, dass mittels der Verwendung von „processing maps" diese Instabilitäten nicht gut genug abgebildet werden können. Jedoch werden „processing maps" von Wissenschaftlern und Industrie häufig genutzt, da sie leicht zu erstellen sind. Ein weiterer Nachteil von den „processing maps" liegt darin, dass es noch keine allgemein gültige physikalische Erklärung hinter den Ansätzen der „processing maps" gibt.

Schlussendlich können „deformation maps" eine hilfreiche Methode sein um das optimale Prozessfenster (in Abhängigkeit von Temperatur und Dehnrate, für eine gegebene Dehnung) aufzuzeigen. Der Ansatz der „Instabilitätskarte" sollte jedoch überarbeitet werden.

Abbreviations

Abbreviation	Meaning
AZ	Magnesium, alloyed with aluminium and zinc
BC	Before Christ
bcc	Body centred cubic
BSE	Back scattered electrons
CCT	Continuous cooling transformation
cDRX	Continuous dynamic recrystallization
CI	Confidence index
dDRX	Discontinuous dynamic recrystallization
DMM	Dynamic material model
DRV	Dynamic recovery
DRX	Dynamic recrystallization
EBSD	Electron backscatter diffraction
EDX	Energy dispersive X-ray
fcc	Face centred cubic
FEG-SEM	Field emission gun – scanning electron microscope
FEM	Finite element models
FFT filter	Fast Fourier Transform filter
gDRX	Geometric dynamic recrystallization
HAGB	High angle grain boundaries
hcp	Hexagonal close packed
IPF	Inverse pole figure
IQ	Image quality
LAGB	Low angle grain boundaries
LVDT	Linear variable differential transducer
LOM	Light optical microscope
mDMM	Modified dynamic material model
mDRX	Meta dynamic recrystallization
ND	Normal direction
OIM	Orientation imaging microscopy
PSN	Particle stimulated nucleation
RD	Rolling direction
RX	Recrystallization
SEM	Scanning electron microscopy
SFE	Stacking fault energy
TD	Transverse direction
α	Hexagonal crystallographic structure of Ti
β	Cubic crystallographic structure of Ti

Symbols

Symbol	Unit	Meaning
A	[mm^2]	Cross-sectional area
A	[s^{-1}]	Material constant (constitutive equations)
A_0	[mm^2]	Initial cross-sectional area
$\mathrm{A_{c1}}$	[°C]	Temperature of the beginning of the austenite formation on heating
$\mathrm{A_{c3}}$	[°C]	Temperature of the completion of the austenite formation on heating
$\mathrm{A_{r1}}$	[°C]	Temperature of the beginning of the ferrite formation on cooling
$\mathrm{A_{r3}}$	[°C]	Temperature of the completion of the ferrite formation on cooling
$\mathrm{B_f}$	[°C]	Bainite finish temperature
$\mathrm{B_s}$	[°C]	Bainite start temperature
c	[MPa^{-1}]	Stress multiplier
d	[mm]	Diameter
D_0	[µm]	Ratio of the starting grain size
d_0	[mm]	Initial diameter
$D(\dot{\varepsilon})$	[-]	Dissipative function
D_R	[µm]	Ratio of the recrystallized grain size
Δd	[mm]	Change in diameter
Δl	[mm]	Change in length
ΔT	[°C]	Change in temperature
F	[N]	Force
G	[MPa s^{-1}]	Content
J	[MPa s^{-1}]	Co-content
l	[mm]	Length
l_0	[mm]	Initial length
m	[-]	Strain rate sensitivity
$\mathrm{M_f}$	[°C]	Martensite finish temperature
$\mathrm{M_s}$	[°C]	Martensite start temperature
n	[-]	Stress exponent
n_WH	[-]	Work hardening coefficient
P	[MPa s^{-1}]	Power
Q	[kJ mol^{-1}]	Apparent activation energy
R	[Jmol^{-1}K^{-1}]	Gas constant
t	[s]	Time
T	[°C]	Temperature
x	[mm]	Axial coordinate
Z	[s^{-1}]	Zener-Hollomon parameter
K, k, K', A, B, c	[-]	Material constants

Symbol	Unit	Meaning
$\frac{d^iS}{dt}$	[MPa (Ts)$^{-1}$]	Rate of production of irreversible entropy
α_{SJ}	[-]	Flow localization parameter
γ’	[-]	Softening parameter
δ_{SS}	[µm]	Steady state grain size
ε	[-]	Engineering strain
$\dot{\varepsilon}$	[s^{-1}]	Strain rate
ε_{c}	[-]	Critical strain
$\dot{\varepsilon}_{\mathrm{min}}$	[s^{-1}]	Minimum strain rate
ε_{n}	[-]	Nucleation strain
ε_n^0	[-]	Limit nucleation strain
ε_{p}	[-]	Peak strain
$\varepsilon_{\mathrm{SS}}$	[-]	Steady state strain
ε_{T}	[-]	True strain
η_{M+R}	[-]	Dissipation efficiency (Murty and Rao)
η_P	[-]	Dissipation efficiency (Prasad)
κ	[-]	Instability parameter (Murty and Rao)
κ_{j}	[-]	Instability parameter (Poletti)
ξ	[-]	Instability parameter (Prasad)
σ	[MPa]	Engineering stress
σ_{C}	[MPa]	Critical stress
σ^I	[MPa]	Isothermal corrected flow stress
σ_{p}	[MPa]	Peak stress
σ_{T}	[MPa]	True stress

Table of contents

1 Introduction

Thermomechanical processing of metallic products [1] has played an important role in the human evolution. Metal-forming operations such as forging, extrusion or rolling are widely used all over the world. One of the earliest metal-forming operations occurred around 3000 BC and was the forging of bronze.

Thermomechanical processes have two main consequences. On the one hand, they influence the macro-scale to obtain desired shapes. On the other hand, modification at the micro-scale occurs, producing changes in the microstructure. Thermomechanical processes describe both heating and shaping operations. Due to these processes, relatively simple materials can become easily a high quality component. Today the interest of the effect of temperature and deformation on the microstructures has been highly increased, because the microstructure determines the mechanical and physical properties of the final product.

It is difficult to perceive a priori which microstructure will be obtained during each thermomechanical treatment. Process parameters such as strain rate, strain, temperature, starting microstructure and the applied cooling method have a profound influence on the microstructure of materials. Therefore, many efforts have been done to predict the final microstructure and to find an optimal processing parameter window for different thermomechanical processes and different alloys.

One possibility to identify and predict deformation mechanisms is to use rheological relationships, known as constitutive equations [2], [3]. Another possibility is to use the so-called deformation mechanism maps, which offer the possibility to select the temperature- and strain rate range for a given alloy to obtain high formability. Different types of these maps got developed in the past, as by Frost and Ashby [4], Raj [5], as well as the so called processing maps, developed by Prasad [6] and Murty and Rao [7]. These last ones are related to the approach of dynamic material model (DMM) and consist of two superimposed maps: an efficiency of power value- and an instability map.

The efficiency of power dissipation and the instability values are calculated from the flow data, and it is stated that this correlates to microstructural changes in the material. Microstructural changes are for example dynamic recrystallization (DRX), dynamic recovery (DRV) and twinning. On the other hand the instability parameter should be related to flow localization, adiabatic heating effects, shear band- or deformation band formation, cracking and formation of voids. Thus, processing maps are constructed to show the area in which good hot formability can be reached, i. e. the area where instabilities do not take place and where the largest value of efficiency of power occurs.

Because of the simplicity of processing maps based on DMM, they are widely used in the industry. On the other hand, many controversies [8], [9], [10], [11] were generated because the physical foundation of the model is not clear. Then, the following questions arise: which type of deformation map is reliable? Are processing maps useful for predicting the optimal processing window? Which changes in the model could be made to get a correlation of deformation mechanisms with process parameters?

To answer the above questions, the aims of the following work were set as follows:

a) to study the hot deformation behaviour of different alloys with different stacking fault energies (SFE), different crystal structures and phases conditions
b) to calculate and compare different types of processing maps
c) to correlate the developed microstructure with the models of processing maps and constitutive equations
d) to make a decision about the acceptance of processing maps by DMM
e) to discuss alternative methods for the calculation of deformation maps.

This work is divided into seven main chapters and a very short description of every chapter is given as follows. The chapter two “State of the art” will give an overview of the background which is useful for understanding this work. This chapter is subdivided into: forming, plasticity, damage, flow localization and flow instabilities, restoration mechanisms, hot deformation of Mg-alloys, Ti-alloys and steel, hot deformation studies: methodology, deformation mechanism maps and constitutive equations. The third part of this work, “Description of methodology” describes the materials used and their chemical composition, and explains the experimental work. In the fourth chapter, “Results” the most relevant results are shown and described. The results for the four different materials are shown separately. In chapter five, “Discussion” firstly a subdivision into the four different studied materials is made. The hot deformation of every material is discussed separately. Then, a discussion is made to figure out if processing maps are working, independently of the material, or not. Chapter six “Summary and conclusions” summarizes the work and gives a final statement about the practicability of processing maps. The last chapter “Outlook” shows ideas for further necessary work.

2 State of the art

This chapter introduces some aspects and concepts to be used along this work. Forming mechanisms will be explained and their main objectives are stated. Afterwards plasticity, damage and restoration mechanisms will be shown. Later on, studies on hot deformation behaviour of investigated materials will be presented. Furthermore, experimental methodology used to study the hot deformation is explained. Finally, the main sub chapters are related to the deformation mechanism maps and to the constitutive equations.

2.1 Forming

Forming is a group of processes in which metallic billets or blanks are shaped by tools or dies. The control of such processes is complex because many influencing parameters have to be considered. Influence factors are the workpiece material, the condition at the tool/workpiece interface, the used equipment, the mechanism occurring during the plastic deformation, the finished product requirements and the applied deformation temperature, strain rate and strain. Metalworking is one of the major technologies and oldest mechanism to fabricate metal products [12].

Forming mechanisms can be classified by the load of forming (tensile, compression, bending), by the temperature (cold or hot forming) and by the form (massive- or sheet metal forming). Processes which belong to massive forming have some specific features. The workpiece undergoes large plastic deformation and results in a change of shape. Furthermore, the amount of material undergoing plastic deformation is much larger than the portion undergoing elastic deformation. Processes for massive deformation are extrusion, rolling, forging and drawing. On the other hand, the characteristics for sheet metal forming processes are different. The deformation causes a change of shape but not in the cross-sectional area, and sometimes the magnitudes of the plastic and elastic deformations are comparable. Processes are for example bending and surface contouring. Nearly all technical used metals and alloys are exposed to a forming process at least once during their production.

The main objectives of the forming processes are:

- to achieve a desired shape
- to improve the workability in subsequent deformation steps
- to reach a desired microstructure

and finally:

- to achieve specific mechanical and physical properties of the workpiece.

Hot forming occurs above a certain temperature which is dependent on the material. If the deformation is carried out at temperatures above $0.4T_\mathrm{m}$, the plastic deformation is influenced by thermally activated processes and therefore the flow stress becomes temperature and strain rate dependent [1]. Furthermore, softening takes place during the deformation, such as DRV or DRX.

2.2 Plasticity

During a deformation process a metal first deforms elastically up to reaching the yield stress where the material begins to deform plastically meaning that the metal retains a permanent change in the shape.

Important criteria to describe the stress-strain curve are the work hardening coefficient n_{WH} and the strain rate sensitivity m. Hollomon proposed in 1945 a simple equation, showing that many alloys obey a simple power law [13], (Equation 1):

$$\sigma = k\,\varepsilon^{n_{WH}} \qquad \textbf{Equation 1}$$

where k and n_{WH} are constants. They are determined from the true stress-strain curve by logarithmic calculus of both sides of the equation. This is the equation of a line whose slope is n_{WH} and that intercept is (ln k) as presented by Equation 2:

$$(ln\sigma) = n_{WH}(ln\varepsilon) + \ln k \qquad \textbf{Equation 2}$$

Generally, the work hardening coefficient is defined by Equation 3:

$$n_{WH} = \frac{\partial \ln \sigma}{\partial \ln \varepsilon} \qquad \textbf{Equation 3}$$

n_{WH} expresses the amount of uniform plastic strain that the material can undergo before strain localization or necking takes place. At low temperatures, meaning temperatures below $0.4T_{\mathrm{m}}$, the stress-strain curve is independent of the strain rate, at least for conventional rates [1].

In the case of higher temperatures, the strain rate has a significant influence on the plastic flow stress. Therefore, the strain rate sensitivity *m* describes the flow dependency on the strain rate. The strain rate sensitivity can be obtained by a power law:

$$\sigma = k'(\dot{\varepsilon})^{m} \qquad \textbf{Equation 4}$$

The strain rate sensitivity may be a constant as in Equation 4 or may depend on the strain rate as in Equation 5.

$$m = \left(\frac{\partial ln\sigma}{\partial ln\dot{\varepsilon}}\right)_{T,\varepsilon} \qquad \textbf{Equation 5}$$

m is determined experimentally by tension or compression tests. At room temperature *m* has values up to 0.015. If the temperature is increased above half of the melting point, *m* will increase rapidly. Therefore, *m* takes values from about 0.05 for moderate temperatures to 0.5 or higher for specific materials. High values can be correlated to superplastic behaviour [1], [14].

For the physical meaning of *n* and *m* it can be said that the work hardening coefficient affects the flow curve up to the uniform strain and the strain rate sensitivity affects the behaviour in the post uniform region. Increasing the values of *n* and *m*, the total strain to failure increases, meaning that the formability of the material increases [13].

2.3 Damage, flow localization and flow instabilities

In the year 1885 the scientist Considère [15] developed a parameter to describe instability for tension. Furthermore, Hart [16] discussed the flow stability in tension in the year 1967 and in 1984 Semiatin and Jonas [17] developed an instability model for deformation under compressive load. In the year 1984 Aifantis was one of the first scientists who introduced the term “material instabilities”. Aifantis et al. described the occurrence and evolution of deformation-induced material instabilities as there are dislocation patterns, shear bands and traveling strain fronts [18]. Until the publication of the work of Aifantis, no convincing theory was available associating plastic instability with material softening.

The flow localization or damage during hot deformation limits the capacity to carry out deformation processes and is influenced by the temperature, the deformation rate and the stress value. One early investigation of the localization of plastic deformation was published by Rice in 1976 [19]. One example of localization in plastic deformation of metals is the so-called Lüders band formation. Furthermore, due to varying flow a concentration of deformation may appear and forms slip bands and shear bands which lead to ductile fracture. A further flow instability is the so-called adiabatic shear band, which get produced due to high strain rates of deformation and large strains. The reason is an increase in the temperature which leads to some strain localization in narrow bands. Adiabatic shear bands are typical nucleation sites for cracks and their propagation [20].

One of the goals in modelling hot working processes is to predict and describe defects and plastic instability phenomena. In the worst case, not only defects can occur, but also catastrophic damage is possible.

2.4 Restoration mechanisms

Restoration mechanisms are related to the decrease of stored energy and dislocation density. Due to cold deformation metals increase their stored energy by increasing the dislocation density. If the material is then heated to elevated temperatures, usually above $0.4T_{\mathrm{m}}$, the strain hardening which is achieved by the deformation, decreases by static restoration processes meaning the material softens due to annihilation and re-accommodation of dislocations, decreasing the stored internal energy [1], [21].

Restoration or softening mechanisms can be classified on the one hand by the occurrence of the mechanism, during or after the deformation, and on the other hand by the mechanism itself: recovery or recrystallization.

Mechanisms which take place during annealing after cold deformation are called static, whereas mechanisms during hot deformation are called dynamic. Furthermore two different types of restoration are possible – recovery and recrystallization. These are competing processes because both are driven by the stored energy and at the same time, both decrease the stored energy. Thus, if recrystallization has occurred, no further recovery is possible. Recovery lowers the driving force for recrystallization and on the other hand, the mechanism of recovery plays an important role for nucleation of recrystallized grains.

Dynamic mechanisms can be found in hot forming industrial processes such as rolling, extrusion and forging. The importance of dynamic restoration in these processes is due to the fact that it lowers the flow stress of the material [22], making the material easier formable.

Another mechanism, called metadynamic recrystallization (mDRX), should be mentioned. This process occurs if the temperature is kept high during a very short period after the hot deformation by a continued growth of nuclei which were formed as a result of DRX [23].

An example which shows the effect of the two different softening mechanisms on the flow stress is displayed in Figure 1 [24]. The flow behaviour is presented for plain carbon steel once alloyed with silicium (Si) (dotted line) and once without a Si addition (full line) for two different strain rates. 2.9% Si are added to a 0.035% C steel and stabilizes ferrite and the bcc lattice is retained even at 1000°C. It can be seen that the steady state flow stress is low in this high stacking fault energy material. If no Si addition is made and the material is in its fcc lattice, the flow curves show much higher stresses (about three times higher) suggesting that the dislocation density is about one order of magnitude larger. In the austenite range, where low to moderate stacking fault energy is characteristic, DRX occurs as seen in the oscillation of the flow stresses for the non-alloyed plain carbon steel. If Si is added to the steel, the shape of the flow curve changes to a typical dynamic recovery flow curve.

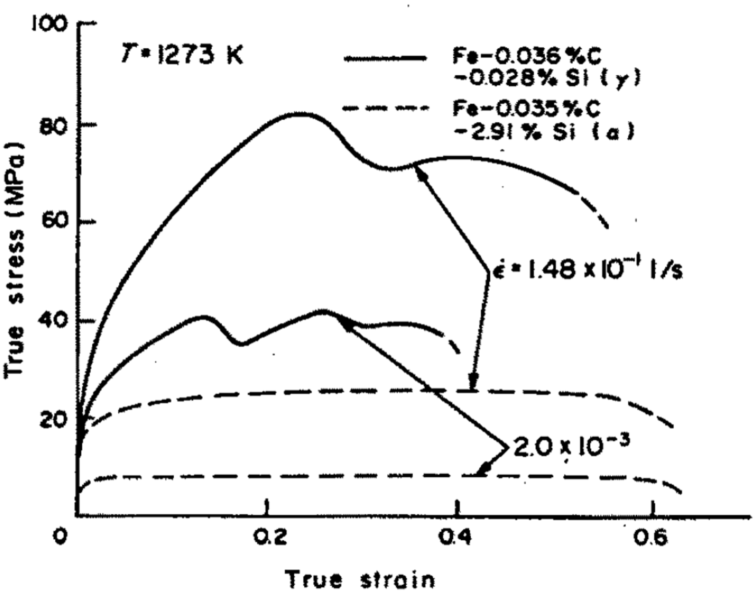

Figure 1. Stress-strain curves showing differences in recovery (dotted line) and recrystallization (full line) [24].

Generally, a flow curve can be split into different areas in which different mechanisms appear. Figure 2 shows the distribution of these areas for typical DRX (blue curve) and DRV (red curve) flow curves. Up to small strains, work hardening, twinning and DRV (in low amount compared to work hardening) may occur. With reaching a critical strain, still work hardening occurs but now DRX is possible to start. In the third stage, flow steady state may be achieved as a consequence of equilibrium between softening produced by DRX and plastic deformation.

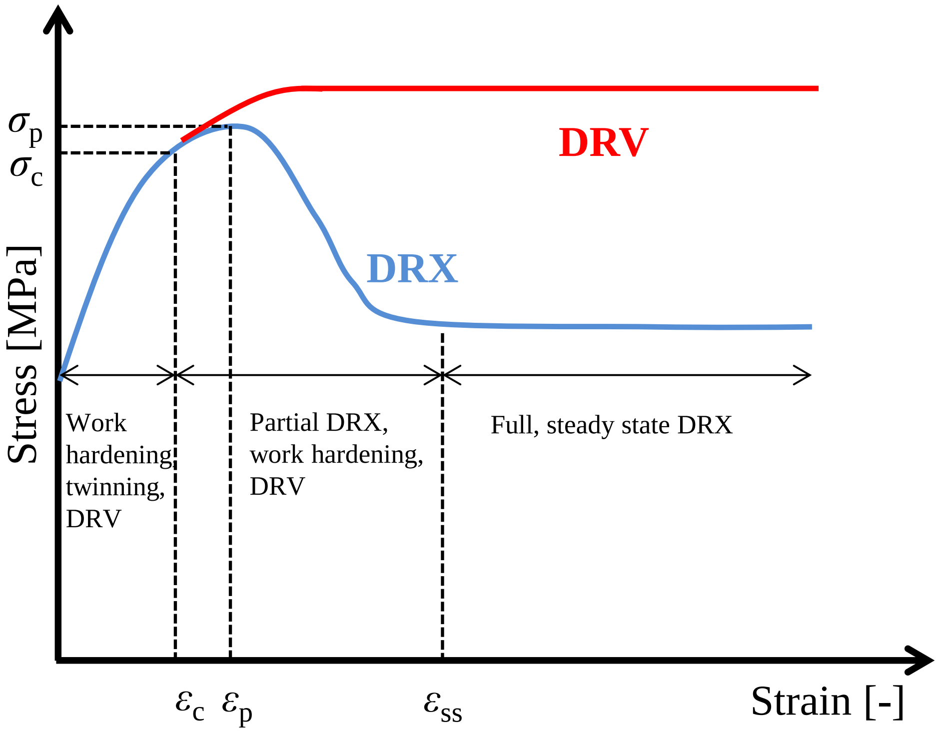

Figure 2. Flow curves representing DRX and DRV behaviours and different mechanisms occurring during the deformation.

2.4.1 Recovery

During deformation at low temperatures (cold working), grains get elongated and it comes to an increase of the dislocation density. An increment of the temperature can result in recovery with a consequently decrement of the dislocation density.

During static recovery mechanisms the dislocation structure of a material changes due to the movement of dislocations via climbing, cross-slipping or gliding [22]. These microstructural changes are: dislocation tangles, cell formation, annihilation of dislocations within cells, subgrain formation and growth. If all or only some of these steps occur, depends on the material, the strain, the deformation and annealing temperature.

The two main mechanisms taking part during recovery to lower the stored energy are annihilation of dislocations and re-arrangement of dislocations into lower energy configurations. Dislocations of opposite sign on the same glide plane can annihilate by gliding towards each other, which is also possible at low temperatures. The annihilation that occurs due to a combination of glide and climb requires higher temperatures because the mechanism of climbing is thermally activated. The rearrangement of dislocations into ordered subgrain boundaries can occur via polygonization or via subgrain formation.

The kinetics of recovery is influenced by every factor which inhibits or promotes the dislocation motion. In particular, it is affected by the temperature, the solute content in the matrix, the presence of second phase particles and the SFE. The influence of the temperature can be seen as follows: with a higher annealing temperature, the recovery is more completed, because dislocations can rearrange much faster. Solute atoms can influence recovery through the SFE, by pinning dislocations or affecting the concentration or mobility of vacancies. Second phase particles may affect the recovery in different ways. When dislocations annihilate or rearrange to form low angle grain boundaries (LAGB), fine dispersed particles may pin the dislocations and thus hinder the recovery. Furthermore, these particles may have a strong pinning effect on subgrains and therefore, stabilize the recovered substructure avoiding subgrain growth. It is necessary, that these particles are stable at high temperatures to keep always the same effect. The SFE determines the energy needed to form stacking faults, which, when formed, will act as barrier for the climb and cross-slip of dislocations. Thus, materials with a high SFE such as aluminium alloys and ferrite tend to recover because the movement of dislocations is easy possible. On the other hand materials with a low SFE tend to the mechanism of recrystallization because arrangement of dislocations in lower energy configurations is impeded by the presence of stacking faults. Magnesium, which has a moderate SFE, should hence recover but Ion et al. [25] showed that DRX is an important mechanism at high temperature deformation. If you increase the temperature, you may “reach” the necessary energy needed to form stacking faults, and they indeed will form, hindering the movement of dislocations, promoting recrystallization. This is all true in the dynamic state, while in the static mechanisms, the dependency on SFE is much less.

If recovery occurs during the hot deformation it is called DRV. The mechanisms during DRV are the same as for static recovery, climb, cross-slip and glide. With beginning of the deformation an increase in the flow stress can be seen because dislocations are interacting and multiplying. With the rise of the dislocation density also the rate of recovery increases. The microstructure is changing and low angle boundaries get formed. If a certain strain is reached, the rates of work hardening and recovery reach equilibrium and the flow stress reaches a steady state. In Figure 3 an overview of the microstructural evolution is given. It can be seen that at the beginning the dislocation density increases and subgrains develop. With a certain strain the dislocation density remains constant and the subgrains remain equiaxed with a constant mean size and misorientation. The original HAGB migrate producing a change of the shape of the grains during deformation. Therefore, the flow stress remains constant due to steady state subgrain size, followed by softening due to cDRX.

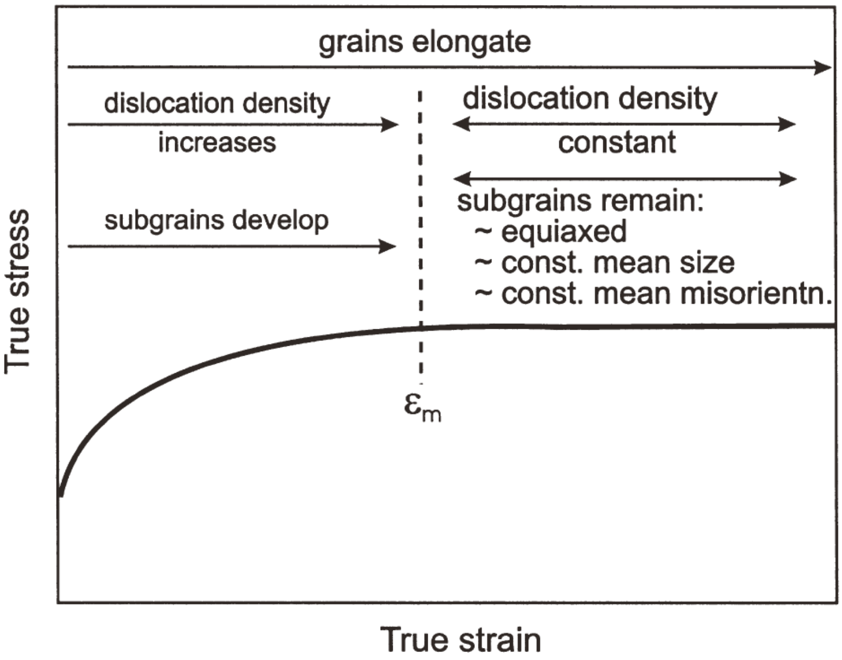

Figure 3. Schematic flow curve showing microstructural changes occuring during DRV [22].

2.4.2 Recrystallization

Recrystallization occurs in metals in which recovery processes are slow. Recrystallization is favoured to emerge if the SFE is low such as in copper or austenite or at high temperatures, where stacking faults can be formed. Analogous to recovery, static or dynamic recrystallization can take place.

Static recrystallization is characterised by the formation of new high angle grain boundaries (HAGB) and consumption of the old deformed structure. Following rules for recrystallization are applied: a) a minimum deformation is necessary to initiate static recrystallization (SRX), b) the temperature at which SRX occurs decreases when the time of annealing increases, c) the temperature at which recrystallization occurs decreases with increasing strain, d) the recrystallized grain size by 100% of recrystallization depends on the stored energy, being smaller for large cold deformation and e) for a given deformation, the recrystallization temperature will be increased on the one hand by a large starting grain size and on the other hand by a higher deformation temperature.

On the other hand, DRX can take place during hot deformation. The discontinuous dynamic recrystallization (dDRX) is similar to the static recrystallization and is characterised by nucleation and growth driven by the stored energy difference between adjacent grains. New grains nucleate from recovered grains and start growing due to a dislocation density difference. Dynamically recrystallized grains may nucleate at original grain boundaries, boundaries of dynamically recrystallized grains or phase boundaries [26]. To initiate DRX a critical deformation (ε_c) is necessary, and this ε_c decreases with decreasing stress. If the material continues to deform, the dislocation density of the new grains increase. Due to the increment of the dislocation density the further growth of grains is reduced. Another factor limiting the growth of new grains is the nucleation of further grains at the migrating boundaries.

Figure 4 shows some stress-strain curves with typical characteristics of DRX at different temperatures and at the same strain rate for a 0.68% C steel. At low deformation temperatures only one broad single peak is observed. As the temperature increases, the curve is shifted to lower stresses and multiple peaks appear. This phenomenon is explained by Luton and Sellars [27] as follows: at low stresses, the material recrystallizes completely before a second cycle of recrystallization begins and this process is then repeated. Therefore, the flow stress, which depends on the dislocation density, oscillates with the strain. At high stresses, subsequent cycles of recrystallization begin before the previous ones are finished. The material is therefore always in a partly recrystallized state after the first peak and the stress-strain curve is smoothed out, resulting in a single broad peak.

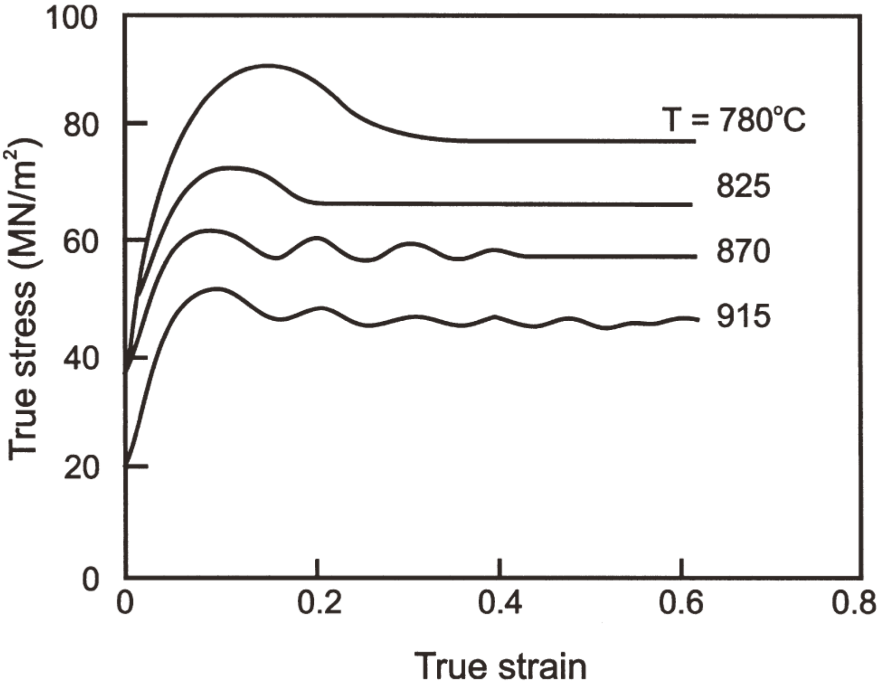

Figure 4. The effect of temperature on the stress-strain curves for a given strain rate [22].

The oscillations in the flow curves are a function of strain rate and temperature of deformation, but also a function of the initial grain size. Sakai and Jonas in [24] explain that the shape of the stress-strain curve is dependent on the ratio of the starting (D_0) and recrystallized grain sizes (D_R). In the case of (D_0/D_R) > 2, the microstructure which develops is only partly recrystallized (except at very high strains) and a smooth curve with a single peak results. If (D_0/D_R) < 2, new grains develop all at the same time because there are enough sites for recrystallization. This structure undergoes further deformation and recrystallizes again, showing an oscillation in the curve.

The shape of the stress-strain curve can be referred to the Zener-Hollomon parameter *Z* and the initial grain size as seen in Figure 5 [22].

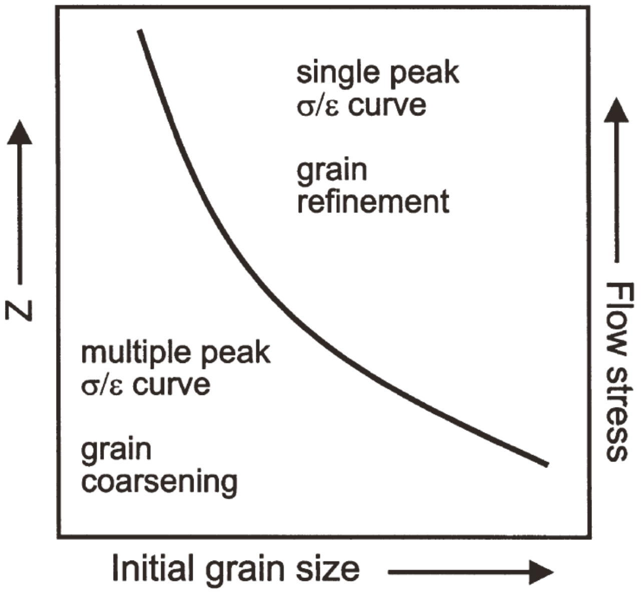

Figure 5. Dependency of the flow stress on *Z* and the initial grain size [22].

The microstructure developed due to DRX can be seen in Figure 6. The dotted lines show the prior HAGB. It can be realised, that in the case that the diameter of the recrystallized grains is much smaller than the diameter of the prior grains, a necklace structure is formed. Figure 6 shows fully recrystallized structures for d) a large initial grain size and for e) a small initial grain size.

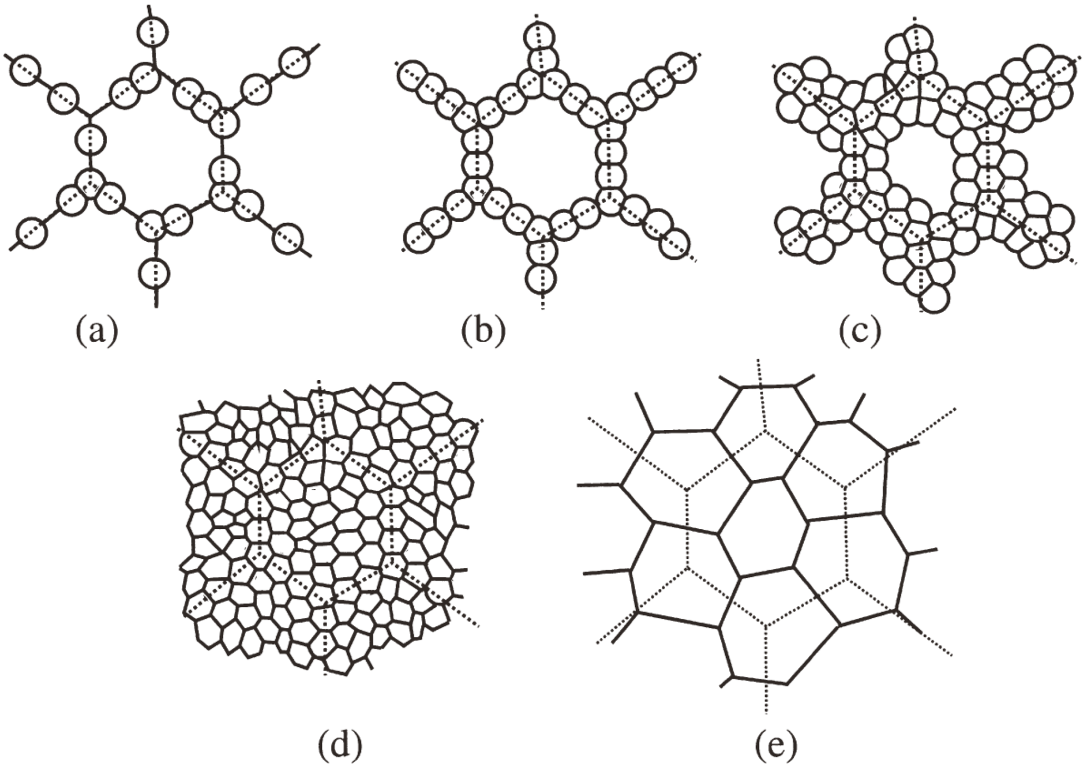

Figure 6. Development of the microstructure during DRX [22].

A further type of DRX is the continuous dynamic recrystallization (cDRX). In the cDRX there is no nucleation as in the dDRX and grains are formed as strain occurs. Two different types of continuous phenomena are described in the literature: the cDRX by progressive lattice rotation and the geometric DRX (gDRX). In both cases, dynamic recovery takes place, and sometimes these mechanisms are referred as extended dynamic recovery.

The mechanism of cDRX is often found in materials in which dislocation motion is inhibited by a lack of slip systems or by solute drag. This occurs for example in Mg-alloys or in Al-alloys. In the work of Gourdet and Montheillet [28] the cDRX process is described as result of a combination of three mechanisms: subgrain boundaries are formed as a result of DRV, subgrain boundaries transform into HAGB and the subgrain boundaries and grain boundaries are eliminated. In other words, the material is strained and a progressive rotation of subgrains adjacent to existing grain boundaries occurs. The old grains develop a misorientation gradient from the centre to the edge and at large strains HAGB may develop. The mechanism occurring in Mg-alloys is shown schematically in Figure 7 [25]. This mechanism is based on the local shearing close to HAGB. Therefore DRV of the geometrically necessary dislocation occurs, resulting in the formation of new subgrains or grains. The process is called progressive because there is no clear division between nucleation and growth steps.

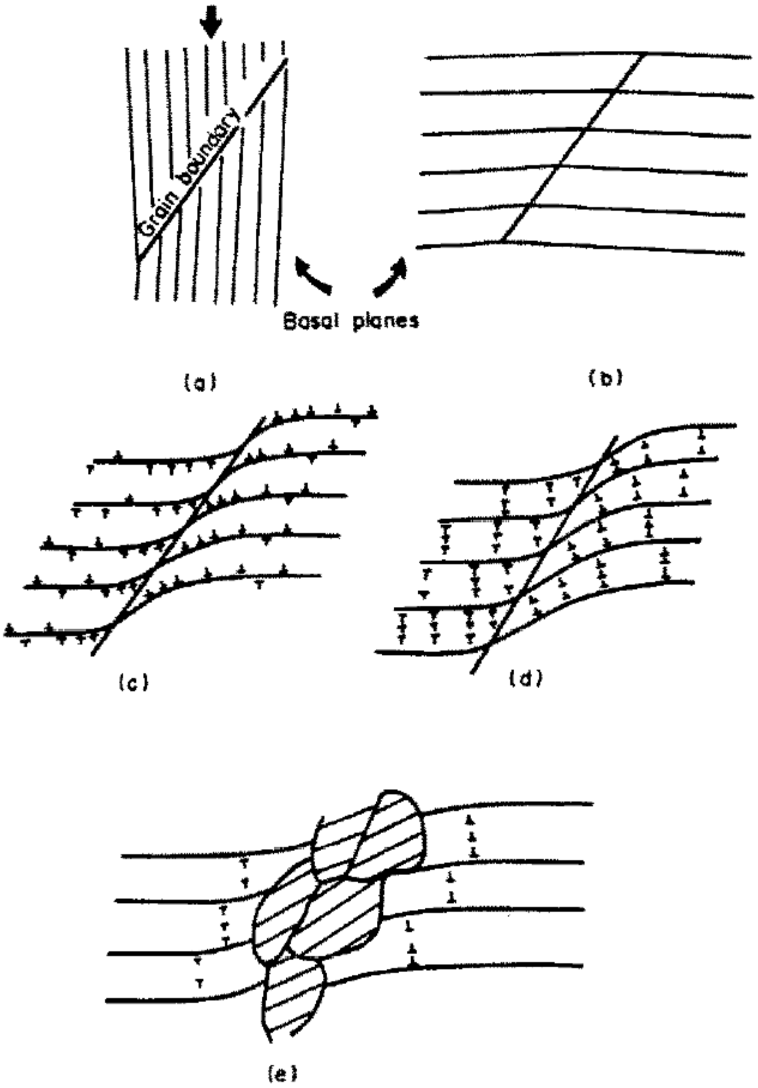

Figure 7. Schematic draw showing cDRX by progressive lattice rotation [25].

The second mechanism, geometric dynamic recrystallization (gDRX) [22] occurs also without nucleation and growth stages. The microstructure evolves homogeneously throughout the material. In the gDRX, the material is hot rolled or hot compressed, meaning that a large reduction in cross section provokes that the original grains become flattened. The steady state subgrain size, which depends on the time and strain rate, is not changing during the deformation. The fraction of HAGB increases with the strain. The boundary becomes serrated with an amplitude comparable to the grain thickness. Finally, and at larger strains, there is a pinching off of HAGB as shown in Figure 8 schematically, and it can be realized that finally a microstructure of only HAGB is formed.

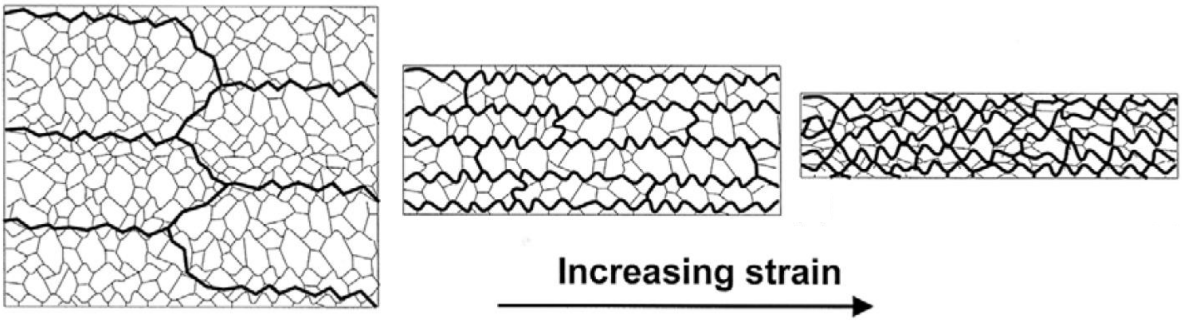

Figure 8. gDRX, with increasing strain HAGB become closer and result in a microstructure of mainly HAGB [22].

2.5 Hot deformation of Mg-alloys

Plastic deformation of Mg-alloys occurs by slip and twin formation [29]. The sliding occurs on a specific crystallographic plane and in a certain direction. At room temperature the most important slip system for the deformation of magnesium is the (0001) basal plane in the $[11\bar{2}0]$ direction. At room temperature only two independent slip systems are available [30]. As defined by the rule of Mises, at least five independent slip systems have to operate in polycrystalline material to achieve a uniform deformation without failure. With increasing the temperature to values higher than 225°C further slip systems (prismatic and pyramidal slip systems) are activated and the plasticity is increasing rapidly and gets similar to that of cubic materials.

Twinning is observed on several crystallographic planes but predominantly on the $[10\bar{1}2]$ plane. The $[10\bar{1}2]$ twinning can occur via tension along the c-axis, preferred with the tension applied perpendicular to the basal plane or it can occur when compression is applied parallel to the basal plane [31]. Twinning is favoured at low temperatures and high strain rates [32]. As mentioned before, at low temperatures the number of slip systems is limited and therefore, twinning easily initiates. For high temperatures, non-basal slips become more active and therefore twinning is suppressed [33].

Many investigations were done on the AZ31 and AZ91 alloy [34], [35], [36], [37], [38], [39], [40], in which it is shown that DRX occurs during the plastic deformation initiated at temperatures at about 300°C. In Mg-alloys both types of DRX can occur: the discontinuous and the continuous dynamic recrystallization. Discontinuous DRX which involves the nucleation of new grains at prior grain boundaries and the consumption of the old structure was reported in many works as in [40]. Furthermore, twinning takes place at low strains to reorient grains which are not suited for slip. The cDRX was found in the work of Peng et al. for AZ31 in a temperature range of 200–280°C and a strain rate range of 0.0004–0.004 s^{-1} [41].

2.6 Hot deformation of Ti-alloys

Pure titanium has a hexagonal (α) crystallographic structure which transforms to a cubic (β) one at 882°C [42]. The unit cells of the hexagonal and of the cubic structure are shown in Figure 9. To achieve better performance with respect to mechanical properties and hence, to widen the application fields, pure titanium is usually alloyed. Alloying elements can be classified into α or β stabilizing elements depending if they increase or decrease the β transformation temperature (T_β) of pure titanium. Elements that stabilize the α-phase raise the β transformation temperature and on the contrary, those who stabilize the β-phase decrease it. Typical α stabilizer are aluminium, oxygen, nitrogen and carbon and β stabilizers are vanadium, molybdenum, manganese and iron.

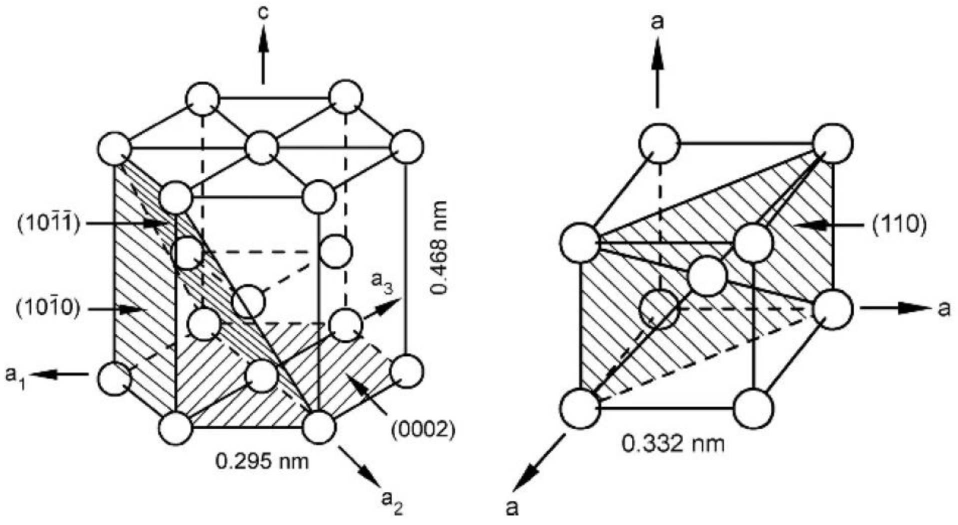

Figure 9. Unit cell of titanium for the α- and β-phase [42].

Ti-alloys can be separated into three different groups: α, α+β and β-alloys. Furthermore, two subgroups can be defined: near α- and near β-alloys.

The α-alloys consist of pure titanium and other alloying elements with an amount lower as 5 vol% of β-phase. Important for their application is, that this type of alloys has higher temperature strength as β-alloys and thus, good creep resistance. Furthermore, they show good weldability. The disadvantage of this group is that they cannot get strengthened by heat treatment because the α-phase is stable.

Near α-alloys contain a small volume fraction of β-phase and have an amount of up to 2% of β stabilizers. This group shows the highest creep resistance.

On the other hand, the β-alloys have a certain amount of β stabilizing elements to avoid the formation of martensite when cooling from the β-field meaning that they can retain 100% of β-phase. If this group is compared to α-alloys they show higher strength up to 300°C and due to their cubic structure better formability. But because of their in general high amount of vanadium, iron, chromium and other heavy elements, their disadvantage compared to α-alloys with aluminium is the density. Therefore, the usage of them in technical applications is less.

The near β-Ti-alloys or also named metastable Ti-alloys, can retain up to 100% β-phase due to quenching. They have a very good formability and a good corrosion resistance.

The α+β-alloys show due to the addition of β stabilizing elements as vanadium, α- and β-phase at room temperature. The Ti-alloy which is widely used belongs to this group: Ti-6Al-4V. This alloy is used in aerospace as well as in biomedical applications [43].

The ductile deformation behaviour of α-Ti-alloys results from the activation of twinning in addition to conventional slip by dislocations. The behaviour of the β-phase also shows twinning but it is limited to the single phase state and decreases with increasing solute content. The main slip directions for α-Titanium are the three close-packed directions of the type <$11\bar{2}0$>. The slip planes are the (0002) plane, the three {$10\bar{1}0$} planes and the six {$10\bar{1}1$} planes. Altogether there are 12 slip systems but they have to be reduced to only 4 independent slip systems, because the shape changes which are produced by the combined action of slip system types 1 and 2 are the same as those of slip system type 3. As for Mg the von Mises criterion is not achieved. The slip systems for the β-alloys are {110}, {112} and {123}. Twinning planes in α-Titanium are {$10\bar{1}2$}, {$11\bar{2}1$} and {$11\bar{2}2$} [42].

2.7 Hot deformation of steel

Pure iron shows three different crystallographic structures. Up to 910°C a cubic body centred (bcc) structure is present, named as α-iron or α-ferrite. Between a temperature range of 910–1390°C, γ-iron (austenite) is present with a face centred structure (fcc). The highest temperature modification is δ-iron which is present until the pure iron melts at 1536°C. If iron gets alloyed with carbon up to an amount of 2.06% it is named steel. Due to the fact that the different atomic structures have different densities, the phase transformation can be easily obtained using a dilatometer. Figure 10 shows the crystallographic structures of ferrite and austenite of pure iron.

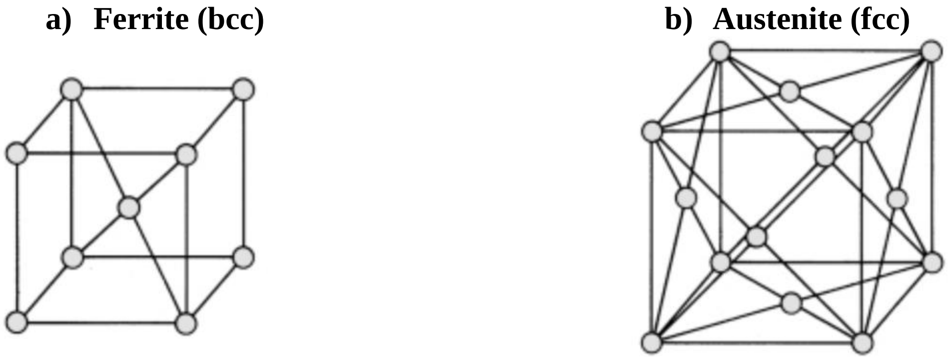

Figure 10. Crystallographic structures of pure iron for a) ferrite and for b) austenite.

Different groups of steels are available and they can be separated due to EN 10020 into non-, micro-, low- and high alloyed steels when referring to other alloying elements than C. Important for the non-alloyed steels is the amount of carbon. The alloyed steels can be separated into low alloyed steels (alloying elements < 5%) with good hardenability, good tempering and good through-hardening ability and high alloyed steels (alloying elements > 5%) with good corrosion and creep resistances.

Many investigations were carried out related to hot deformation of low alloyed steels. In the work of Colás [44] the high temperature flow curve is described for low carbon steel by the superimposition of work hardening and dynamic recrystallization mechanism. In previous works named here, it was determined that DRV is the main important softening mechanism taking place in ferrite due to the high SFE of ferrite. However, the existence of DRX in ferrite was reported in [45], [46] at high temperatures and low strain rates after reaching a critical strain. However, the problem in the past was the distinction between the subgrains which usually form during hot deformation of ferrite, and the new recrystallized grains with the LOM. Nowadays, with the usage of EBSD facilities this distinction can easily be made.

For the austenite, DRV is slow due to its relatively low SFE, and therefore DRX is the “pushing” softening mechanism which will take place once a critical strain is reached. Momeni et al. [47] studied the DRX behaviour of austenite and figured out that DRX occurs at temperatures higher than 950°C. Furthermore, the effect of the strain rate on the DRX behaviour was investigated for 1100°C and it could be clearly seen that even at high strain rates (1 s^{-1}) DRX occurred. The scientists Eghbali et al. [48] investigated in the influence of the deformation temperature on the ferrite grain refinement for low carbon Nb-Ti steel. Flow curves are presented for a deformation temperature of 1100°C and a strain rate of 0.01 s^{-1}, presenting no advice for DRX. If the temperature is decreased to 950°C, the curve shows strong work hardening, but with further decrease of the temperature, just above A_{r3} to temperatures of 845°C, the flow curve does not show work hardening after reaching a strain of 0.32 and the flow stress remains constant with increasing the strain. This behaviour is correlated to a further transformation of austenite to ferrite, which results also in softening, because the produced ferrite is much softer than the austenite under these conditions.

2.8 Hot deformation studies: methodology

In this chapter the methodology of how to study hot deformation will be discussed and summarized. Firstly, hot deformation tests are explained and secondly, advantages as well as disadvantages of hot deformation devices are discussed.

2.8.1 Hot deformation tests

To investigate the flow behaviour, different tests such as tensile, compression or torsion tests can be used [49]. Compression tests are suitable tests to study the flow behaviour and can be related to most commercial bulk metal working processes (rolling, forging, extrusion) which are compressive [50]. Uniaxial compression tests require a minimum of material compared to tensile tests and additionally, the geometry of the samples is easy to produce. Furthermore, relatively large strains can be reached, no or little necking and no or only little damage will occur. Tensile tests are used to simulate processes as for example deep drawing. Torsion tests allow very large strains and strain rates [36], [37] as achieved for example in friction stir welding processes. In the non-uniaxial deformation, which can occur due to friction, temperature gradients, etc., different kinds of stresses are present during the compression tests. Compressive stresses give low deformation and shear stresses high deformation. Thus, during the deformation some kind of deformation cross is produced, as can be seen in Figure 11.

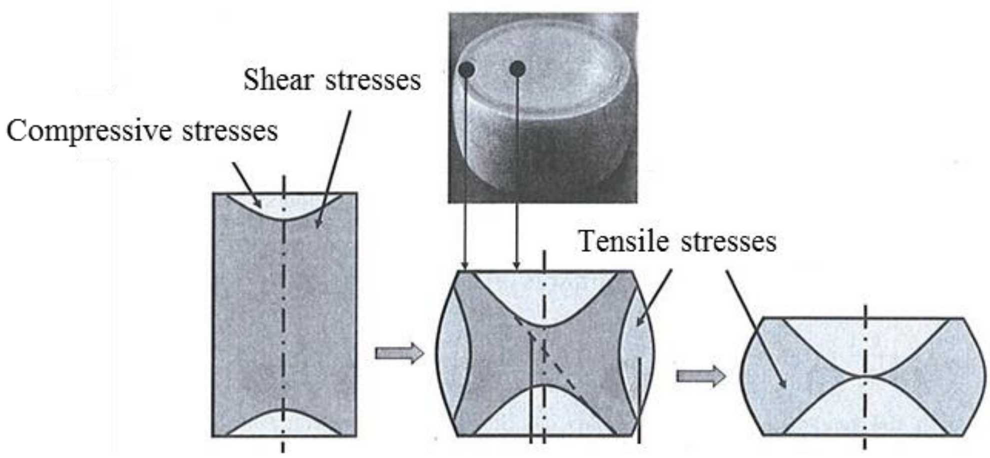

Figure 11. Stress modes in a compression test sample submitted to non-uniform deformation [49].

2.8.2 Hot deformation devices

Different hot deformation devices can be used to carry out hot compression tests. The usual devices are based on a servo-hydraulic deformation system and can be separated into three groups. The first group has a furnace heating (e. g.: Servotest® machine), the second group an induction heating (e. g.: dilatometer) and the third group an ohmic heating system (e. g.: Gleeble®). In this work a Gleeble®1500 or 3800 was used and therefore this paragraph will mainly focus on the Gleeble® system.

The Gleeble® system is a closed loop control thermal and mechanical testing system. The main specifications are a heating rate up to 10000°C/s, a maximum stroke rate of 2000 mm/s, a maximum stroke of 100 mm and a maximum force of 10 tons in tension and 20 tons in compression. There are different control modes like stroke, force, lengthwise change, diameter change, strain and stress. Specimen sizes and geometries can vary between 5–10 mm diameter for round samples, 6–11 mm for square samples and 2 x 50 mm for flat strips. The thermal system is based on direct resistance heating. Due to high thermal conductivity grips, which hold the specimens, high cooling rates can be reached. For measuring the temperature, thermocouples of different types are used. One of the main advantages using a Gleeble® system compared to other systems is the in-situ water quenching possibility. Another advantage in the mechanical system is the option to switch from one control mode to another during any running test. There are different possibilities for heating a sample doing compression tests. The Gleeble® system uses resistance heating because it is faster than other heating methods, as there are furnace heating or induction heating. The disadvantages using furnace heating such as in Servotest® systems or other universal testing machines are the very slow heating rates. The induction heating as used for example in the Bähr dilatometer may have a markedly larger heating rate, still sensitive smaller than the ohmic heating. The direct heating method reaches heating rates up to 10000°C/s [51]. Concerning the cooling rate, while Gleeble® devices allow in situ water quenching, other configurations result either in time delays before water quenching takes place (Universal and Servotest® machines) or in a slower rate due to the use of gases instead of water (dilatometer). On the other hand, the forces reached in the Gleeble® are smaller compared to the 500 kN reached with the Servotest® [52], although larger than in the Bähr deformation dilatometer (20 kN [53]). Also the velocities of 3 m/s at 0 kN and 1.6 m/s at 400 kN reached in the Sevotest® is markedly larger than in the Gleeble® devices.

2.9 Deformation mechanism maps

Many products are produced by forming processes. Therefore, great importance has been attached to optimize the efficiency of hot deformation processes like forging, extrusion and hot rolling, as well as in the control of the microstructure throughout these processes. With the use of processing maps an optimal processing window, i. e. a range of temperatures and strain rates, can be chosen to get a good formability and to avoid instabilities, like shear bands, cracks, porosity or adiabatic influence.

It was observed that flow curves alone cannot be used to interpret the hot deformation behaviour. Furthermore, the characteristics of flow curves can lead to misleading interpretations. Finally, the use of constitutive equations to model hot deformation behaviour is too general, as will be explained in detail in the following chapters.

2.9.1 Different models for deformation mechanism maps

2.9.1.1 Frost and Ashby: creep deformation maps

Frost and Ashby [4] were the first scientists, who realized the importance in deformation mechanism maps to summarize information about forming mechanisms for a given alloy. An example of these maps is shown in Figure 12, where on the abscissa the homologous temperature and on the ordinate the normalized stresses are plotted. The map is divided into different fields describing deformation mechanisms, such as DRX and creep or diffusional flow. The strain rates obtained by a combination of applied stress and temperature are plotted. All these maps are based on experimental creep data, thus at low strain rates (usually below 10^{-1} s^{-1}).

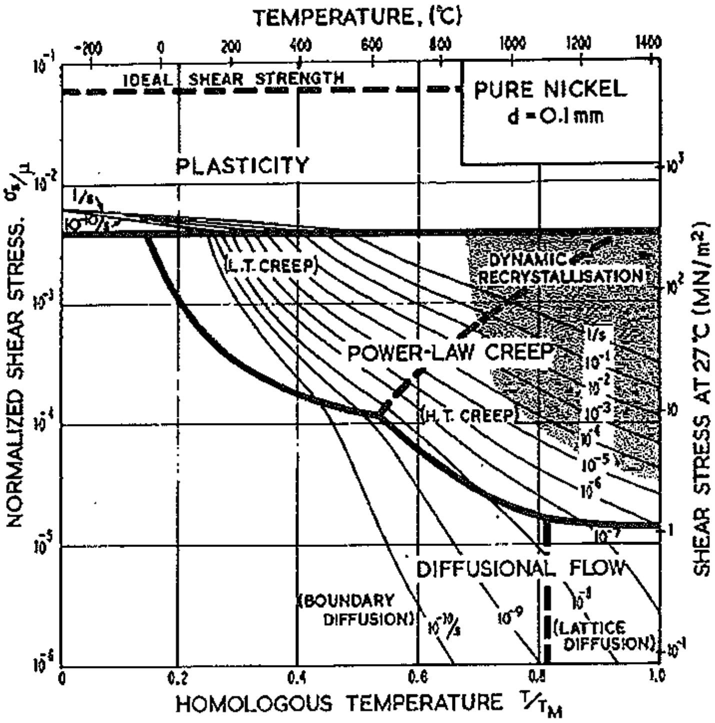

Figure 12. Stress - temperature map, showing the occurring deformation mechanisms during hot deformation of pure nickel [4].

This main idea was then intended to be extended to hot forming processes, carried out at higher strain rates.

2.9.1.2 Raj: damage during hot deformation

Rishi Raj [5] developed processing maps for the use in warm and hot forming processes mainly to describe damage. The maps are calculated for strain rates higher than 10^{-3} s^{-1} (range of hot forming processes) and for temperatures between $0.4T_m$–$0.8T_m$. The maps in these studies are based on cavity nucleation mechanisms, wedge cracking at grain boundaries, DRX and adiabatic heating effects.

The first damage mechanism considered, the cavity nucleation, is based on the influence of hard particles which play an important role for the low temperature ductility. Particles do not deform and therefore, the matrix around the particles is submitted to a larger deformation than the average. This results in an increment of the local work hardening. If the local stress is large enough, the particle may crack. The second damage mechanism considered in these processing maps is wedge cracking. Grain boundaries slide easily at a certain temperature ($\geq 0.4T_m$) and low strain rates and therefore, stress concentrations appear at triple junctions. Then, micro-cracks are produced by diffusion mechanisms. The probability of wedge cracking is dependent on the applied strain rate and deformation temperature. Wedge cracking will preferably occur at low strain rates and high temperatures, because there is enough time to relax the high stresses at triple junctions. On the other hand, if high strain rates are applied, the matrix will deform much faster than the boundaries and therefore, the sliding effects would be negligible and wedge cracking will not occur. In addition to the two applied damage mechanisms, these maps are overlapped with DRX because of the grain refinement or homogenization of the structure and because DRX may produce shear bands. The last superimposed mechanism is adiabatic flow behaviour, which can produce heterogeneities in the material in the form of shear bands, which can lead in catastrophic damage.

These different mechanisms are calculated and plotted separately and then superimposed to delineate the safe processing region. An example for aluminium is shown in Figure 13. Different equations are used for calculating the mechanisms. For the cavity formation at particles a plot of strain rate vs. temperature or various values of the particle size and different values of the ratio of the nucleation strain and the limit nucleation strain $(\frac{\varepsilon_n}{\varepsilon_n^0})$ are used. The ratio of $(\frac{\varepsilon_n}{\varepsilon_n^0})$, in which ε_n is the nucleation strain and ε_n^0 is the limit nucleation strain, is on the one hand dependent on the DRV in the material and on the other hand on the strain rate.

It is observed that at high strain rates, wedge cracking is not taking place, independently of the temperature. The critical strain rate above which stability occurs depends on one hand on the grain size and on the other hand on the size and spacing of second phase particles. The data of Sellars and Tegart [2] is used to define the DRX area in this map for aluminium. If calculating maps for steel many data is published which can be used to determine the recrystallization area. The adiabatic heating effect is determined by assuming that this effect appears at intermediate temperatures and high strain rates. Therefore, the "area" of this map, as the map of DRX, only gives an idea where adiabatic heating effects can occur.

a) Cavity initiation map **b) Wedge cracking map**

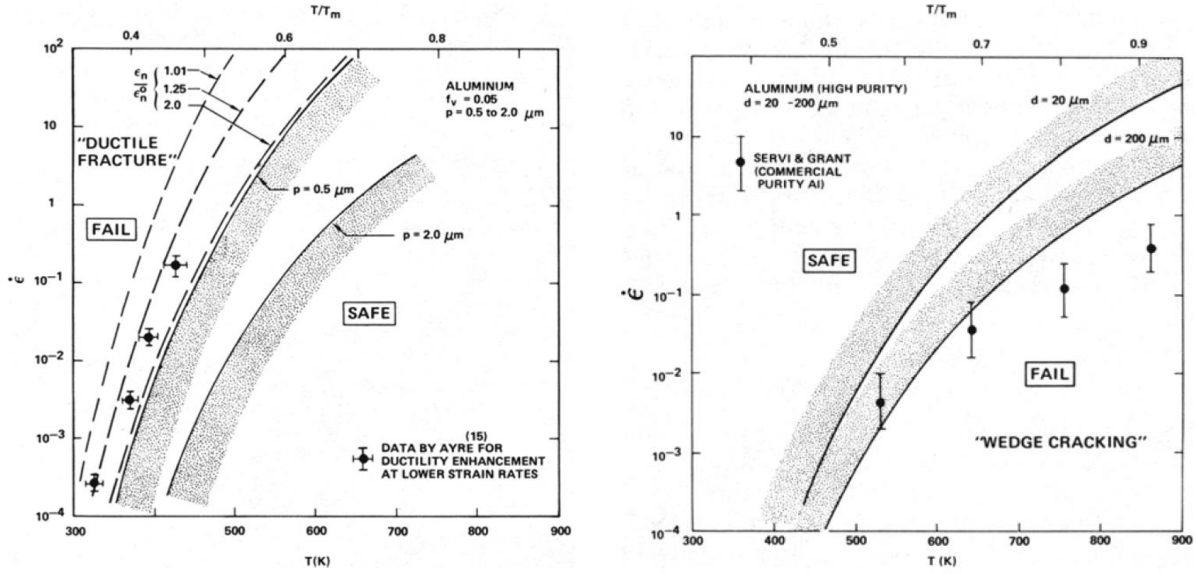

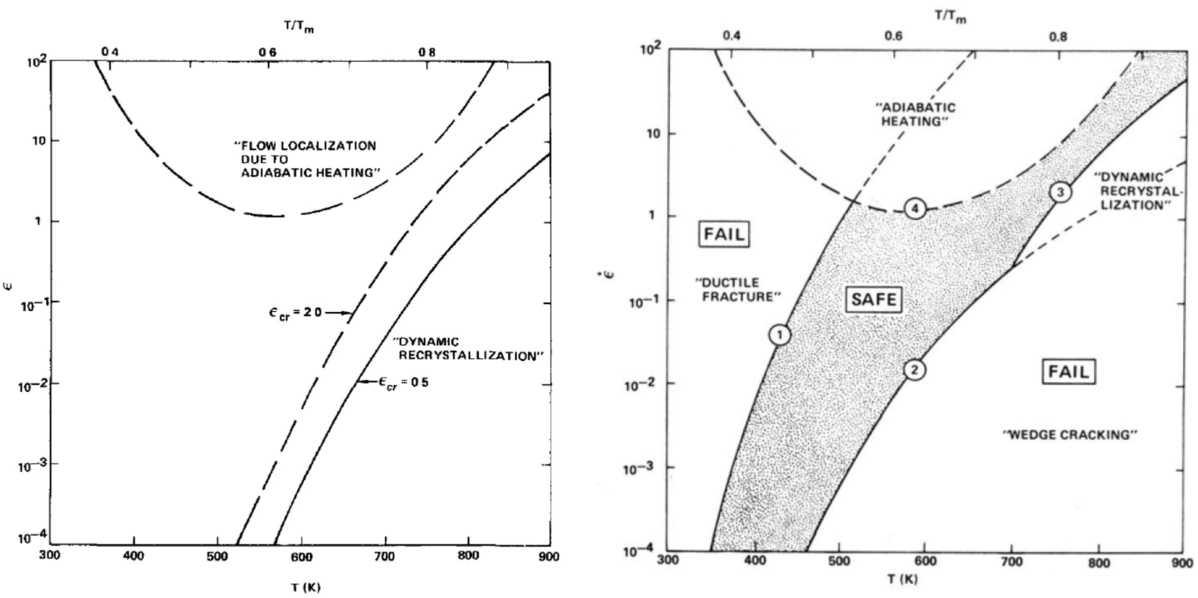

c) DRX map

d) Superimposition of a-c)

Figure 13. Separated deformation and damage mechanisms plotted as processing maps (a-c) and d) superimposed maps, delineating the save and fail area for aluminium [5].

To summarize, these maps show that ductile fracture occurs at high strain rates and low temperatures, whereas wedge cracking appears at low strain rates and high temperatures. DRX without damage is predicted at high strain rates and high temperatures and adiabatic heating at moderate temperatures and high strain rates.

2.9.1.3 Dynamic material model (DMM)

The main idea behind the DMM is to give a possibility to model the material behaviour during the hot deformation. Furthermore, the models should describe the deformation behaviour independently of the SFE, multi-phases or crystal structures.

The processing maps developed using DMM consist of two overlapped maps: an efficiency of power dissipation- and an instability map. It is stated that the efficiency of power of dissipation value can be directly correlated to microstructural changes (e.g.: dynamic recovery, dynamic recrystallization and twinning in the material). Instabilities can be related to flow localization, adiabatic heating effects, shear band formation, cracking and the formation of voids. These maps are developed by Prasad et al. [6].

In this model, the metal processing is considered to be the thermodynamic system. The processing system consists of different parts, as there are the source of power (hydraulic power pack), a storage of power (tools, like anvils or dies) and a dissipator of power (the workpiece) [54]. During the deformation the workpiece undergoes plastic deformation to reach the imposed shape. For the dissipator element (the workpiece) some assumptions should be taken into account:

- The workpiece dissipates all the power which is imparted during the deformation.

- The relation between strain rate and flow stress is non-linear for a wide range. Therefore, the workpiece is a non-linear dissipator of power.
- The system is dynamic, meaning that it depends on the strain rate as an independent variable.
- The system is irreversible because the workpiece undergoes large plastic deformation.
- Finally, the system is far from equilibrium conditions since the strains are not imposed in infinitesimally small increments and the strain rates normally encountered in metal forming are large [54].

The total rate of entropy production consists of two separable terms, the internal and the thermal entropy. These two terms are related to mechanical dissipation and to heat conduction, respectively. The total power dissipated is related to the rate of production of internal entropy $d^{i}S/dt$ (Equation 6):

$$P = \sigma \cdot \dot{\varepsilon} = \frac{d^{i}S}{dt} T \geq 0$$ **Equation 6**

The inequality sign mentions irreversible deformation. For any given temperature, the input power P given to the workpiece is $P = \sigma\dot{\varepsilon}$. The proposed partition is then mathematically expressed as:

$$P = \sigma \cdot \dot{\varepsilon} = \int_{0}^{\dot{\varepsilon}} \sigma d\dot{\varepsilon} + \int_{0}^{\sigma} \dot{\varepsilon} d\sigma = G + J$$ **Equation 7**

in which *G* is interpreted as the power dissipated by plastic work and converted into heat, although this statement is not proved. The remaining small part is stored as lattice defects. Furthermore, *J* is attributed to metallurgical mechanisms. Similarly as for *G*, *J* is attributed to be related to the metallurgical changes, although there is no thermodynamically based statement for this. In Figure 14 the relationship interpreted by the DMM between the power and the dissipation due to heat transfer and metallurgical phenomena is shown for constant temperature and strain. The content *G* is related to the area under the curve and the co-content *J* to the area above the function.

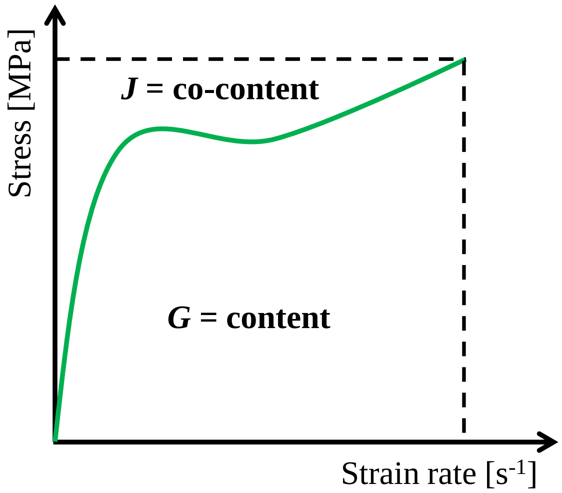

Figure 14. Schematic representation of the *G* and the *J* co-content for a non-linear dissipator.

The physical interpretations of *G* and *J* are stated to be derived from thermodynamic principles, and although some separation of thermal and mechanical dissipation can be found in thermodynamics, such as in [55], the definition of *J* and *G* could not be identified. For any given temperature and strain the relation between *J* and *G* can be expressed as in Equation 8:

$$\left(\frac{\partial J}{\partial G}\right)_{T,\varepsilon} = \left(\frac{\partial \ln \sigma}{\partial \ln \dot{\varepsilon}}\right)_{T,\varepsilon} = m$$ **Equation 8**

J can be evaluated by integrating Equation 9 as:

$$J = \int_0^{\sigma} \dot{\varepsilon} d\sigma$$ **Equation 9**

With the use of Equation 10

$$\dot{\varepsilon} = K'\sigma^{\left(\frac{1}{m}\right)}$$ **Equation 10**

and Equation 7, *J* can be calculated as shown in Equation 11:

$$J = \int_0^{\sigma} \dot{\varepsilon} d\sigma = \int_0^{\sigma} K'\sigma^{\left(\frac{1}{m}\right)} d\sigma = \left[\frac{K'm\sigma^{\left(\frac{1}{m}\right)+1}}{m+1}\right] = \frac{mK'\sigma^{\frac{1}{m}}\sigma}{m+1} = \frac{m\sigma\dot{\varepsilon}}{m+1}$$ **Equation 11**

The maximal possible *J* value (Equation 12) is

$$J_{max} = \frac{P}{2}$$ **Equation 12**

for m = 1 and where the workpiece acts as a linear dissipator. The representation of J_{max} is given in Figure 15 for an ideal linear dissipator.

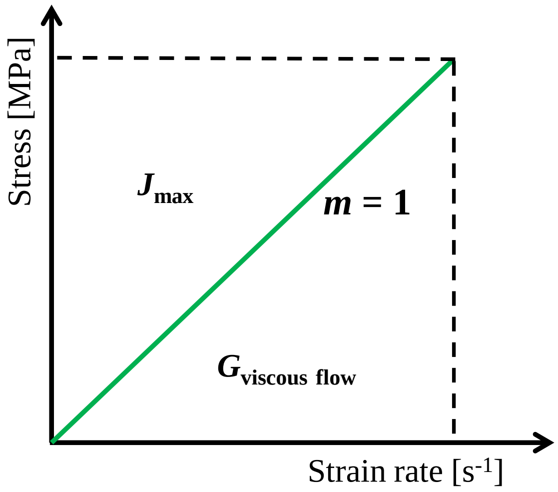

Figure 15. Schematic representation of J_{max}.

The efficiency of power dissipation (Equation 13) is defined as the ratio of the J dissipated by the system with respect to J_{max}.

$$\eta_P = \frac{J}{J_{max}} = \frac{2m\sigma\dot{\varepsilon}}{\dot{\varepsilon}\sigma(m+1)} = \frac{2m}{m+1} \qquad \textbf{Equation 13}$$

where the subscript “P” refers to the model expressed above developed by Prasad et al. For the integration of J, m is assumed to be independent of the strain rate and the temperature. However, m is dependent on these parameters and this is the reason why Murty and Rao developed the mDMM.

Mechanisms like DRV, DRX, dynamic dissolution or growing of particles, dynamic phase transformation and any dynamic metallurgical transformations will lead to changes in the microstructure which will be reflected in the co-content J. The dimensionless parameter η_P is plotted as a function of temperature and strain rate for a given strain to obtain a map.

Furthermore, if a material obeys the power creep law $m = 1/n$ (for a given temperature and strain), the split-up of G and J is related to both, the exponent n or its reciprocal m. At high stresses or multiphase transformation, materials do not obey this power law but still obey the relationship of $\eta = J/J_{max}$. In Figure 16 the possibility for the maximal J value is shown. The area below each curve represents the corresponding J and is correlated to n and m.

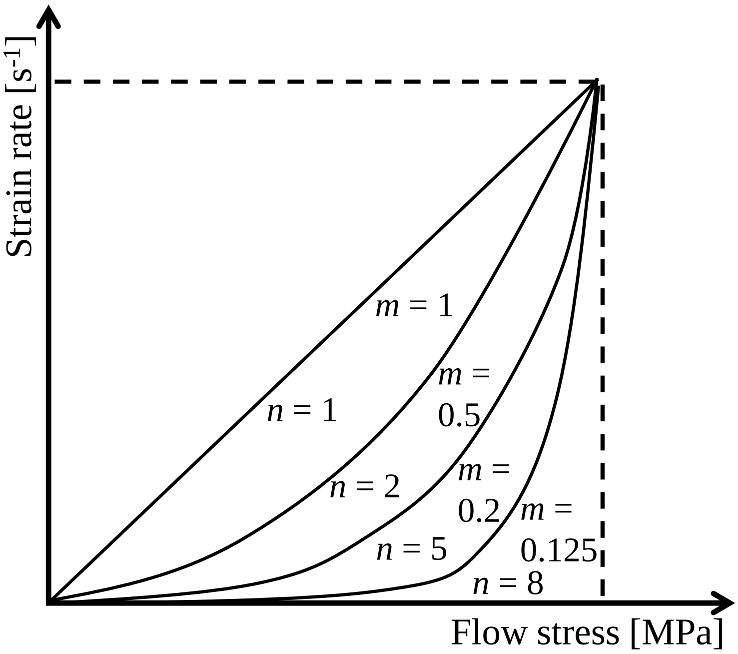

Figure 16. The maximal *J* value is given for a linear dissipator in the case *n* = *m* = 1.

Many scientists were and still are using the approach of DMM to calculate processing maps for different metal alloys [56], [57], [41], [58], [59], [60]. Prasad et al. are using the DMM for different alloys as there are e. g. titanium and AZ31. In their first work for titanium [56], a pure α-Titanium, a Ti-6Al-4V and IMI 685 (near α-Ti-alloy) were investigated. The aim was to correlate flow curves and the obtained microstructures with the calculated maps. In work [57] the Mg-alloy AZ31 was deformed and quenched with water. In this work the anisotropy of hot working was investigated because due to thermomechanical treatment strong crystallographic texture got developed. Processing maps were calculated for the rolling direction (RD), the normal direction (ND) and the transverse direction (TD) specimens. The maps of TD and ND specimens showed the same trend, but RD differs. For TD and ND two DRX regions were seen in the map and also confirmed with micrographs. For the RD only one section of DRX was seen. In the work of Anbuselvan et al. [59] an extruded ZE41A Mg-alloy was investigated. Hot compression tests were carried out using a servo-controlled universal testing machine. The area with the highest dissipation efficiency value was obtained at a temperature of 450°C for a strain rate of 0.01 s^{-1}. With the obtained micrograph, DRX was proven and the processing maps based on DMM worked. It should be noted, that in most of the works presented in the literature, less information of experimental issues such as cooling rate and barrelling are analysed. Thus, sometimes static RX is interpreted as DRX due to slow cooling rates. Furthermore, LOM pictures positioned at any position in a heterogeneously deformed sample are presented and are correlated to the global strain rate and temperature of deformation.

2.9.1.4 Modified DMM

Murty and Rao developed a model [7] based on the DMM of Prasad, called modified DMM (mDMM). They explained that because the strain rate sensitivity *m* varies with the strain rate and the temperature, the *J* cannot be obtained as from Equation 11, since *m* is not constant.

Therefore, the calculation of *J*, which is necessary for the calculation of η, will be erroneous [7]. Murty and Rao use the same definition of η as Prasad, but the calculation varies [61], [62]. The calculation is based on the integration of *G* (Equation 14), in which $\dot{\varepsilon}_{min}$ is the minimum strain rate experimentally tested.

$$G = \int_0^{\dot{\varepsilon}_{min}} \sigma d\dot{\varepsilon} + \int_{\dot{\varepsilon}_{min}}^{\dot{\varepsilon}} \sigma d\dot{\varepsilon} = \left[\frac{\sigma\dot{\varepsilon}}{m+1}\right]_{\dot{\varepsilon}=\,\dot{\varepsilon}_{min}} + \int_{\dot{\varepsilon}_{min}}^{\dot{\varepsilon}} \sigma d\dot{\varepsilon} \qquad \textbf{Equation 14}$$

The first term of the integral (Equation 15) is evaluated by assuming the power law (Equation 4).

$$\int_0^{\dot{\varepsilon}_{min}} \sigma d\dot{\varepsilon} = \int_0^{\dot{\varepsilon}_{min}} K\dot{\varepsilon}^m d\dot{\varepsilon} = \left[\frac{K\dot{\varepsilon}^{m+1}}{m+1}\right]_{\dot{\varepsilon}=\dot{\varepsilon}_{min}} = \\ = \left[\frac{\sigma\dot{\varepsilon}^{m+1}}{\dot{\varepsilon}^m(m+1)}\right]_{\dot{\varepsilon}=\dot{\varepsilon}_{min}} = \left[\frac{\sigma\dot{\varepsilon}}{(m+1)}\right]_{\dot{\varepsilon}=\dot{\varepsilon}_{min}} \qquad \textbf{Equation 15}$$

For the calculation of the second term of Equation 14 usually a cubic spline is used to fit the experimental data. Finally $\eta_{\mathrm{M+R}}$ can be calculated using Equation 16:

$$\eta_{\mathrm{M+R}} = \frac{2J}{P} = \frac{2(P-G)}{P} \qquad \textbf{Equation 16}$$

Different authors [63] were using the model of Murty and Rao because they agreed in the better mathematical expression. Furthermore in the work of Poletti et al. [64] a comparison between these two approaches was made and as a result it is mentioned that the behaviour of the material fits better for the mDMM as for the DMM. For this investigation, Ti662 unreinforced and reinforced with TiC particles were undergone compression tests using a Gleeble® and a Servotest® machine. Afterwards using the equation above η_{P}, $\eta_{\mathrm{M+R}}$ and *m* were calculated. The values were plotted in one diagram and the comparison showed that the tendencies of *m* and η_{P} values are similar. The $\eta_{\mathrm{M+R}}$ showed fluctuating values according to the flow behaviour which does not obey the power law. Finally the model of Murty and Rao is in better agreement with the microstructure and the flow curves shapes.

2.9.2 Flow instability parameters by DMM

The criterion of flow instability based on the continuum principles as applied to large plastic strain proposed by Ziegler [65], in which the system will become instable when:

$$\frac{\partial D}{\partial \dot{\varepsilon}} < \frac{D}{\dot{\varepsilon}} \qquad \textbf{Equation 17}$$

where *D* ($\dot{\varepsilon}$) is the dissipative function of a material exposed to plastic deformation at a given temperature. In the DMM, what is understood as “microstructural instabilities” is derived from a “microstructural dissipation”, meaning *D* ($\dot{\varepsilon}$) is equivalent to the *J* co-content. However and as already mentioned for the definition of *J* and *G*, this is an assumption that lacks of proofs. This represents the power dissipation through microstructural changes and the Equation 17 is transformed to [66] Equation 18:

$$\frac{\partial J}{\partial \dot{\varepsilon}} < \frac{J}{\dot{\varepsilon}}$$ **Equation 18**

which can be written as in Equation 19:

$$\frac{\partial lnJ}{\partial ln\dot{\varepsilon}} < 1$$ **Equation 19**

Assuming the power law nature of stress distribution (Equation 20),

$$\sigma = K\,\dot{\varepsilon}^{m}$$ **Equation 20**

the *J* co-content is given as Equation 21:

$$J = \int_0^\sigma \dot{\varepsilon} d\sigma = \frac{m}{m+1}\sigma\dot{\varepsilon}$$ **Equation 21**

and logarithmic calculus gives Equation 22:

$$\ln J = \ln\left(\frac{m}{m+1}\right) + \ln\sigma + \ln\dot{\varepsilon}$$ **Equation 22**

Differentiating Equation 21 with respect to ln $\dot{\varepsilon}$ gives Equation 23:

$$\frac{\partial \ln J}{\partial \ln \dot{\varepsilon}} = \frac{\partial \ln(\frac{m}{m+1})}{\partial ln\dot{\varepsilon}} + \frac{\partial \ln\sigma}{\partial ln\dot{\varepsilon}} + 1$$ **Equation 23**

Finally, using the strain rate sensitivity and Equation 23, the instability as obtained by Prasad is [67] given with Equation 24:

$$\xi = \frac{\partial \ln\left(\frac{m}{m+1}\right)}{\partial \ln \dot{\varepsilon}} + m < 0$$ **Equation 24**

If a power law is assumed (Equation 20), the first term in Equation 24 will be zero and the approach reduces to $\xi = m < 0$.
Murty and Rao [61], [68] developed their instability parameter similarly than the Prasad’s ξ as in Equation 25:

$$\kappa = \frac{2m}{\eta} - 1 < 0$$ **Equation 25**

This equation uses the approach of $2m < \eta$ and if $J = 0 \Rightarrow \eta = 0$ and results that instability for any flow stress distribution can be written as Equation 26:

$$2m < \eta \leq 0 \qquad \textbf{Equation 26}$$

These instability criteria (Prasad and Murty and Rao) have a strong dependence on the strain rate sensitivity m. To avoid this, another instability parameter κ_j (Equation 27) was developed just using Equation 19 [69].

$$\kappa_j = \frac{\partial lnJ}{\partial ln\dot{\varepsilon}} - 1 < 0 \qquad \textbf{Equation 27}$$

In the work of Xiong et al. [70] a comparison for different flow instability criteria is given for a Ti-alloy. It is mentioned although the instability criteria of Prasad and Murty and Rao are quite different, the tendency of the instability maps is the same.

Montheillet et al. [9] based in basic thermodynamics, derived the following instability condition using the concept that all the input power is dissipated, meaning $D = P$.

$$\frac{dP}{d\dot{\varepsilon}} < \frac{P}{\dot{\varepsilon}} => \dot{\varepsilon}\frac{\partial\sigma}{\partial\dot{\varepsilon}} + \sigma < \sigma => m < 0 \qquad \textbf{Equation 28}$$

2.9.3 Instability criterion by Considère

Considère proposed one of the first criteria to determine the starting point of flow instabilities at room temperature. During a tensile test the force on the sample increases due to work hardening and the cross section decreases. At the point of maximal force, flow instability occurs and flow localization takes place producing necking. This is named geometric softening or Considère criterion [71]. This criterion will not be used in this work, and is introduced here as a base of the following instability criterion.

2.9.4 Instability criterion by Semiatin and Jonas

The flow localization parameter α_{SJ} proposed by Semiatin and Jonas [17] is based on variations in strain, strain rate and temperature within the workpiece required to maintain force equilibrium. This parameter is derived similarly as the one developed by Considère [15] for tension and which was modified by Hart for visco-plastic materials [16].

In the case that there are no inertial effects, the axial force F transmitted through a cylindrical workpiece remains constant. Using an axial coordinate by x, defined with respect to specimen or material coordinates, this condition is $\mathrm{d}F/\mathrm{dx} = 0$ (and in normalized terms: $\mathrm{dln}F/\mathrm{dx} = 0$). Under uniaxial stress conditions, the axial force is $F = \sigma A$, where A = the cross-sectional area of the workpiece and σ is the axial principal stress. At any time t, force equilibrium requires (Equation 29):

$$\left.\left(\frac{\partial lnF}{\partial x}\right)\right|_t = 0 = \left.\left(\frac{\partial lnA}{\partial x}\right)\right|_t + \left.\left(\frac{\partial \ln \sigma}{\partial x}\right)\right|_t \qquad \textbf{Equation 29}$$

In the most general case, the normalized gradient in cross section at any time can be expressed in terms of the variation in initial cross section A_0 and the total strain ε at any point (Equation 30):

$$\left(\frac{\partial lnA}{\partial x}\right)\Bigg|_t = \left(\frac{dlnA_0}{dx}\right) - \left(\frac{\partial \varepsilon}{\partial x}\right)\Bigg|_t$$ **Equation 30**

due to constant volume assumption.

A dependence $\sigma = \sigma\ (\varepsilon,\ \dot{\varepsilon},\ T)$ is assumed, in which the influence of each can be described independently of the other two. Finally, any variation in the flow stress of the material, dσ, is considered to involve the following three components as in Equation 31:

$$d\sigma = \left(\frac{\partial \sigma}{\partial \varepsilon}\right)\Bigg|_{\dot{\varepsilon},T} d\varepsilon + \left(\frac{\partial \sigma}{\partial \dot{\varepsilon}}\right)\Bigg|_{\varepsilon,T} d\dot{\varepsilon} + \left(\frac{\partial \sigma}{\partial T}\right)\Bigg|_{\varepsilon,\dot{\varepsilon}} dT$$ **Equation 31**

The first term is neutral or destabilizing if flow softening occurs. The second term is usually stabilizing because the strain rate sensitivity $m > 0$. The third term, the temperature dependent term is typically destabilizing describing thermal softening. Now, the strain and the thermal terms are put together and a normalized, constant strain rate strain hardening rate γ' (softening parameter) is defined as in Equation 32:

$$\gamma' = \left(\frac{1}{\sigma}\frac{d\sigma}{d\varepsilon}\right)\Bigg|_{\dot{\varepsilon}} = \frac{\left(\frac{\partial \sigma}{\partial \varepsilon}\right)\Big|_{\dot{\varepsilon},T} d\varepsilon + \left(\frac{\partial \sigma}{\partial T}\right)\Big|_{\varepsilon,\dot{\varepsilon}} dT}{\sigma d\varepsilon}$$ **Equation 32**

With the definition of γ' and using m, the second term on the right hand side of Equation 29 is found to be (Equation 33):

$$\left(\frac{\partial \ln \sigma}{\partial x}\right)\Bigg|_t = \gamma' \left(\frac{\partial \varepsilon}{\partial x}\right)\Bigg|_t + m\left(\frac{\partial ln\dot{\varepsilon}}{\partial x}\right)\Bigg|_t$$ **Equation 33**

Using Equation 29, Equation 30 and Equation 33, the load equilibrium equation is given by Equation 34:

$$m\left(\frac{\partial ln\dot{\varepsilon}}{\partial x}\right)\Bigg|_t = \left(\frac{\partial \varepsilon}{\partial x}\right)\Bigg|_t (1-\gamma') - \frac{dlnA_0}{dx}$$ **Equation 34**

This equation relates the axial strain rate and strain gradients to the material properties and A_0 (x). Otherwise it is possible to find an equation as Equation 35:

$$m\delta \ln \dot{\varepsilon} = (1-\gamma')\,\delta\varepsilon - \delta lnA_0$$ **Equation 35**

which shows the variation of ε, $\dot{\varepsilon}$, A_0 between a given material point and its neighbour.

Finally, the α_{SJ} parameter is defined as in Equation 36:

$$\alpha_{SJ} = -\frac{\delta \ln \dot{\varepsilon}}{\delta\varepsilon}$$ **Equation 36**

If there is no initial variation of cross section $\delta ln A_0 = 0$, an initial variation in hardness state may give rise to strain and strain rate gradients whose growth may be evaluated by the α_{SJ} parameter obtained as Equation 37:

$$\alpha_{SJ} = -\frac{\delta ln\dot{\varepsilon}}{\delta\varepsilon} = \frac{\gamma' - 1}{m}$$ **Equation 37**

α_{SJ} can be used to determine the tendency of a material to form marked or catastrophic strain concentrations. Furthermore, α_{SJ} is a function of the material properties, γ' and *m*, either or both of which may be functions of ε, $\dot{\varepsilon}$ and *T*. Flow localization corresponds to $\alpha_{SJ} > 0$, this corresponds to materials that exhibit $\gamma' > 1$, and that is a large flow softening rate (stress and strain are both negative in compressive deformation). Materials will show significant flow localization in the case $\alpha_{SJ} \geq 5$.

2.9.5 Controversies

Many controversies were generated with respect to the development of DMM, as shown in [8], [9], [10] and [11]. The first scientists who criticized the approach of DMM by Prasad were Montheillet et al. [9]. Montheillet et al. criticize the way of separating the terms *G* and *J* into thermal and metallurgical processes, respectively. In the DMM metallurgical processes which occur during the hot working are associated only with *J*. To calculate the maximum workability, the dissipation efficiency value in Equation 13 has to be maximised. Thus, the goal is to determine the temperature and strain rate range, in which the *m* values reach their highest values. However, if the separation of *G* and *J* is not correct, meaning that *G* and *J* are both contributing to the mechanical dissipation, the determination of η will be wrong. The analysis concluded that higher values of *m* are correlated to lower rates of flow concentration and that, therefore, it makes more sense to analyse both, the sign and the value of *m* in form of a processing map. Sudipto Ghosh describes in [8] three points of discrepancy with the DMM approach regarding to the microstructural evolution. Firstly he points out that according to DMM the η value for pure diffusional flow is 1, while for DRX the η value is between 0.3–0.5. However, if no microstructural changes occur during diffusional flow, and microstructural changes do occur during dynamic recrystallization, what is the information given by η? The second investigated point regards structural superplasticity and the third point explains that if DMM is based on thermodynamics, it should be applicable for any system that is dynamic. This means also liquids, glass and polymers should show this behaviour, but they don’t.

Due to these reasons Ghosh is the opinion that neither η nor *m* provides any information on partitioning of energy dissipation between dissipation through storage and thermal dissipation. In another work of Ghosh [10] he criticizes the usage of DMM for predicting flow localization. He explains that in some cases the flow predictions are not only not good but give incorrect predictions and furthermore he states, that the instability parameter by Semiatin and Jonas shows good prediction of damage. Bozzini and Cerri [11] analyse the numerical reliability of hot working processing maps. It is mentioned that data elaboration has a critical bearing on the final results of the maps.

2.10 Constitutive equations

Generally, constitutive equations are rheological relationships between two or more physical parameters. They are used for a specific material and give information about the response of the material if some “force” is applied. Furthermore, constitutive equations were developed to correlate deformation parameters as there are, the strain rate, the stress and the temperature, with an activation energy Q and a stress exponent n, both related to the deformation mechanisms.

The power creep law describes the correlation of strain rate, temperature of deformation and stress in the low stress range as [72]:

$$\dot{\varepsilon} = A\sigma^n \exp(-\frac{Q}{RT})$$ **Equation 38**

while at high stresses, an exponential relationship is used:

$$\dot{\varepsilon} = A \exp(\beta\sigma) \exp(-\frac{Q}{RT})$$ **Equation 39**

Sellars and McTegart studied the mechanism of hot deformation intensively [2] and proposed a correlation for hot deformation data in the form of Equation 40. Therefore, they combined the power creep law for low stresses (Equation 38) and an exponential law for high stresses (Equation 39):

$$\dot{\varepsilon} = A\,(\sinh c\sigma)^n \exp(-\frac{Q}{RT})$$ **Equation 40**

A and *c*, are constants independent of the temperature, and *R* is the gas constant. This equation is used to describe the interdependence of the stress value with the strain rate and the temperature.
Furthermore, these equations can be correlated to Zener-Hollomon parameter *Z*, defined as:

$$Z = \dot{\varepsilon} \exp(\frac{Q}{RT})$$ **Equation 41**

With the use of n and Q, an idea about the occurring hot deformation mechanism can be given. In the case that $n = 1$ the mechanism can be related to diffusional flow (movement of vacancies in the bulk of the material), $n = 2$ means grain boundary sliding diffusion controlled and n between 3 and 5 means dislocation creep. For values larger than 8 no physical meaning exists [73], [74].

Z can be correlated with the microstructure using Equation 42 [75]:

$$\delta_{SS} = A - B\ lnZ$$ **Equation 42**

where *A* and *B* are constants and δ_{SS} is the steady state grain size.

Constitutive equations are widely used for studying the hot workability or deformation behaviour for different metal alloys [37], [76], [77], [78]. In the work of Zeng et al. [79] constitutive equations were used for pure titanium. The plastic flow properties should be described in a form which can be used to model forging response under loading conditions.

3 Description of methodology

3.1 Materials description

Four different materials were investigated within this work, with different densities, crystal structures and stacking fault energies: Mg-4Al-2Ba-2Ca, Ti-5V-5Mo-5Al-3Cr-1Zr and two types of microalloyed steels.

Magnesium has a hexagonal close packed (hcp) crystal structure with a c/a ratio of 1.623. The SFE of this phase is 125 mJ m^{-2} and it increases with adding other elements such as Al. The density is 1.738 g cm^{-3}, it belongs to the light metal group and its melting point is 650°C. Pure titanium has a hcp crystal structure below 882°C (transus temperature T_β) and a body-centred (bcc) structure above T_β. The SFE has a value of 307 mJ m^{-2} for a pure α-Ti. Titanium is also a light metal with a density of 4.50 g cm^{-3}. Its melting point is 1668°C. Iron crystallizes cubic body-centred (ferrite) below 911°C and face-centred (austenite) above 911°C. Its melting point is 1536°C. Non alloyed steel has a density of 7.58 g cm^{-3}. Austenite in a stainless steel has a very low SFE of 21 mJ m^{-2}.

3.1.1 Mg-4Al-2Ba-2Ca

A creep resistant Mg-alloy Mg-4Al-2Ba-2Ca (DieMag422) was studied and its chemical composition in weight per cent is shown in Table 1.

Table 1. Chemical composition of Mg-4Al-2Ba-2Ca in wt%.

Content in wt%					
Mg	Al	Ba	Ca	Mn	Sr
Base	4.25	1.50	1.51	0.02	0.01

The material was provided by Helmholtz-Zentrum Geesthacht and was produced by melting highly purified magnesium (Mg-HP, > 99.9%), pure aluminium (99.9%), barium (> 99.0%) and calcium (99.5%). The melt was held for 10 minutes at 720°C and casted in preheated rectangular moulds. The temperature of the mould was 300°C and afterwards the mould was cooled with water [80].

Aluminium is a common alloying element for magnesium because it improves the strength and the hardness of the material by solution hardening. On the other hand Al addition promotes the formation of the phase $Mg_{17}Al_{12}$, which has a poor thermal stability and therefore limits the creep resistance. To improve the creep behaviour calcium is added, provoking the replacement of $Mg_{17}Al_{12}$ phase with Al_2Ca. Solid solution strengthening is provided by barium, with an atomic radius 1.36 times larger than that of the Mg-atom.

Another main advantage of this alloy is that it does not contain rare earth metals. Rare earth metals are expensive due to its low produced amount, and their unstable price.

Finally, this material is conceived to be used for automotive applications and power trains, although it still has no commercial applications.

3.1.2 Ti-5V-5Mo-5Al-3Cr-1Zr

The hot deformation behaviour of the near β-Ti-alloy Ti-5V-5Mo-5Al-3Cr-1Zr (Ti55531) was studied in this work. Its chemical composition in weight per cent is given in Table 2 [81].

Table 2. Chemical composition of Ti-5V-5Mo-5Al-3Cr-1Zr.

Content in wt%										
Ti	Al	V	Fe	Mo	Cr	Zr	C	O	N	H
Base	5.510	5.040	0.320	5.010	2.850	1.130	0.005	0.066	0.009	0.001

The Ti-alloy was provided by Böhler Schmiedetechnik. The material was double melted and pre-forged (by cogging) to billet dimensions with a final forming step in the α+β-field [82]. Afterwards an ageing heat treatment below the T_β has been done. The T_β for this alloy was determined to be 803°C [83] which is lower than the T_β in Ti-5Al-5Mo-5V-3Cr [84]. Due to their characteristics mentioned in Chapter 2, near β-alloys are mainly used in the production of light weight parts for aircraft, automobile and offshore applications [85].

3.1.3 Microalloyed steel containing nitrogen (N)

A microalloyed steel containing nitrogen (N) was investigated. The chemical composition of the alloy in weight per cent can be seen in Table 3 [86].

Table 3. Chemical composition of a microalloyed steel containing N.

Content in wt%													
Steel	C	Si	Mn	P	S	Al	Cr	Ni	Mo	V	Nb	Cu	Ti	N
Base	0.155	0.02	1.46	0.009	0.005	0.026	0.028	0.019	0.006	0.051	0.002	0.026	0.002	0.0108

The studied microalloyed steel was produced by continuous hot rolling and provided by Voestalpine Linz. The samples were taken from the surface of the slab, where the finer microstructure was produced.

3.1.4 Microalloyed steel containing vanadium (V)

The microalloyed steel containing vanadium (V) was produced in the same way as the microalloyed steel containing N and has around double amount of V than the previous alloy. The chemical composition in weight per cent is given in Table 4 [86].

Table 4. Chemical composition of a microalloyed steel containing V.

Content in wt%														
Steel	C	Si	Mn	P	S	Al	Cr	Ni	Mo	V	Nb	Cu	Ti	N
Base	0.165	0.017	1.47	0.009	0.006	0.019	0.033	0.019	0.006	0.099	0.002	0.026	0.002	0.006

Vanadium has a higher solubility compared to niobium in presence of carbon and nitrogen. The result is that shorter times of heat treatment and lower rolling forces are necessary which leads overall to a reduction of the costs in the forming processes to similar mechanical properties of the final product [87]. This sort of steels is mainly used in automobile, structural, naval and defence applications [88].

3.2 Heat treatment and extrusion

Samples of DieMag422 and Ti55531 were heat treated in a furnace or in the Gleeble®1500 before the hot deformation tests. The heat treatments were carried out mainly for two reasons: to get a uniform, homogenized grain structure and to achieve phase equilibrium.

Mg samples were held during periods of 30 minutes, 5 hours, 15 hours and 24 hours at 500°C to study the microstructure changes during homogenization treatment. Finally, all as-cast Mg samples were heat treated in a furnace (Rath) at 500°C under argon atmosphere for 15 hours before hot deformation. Extruded Mg samples were heat treated at 467°C, under argon for 15 hours. The heat treatments for the Ti55531 alloy were carried out based on the knowledge obtained in [82], in which phase equilibrium was observed after 15 minutes. Samples were held in a box furnace at the deformation temperature in the α+β-field (763, 783, 803°C) for 1 hour to achieve phase equilibrium at the deformation temperature. In the β-field the heat treatment was done for 10 minutes (823, 843°C) to obtain a fully recrystallized β structure. The 10 minutes heat treatments were carried out in the Gleeble®1500 and the deformation tests were done immediately afterwards.

The cooling was done with air for all treatments and the heat treatment parameters are summarized in Table 5.

Table 5. Heat treatment carried out for the Mg- and Ti-alloys.

	Temperature [°C]	**Duration [hour]**	**Cooling media**	**Inert gas**
DieMag422 (as-cast)	500	15	air	Ar
DieMag422 (extruded)	467	15	air	Ar
Ti55531 (< T_β)	763, 783, 803	1	air	Ar
Ti55531 (> T_β)	823, 843	0.17	-	Ar

The DieMag422 alloy was extruded with a speed of 1 mms^{-1} after heating to a temperature of 400°C and holding there for 5 minutes.

The extrusion process should eliminate the dendritic structure and hence, a better formability should be achieved. Figure 17 a) shows the extrusion machine and Figure 17 b) the billet before and after the extrusion.

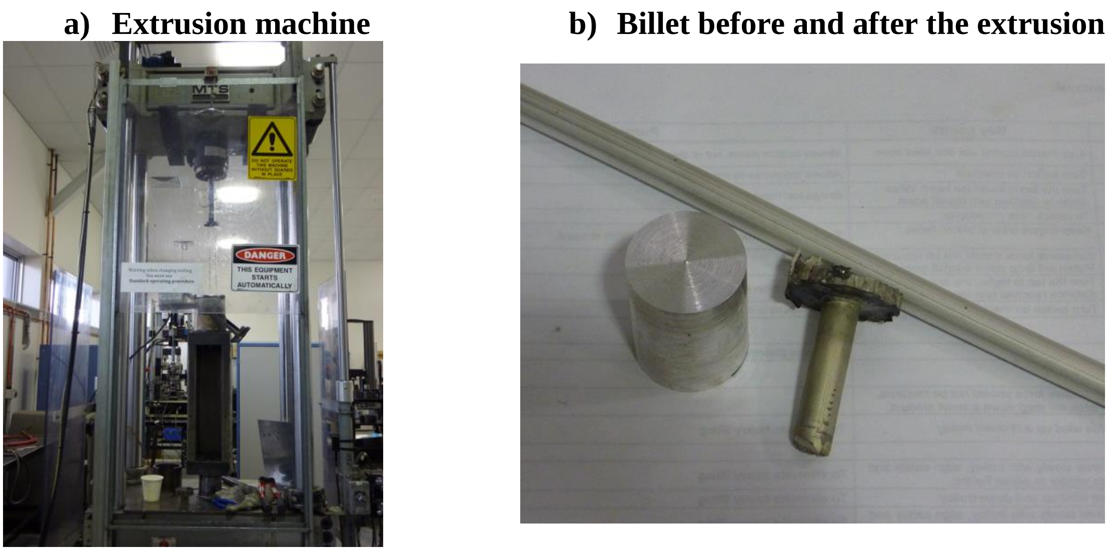
a) Extrusion machine

b) Billet before and after the extrusion

Figure 17. a) Extrusion machine and b) the billet before and after the extrusion.

3.3 Metallography and microstructure investigations

Metallography, consisting of embedding, grinding, polishing and etching, is required to reveal the microstructure of the samples. The microstructure of the base material, and the microstructure developed during thermal and thermomechanical treatments were investigated. Two different observation techniques were used: light optical microscopy–LOM with and without etching, scanning electron microscopy–SEM with BSE, SE and electron backscattered diffraction–EBSD detectors and EDX analyser.

3.3.1 Metallography—sample preparation

The samples were firstly cut with an Accutom 5 cutting machine, parallel to the deformation axis in the case of deformed samples. The magnesium was embedded in Technovit® 4071, which is a cold-curing resin for metallographic testing. Ti-alloy- and steel samples were mounted by means of Struers Predopress in a hot mounting resin (MultiFast® or PolyFast®). The sample and the resin were put into the machine and preheated at 180°C for 5 minutes; afterwards they were pressed at 35 kN for 10 minutes and cooled for at least 5 minutes. Grinding and polishing were done semi-automatically with a Struers Tegra Pol-31 by the method seen in Table 6.

Table 6. Steps for samples grinding and polishing.

a) DieMag422

Steps	Consumables	Lubricant	Time [min]	Force [N]/sample
Grinding	SiC paper 320	Water	2	20
	MD-Largo 9 µm	Lubricant Blue	6	20
Polishing	MD-Mol 6 µm	Lubricant Blue	6	20
	MD-Mol 3 µm	Lubricant Blue	6	10
	MD-Mol 1 µm	Lubricant Blue	10	10
	MD-Chem OPS	-	30	10

b) Ti55531

Steps	Consumables	Lubricant	Time [min]	Force [N] /sample
Grinding	SiC paper 220	Water	2	20
	Allegro 9 µm	Lubricant Blue	5	20
	Largo 9 µm	Lubricant Blue	5	20
Polishing	MD-Dur 3 µm	Lubricant Blue	6	30
	MD-Mol 1 µm	Lubricant Red	15	30
	OPS	-	30	10

c) Microalloyed steels

Steps	Consumables	Lubricant	Time [min]	Force [N] /sample
Grinding	SiC paper 80	Water	2	25
	SiC paper 120	Water	2	25
	SiC paper 220	Water	2	25
	SiC paper 320	Water	2	15
	SiC paper 500	Water	2	15
	SiC paper 800	Water	2	15
	SiC paper 1200	Water	1.5	15
	SiC paper 4000	Water	1.5	15
Polishing	MD-Dur 3 µm	Lubricant Blue	3	25
	MD-Mol 1 µm	Lubricant Blue	3	25

Between each grinding and polishing step the samples were cleaned with ethanol and an ultrasonic bath for at least 5 minutes. The final polishing step of the Mg-alloy was done with pure OPS. The OPS used for the Ti-alloy consists of 9 parts of OPS and 1 part of hydrogen peroxide. After the polishing with OPS, Mg and Ti samples were cleaned with ethanol and water, respectively, to avoid crystallization of OPS.

Etching was used to determine the microstructure in the light optical microscope. Two different types of etching were tried for DieMag422: 2% Nital (300 ml water and 6 ml nitric acid) and a picric acid solution consisting of 10 ml acetic acid, 10 ml water, 70 ml ethanol and 4.2 g picric acid. The specimens were etched for 10 seconds. Both methods were used to obtain a grain boundary contrast. The Ti-alloy was etched for 25 seconds with Kroll solution consisting of 91 ml water, 2 ml hydrofluoric acid and 4 ml nitric acid. Steel samples were etched on the one hand with a 2% Nital solution for 8 seconds and on the other hand with Beraha 1 (100 ml stock solution and 1 g potassium metabisulfite; stock solution: 1000 ml water, 200 ml hydrochloric acid, 24 g ammonium bifluoride) for 10 seconds. Beraha 1 is a colour etching method in which martensite becomes blue to brown and retained austenite remains white.

3.3.2 Light optical microscopy

LOM is one of the easiest and also less expensive possibilities for analysing the microstructure. In most of the cases, etching is necessary to reveal the microstructure, and no further difficult preparation steps are required in this work, as removing the embedding material from the sample for better conductivity in the SEM. The limitation of the LOM is given by the maximum magnification of 1500x.

The light optical microscope Zeiss Observer Z1m was used in order to reveal the microstructure of the non-deformed as well as of the deformed samples. Pictures were taken from specific positions to follow the microstructure as a function of values of local deformation and temperature. Therefore pictures were taken in the middle of the sample, at 2 mm from the centre and at 2 mm from the border, as can be seen in Figure 18. Photos were obtained digitally with an Axio Cam MRC5 (Zeiss) camera connected to the microscope.

As mentioned in [89], the use of polarized light can be useful to obtain qualitative information of the crystal orientation.

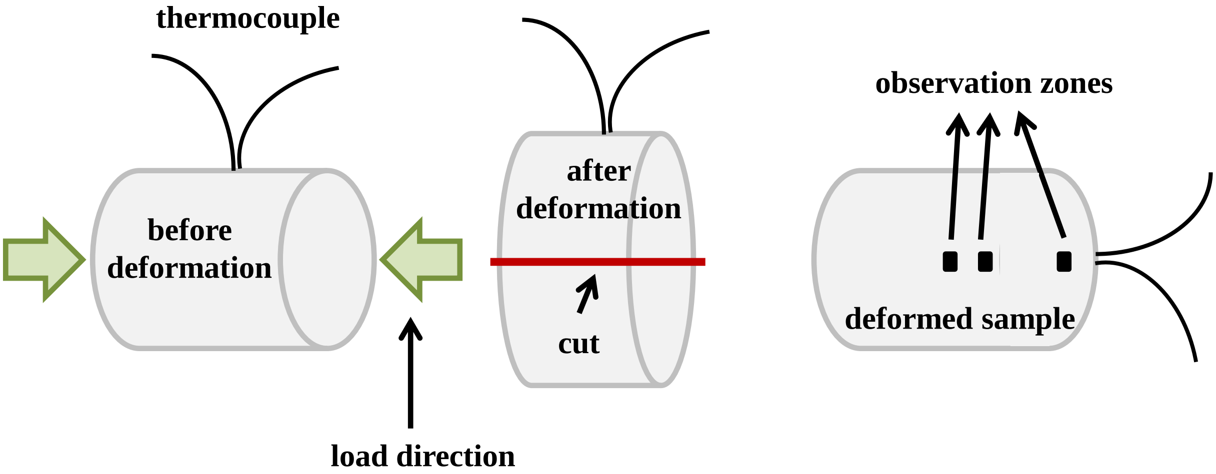

Figure 18: Black squares show the area analysed with LOM in a deformed sample.

3.3.3 Scanning electron microscopy

SEM investigations were done to reveal microstructural features which could not be observed with LOM and to obtain chemical composition by energy dispersive X-ray spectroscopy (EDX). For DieMag422 the FEI Quanta 200 FEG-SEM was used to obtain information of precipitates and intermetallic phases in general. Parameters used for the analysis were a voltage of 10 or 15 kV, a spot size of 4 or 5 nm and a working distance of 10 mm. For the Ti-alloy the focus was the determination of α/β relative amount as well as of alloying elements in the α- and β-phase. The measurements were carried out on a FEI Philips XL30 with a voltage of 15 kV, a spot size of 5 nm and back scattered electron (BSE) mode. Due to the different amount of stabilizing elements in α- (Al) and β-phase (V, Mo, Cr), a contrast can be detected. The α-phase looks dark and the β-phase brighter.

3.3.4 Electron backscattered diffraction

EBSD is a technique which allows determining the crystal orientation and the misorientation between crystallites and thus, allows the quantitative analysis of grains and subgrains. To obtain a good measurement of Kikuchi bands, a good polished surface free of surface strain and scratches is necessary.

EBSD measurements were carried out for three different materials with a FEI Quanta 2000 FEG and a Zeiss ULTRA 55 at 2 mm from the centre of the sample, which corresponds to a local strain of 1 as calculated by finite element calculations (FEM) using DEFORM-2D™ [82]. The specimens were tilted 70° from the horizontal plane to carry out the EBSD measurement as mentioned in [90].

The EBSD measurements in the Mg samples were carried out under a voltage of 20 kV and for three different step sizes: 0.3 µm, 1 µm and 2.5 µm. For the Ti-alloy the following parameters were chosen: an accelerating voltage of 25 kV and a working distance of 10 mm, a step size of 0.15 µm and 0.7 µm in the α/β and in the β-field, respectively. For the steel

samples a working distance of 12 mm, step sizes of 0.20 µm for the detailed analysis and 2.00 µm for a macro analysis were chosen.
The obtained data were treated using Orientation Imaging Microscopy Software (OIM) [91]. IPF maps were the first maps plotted in the OIM software, however the quality of these maps based on rough data could be increased using different cleaning steps.
The first step was the Grain Confidence Index (CI) Standardization which is not changing any orientation. This method identifies points which are correctly indexed but have a low CI and therefore changes this low CI value into the value of the neighbours (Figure 19).

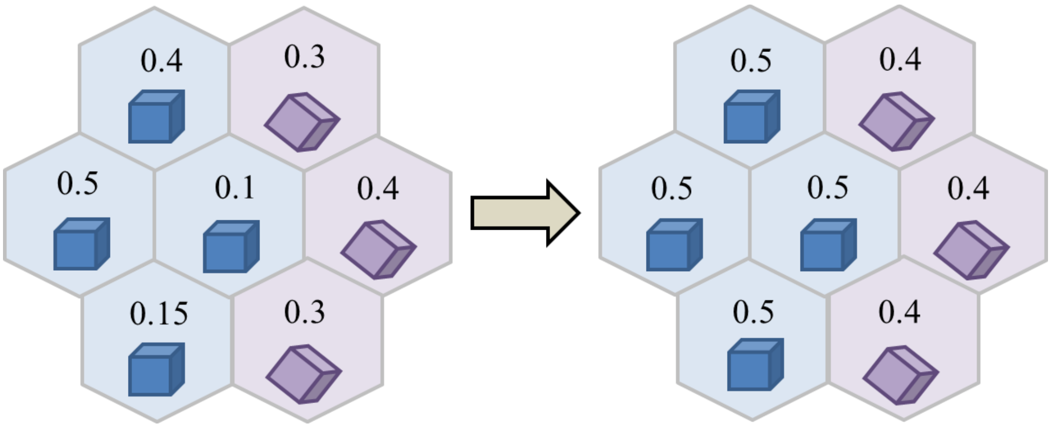

Figure 19. Schema of the grain CI standardization. The numbers represent exemplary CI values.

Afterwards, a cleaning by neighbour CI correlation (Figure 20) was done, in which the orientation value of the measured point with low CI changes to the value of the neighbour with the highest CI.

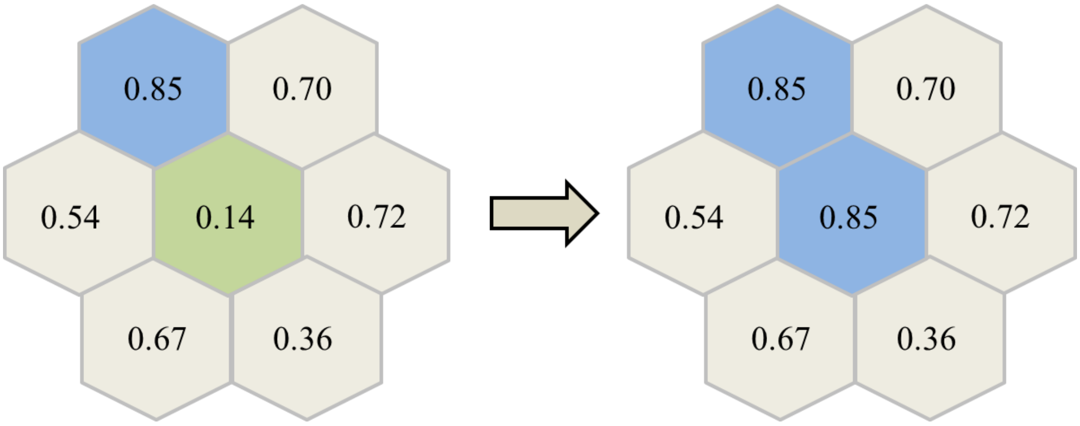

Figure 20. Schema of the neighbour CI correlation. The numbers represent exemplary CI values and the colours, crystal orientations.

In some cases a Grain Dilation treatment (Figure 21) was carried out, in which if the majority of neighbours, in this case the ones with the green orientation are belonging to the same grain, one non-belonging point will change the orientation in order to belong to this grain.

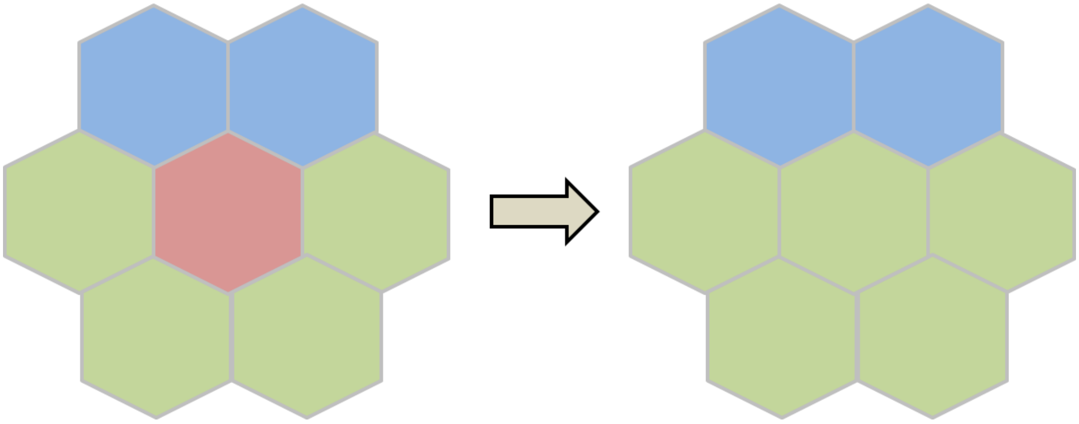

Figure 21. Schema of the Grain Dilation data treatment. The colours represent crystal orientations.

Quantification was carried out to get specific information of the microstructure such as misorientation within a grain, grain and subgrain sizes, etc. The definition of “grain” is referred to a region surrounded by HAGB. The selection of HAGB limit was chosen as 15° of misorientation. The misorientation profile within and along one grain can be measured with a “Vector Profile Mode”. To do this, a line is drawn from the middle of a grain to one grain boundary and all the points along the line are highlighted with misorientation, see Figure 22. The misorientation between a point on the line and the previous point on the line (point to point), and the misorientation between a point on the line and the origin (cumulative misorientation) can be obtained.

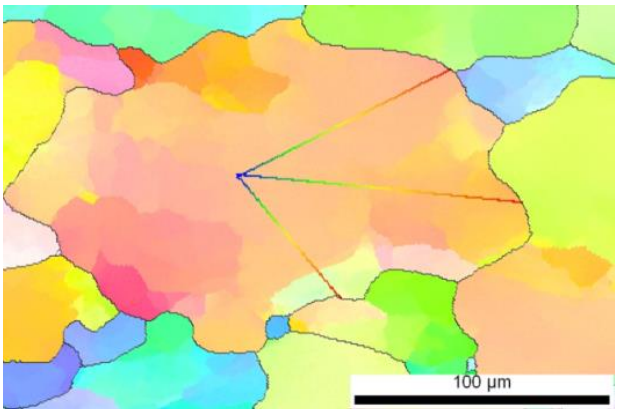

Figure 22: Misorientation profile lines through one grain.

The OIM software displays as well the local misorientation. Two types of misorientation were used in this work: the grain misorientation and the kernel based misorientation [91]. The “Grain Orientation Spread” calculates the average orientation within one grain. Then the misorientation between this average orientation and the orientation of each individual point is calculated. This misorientation is then assigned to each point within the grain. The second method is the “Kernel Average Misorientation”. The misorientation between a grain at the centre of a kernel and all points at the perimeter of this kernel are measured. The resulting local misorientation is the average of these misorientations.

A further application of the EBSD used in this work was the calculation of the grain size. It can be done easily if considering some parameters such as the tolerance angle, the minimum grain size and the minimum confidence index. The software [91] determines that two scan points belong to the same grain if the misorientation between them is below a value chosen by the user, which is the grain tolerance angle. Furthermore, the minimum grain size defines the minimum number of scan points that are considered to be a grain.

3.3.5 Image J analysis

The software Image J [92] was used to quantify the α-percentage in the Ti-alloy. A microstructure picture taken with SEM-BSE was loaded into the program and the file was transformed into an 8-bit picture. In a next step the picture got sharped and the area to be analysed was selected. Using a contrast threshold, the two phases α and β were separated into different colours and the amount of the two phases could be calculated afterwards.

3.3.6 Grain size investigations

The grain size of the DRX grains in the DieMag422 was calculated on the base of the ASTM interception method from “Standard Test Methods for Determining Average Grain Size” [93]. Therefore, lines were drawn parallel over the LOM pictures and the grain boundaries which cut these lines were counted. To calculate the average grain size, the length of all the lines was divided by a product of the amount of grains with the magnification of the scale on the LOM picture. The same investigations were done for subgrains in Ti55531 using IPF pictures.

3.4 Dilatometry

Dilatometry tests were done to estimate the phase transformation temperatures A_{c1}, A_{c3}, A_{r1}, A_{r3}, B_s, M_s and M_f for the two microalloyed steels.

Experiments were carried out using a Bähr DIL-805A/D dilatometer under vacuum. Cylindrical specimens with a diameter of 5 mm and a length of 10 mm were used for the investigations. Each sample was placed in the dilatometer between two quartz tubes, the chamber was evacuated and the sample heated by induction. The temperature was controlled by a type S-thermocouple welded in the middle of the sample and the elongation of the sample was measured with a LDTV. Both signals were logged continuously by a computer. The samples were heated with 5 K s^{-1} to austenitization temperature and cooled down with two controlled cooling rates. The first cooling rate was 1 K s^{-1} to determine the phase transformations sequence before hot deformation. The second one was a fast cooling with He, done to simulate a similar cooling rate which would be achieved after the hot deformation tests in the Gleeble®3800 during water quenching. Samples containing N, were heated up to 1000°C, held for 2 minutes before two different cooling options were applied: 1 K s^{-1} and helium quenching. The investigations for the steel containing V were carried out applying different treatments to estimate a fully austenitic structure and an optimal starting grain size. Therefore, the following treatments were tested: a) heating to 1000°C and held for 5 minutes, b) heating to 1000°C and held for 15 minutes and c) heating to 1150°C and held for 2 minutes. The change in length plotted versus the temperature was used to determine the transformation temperatures by the tangent method [94]. A line was drawn following this curve and the transformation temperature was defined as the point where the tangent deviated from the curve.

3.5 Compression tests

Hot compression tests were carried out using a Gleeble®1500 for the Ti-alloy and a Gleeble®3800 machine for all other materials. The Gleeble® system is a servo hydraulic machine which is schematically represented in Figure 23 a). Temperatures can be measured with thermocouples spot welded on the sample or with an infrared pyrometer. In this work thermocouples were used because they have a much faster thermal response in time than pyrometers. Different types of thermocouples (K, S, R, and B) can be used. In the Gleeble® system the temperature of the specimen is measured when the current is not flowing through the specimen, so the heating current does not affect the temperature measurement.

For the hot deformation tests, cylindrical samples with a length of 15 mm and a diameter of 10 mm were machined from all materials.

The Mg-alloy samples were heated up in air to a temperature range between 300–500°C with a heating rate of 5 K s^{-1}, held for 5 minutes and deformed at different strain rates between 0.001–10 s^{-1}. Finally, a cooling step with water under pressure followed. The compression tests for the Ti-alloy were carried out in argon atmosphere. The specimens were heated up with a rate of 5 K s^{-1} to the deformation temperature between 763°C and 843°C, held for 5 minutes (plus 10 minutes heat treatment for the ones deformed in the β-field), deformed in a range of strain rates between 0.001 and 10 s^{-1} and quenched with water. The specimens of microalloyed steel with N were heated with 5 K s^{-1} up to 1000°C, held for 2 minutes, cooled down with 1 K s^{-1} to the deformation temperature, ranging between 750°C and 1000°C, and deformed with strain rates from 0.01 to 100 s^{-1}. The tests were carried out in vacuum, which was turned off before the samples were in-situ water quenched to avoid the flow of water into the vacuum pump. The second steel alloyed with V was heated with 5 K s^{-1} to 1150°C, held for 2 minutes and cooled with 1 K s^{-1} to the deformation temperature. The strain rate range was 0.01 to 80 s^{-1} and the deformation temperatures between 750 and 1150°C. The experiments were carried out under argon atmosphere and the cooling was done with water immediately after the deformation step.

Lubrication is used to avoid friction between the sample and the anvil and on the other hand to reduce the temperature gradient in the sample. A uniform temperature along the specimen axis is reached because the graphite foil or other lubricants increase the electric resistance at the interface. The lubrication between the three materials was performed differently. Graphite foil was used for the Mg-alloy, and a “sandwich” of graphite foil, nickel based paste, and a molybdenum or tantalum foil was used for the Ti-alloy and steel samples (Figure 23 b)). Graphite burns above 650°C, reacts with Ti and steel and has bad heat conduction in the transversal direction. Nickel paste supports higher temperatures. Ta and Mo support high temperatures and have bad electrical and thermal conductivity. Especial care was taken to build the anvils equally, to avoid different heating transfer differences. The temperature was controlled with a type K-thermocouple, welded at the middle of the sample. An additional thermocouple was welded 1 mm from the edge to measure the temperature gradient. In order to calculate the strain, two different configurations were used: the change in the diameter was recorded with a C-Gauge or the change in length was measured with an L-Gauge by working with the Hydrawedge system. During the hot deformation test, all the parameters are recorded digitally with a pre-defined rate of acquisition.

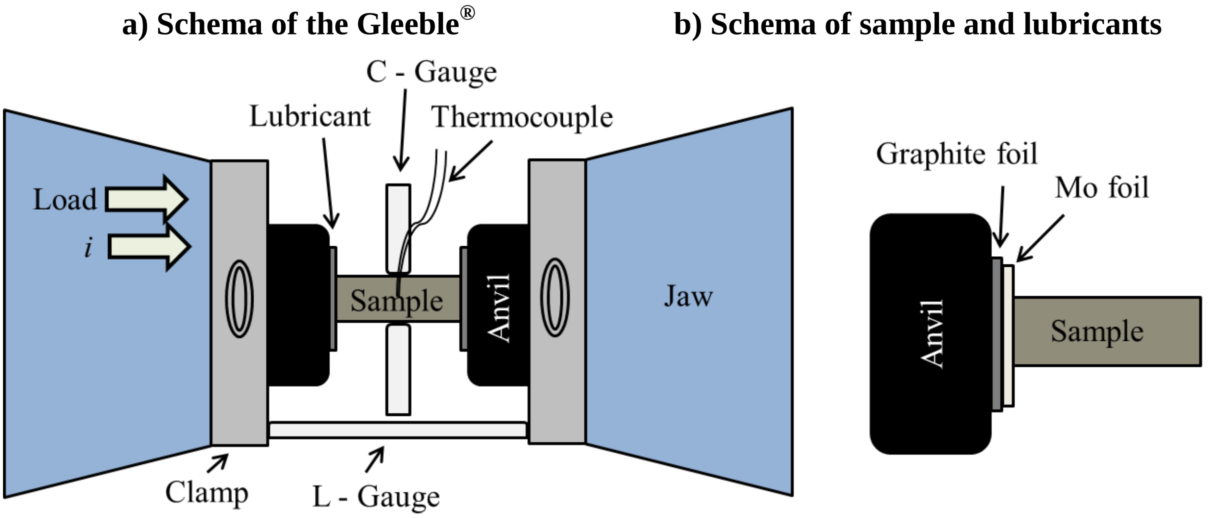
a) Schema of the Gleeble®

b) Schema of sample and lubricants

Figure 23: a) Schema of the Gleeble® machine arrangement for compression tests and b) sample and lubricants.

A summary of the hot compression tests for the different materials is given in Table 7 for the deformation parameters of temperature, atmosphere, quenching, strain rate, and sample number. All tests were carried out up to 0.7 of total strain.

Table 7. Hot compression tests carried out in the Gleeble® system.

Material	Temp. [°C]	Atmosphere	Quenching	Strain rate [s^{-1}]	Sample Number
Mg 422 as-cast	300	Air	Water	0.001	18
				0.01	21
				0.1	20
				1	40
				10	17
	350			0.001	29
				0.01	32
				0.1	31
				1	30
				10	28
	400			0.001	23
				0.01	26
				0.1	25
				1	24
				10	39
	450			0.001	16
				0.01	15
				0.1	38
				1	13
				10	12
	500			0.001	34
				0.01	35
				0.1	41
				1	37
				10	33

Material	Temp. [°C]	Atmosphere	Quenching	Strain rate [s^{-1}]	Sample Number
Mg 422 extruded	250	Air	Water	0.001	2
				0.1	1
				10	6/15
	300			0.001	5
				0.1	4/17
				10	16
	350			0.001	8
				0.1	9
				10	10
	400			0.001	11
				0.1	12
				10	13

Material	Temp. [°C]	Atmosphere	Quenching	Strain rate [s^{-1}]	Sample Number
Ti 55531	763	Argon	Water	0.001	27/30
			Water	0.01	6
			Water	0.1	31
			Water	1	8
			Water	10	29/60
	783		Water	0.001	22/26
			Water	0.01	9
			Water	0.1	23
			Water	1	15
			Water	10	24/25/17/36
	803		Water	0.001	12/16
			Water	0.01	4
			Water	0.1	11
			Water	1	7
			Water	10	14/10/19
	823		Water	0.001	65/45
			Water	0.01	52
			Air	0.1	109
			Water/Air	1	58/74
			Water	10	21/51
	843		Water	0.001	20/59
			Air/Air/Water	0.01	83/96/38
			Air	0.1	88/95
			Air/Air/Water	1	75/93/37
			Water	10	18/57

Material	**Temp. [°C]**	**Atmosphere**	**Quenching**	**Strain rate [s^{-1}]**	**Sample Number**
Steel with N	750	Vacuum	Water	0.01	39
				0.1	51
				1	53
				10	9
				100	8
	800			0.01	42
				0.1	50
				1	54
				10	7
				100	6
	850			0.01	43
				0.1	49
				1	55
				10	4
				100	5
	900			0.01	36
				0.1	47
				1	37
				10	2
				100	3
	950			0.01	45
				0.1	48
				1	52
				10	1
				100	19
	1000			0.01	40
				0.1	46
				1	41
				10	17
				100	18

Material	**Temp. [°C]**	**Atmosphere**	**Quenching**	**Strain rate [s^{-1}]**	**Sample Number**
Steel with V	750	Argon	Water	0.01	21
				0.1	30
				1	20
				10	39
				80	47
	850			0.01	31
				0.1	13
				1	14
				10	36
				80	37
	950			0.01	12
				0.1	8
				1	9
				10	41
				80	38
	1050			0.01	5
				0.1	6
				1	7
				10	42
				80	45
	1150			0.01	17
				0.1	16
				1	15
				10	43
				80	44

3.6 Flow curves calculation

Hot compression tests were done to obtain flow curves. Once a deformation test on the Gleeble® system has finished, the data was automatically loaded with Origin™ software. Firstly, all the received change in length Δl or change in diameter Δd values were multiplied by (-1). Secondly, the true stress and true strain values were calculated. Therefore the following equations have been used:

$$\varepsilon_T = ln\frac{l}{l_0} = 2\,ln\frac{d}{d_0} = 2\,ln\frac{\Delta d + d_0}{d_0}$$

Equation 43

$$\sigma_T = \frac{F}{A} = \frac{4F}{\pi\,(\Delta d + d_0)^2}$$

Equation 44

where l_0, d_0 are the initial length and initial diameter, respectively, and F is the applied force. In some cases, as for deformations carried out with the Hydrawedge module of the Gleeble® 3800, the obtained data were already the true stress and strain values calculated with the same equations.

The obtained flow data were interpolated with a cubic spline function and then smoothed. Different smoothing procedures have been tried: Savitzky-Golay, Adjacent-Averaging, Percentile filter and FFT filter. As the most practicable one, the Adjacent-Averaging filter technique was chosen. The Adjacent-Averaging filter technique takes the average of a certain number of data points for each value and replaces this point with the new average value [95]. A certain number of data points have to be chosen carefully not to lose information. Finally the elastic part was deleted.

3.7 Calculation of processing maps and constitutive equations

Different models of processing maps, instability values and constitutive equations were used in this work. The calculation methods are shown below.

The apparent strain rate sensitivity m, which is varying with the temperature and strain, was calculated with Equation 5. Therefore, a curve of ln $\dot{\varepsilon}$ - ln σ for each temperature and strain was drawn and fitted with a polynomial of third order (Equation 45).

$$y = Intercept + B1x^1 + B2x^2 + B3x^3$$ **Equation 45**

The Equation 45 got derivate (Equation 46) in which x = ln $\dot{\varepsilon}$ to obtain Equation 47.

$$y' = B1 + 2B2x + 3B3x^2$$ **Equation 46**

$$y' = m$$ **Equation 47**

The efficiency of power η_{P} was calculated with Equation 13 for each T and ε. Similarly to the calculation of m, a curve of ln $\dot{\varepsilon}$ - ln$\frac{m}{m+1}$ was drawn and fitted with a polynomial of third order, where the equation got derivate afterwards. To obtain ξ the values had to be summed up with the values of m as shown in Equation 24.

The calculation of $\eta_{\mathrm{M+R}}$ (Equation 16) is shown in the equations mentioned before and in the diagrams. G is separated into two terms (Equation 14) what can be seen in Figure 24.

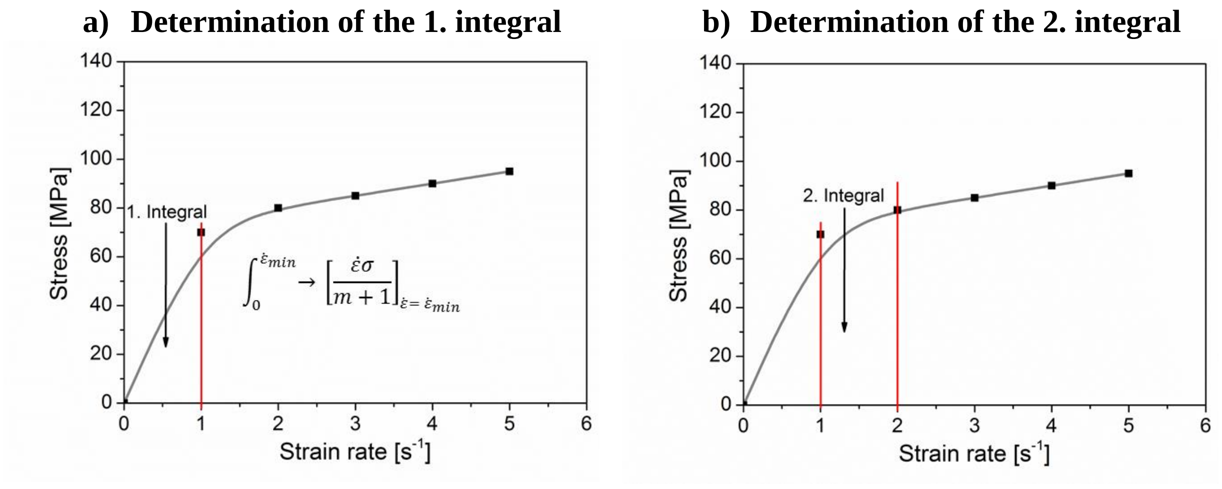
a) Determination of the 1. integral

b) Determination of the 2. integral

Figure 24. Schema for calculating the two terms of *G*.

The first and the second integral of Equation 14 were calculated using a diagram of stress and strain rate as shown in Figure 24. Afterwards the curve was numerically integrated in Origin® and the values were shown. To calculate the *G*, a sum was made out of the first and the second integral. The instability κ was calculated with Equation 25.

The instability parameter κ_j (Equation 27) was calculated by drawing a curve of ln $\dot{\varepsilon}$ - ln *J* and fitted with a polynomial of third order, which was derivate afterwards.

The instability parameter α_SJ from Equation 37 was calculated using two different ways: once the effect of the temperature increment was taken into account and in a second time this temperature term was neglected. For calculating the strain dependent term a polynomial fit of second order was used to fit the flow curves. The fitting curve was numerically derived, and the result was multiplied with the strain value again. To calculate the temperature term a diagram of stress and temperature was plotted for every strain rate, numerically derived and multiplied with the maximal increment of temperature (ΔT) obtained from the Gleeble® data.

After calculating all the values (η_P, $\eta_\mathrm{M+R}$, ξ, κ, κ_j and α_SJ) they were plotted as isolines as a function of T and $\dot{\varepsilon}$ for a given strain. The instability maps were obtained as isolines combining only two different areas with values below or above zero. The area predicting flow instabilities by each model was dashed.

For the calculation of constitutive equations several parameters had to be determined. First of all the stress multiplier *c* (Equation 40) had to be estimated. Therefore different *c* values in a wide range were chosen and diagrams of ln $\dot{\varepsilon}$ - ln [sinh(cσ)] were plotted. The optimal *c* value was the one which resulted in a R^2 closest to 1. Afterwards the stress exponent *n* was obtained as the slope of the ln $\dot{\varepsilon}$ – ln [sinh(cσ)] linear fit curve.
The activation energy *Q* was determined using plots of 1000/*T* - ln [sinh(cσ)] for each strain rate. *Q* was calculated with Equation 48 where the slope means the mean value calculated from all strain rates.

$$Q = slope \cdot R \cdot n \cdot 1000 \qquad \textbf{Equation 48}$$

The Zener-Hollomon parameter *Z* was calculated from Equation 41 and finally the value of the material constant *A* was obtained.

Constitutive equations were calculated for the Mg-alloy and the microalloyed steel using the peak stress values. The equations for the Ti-alloy on the other hand were calculated separately for the two deformation regions, α+β-field and β-field, for a logarithmic strain of 0.4.

4 Results

4.1 Magnesium

4.1.1 As-cast

The homogeneity of the ingot in the as-cast condition was first investigated with the light optical microscope. Therefore, pieces of the casted cylinder were taken from different parts to compare the microstructure from the edge to the middle. It could be seen that there was no difference in the grain size.

The microstructure of the as-cast material can be seen in Figure 25. In picture a) and b) the as-received material is shown, in picture c) the microstructure after a 5 hour heat treatment, and in d) the material after a heat treatment of 15 hours is presented. A 15 hours heat treatment gave the most homogeneous distribution of the grains.

a) As-received **b) As-received**

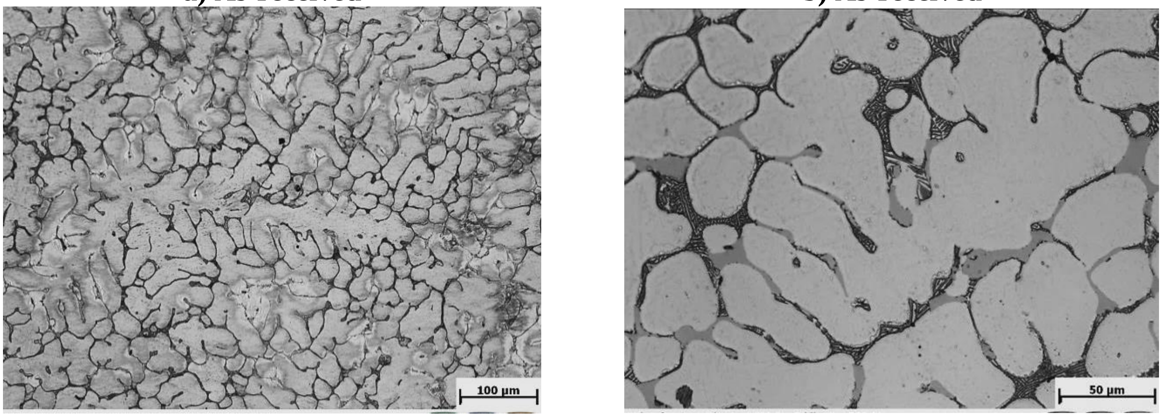

c) Heat treated: 5 hours **d) Heat treated: 15 hours**

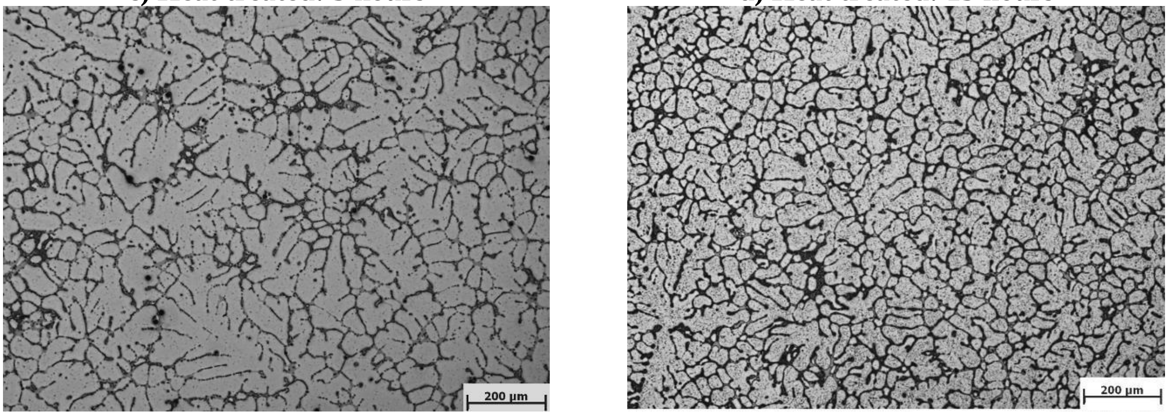

Figure 25. Material a), b) in the as-received form, and after c) a 5 hour heat treatment and d) a 15 hour heat treatment at a temperature of 500°C.

The material shows an inter-dendritic structure formed by a calcium rich phase, as explained in the work of Kim et al. [96]. Due to low diffusivity of Ca solute, constitutional undercooling takes place, producing a dendritic structure in a diffusion layer ahead of the advancing solid/liquid interface. The Mg-alloy contains different intermetallic phases which are shown in Figure 26. In the Mg matrix (light grey), a bulky $Mg_{21}Al_3Ba_2$ phase and a eutectic Al_2Ca phase with a lamellar shape are observed. The composition of the elements was determined using an EDX scan.

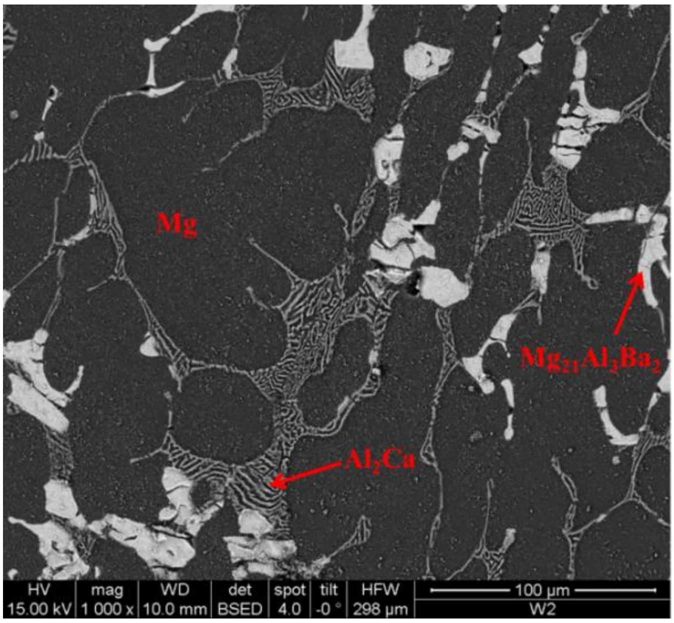

Figure 26. FEG-SEM picture (BSE mode) showing the different phases of the alloy.

An EDX mapping measurement of the heat treated material gives a good impression about the amount and the position of alloying elements, as can be seen in Figure 27. It is confirmed that the light grey phase has a high amount of barium and aluminium and that the lamellar phase consists of aluminium and calcium. Manganese and strontium are impurities of the casting process.

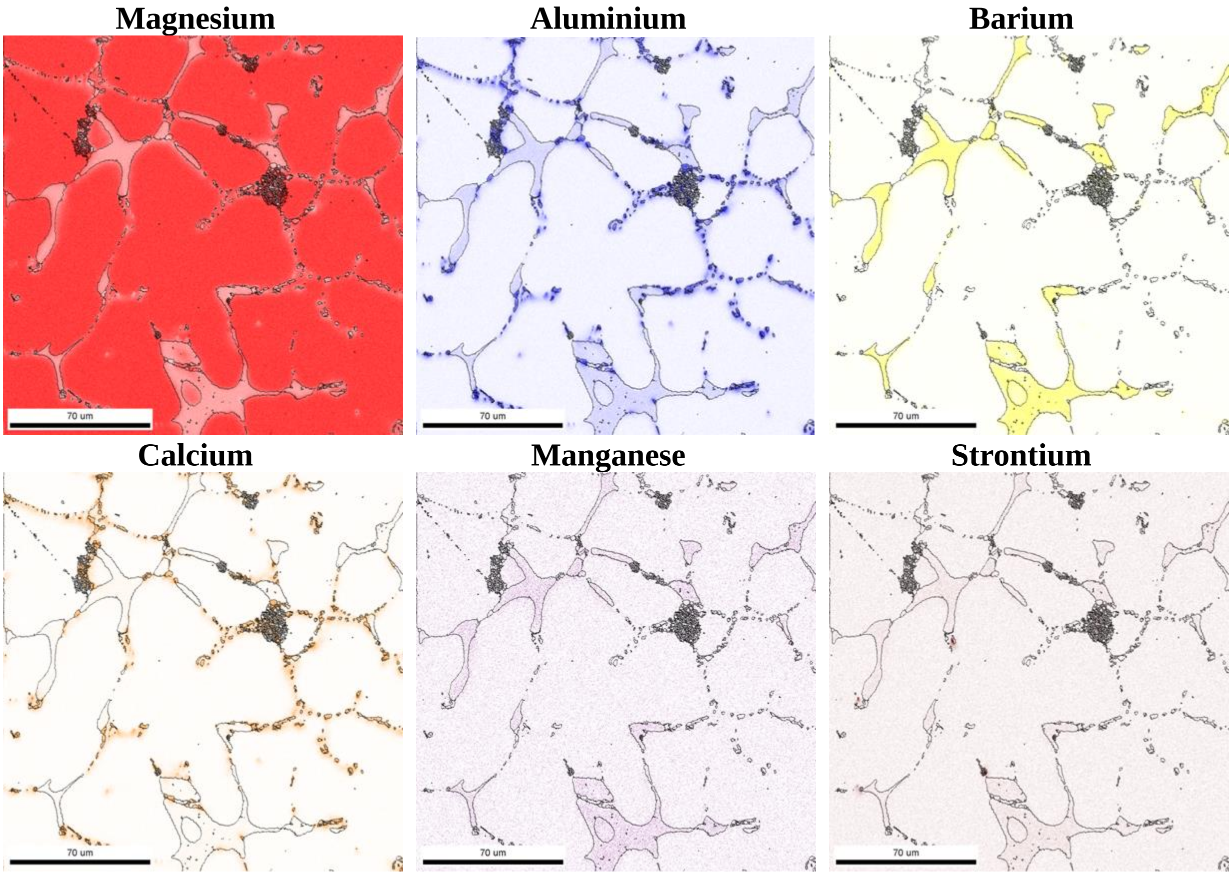

Figure 27. EDX scan showing the distribution of the different alloying elements.

Figure 28 a) shows the colour scale used for the crystal orientation of Mg and b) the directions related to a selected reference. The triangle shows the colour coding for the inverse pole figure (IPF) map. The colour red is assigned to the 0001 crystal direction, blue to $10\bar{1}0$ and green to the $2\bar{1}\bar{1}0$ crystal direction.


a) Triangle of Mg

b) Directions Mg

Figure 28. a) IPF triangle showing the colour coded orientation and b) RD and TD directions.

In Figure 29 two IPF maps of the 15 hour heat treated Mg-alloy are shown in which HAGB are depicted black and LAGB in white.

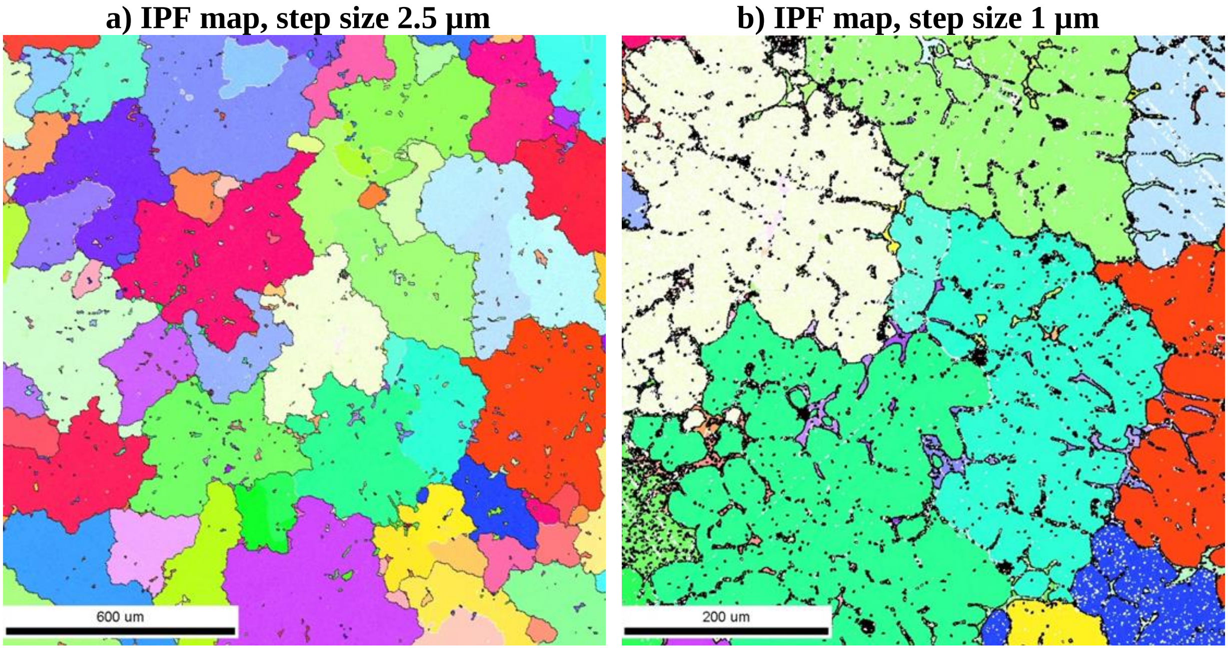
a) IPF map, step size 2.5 µm

b) IPF map, step size 1 µm

Figure 29. Two IPF maps showing the microstructure of the heat treated material.

The EBSD maps show that in the heat treated material nearly no misorientation can be seen within one grain and that less subgrains are present.

These microstructures will be compared with the deformed microstructure to determine the developed restoration mechanisms afterwards.

4.1.2 Wrought material

The as-cast material was extruded at 400°C with a velocity of 1 mm s^{-1} at the Deakin University in Geelong, Australia. The obtained microstructure is shown in Figure 30 a) after extrusion and in b) with a heat treatment of 15 hours at 467°C.

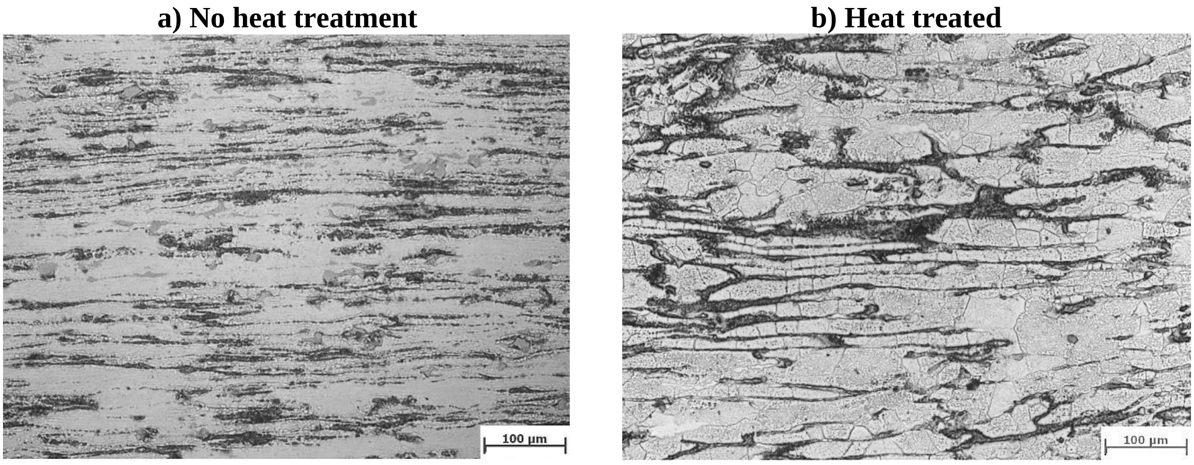

Figure 30. LOM investigated material for a) as extruded and b) after extrusion and a heat treatment of 15 hours at 467°C.

As can be seen in Figure 30 the microstructure is not any more dendritic, especially if compared with Figure 25. After the heat treatment the Mg-grains are easy visible and are showing flat grain boundaries which cannot be seen in the non-heat treated alloy.

4.1.3 Flow curves

Figure 31 shows the flow curves of the as-cast Mg-alloy for all five tested temperatures and strain rates. Additionally, flow curves for lower temperatures between 20–200°C are shown. In the very low temperature range between room temperature and 150°C, the rate of work hardening is very high and fracture occurs shortly after the peak flow stress. Deformation is primarily due to slip and twinning with slip limited to the basal plane. With increasing the temperature it can be seen that the ductility is improved and larger strains are achieved. Softening can be seen before the fracture occurs. For small strains between 300–500°C the initial stage of deformation is work hardening. As the strain is increased, the rate of work hardening is reduced. A change in the hardening slope can be seen in the flow curves at 300°C for all strain rates, and at 350°C and 400°C for the high strain rates. In Figure 31 this change of the slope is indicated with a blue circle. This effect has been observed for Mg-alloy in [35] and [97] as well. When this trend occurs, it impacts upon the strain to the peak flow stress, which is increased out to values of approximately 0.2 of strain. This behaviour is observed at lower temperatures and higher strain rates (high values of Z) where twinning is more prevalent. For the flow curves at 400°C the red circles show a peak in the curve and it can be realized that the peak is shifted to higher strains with decreasing strain rate.

At high strains steady state is reached after a peak stress, especially for low strain rates. The strain at which peak stress occurs is sensitive to temperature and strain rate. Furthermore, the value of peak stress is reduced with increasing temperature, and decreasing strain rate.

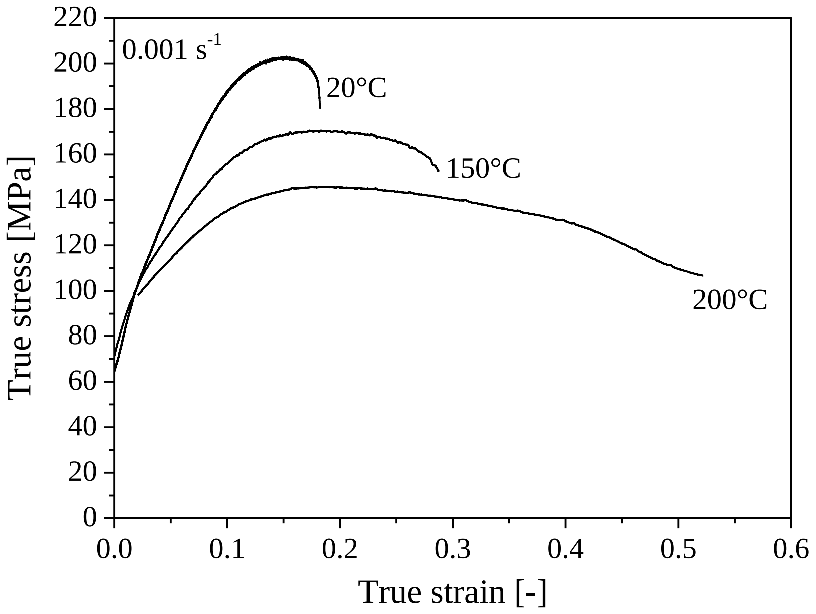
0.001 s^{-1}
20°C
150°C
200°C
True stress [MPa]
True strain [-]
0
20
40
60
80
100
120
140
160
180
200
220
0.0
0.1
0.2
0.3
0.4
0.5
0.6

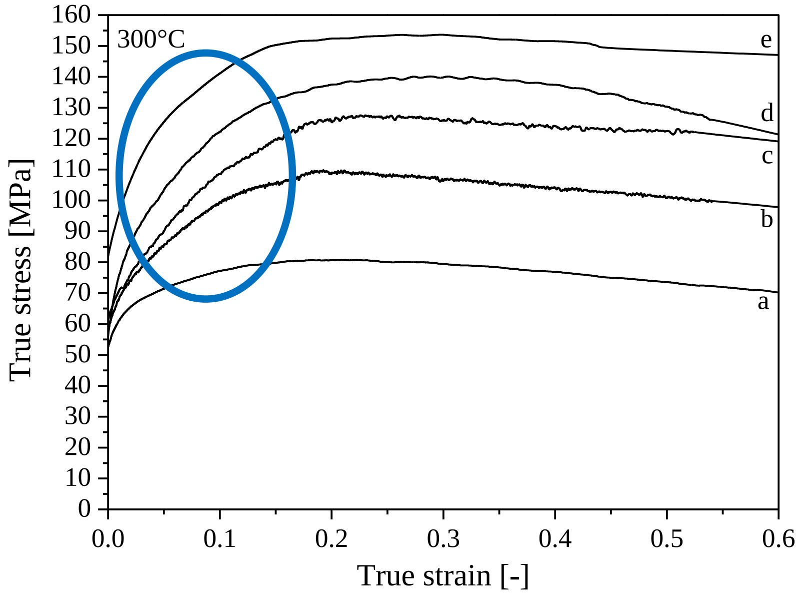
300°C
e
d
c
b
a
True stress [MPa]
True strain [-]
0
10
20
30
40
50
60
70
80
90
100
110
120
130
140
150
160
0.0
0.1
0.2
0.3
0.4
0.5
0.6

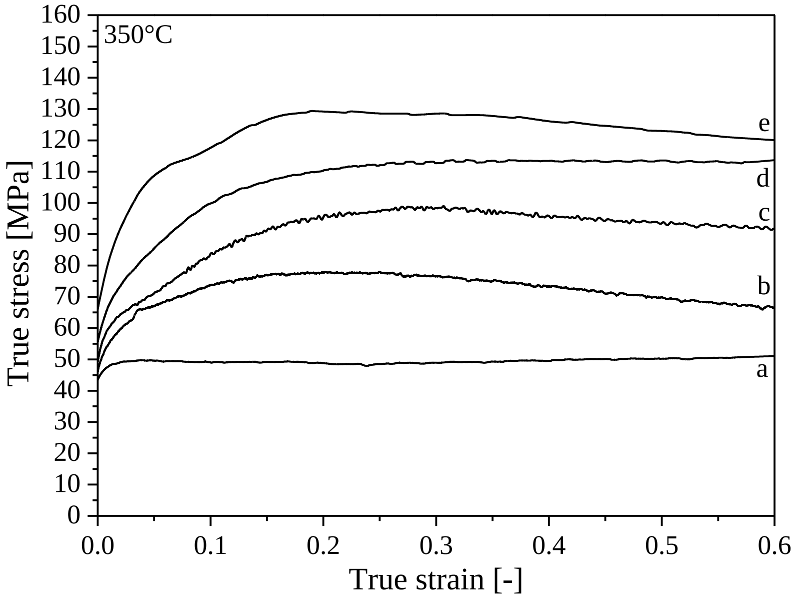
350°C
e
d
c
b
a
True stress [MPa]
True strain [-]
0
10
20
30
40
50
60
70
80
90
100
110
120
130
140
150
160
0.0
0.1
0.2
0.3
0.4
0.5
0.6

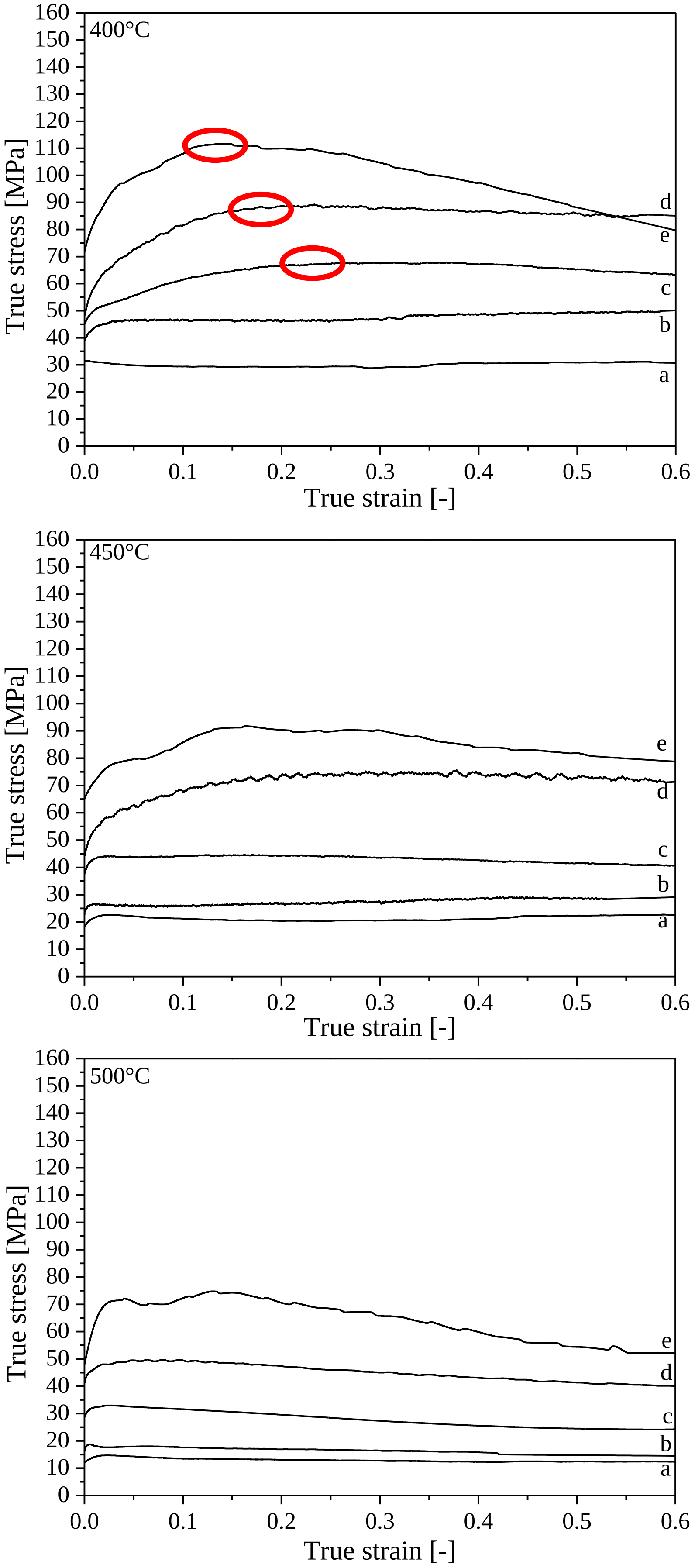

Figure 31. The flow curves at low temperatures are shown in the first picture. Afterwards, the flow curves of as-cast DieMag422 for the five tested temperatures at strain rates of a = 0.001 s^{-1}, b = 0.01 s^{-1}, c = 0.1 s^{-1}, d = 1 s^{-1} and e = 10 s^{-1} are shown.

In Figure 32 the flow curves of the wrought alloy are shown for temperatures between 250–400°C and for strain rates of 0.001, 0.1 and 10 s^{-1}. A peak can be seen at temperatures between 250–300°C for a strain rate of 0.1 and 10 s^{-1} and for temperatures between 350–400°C at a strain rate of 10 s^{-1}.

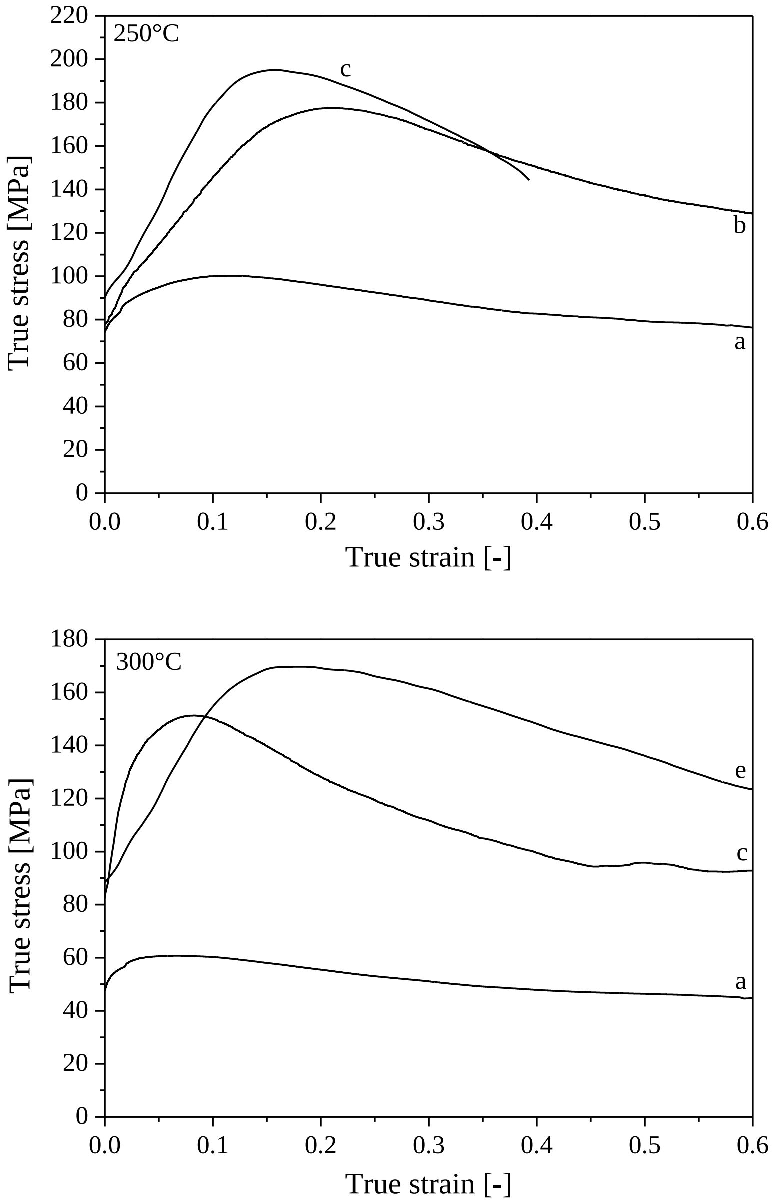

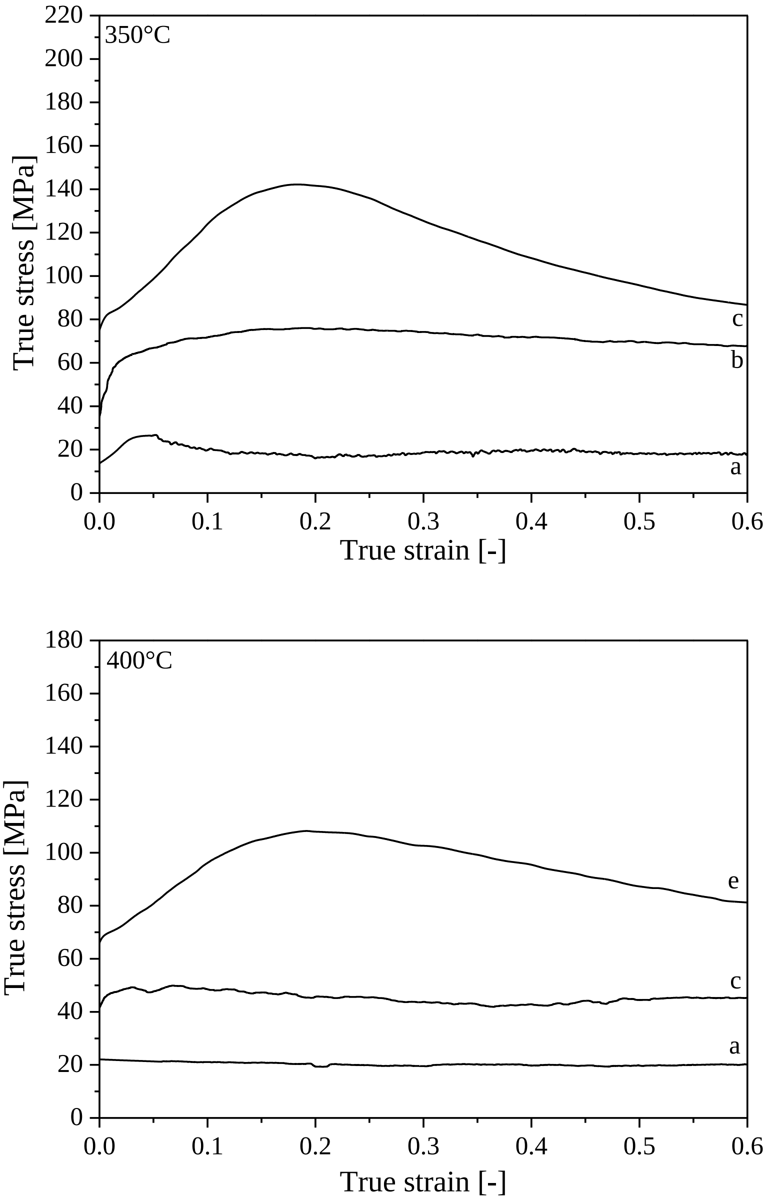

Figure 32. Flow curves of extruded DieMag422 for four deformation temperatures at strain rates of a = 0.001 s^{-1}, b = 0.1 s^{-1} and c = 10 s^{-1}.

Stress values are plotted in Figure 33 versus the strain rate for a constant strain. The stress values at a strain of 0.6 of the as-cast material are always higher than for the wrought alloy. On the other hand, if using the peak stress instead of the stress value at a constant strain, it is observed that in some cases the values of the wrought alloy are higher than that of the as-cast material. Especially for high strain rates and low temperatures, the stress values of the wrought material are higher than the extruded ones.

a) Stress at a strain of 0.6

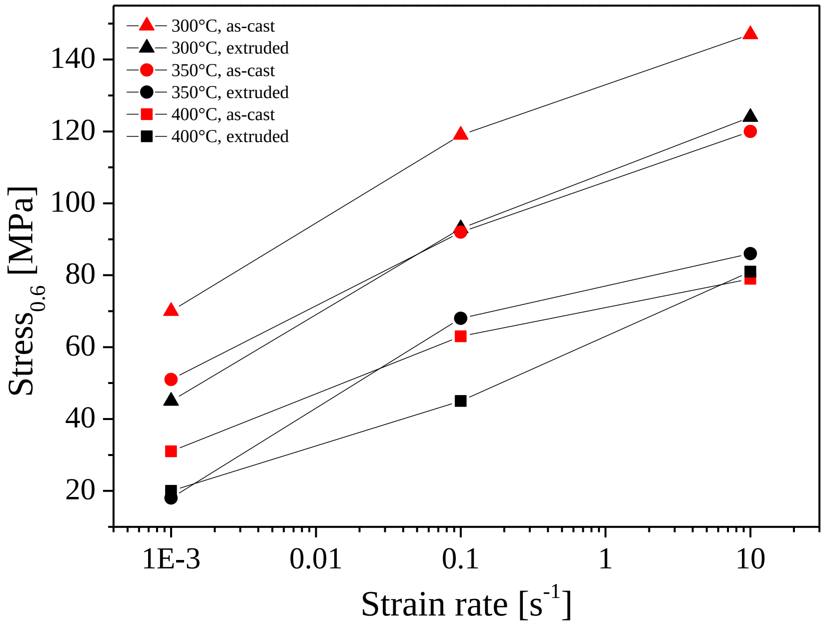

b) Peak stress

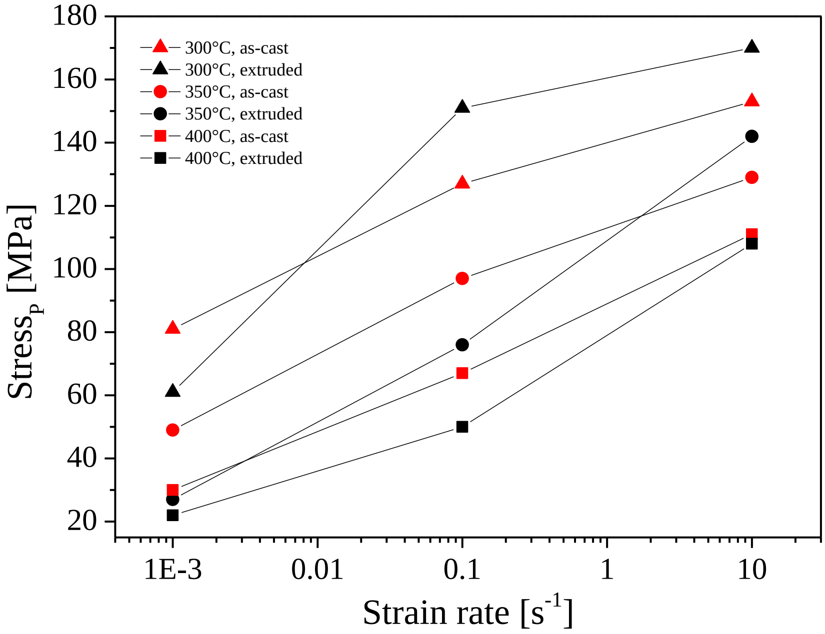

Figure 33. Stress dependency on the strain rate, the temperature and the strain for as-cast and extruded materials for a) the stress at a strain of 0.6 and for b) the peak stress values.

4.1.4 Microstructure after hot deformation

4.1.4.1 Light optical microscope investigations for the as-cast material

Light optical microscope investigations were done and some microstructures after deformation taken from the middle of the sample are shown in Figure 34. At a deformation temperature of 300°C and a strain rate of 0.001 s^{-1}, some small grains can be detected heterogeneously distributed. Twins can be observed after deformation at 300°C and strain rates between 0.1–10 s^{-1}. With a temperature of 400°C small new grains and serrated grain boundaries can be seen. At high strain rates the recrystallization grade increases up to 100% for the highest strain rate.

The size of new grains increases with the deformation temperature. No grain boundaries could be detected for the lowest deformation rate and 500°C.

300°C, 0.001 s^{-1}

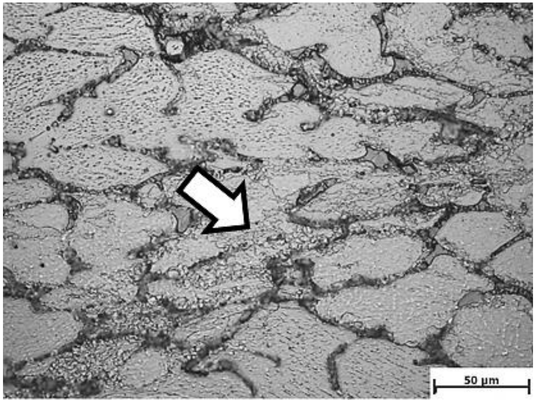

300°C, 0.1 s^{-1}

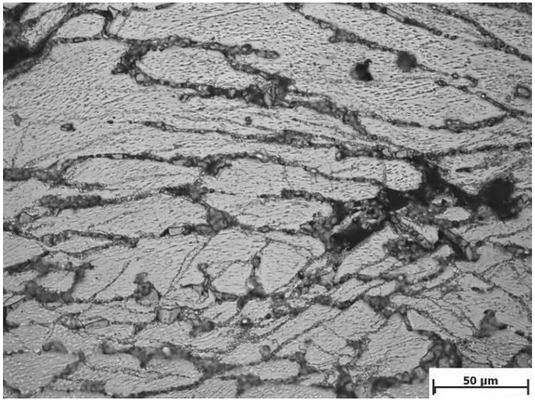

300°C, 10 s^{-1}

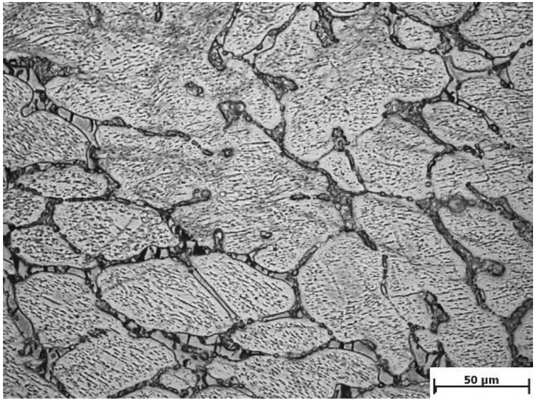

400°C, 0.001 s^{-1}

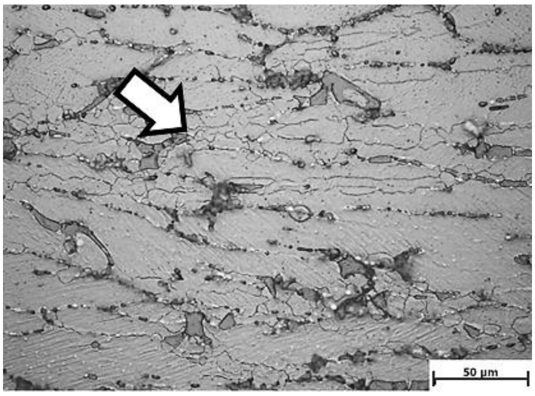

400°C, 0.1 s^{-1}

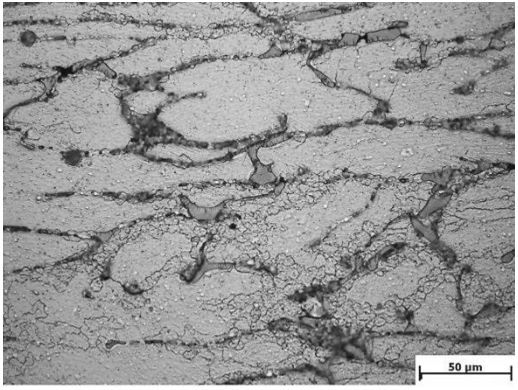

400°C, 10 s^{-1}

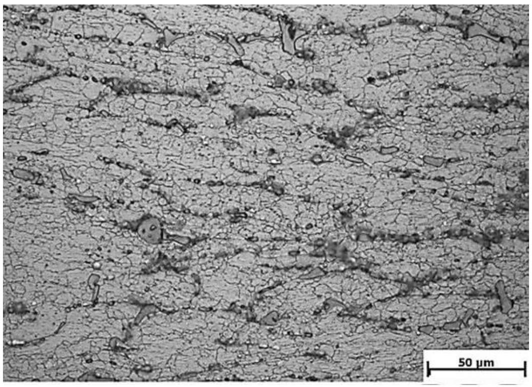

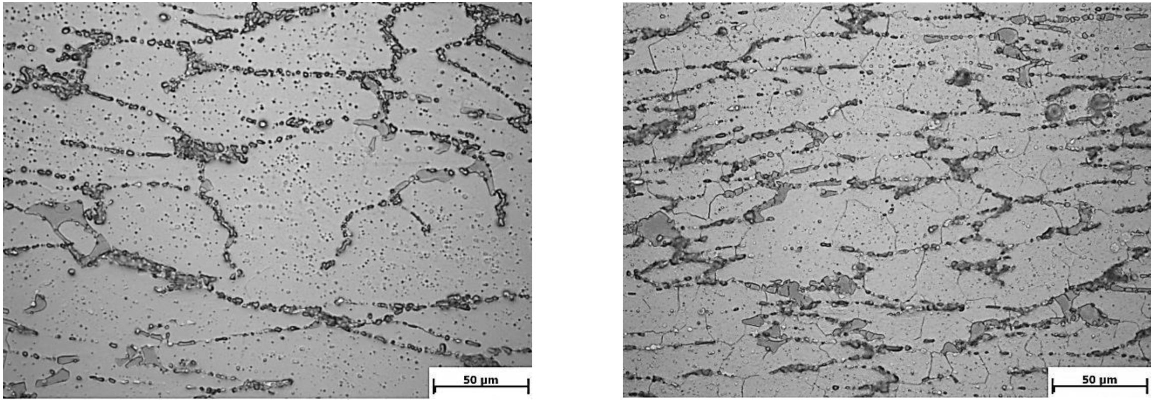

500°C, 0.001 s^{-1} **500°C, 0.1 s^{-1}**

500°C, 10 s^{-1}

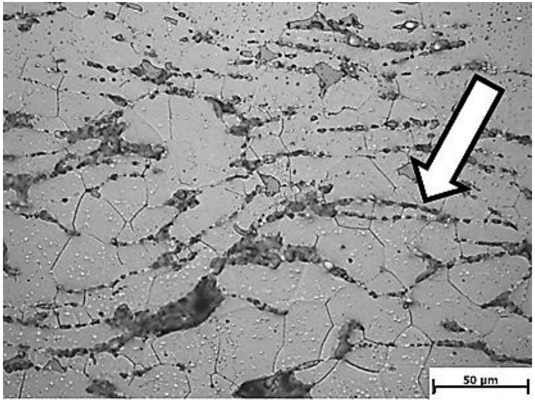

Figure 34. Microstructure of the Mg as-cast alloy after deformation at 300°C, 400°C and 500°C at strain rates of 0.001 s^{-1}, 0.1 s^{-1} and 10 s^{-1}. Pictures taken at a local strain of 1.1, load direction is vertical.

In Figure 35 further light optical- and scanning electron microscope pictures present some details of the microstructure such as twins at low temperatures in Figure a) (300°C, 10 s^{-1}) and b) (150°C, 0.01 s^{-1}). In Figure c) (450°C, 10 s^{-1}) new grains are shown. Figure d) shows flow localization. Figure e) shows new small grains at grain or twin boundaries. In Figure f) damage is visible in form of a void close to intermetallic phases. Finally, picture g) shows recrystallized grains in a former twin.

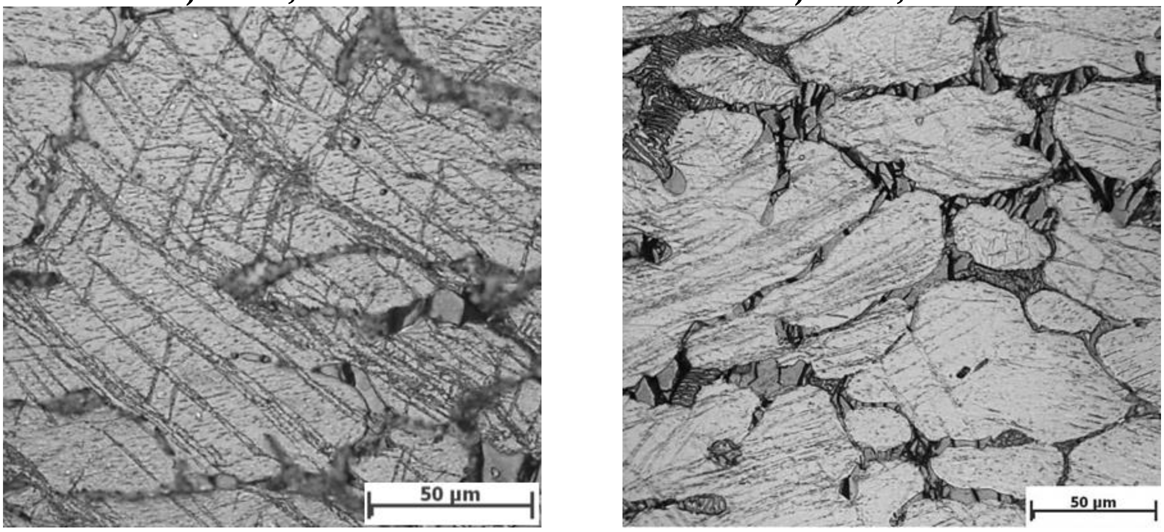

a) 300°C, 10 s^{-1} **b) 150°C, 0.01 s^{-1}**

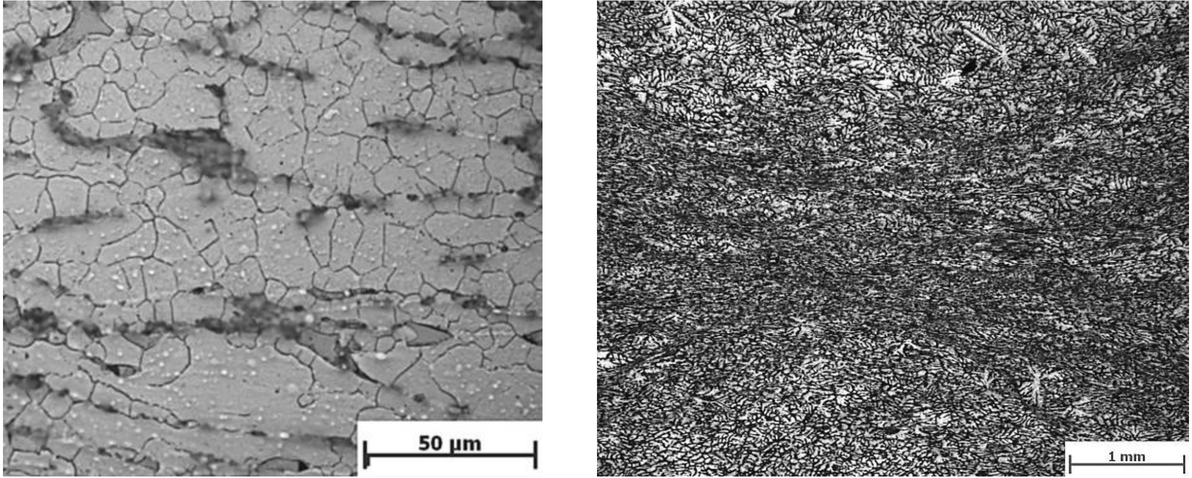

c) 450°C, 10 s^{-1}

d) 400°C, 10 s^{-1}

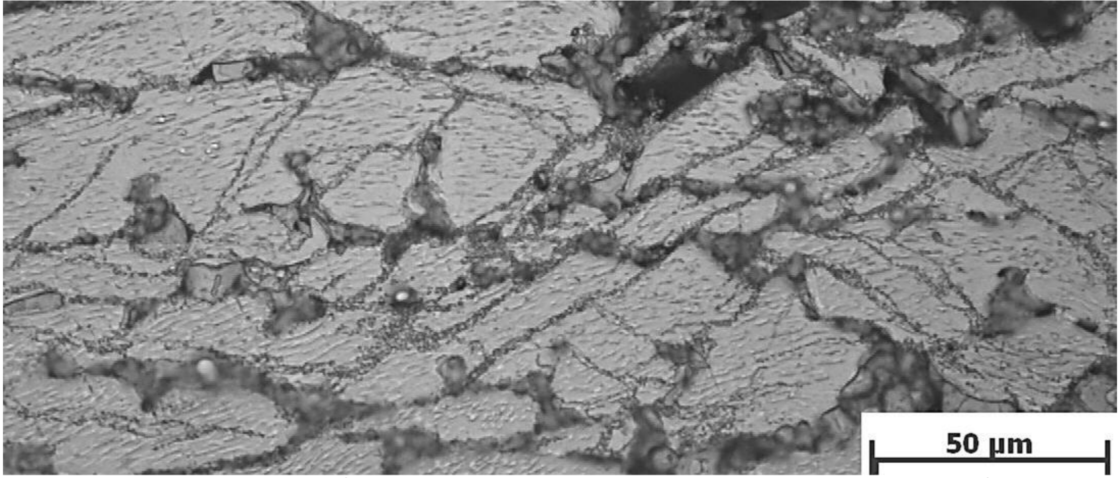

e) 300°C, 0.1 s^{-1}

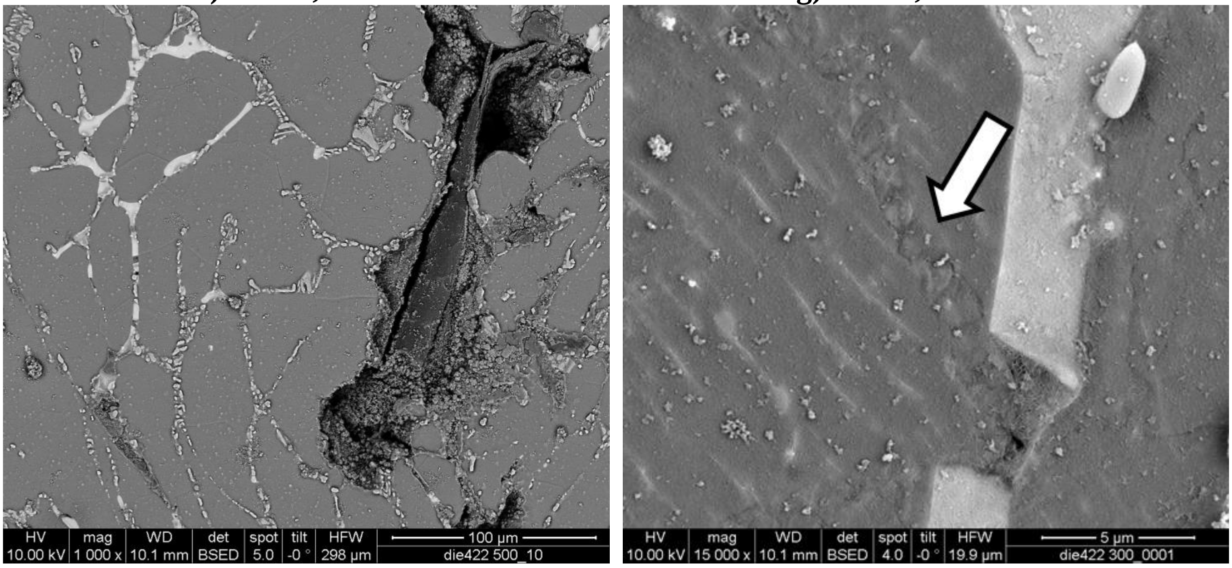

f) 500°C, 10 s^{-1}

g) 300°C, 0.001 s^{-1}

Figure 35. Micrographs showing the formation of twins, new grains, flow heterogeneities and damage for different deformation conditions. The load direction is vertical for the LOM pictures and horizontal for the SEM investigations.

4.1.4.2 Grain size investigations

The size of the recrystallized grains was investigated. In Table 8 a summary of the grain sizes is presented. For the sample deformed at 500°C and a strain rate of 0.001 s^{-1}, it was not possible to use the LOM picture and therefore, the EBSD measurement was used.

Table 8. Overview of the obtained recrystallized grain sizes.

T [°C]	**As-cast**	**300**	**300**	**300**	**400**	**400**	**400**	**500**	**500**	**500**
$\dot{\varepsilon}$ [s^{-1}]	-	0.001	0.1	10	0.001	0.1	10	0.001	0.1	10
Φ [µm]	160	5	2	0	9	5	7	17	21	32

In Figure 36 the relationship of the obtained grain size with the temperature for the 3 different strain rates is shown.

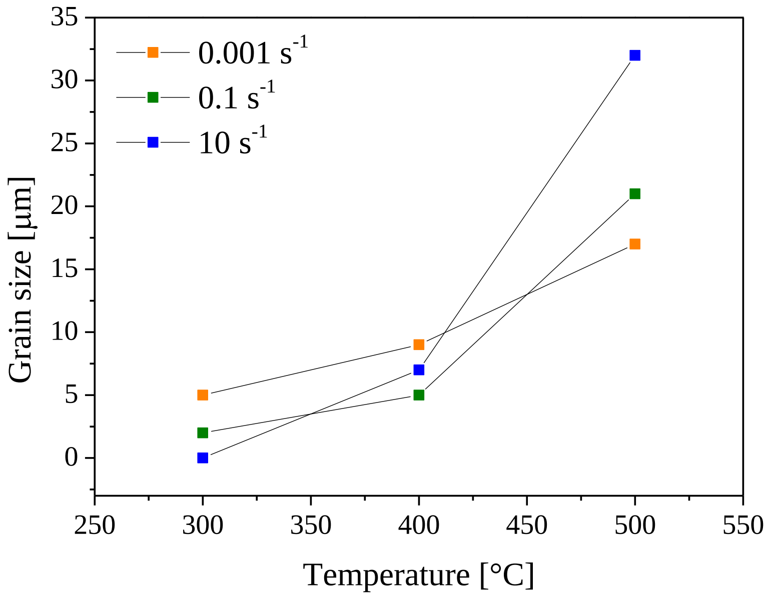

Figure 36. Relationship between temperature and grain size for strain rates of 0.001 s^{-1}, 0.1 s^{-1} and 10 s^{-1}.

4.1.4.3 EBSD measurements for the as-cast material

EBSD investigations were made for three different conditions of deformation. The EBSD investigations were carried out in the middle of the sample. HAGB are depicted in black and LAGB in grey. Figure 37 shows the microstructure of the sample deformed at 400°C with a strain rate of 0.001 s^{-1}. It can be seen that some phases are badly indexed. These phases are the intermetallic phases $Mg_{21}Al_3Ba_2$ and Al_2Ca which fit with the result given by the EDX scan in Figure 38.

A detailed analysis was carried out using a smaller step size (of 0.4 µm), as shown in Figure 37 b). It can be observed on the one hand, that some grains contain high misorientation (green arrows). On the other hand, small grains without any internal misorientation (white arrows) are present.

As mentioned above, in Figure 38 an EDX scan shows the distribution of the elements in the sample. Magnesium is shown in green, aluminium in orange, calcium in red and barium in pink.

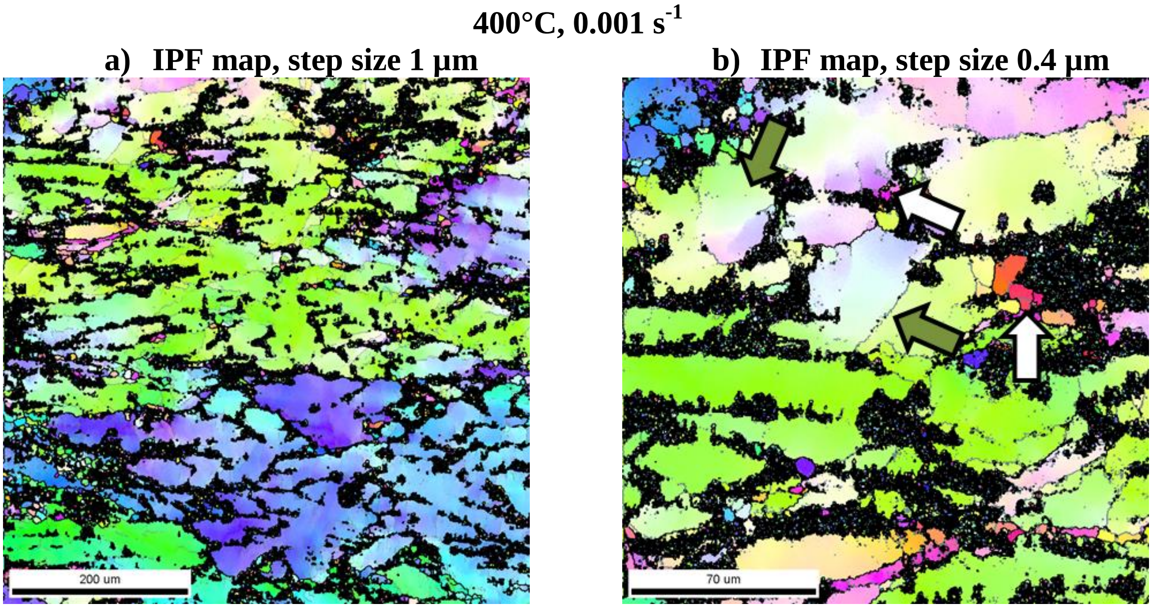
400°C, 0.001 s^{-1}

a) IPF map, step size 1 µm

b) IPF map, step size 0.4 µm

Figure 37. Maps for 400°C and a strain rate of 0.001 s^{-1}. a) IPF map, step size 1 µm; b) IPF map, step size 0.4 µm. Local strain is 1.1, load direction vertical.

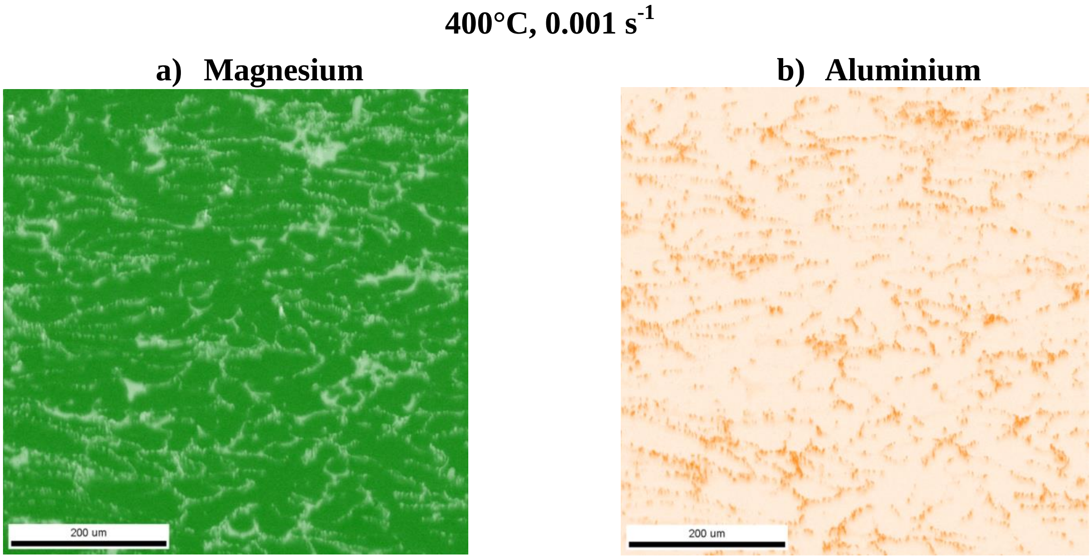
400°C, 0.001 s^{-1}

a) Magnesium

b) Aluminium

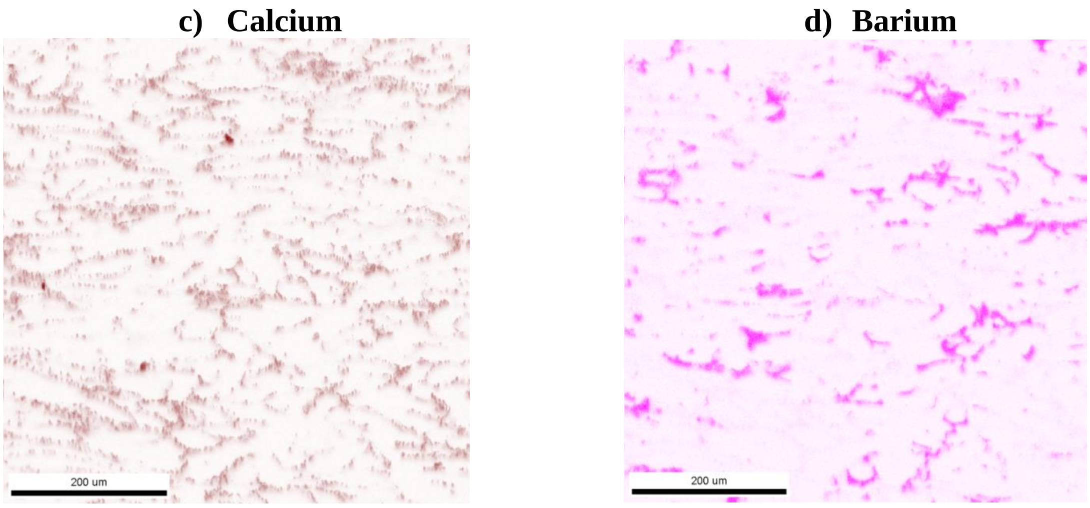
c) Calcium

d) Barium

Figure 38. EDX scan showing the element distribution in the sample. Local strain is 1.1, load direction vertical.

Due to an inhomogeneous strain distribution in the sample a second EBSD measurement was carried out at 2 mm from the middle of the sample, corresponding to a local strain of 1. Figure 39 shows the IPF maps for a) one overview map and in b) for a detailed map. Compared to the map in Figure 37 a) the map now has much more small grains without misorientation. It seems that the blue and green orientations appear without and the orange orientation with new grains.

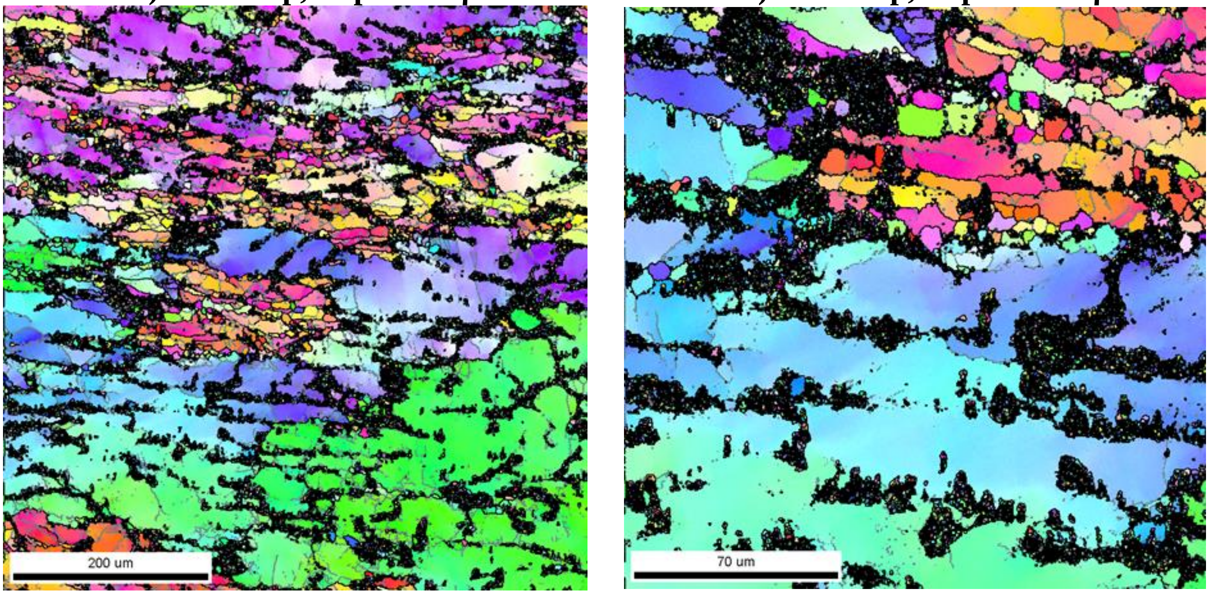
400°C, 0.001 s^{-1}, 2 mm from the middle

a) IPF map, step size 1 µm **b) IPF map, step size 0.4 µm**

Figure 39. Maps for 400°C and a strain rate of 0.001 s^{-1}, 2 mm from the middle. a) IPF map, step size 1 µm; b) IPF map, step size 0.4 µm. Local strain is 1, load direction vertical.

Figure 40 shows the microstructure developed after deformation at 500°C and at a strain rate of 0.001 s^{-1}. The microstructure differs from the ones seen before. There are still some grains showing misorientation and on the other hand there are also new grains. Figure 40 b) shows an overlapping of the IPF with the image quality (IQ) map. The grey shadow of an IQ map gives an idea about good and badly indexed points. Darker grey shadows denote lower IQ values. However, in this case no further information was received.

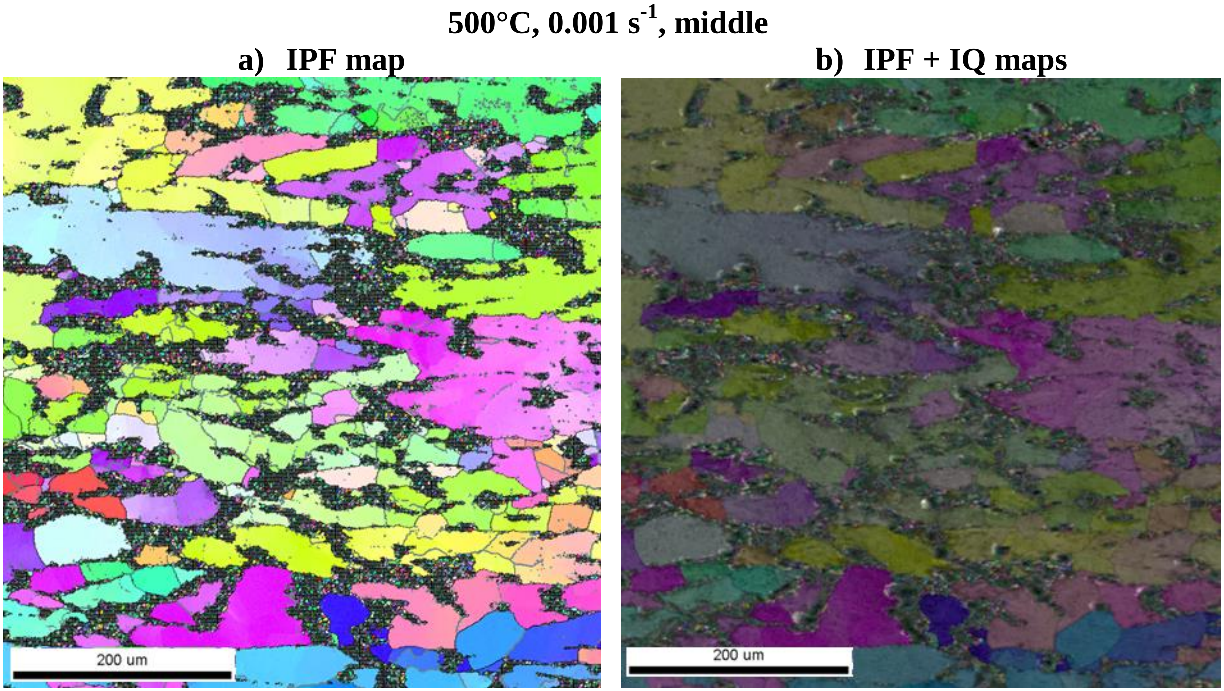
500°C, 0.001 s^{-1}, middle

a) IPF map

b) IPF + IQ maps

Figure 40. Maps for 500°C and a strain rate of 0.001 s^{-1}. a) IPF map, step size 1 µm; b) IPF + IQ map. Local strain is 1.1, load direction vertical.

The next analysis was done for a sample deformed at the same temperature (500°C) but at the highest strain rate of 10 s^{-1}. The result for this EBSD measurement (Figure 41) is a fully recrystallized structure. No grains with misorientation can be detected.

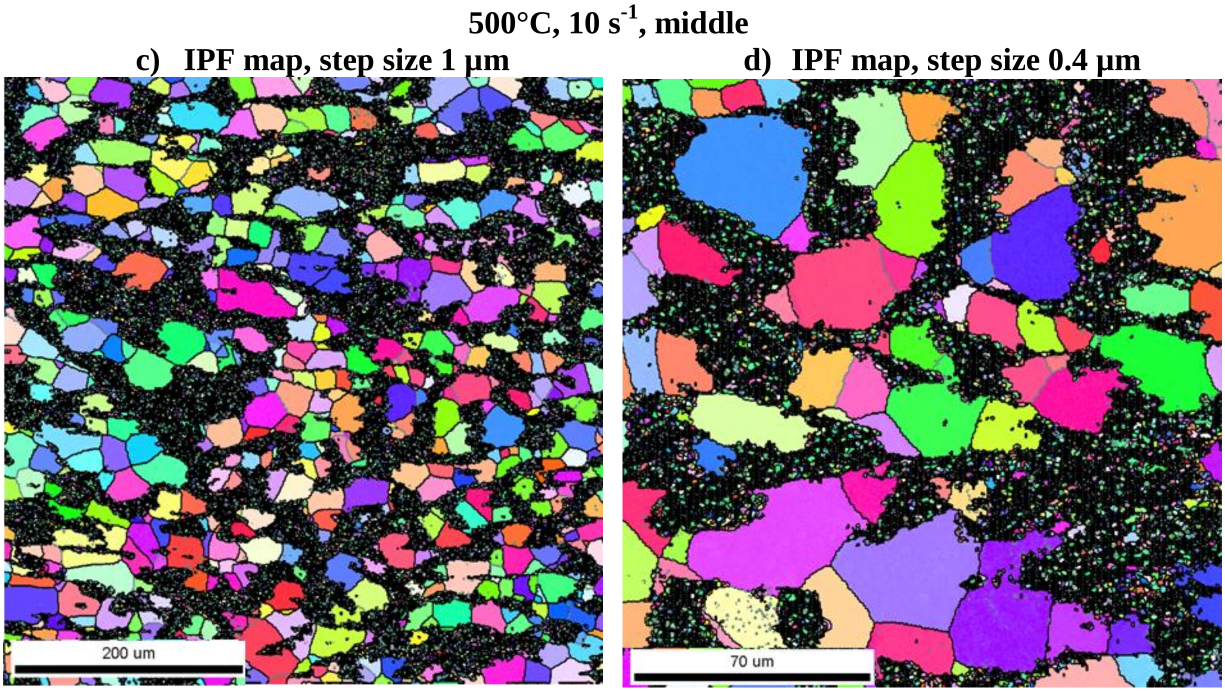
500°C, 10 s^{-1}, middle

c) IPF map, step size 1 µm

d) IPF map, step size 0.4 µm

Figure 41. Maps for 500°C and a strain rate of 10 s^{-1}. a) IPF map, step size 1 µm; b) IPF map, step size 0.4 µm. Local strain is 1.1, load direction vertical.

4.1.4.4 Misorientation

Misorientation measurements were done using grain spread misorientation in the OIM software. In Figure 42 it can be clearly seen that the average misorientation (orange and red areas) decreases with increasing temperature.

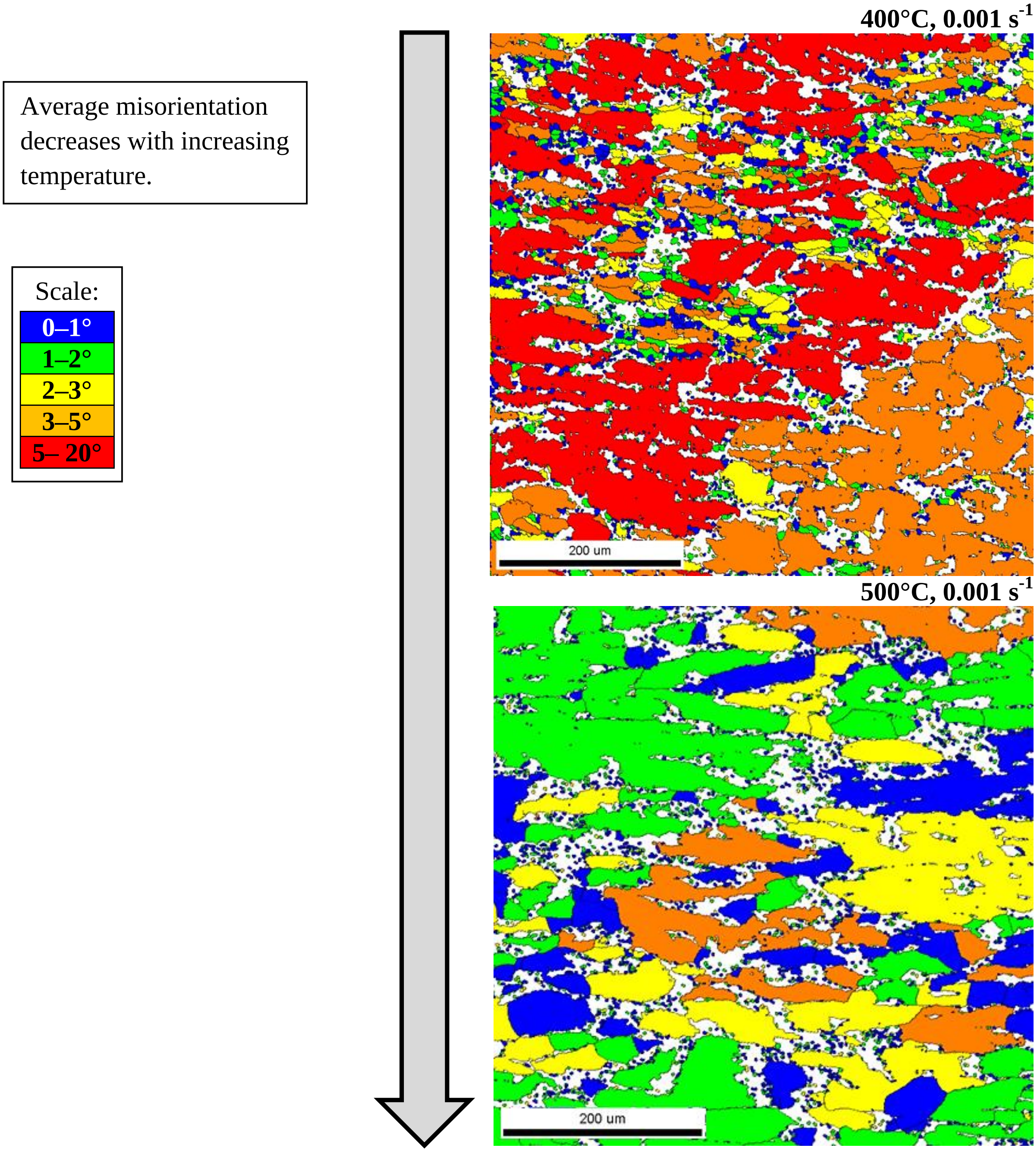

Average misorientation decreases with increasing temperature.

400°C, 0.001 s^{-1}

500°C, 0.001 s^{-1}

Figure 42. Development of misorientation as a function of the temperature.

4.1.5 Constitutive equations

To describe the effect of deformation conditions on the flow stress, constitutive equations have been used. In some cases, especially at high strain rates, no steady state is achieved. Therefore, for calculating constitutive equations the peak flow stress is utilised which is often used by scientists in this case [3].

The relationship between the stress and the strain rate can be described by a power law of the form shown in Equation 4.

For calculating constitutive equations by the model of Sellars and Tegart [2] the stress multiplier c was determined to be 0.03 MPa^{-1} and a stress exponent n of 4.09 was calculated. The apparent activation energy is calculated from the slope of the linear regression for each strain rate in Figure 43 a). The value for Q was determined to be 203 kJ mol^{-1}. The constitutive equation can be written in the form of Equation 49:

$$\dot{\varepsilon} = 3.76 \cdot 10^{12} [\sinh(0.03\sigma_{Peak})]^{4.09} \exp\left(\frac{-202599}{RT}\right)$$ **Equation 49**

In Figure 43 b) the correlation of the Zener-Hollomon parameter versus the flow stress is given and shows a good correlation with a R^2 of 0.99.

a) Determination of *Q*

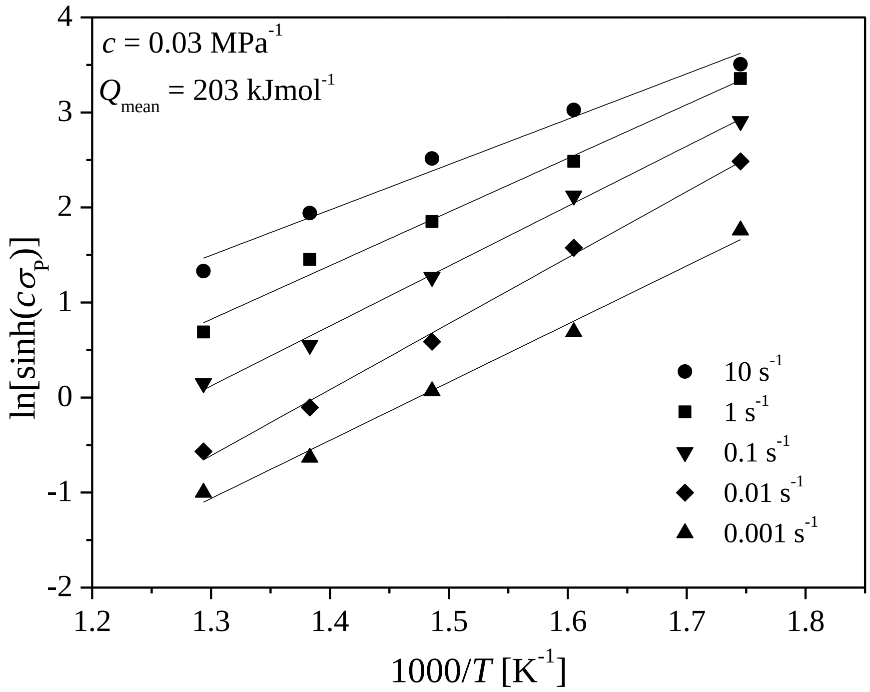

b) Zener-Hollomon vs. flow stress

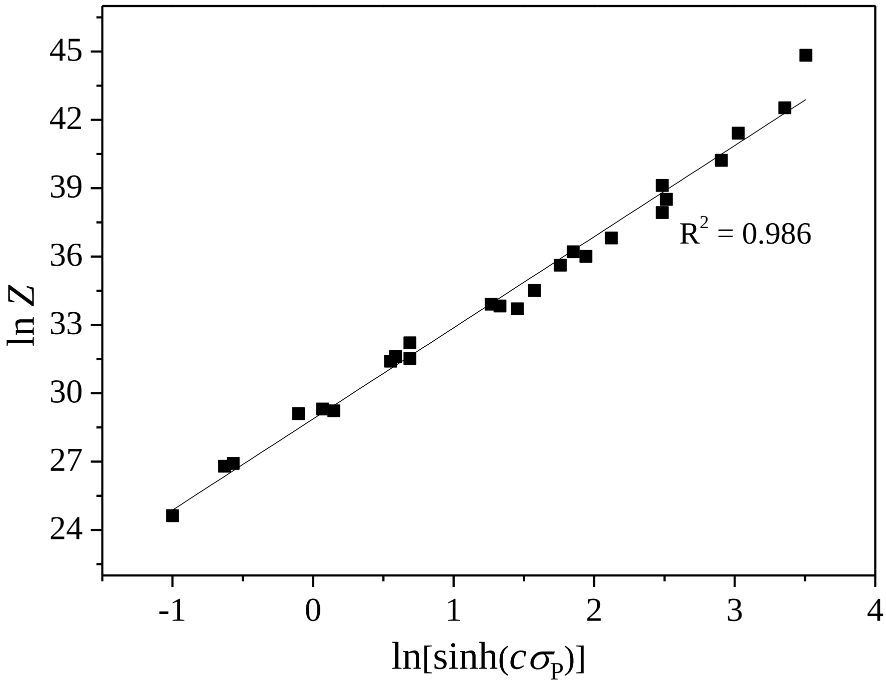

Figure 43. Constitutive equations: a) activation energy *Q* and b) relationship between Zener-Hollomon parameter vs. flow stress.

In Figure 44, a correlation of the recrystallized grain size with the *Z* parameter is given for all measured points.

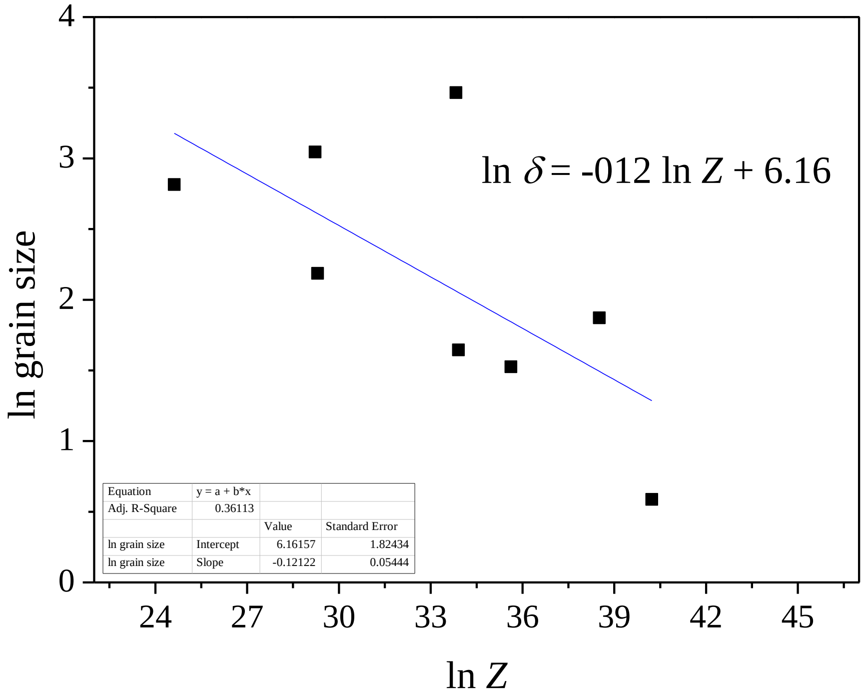

Equation	y = a + b*x		
Adj. R-Square	0.36113		
		Value	Standard Error
ln grain size	Intercept	6.16157	1.82434
ln grain size	Slope	-0.12122	0.05444

Figure 44. Correlation of the grain size with Z for all measured points.

4.1.6 Processing maps

Processing maps were calculated for a strain of 0.2 (Figure 46), 0.3 (Figure 47), 0.4 (Figure 48) and 0.5 (Figure 49). In all the following figures, five different approaches are shown. The isolines represent the dissipation efficiency or m values, which can be correlated to the microstructural changes. Instability predictions are shown as dashed areas using fine lines. The fifth map α_{SJ}, is showing instability values proposed by Semiatin and Jonas and shows the instability in red.

Firstly, Prasad's map based on DMM was calculated using Equation 13 for the dissipation efficiency value. For all strains it can be seen that the highest η_P values occur at low strain rates from low to moderate temperatures as well as around moderate strain rates combined with high temperatures. This trend can be seen in Figure 45 a).

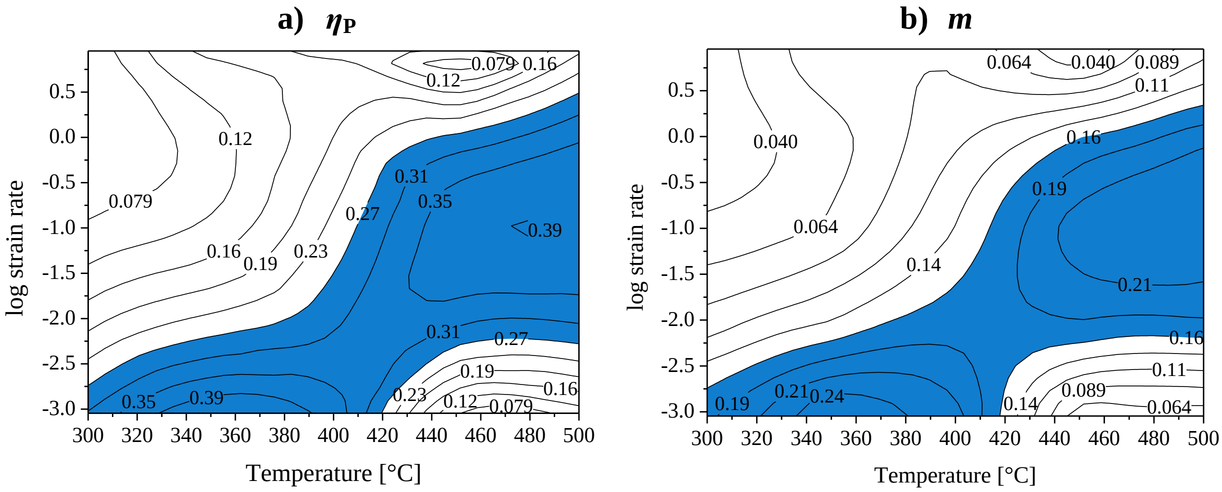

Figure 45. a) Dissipation efficiency map for the model of Prasad showing the highest η values area in blue and b) the m map showing the highest values of m in blue.

With increasing the strain the dissipation efficiency values are decreasing. At a strain of 0.2 the highest η_P value is 0.39 and for a strain of 0.5 the highest η_P value is 0.33. The instability parameter ξ is negative at low temperatures from moderate to high strain rates and at high temperatures combined with high strain rates nearly independent of the strain.

Secondly, the map based on mDMM by Murty and Rao was calculated. Therefore, Equation 16 and Equation 25 were used. The trend that η_{M+R} follows is similar to that one shown in Figure 45. The difference to the model of Prasad is that the η_{M+R} values are higher. Also for this type of processing map the η_{M+R} values are decreasing with increasing strain. Instability calculated based on this approach shows values below zero almost in the whole processing map.

The trend of the third approach, showing the m map can be seen in Figure 45 b) and looks similar to Figure 45 a). Instability occurs if the values of strain rate sensitivity m are smaller than zero.

The processing maps calculated by Prasad follow the same tendency as m, because m is directly used in the calculation for the DMM.

The instability parameter κ_j which is also based on the instability model proposed by Ziegler and DMM, was calculated based on Equation 27. The received values are similar to that proposed by the instability parameter of Prasad and follow the same tendency as ξ.

Finally, the α_{SJ} parameter developed under the assumption of instability for maximal force was calculated using Equation 37. For Ti-alloys it is accepted that instability occurs for values ≥ 5 meaning strong softening. No investigations are made for Mg-alloys, and it is only mentioned in [98] that this value “5” is guilty for all cases. Due to a lack of the necessary investigations and information related to the value “5” it was accepted in this work that instability occurs if $\alpha_{\mathrm{SJ}} \geq 0$ (by definition). At low strain no instability is detected, but with increasing the strain up to 0.4, instability is shown at high strain rates. With increasing strain the area of instability became bigger.

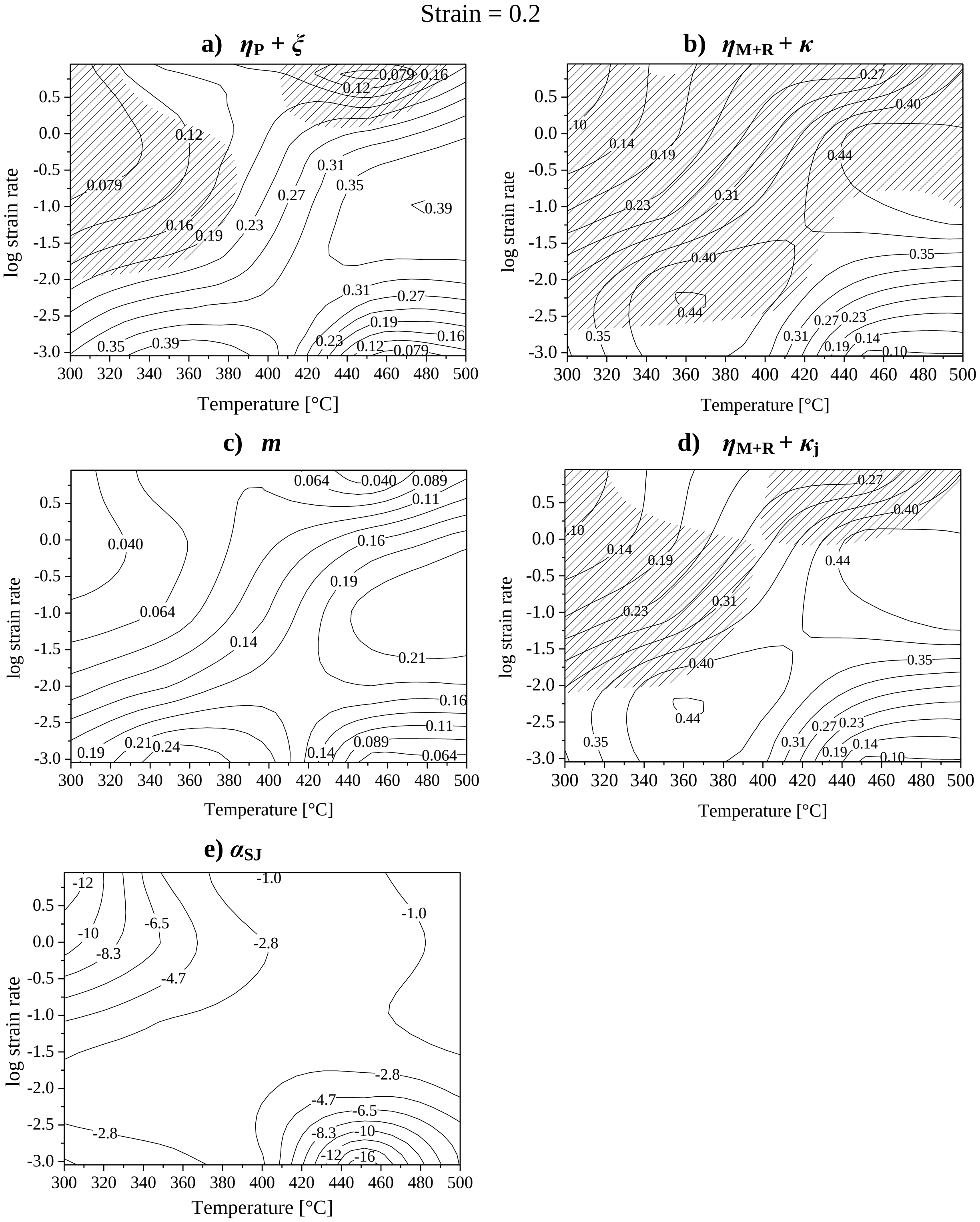

Figure 46. Processing maps for a strain of 0.2. Models of a) Prasad, b) Murty and Rao, c) m, d) Murty and Rao using κ_j as instability parameter and e) the instability model by Semiatin and Jonas.

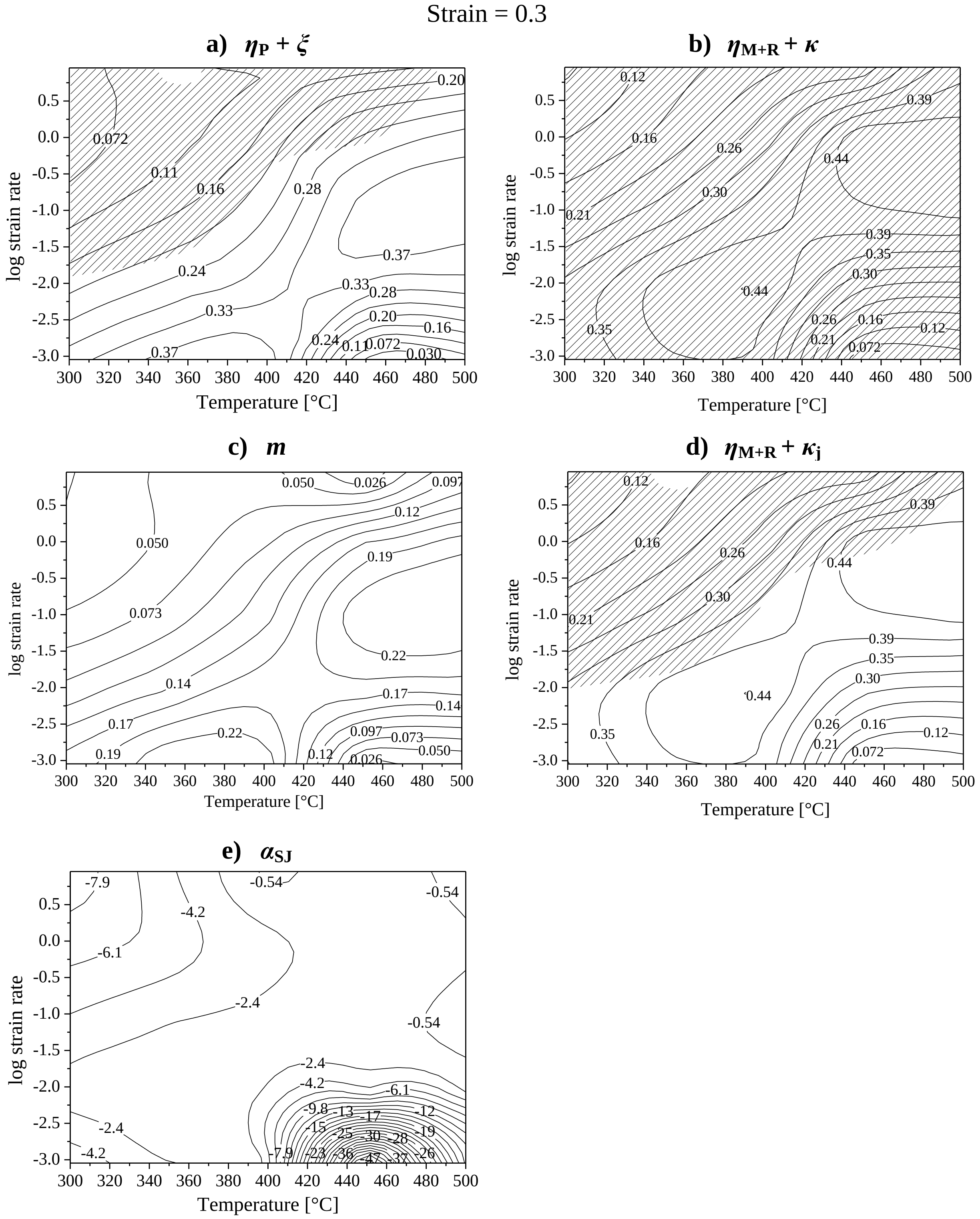

Figure 47. Processing maps for a strain of 0.3. Models of a) Prasad, b) Murty and Rao, c) *m*, d) Murty and Rao using κ_j as instability parameter and e) the instability model by Semiatin and Jonas.

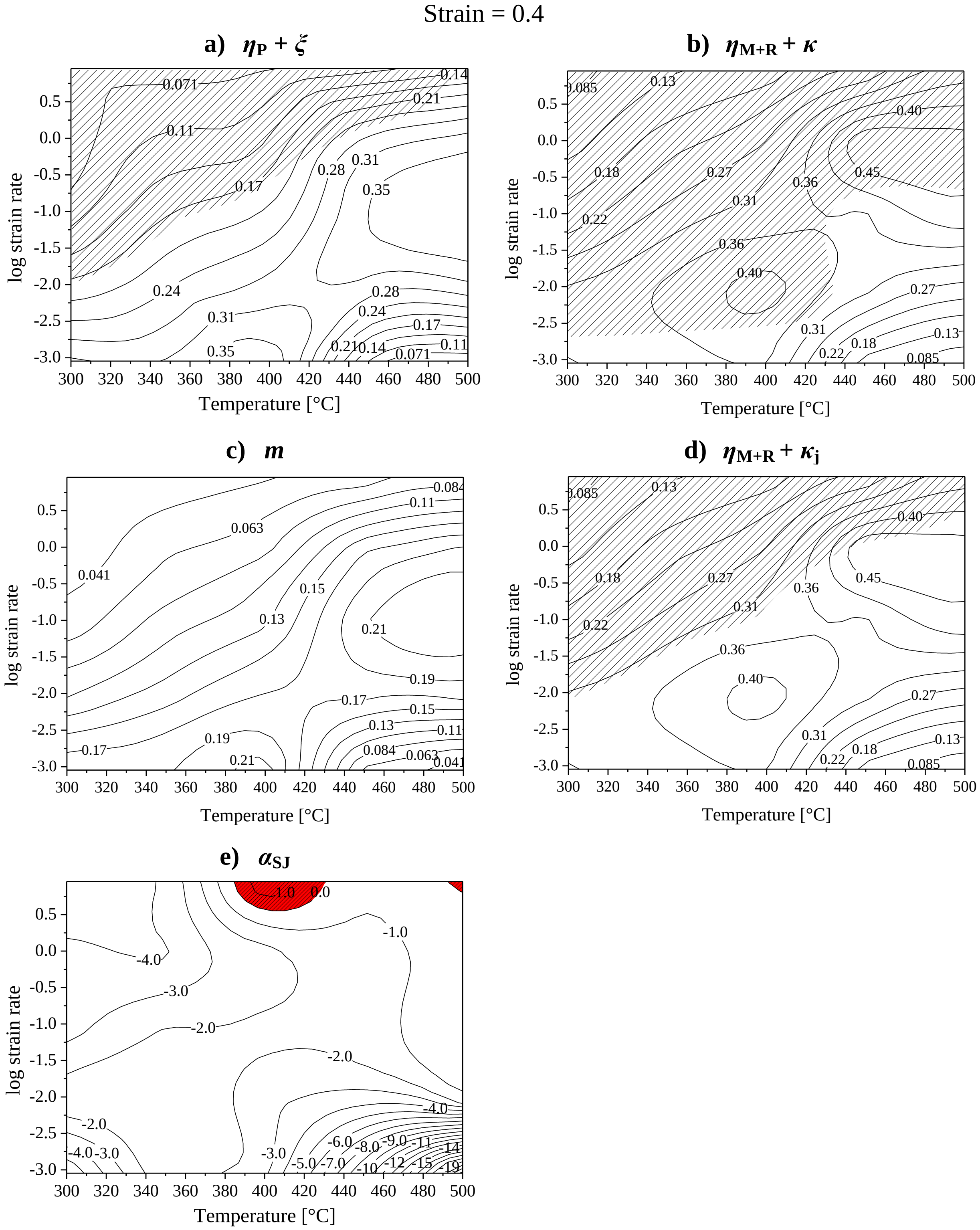

Figure 48. Processing maps for a strain of 0.4. Models of a) Prasad, b) Murty and Rao, c) *m*, d) Murty and Rao using κ_j as instability parameter and e) the instability model by Semiatin and Jonas.

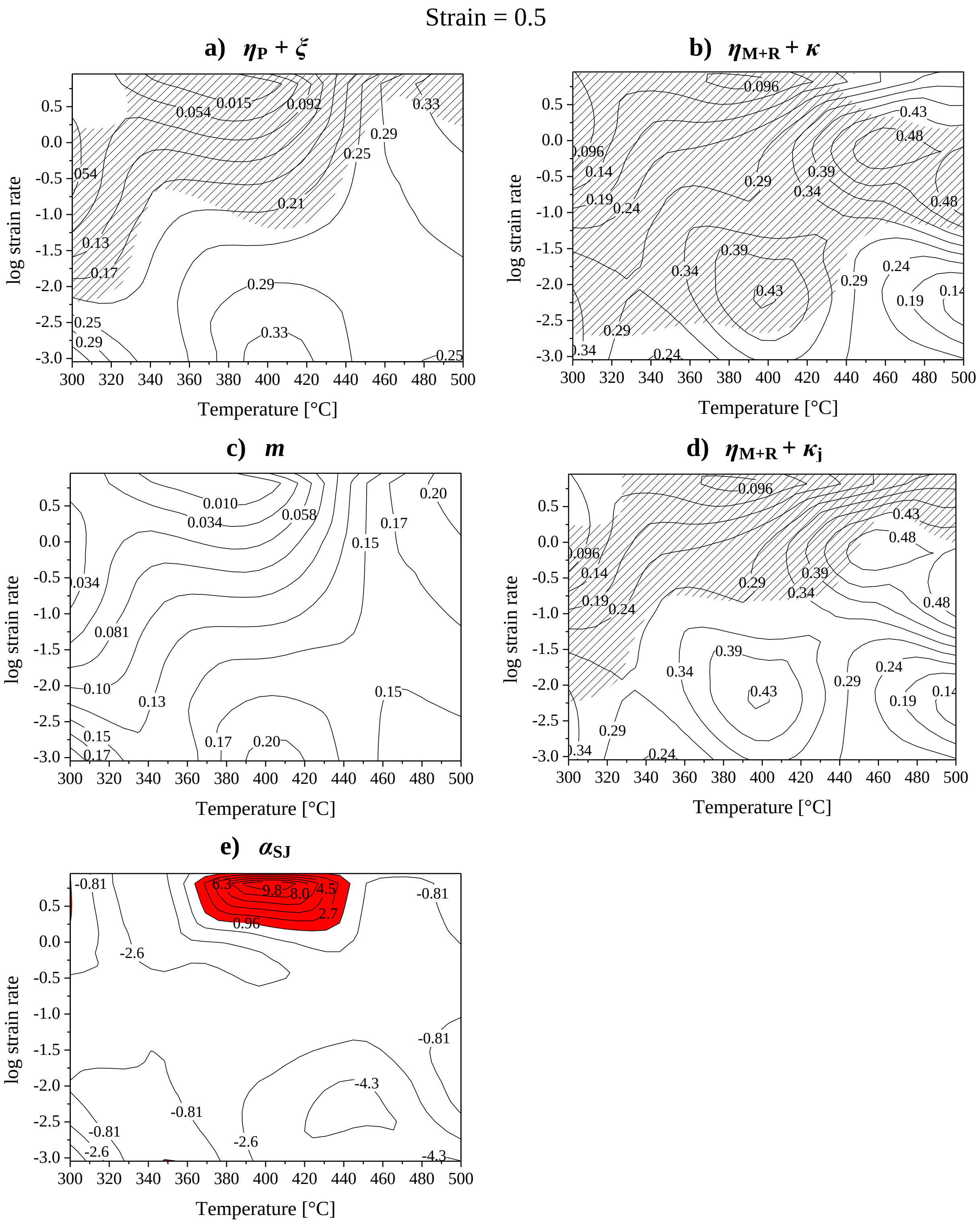

Figure 49. Processing maps for a strain of 0.5. Models of a) Prasad, b) Murty and Rao, c) m, d) Murty and Rao using κ_j as instability parameter and e) the instability model by Semiatin and Jonas.

4.1.6.1 Comparison of *m* for as-cast and the extruded condition

As already known, a higher formability is expected for the extruded than for the as-cast alloy. Therefore, the *m* maps of both conditions are compared for a strain of 0.3. The area depicted in yellow shows the same temperature field. The green arrow indicates the highest *m* value and the red one shows a negative *m* value.

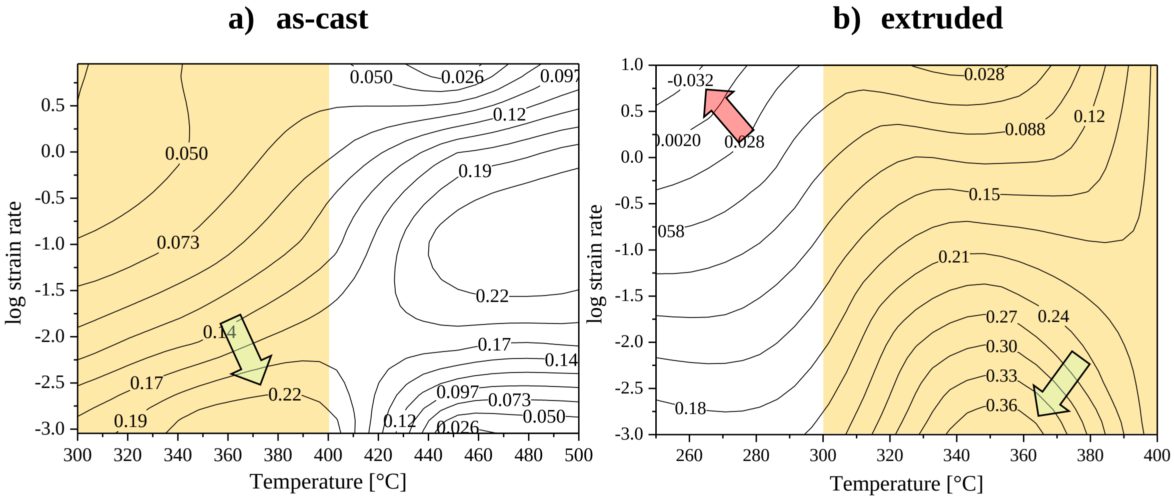

Figure 50. Comparison of parameter *m* for a) as-cast and b) extruded material.

It can be seen that the highest *m* value appears for both cases at temperatures between 340–380°C. The highest value for the as-cast material is 0.22 whereas for the extruded material this value increased to 0.36. In general, the *m* values are larger for the extruded material than for the as-cast one.

4.2 Titanium

4.2.1 As-received material

The microstructure of the as-received material of Ti55531 is shown in Figure 51 [83], which consists of 30% globular α-phase (Figure 51a)), embedded in β grains. Additionally, β subgrains are already present in the initial microstructure as can be seen in Figure 51b). The blue arrow indicates the α-phase whereas the green one indicates the β-phase.

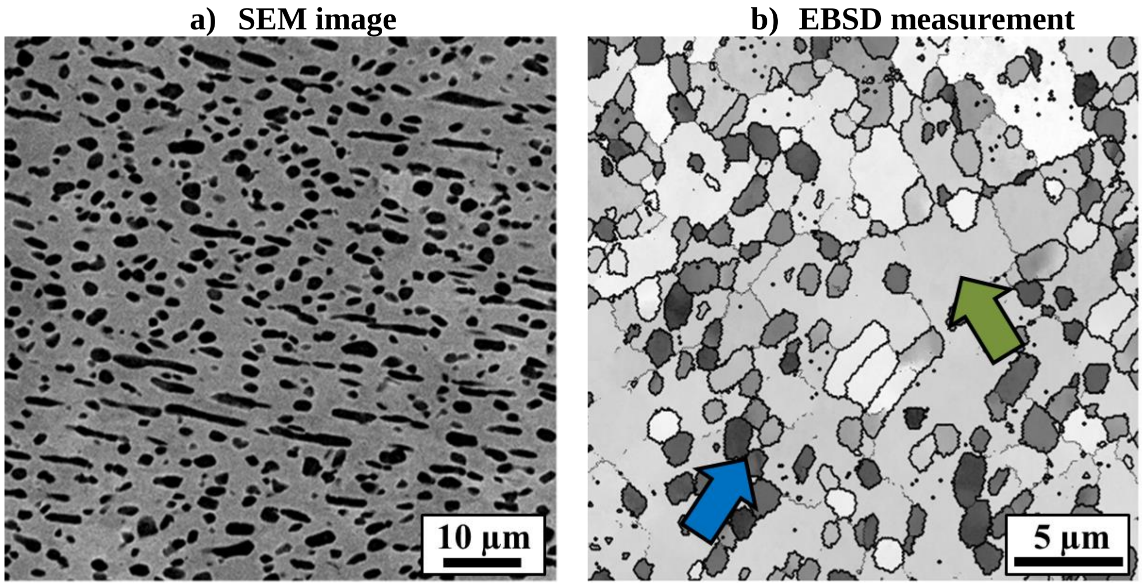

Figure 51. As-received material. a) SEM image in BSE mode, with α-phase in black; b) EBSD measurement: LAGB in grey, HAGB in black; the blue arrow indicates the α-phase and the green one the β-phase [83].

The microstructure after heat treatments and water quenching consists of 13 vol% of α-phase at 763°C and 8 vol% at 783°C. The belonging micrographs are shown in Figure 52 for a) 763°C and b) 783°C.

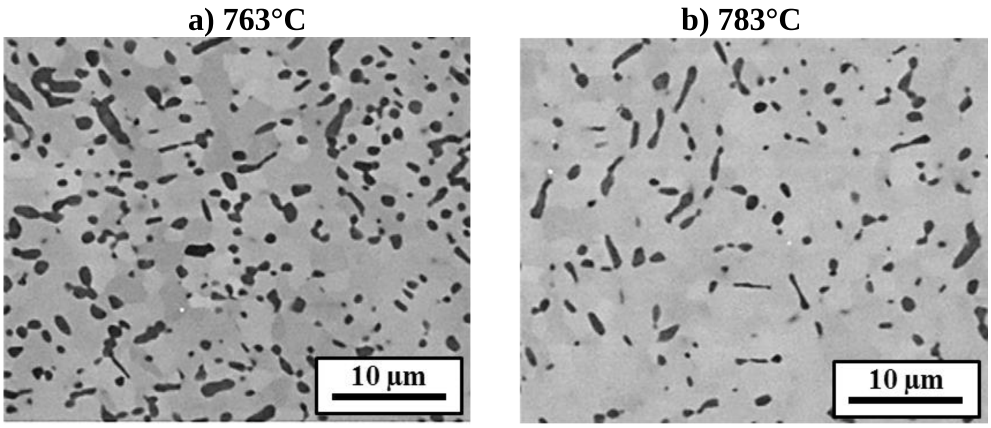

Figure 52. Material before deformation, showing decreasing amount of α-phase by increasing temperature [83].

4.2.2 Flow curves

The flow curves are shown in Figure 53 for the five tested temperatures between 763°C–843°C for all the five strain rates in the range of 0.001–10 s^{-1}. It can be seen that the stress values are decreasing with increasing temperature and decreasing strain rate. In general softening is occurring for nearly all the conditions as can be seen in Figure 54. At high strain rates > 1 s^{-1} multiple peaks are present due to artefacts such as ringing effect and/or self-heating. At moderate and low strain rates a stress peak is followed by strain hardening and then softening. This effect is more marked in the deformations in the single phase β-field.

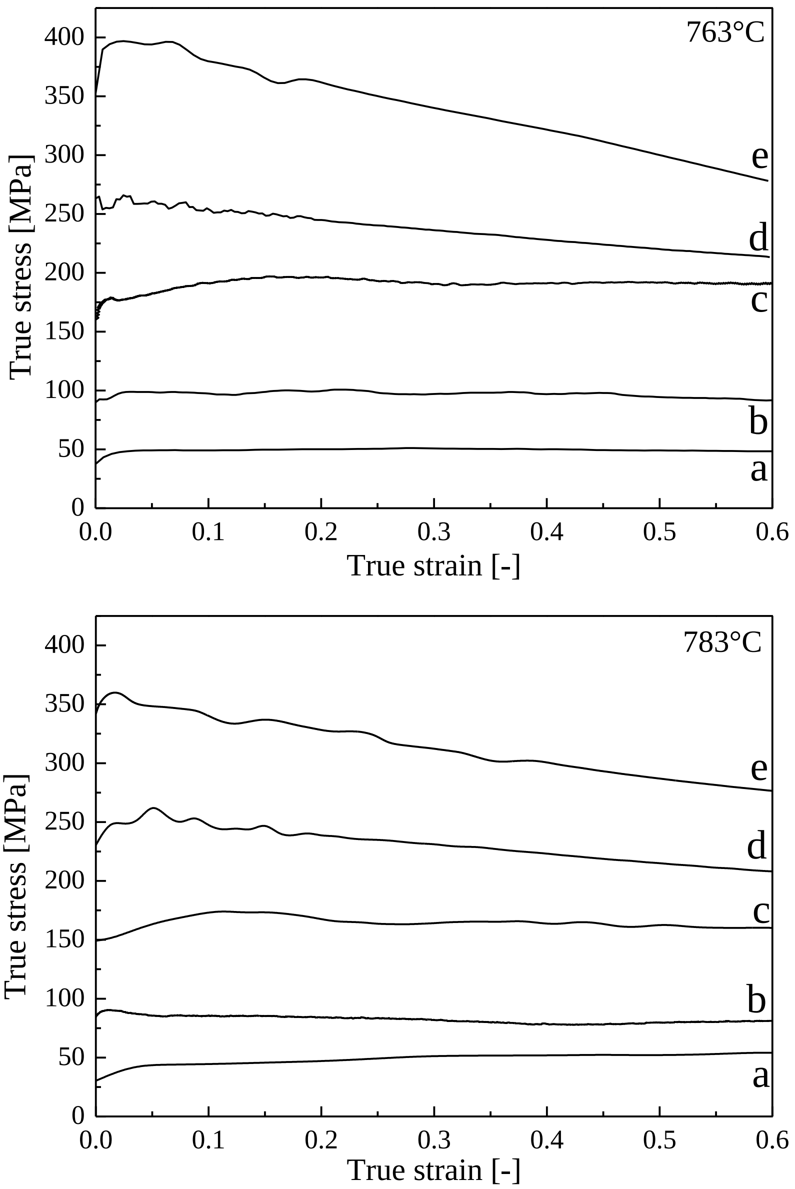

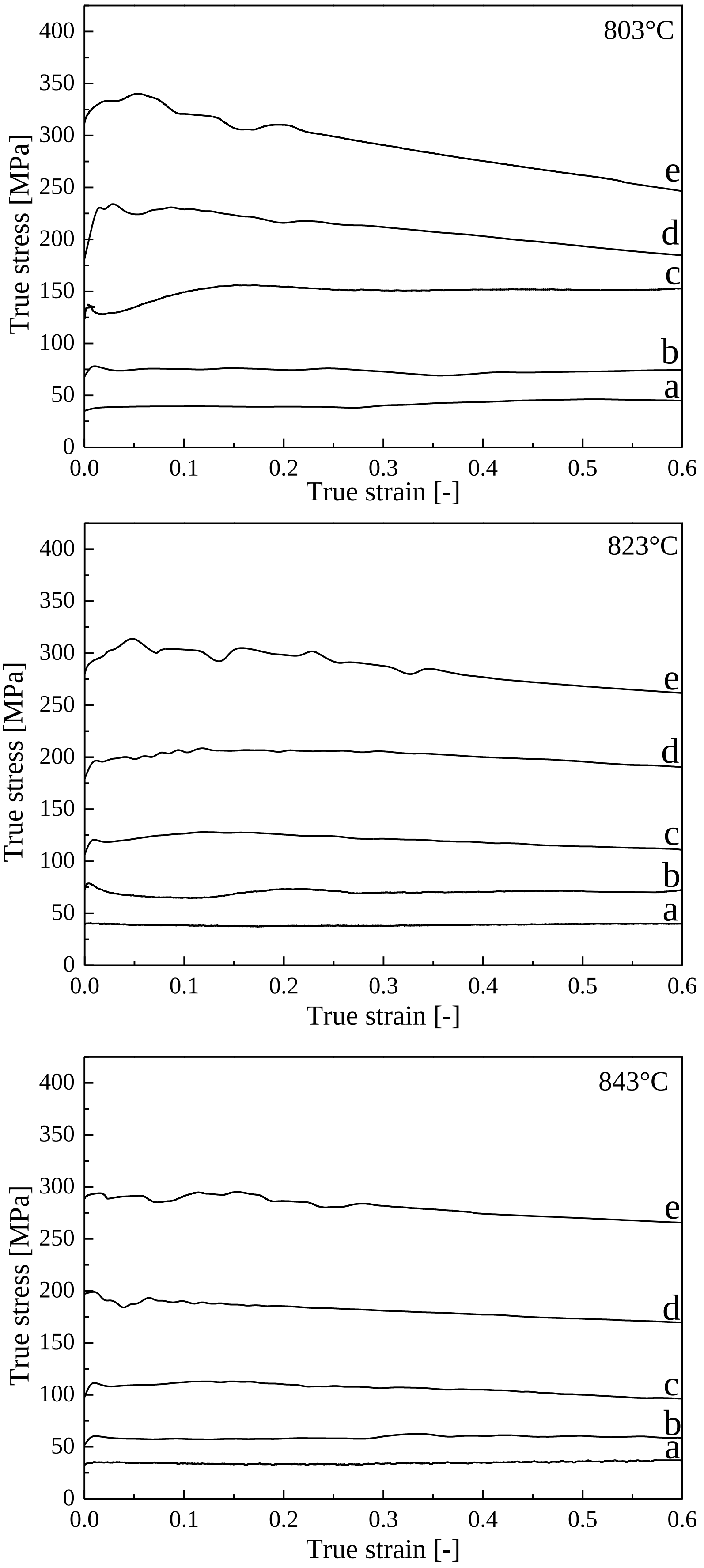

Figure 53. Flow curves of Ti55531 for the five used temperatures and at strain rates of a = 0.001 s^{-1}, b = 0.01 s^{-1}, c = 0.1 s^{-1}, d = 1 s^{-1} and e = 10 s^{-1}.

As mentioned before, softening takes place in nearly every case, although it is difficult to visualise this from Figure 53. Therefore, the relative softening in percentage was calculated as 100 x (peak stress – stress value at 0.6 of strain)/(peak stress) and plotted as a function of the temperature and strain rate (Figure 54). The most intense effect of softening occurs at low temperatures and high strain rates. These values decrease with increasing the temperature and decreasing the strain rate. At very low strain rates and moderate to high temperatures, strengthening and steady state occur, as depicted in the dashed area.

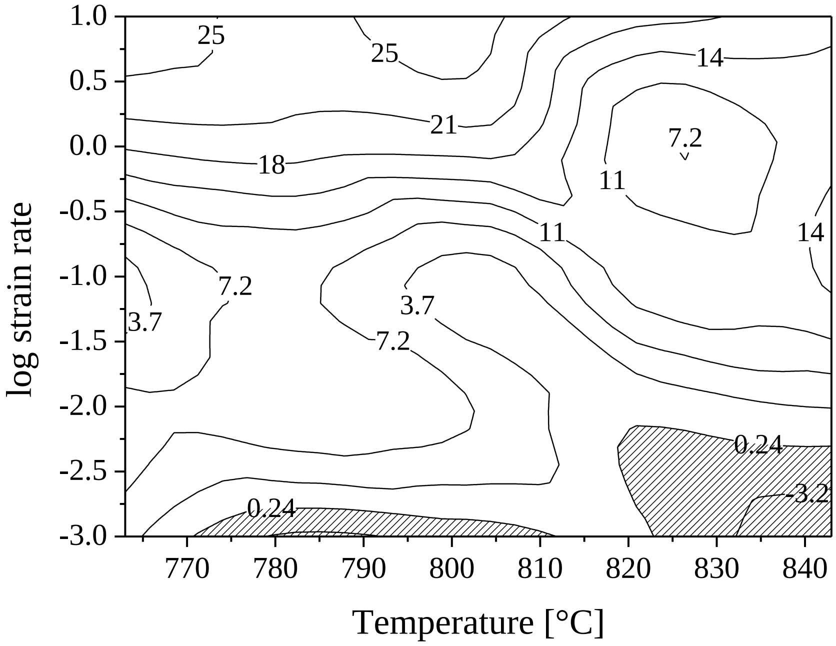

Figure 54. Relative softening isolines as a function of strain rate and temperature. Dashed area shows strengthening.

4.2.3 Microstructure after hot deformation

4.2.3.1 Light optical microscope investigations

In Figure 55 light optical micrographs show the microstructure after deformation at two temperatures (803°C, 843°C) and two strain rates. The following pictures were taken in the middle of the sample and were etched with Kroll.

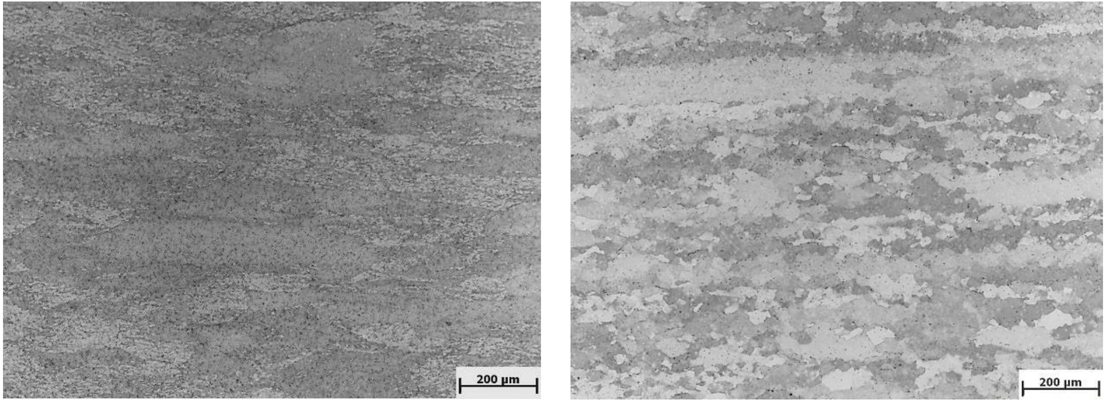
803°C, 0.001 s^{-1}

803°C, 10 s^{-1}

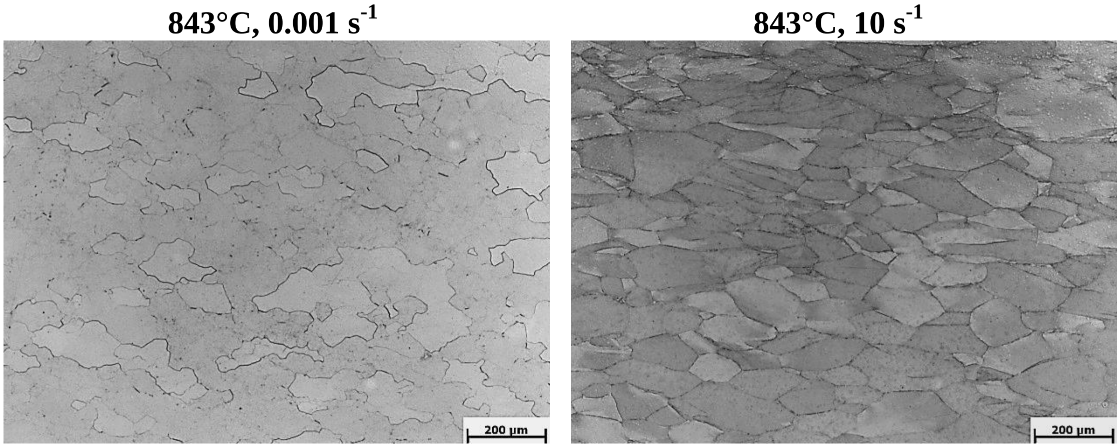
843°C, 0.001 s^{-1}

843°C, 10 s^{-1}

Figure 55. Light optical microscope investigations, pictures taken in the middle of the sample. Local strain is 1.1, load direction vertical.

At 803°C for both strain rates, α-phase is still present. Furthermore, the grain boundaries are serrated. For the LOM investigation at 843°C no α-phase is present and the β grains are clearly distinguishable. The shape of the grains differs and a detailed explanation is given with Figure 56.

The result of the LOM investigations cannot be used to give any idea about subgrains or new grains for this case. Serrated grain boundaries and different grain shapes lead to the idea that grain boundary mobility occurred during the deformation process.

In Figure 56 the micrographs of 4 samples deformed at 843°C for four different strain rates are shown. The pictures are taken at a local strain of 1 and it can be seen that the grain boundaries are not flat but serrated. The waves of the serration are different for the different strain rates. At low strain rates the waves have larger amplitude than at higher strain rates. White arrows mark the serrated grain boundaries.

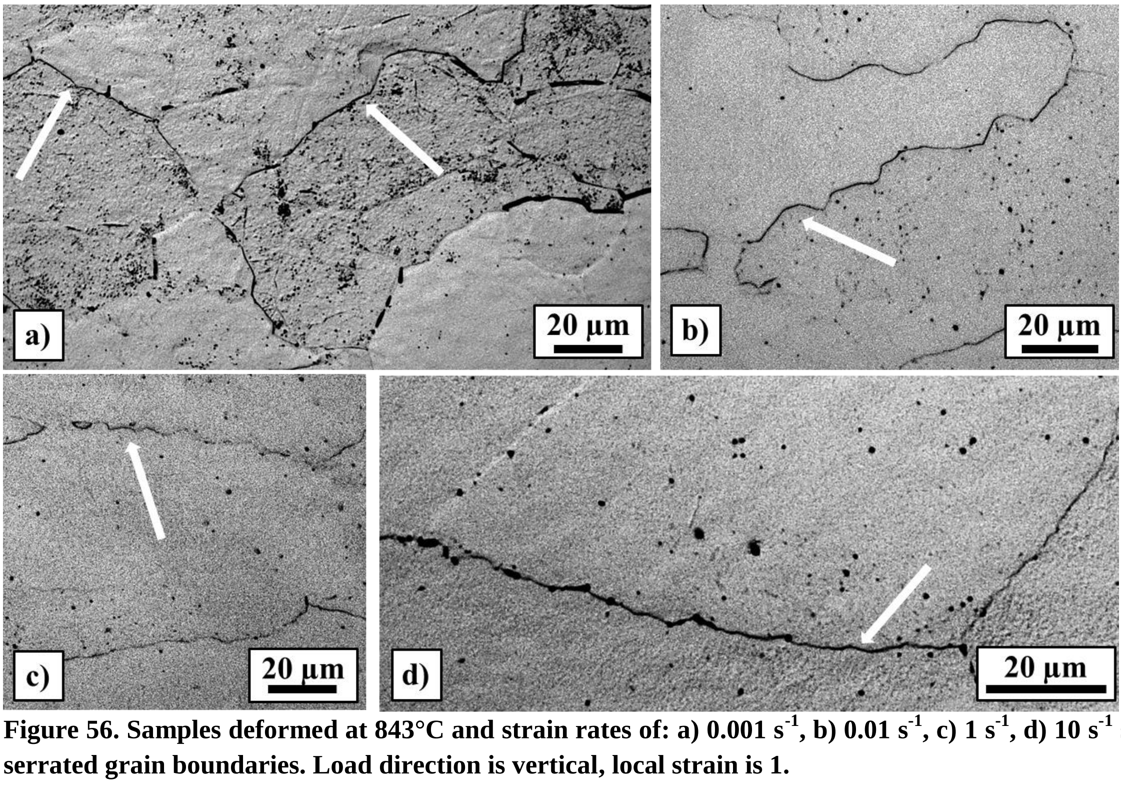

Figure 56. Samples deformed at 843°C and strain rates of: a) 0.001 s^{-1}, b) 0.01 s^{-1}, c) 1 s^{-1}, d) 10 s^{-1} showing serrated grain boundaries. Load direction is vertical, local strain is 1.

4.2.3.2 EBSD measurements

The results of the EBSD measurements are shown in this chapter. In Figure 57 the unit triangles of α-Ti and β-Ti are presented. For α titanium red is correlated to 0001, blue to $10\bar{1}0$ and green to $2\bar{1}\bar{1}0$, for β titanium the colour red is assigned to the 001 crystal direction, blue to 111 and green to 101.

Figure 57. Triangles, showing the crystal orientation for α- and β-phase.

In Figure 58 two IPF maps are shown. The samples were deformed at 763°C at two different strain rates, 0.001 s^{-1} and 10 s^{-1}. The α-phase is depicted in black as well as the HAGB. LAGB are marked in the colour grey. The arrow in Figure 58 a) is pointing at grains free of misorientation that have the size of subgrains. Furthermore, some new grains at the grain boundary and a high amount of subgrains are present for these deformation parameters. The white arrows in Figure 58 b) show small grains at the high angle grain boundaries.

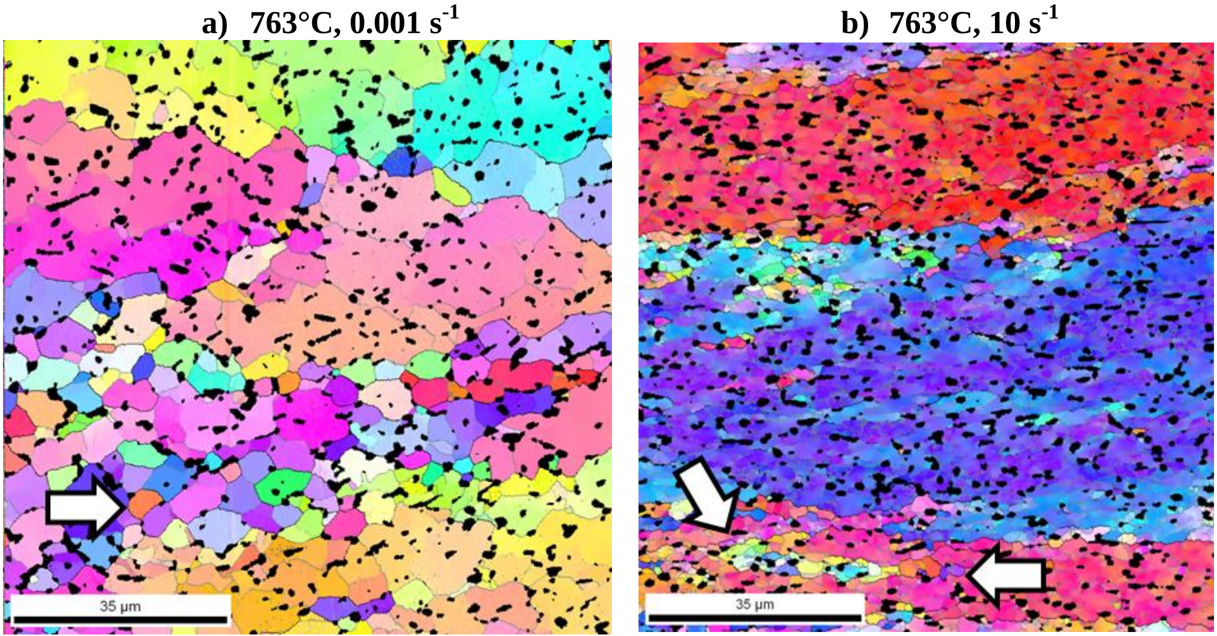
a) 763°C, 0.001 s^{-1}
b) 763°C, 10 s^{-1}

Figure 58. IPF maps of samples deformed at 763°C and a) 0.001 s^{-1}, b) 10 s^{-1}. HAGB and α-phase are depicted in black and LAGB in grey. Local strain of 1, load direction is vertical.

Figure 59 shows the microstructure of two deformed samples at 783°C for strain rates of 0.001 s^{-1} and 10 s^{-1}. HAGB are shown in black and LAGB in grey. After high strain rate deformation (Figure 59 b)), subgrains are smaller than at slower strain rate. Additionally, some small new grains are formed at the grain boundaries.

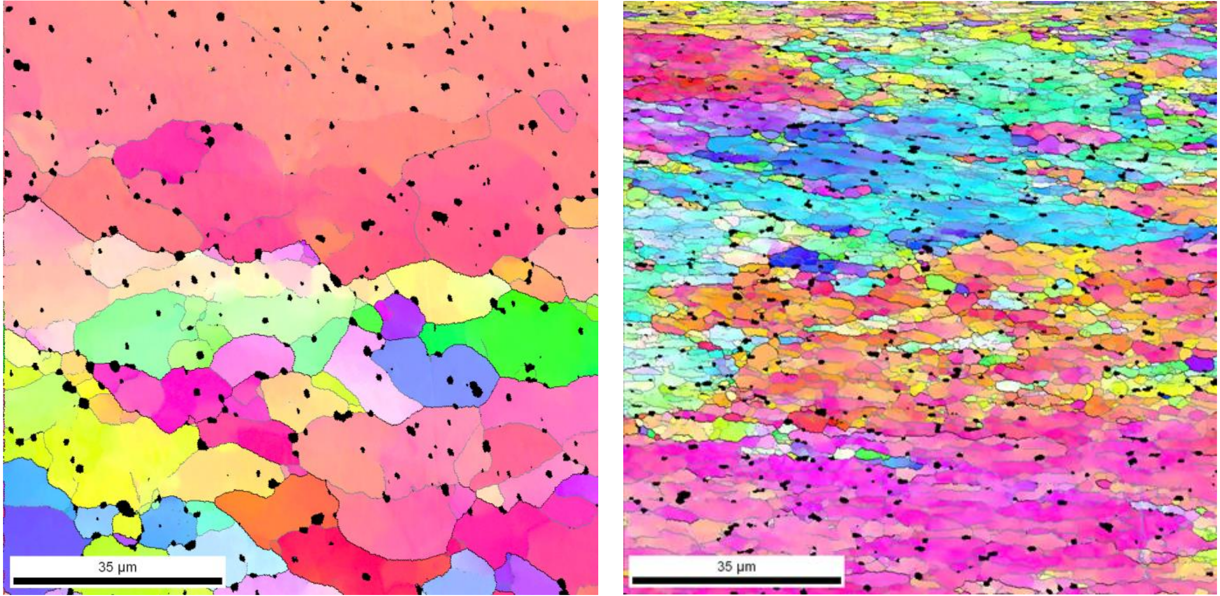
a) 783°C, 0.001 s^{-1} **b) 783°C, 10 s^{-1}**

Figure 59. IPF maps for 783°C a) 0.001 s^{-1} and b) 10 s^{-1}. Local strain of 1, load direction is vertical.

The following two figures are showing IPF maps from EBSD measurements of samples after deformation above the T_β. HAGB are depicted in black and LAGB are shown in grey. In Figure 60 IPF maps after deformation at 823°C and 0.01 s^{-1} and 1 s^{-1} are shown. In picture a) many subgrains were developed (white arrow) and for picture b) large misorientation occurs within one grain (green arrow) and on the other hand very small new grains (blue arrow) were formed at the β-prior grain boundaries.

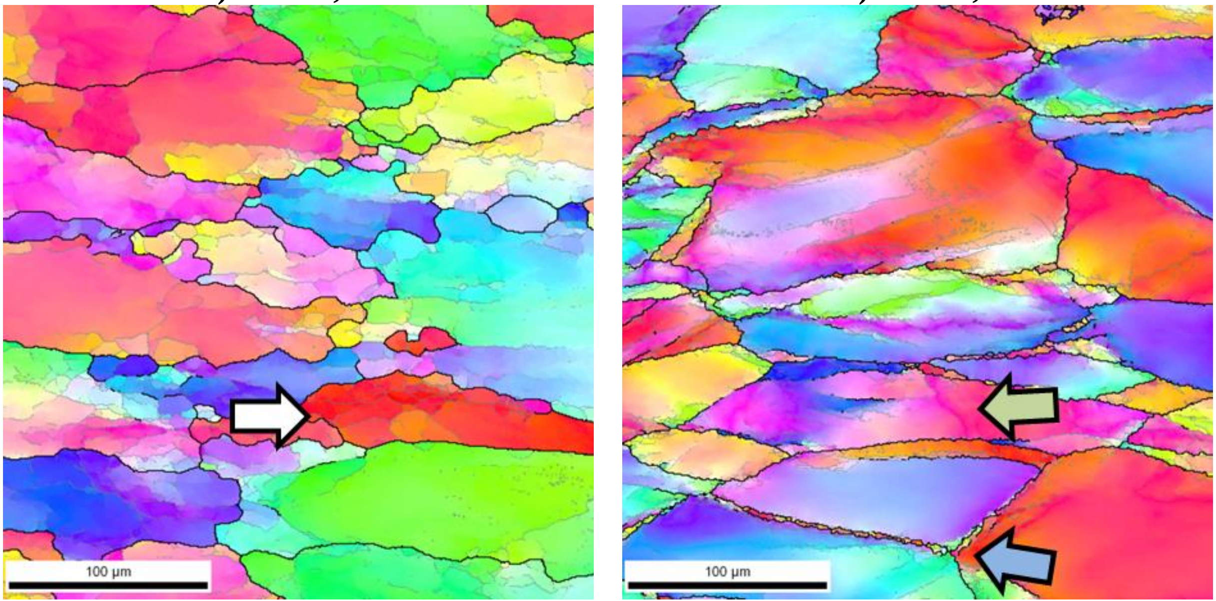
a) 823°C, 0.01 s^{-1} **b) 823°C, 1 s^{-1}**

Figure 60. IPF maps of samples after deformation at 823°C a) 0.01 s^{-1} and b) 1 s^{-1}. Local strain of 1, load direction is vertical.

Figure 61 gives a summary of the microstructural changes of samples deformed at 843°C with increasing strain rate from 0.001 s^{-1} up to 10 s^{-1}. The white arrow in picture a) indicates a subgrain, whereas the arrow in picture d) indicates the misorientation in one grain.

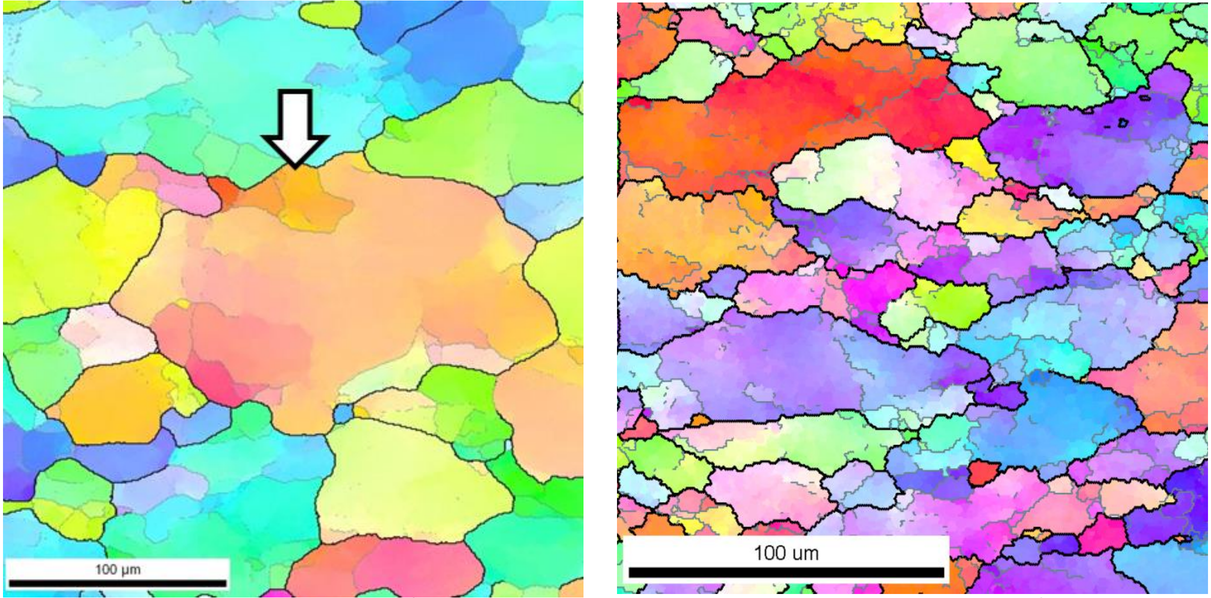

a) 843°C, 0.001 s^{-1} **b) 843°C, 0.01 s^{-1}**

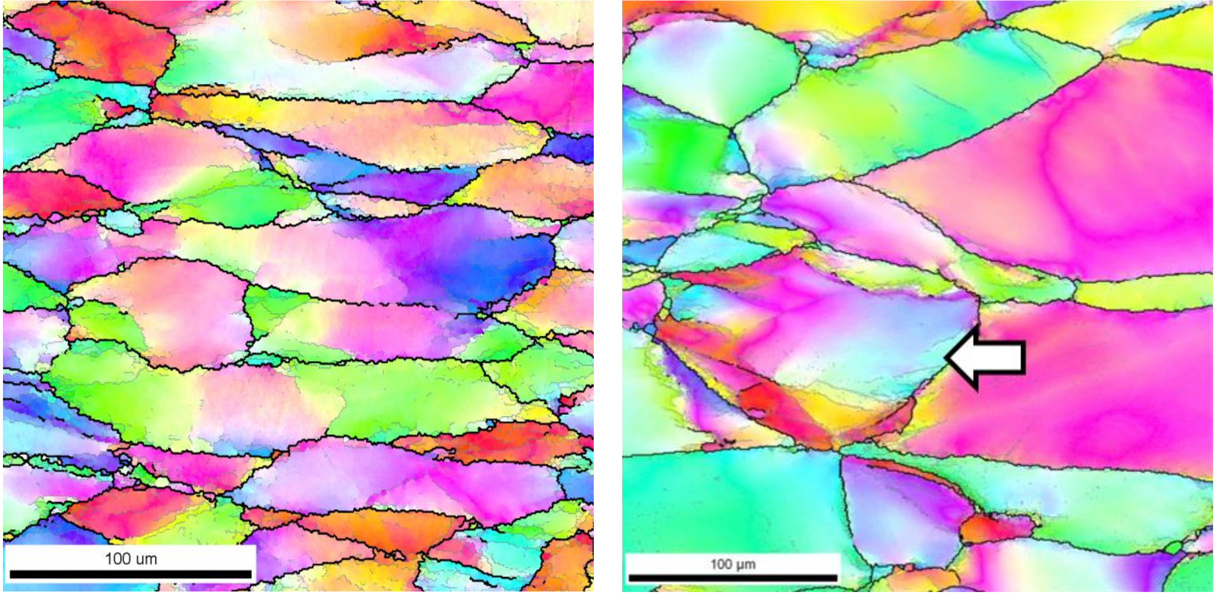

c) 843°C, 1 s^{-1} **d) 843°C, 10 s^{-1}**

Figure 61. IPF maps of samples deformed at 843°C a) 0.001 s^{-1}, b) 0.01 s^{-1}, c) 1 s^{-1} and d) 10 s^{-1}. Local strain of 1, load direction is vertical.

The misorientation within grains is increasing with increasing strain rate.

4.2.3.3 Misorientation profiles

The crystallographic misorientation within and between grains was investigated using different tools.

Firstly, the cumulative misorientation was calculated within one grain along a line. Secondly, the misorientation using a Kernel based model of the OIM software was used to obtain a local map and thirdly, the grain spread misorientation was used to obtain average values.

The cumulative misorientation in the β-phase is shown in Figure 62. In picture a) the misorientation was measured for samples deformed at 763°C and in picture b) for samples deformed at 843°C. For both cases it can be realised that the misorientation is increasing with increasing strain rate. A high increment in the slope of the curve can be seen for deformation rates at 1 s^{-1} and 10 s^{-1}. The white arrows show an increase in the misorientation which occurs when the drawn line hits an α grain.

a) 763°C

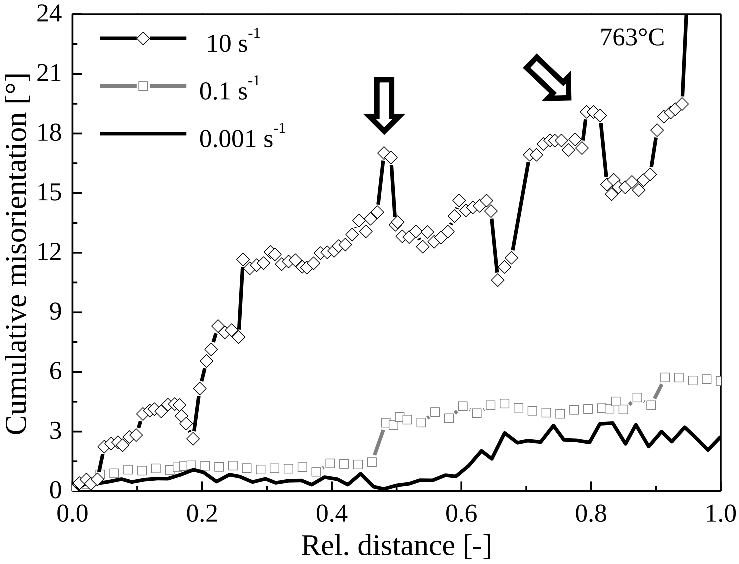

b) 843°C

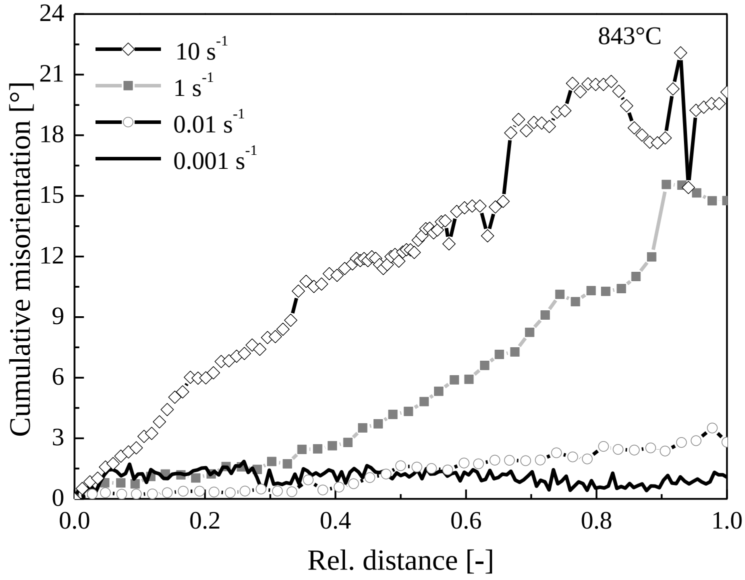

Figure 62. Cumulative misorientation in the β-phase for samples deformed at different strain rates and two temperatures: a) 763°C and b) 843°C.

In Figure 63 the Kernel average misorientation maps are shown for samples deformed at 843°C for a) 0.001 s^{-1} and b) 10 s^{-1}. It is shown that the maximal local misorientation is reached at the high angle grain boundaries especially at the highest strain rate.

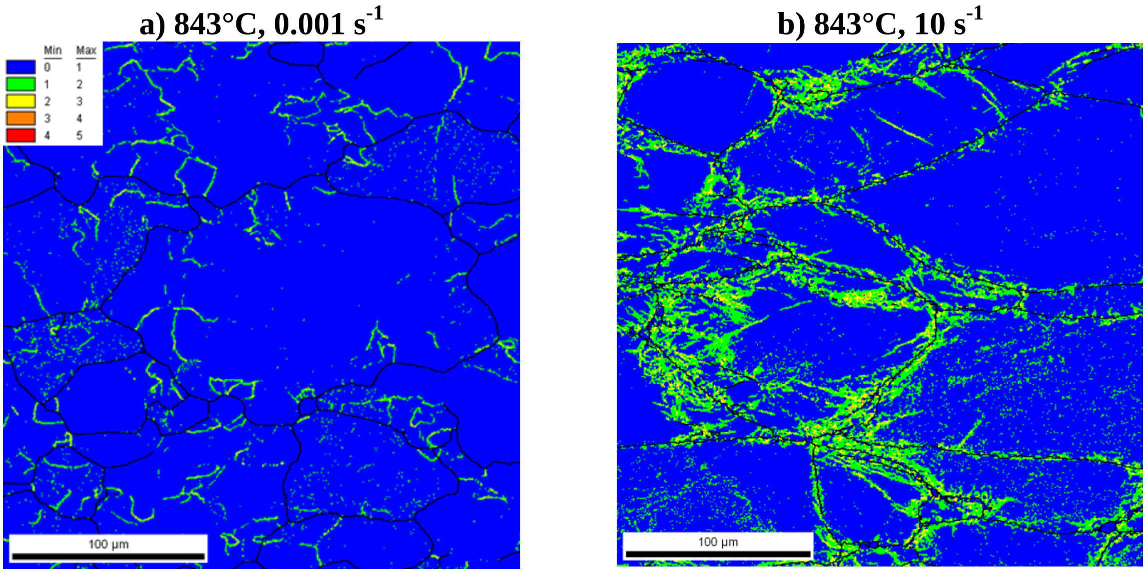

a) 843°C, 0.001 s^{-1}

b) 843°C, 10 s^{-1}

Figure 63. Kernel average misorientation for 843°C a) 0.001 s^{-1} and b) 10 s^{-1}. Load direction is vertical, local strain of 1.

The average grain spread misorientation is shown in Figure 64 for 843°C and the strain rates a) 0.001 s^{-1}, b) 0.01 s^{-1}, c) 1 s^{-1} and d) 10 s^{-1}. The colour blue shows the lowest average misorientation within a grain. With increasing the misorientation values, the colours are green, yellow, orange and red. Generally, it can be seen, that the amount of misorientation within grains is increasing with increasing strain rate.

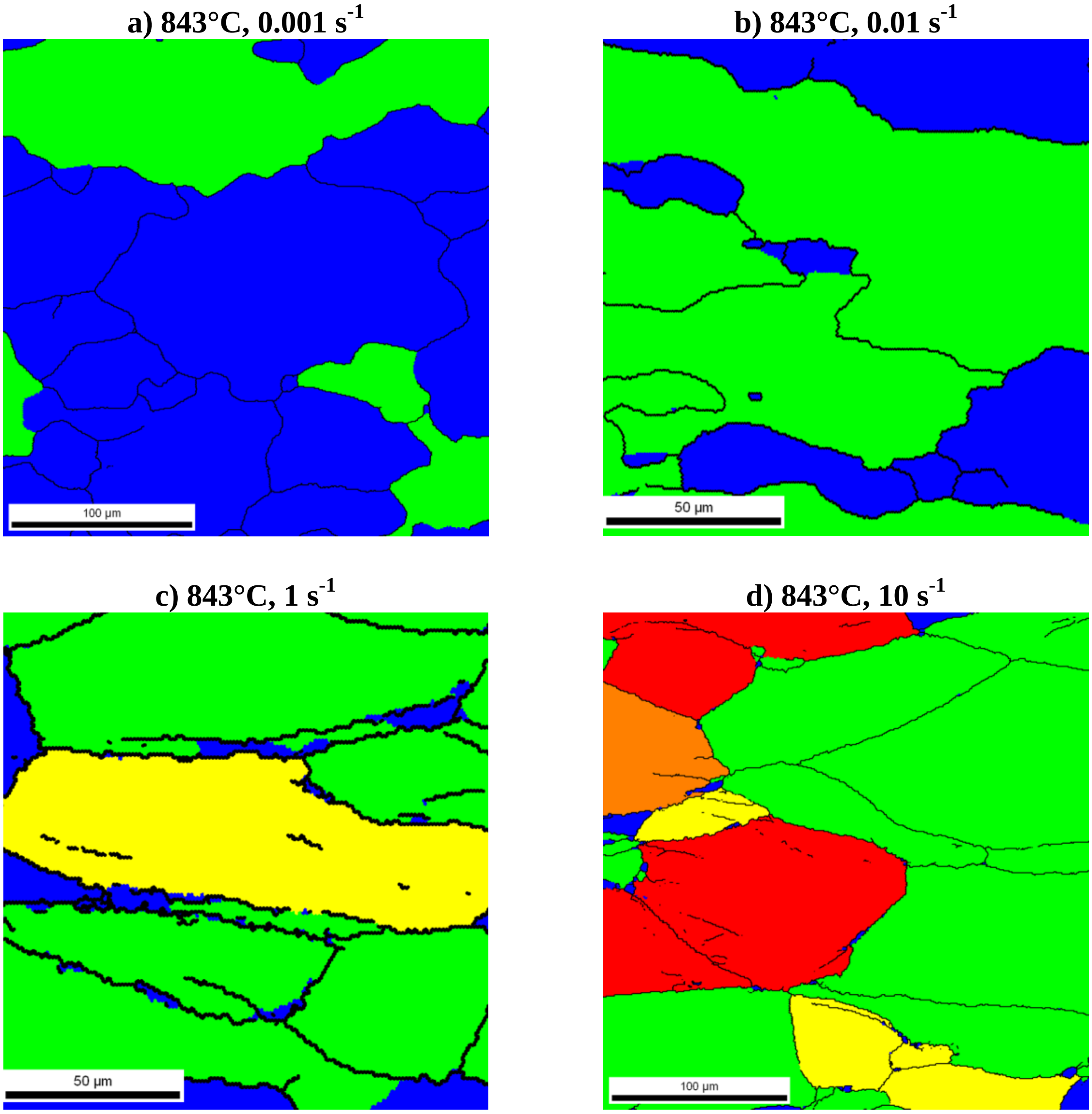

Scale	0–4°	4–9°	9–13°	13–17°	17–22°

Figure 64. Grain spread misorientation for 843°C: a) 0.001 s^{-1}, b) 0.01 s^{-1}, c) 1 s^{-1} and d) 10 s^{-1}. Local strain of 1, load direction is vertical.

However, care has to be taken with this last investigation. Firstly, grains which are at the edge of the picture should not be taken into account. Secondly, the colour red has to be related to misorientation which can appear as a continuous or due to a dense subgrain structure. Thirdly, it has to be considered that the average misorientation in a big grain is much higher than in a small grain. On the other hand, small grains with the colour blue have low misorientation.

4.2.3.4 α-content

The α-content was determined using image analysis of EBSD measurements of the samples deformed at 783°C. The α-amount varied for different strain rates. In Figure 65 the α-phase is shown in dark grey after deformation at strain rates of a) 0.001 s^{-1}, b) 0.1 s^{-1} and c) 10 s^{-1}. The calculated content of α for these conditions was a) 2.73%, for b) 7.27%, and for c) 3.76%, respectively.

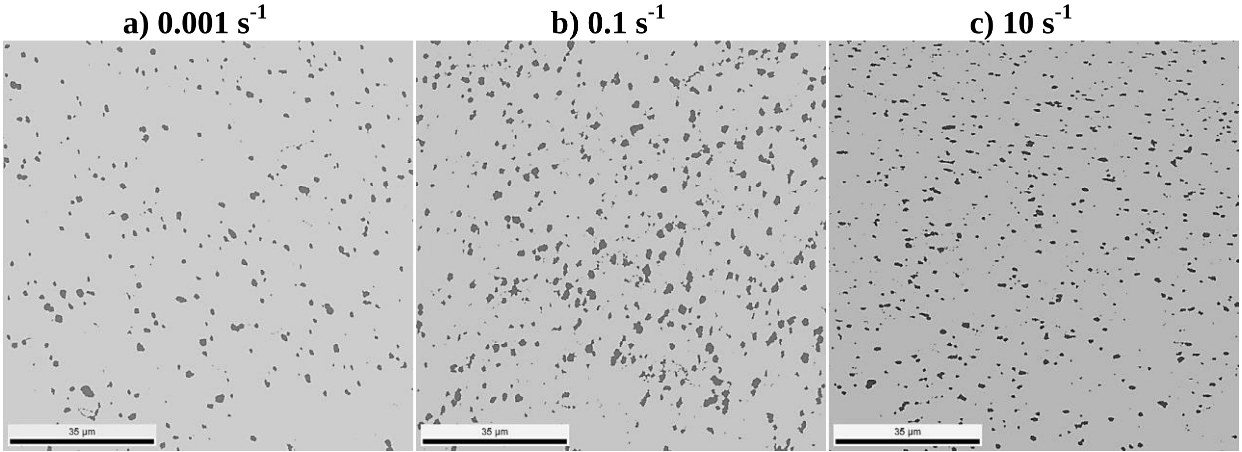

Figure 65. Micrographs showing different amount of α-phase for a strain rate of a) 0.001 s^{-1}, b) 0.1 s^{-1} and c) 10 s^{-1}.

The alloying elements in the α- and β-phases in these samples were measured using spot EDX analysis. The highest amount of molybdenum and vanadium in the β-phase was found in the sample deformed at higher strain rates. The highest amount of molybdenum and vanadium in the α-phase was measured for the lowest strain rate.

Table 9. Amount of Mo and V in α- and β-phase for samples deformed at 783°C.

Element wt%	0.001 s^{-1}	0.1 s^{-1}	10 s^{-1}
β Mo	5.25 ± 1.48	6.12 ± 0.11	6.17 ± 0.13
β V	3.85 ± 1.07	4.58 ± 0.08	4.46 ± 0.08
α Mo	4.03 ± 0.16	4.00 ± 0.24	3.72 ± 0.22
α V	3.21 ± 0.18	3.12 ± 0.32	3.17 ± 0.16

4.2.3.5 Grain size

The β grain size was determined using OIM software. In Figure 66 the calculated values for a) 763°C and b) 843°C are shown for the lowest strain rate in grey and the highest strain rate in yellow. Larger number of grains smaller than 10 µm was observed for the strain rate of 10 s^{-1} compared to the sample deformed at 0.001 s^{-1}. This effect was also observed at 843°C.

a) 763°C

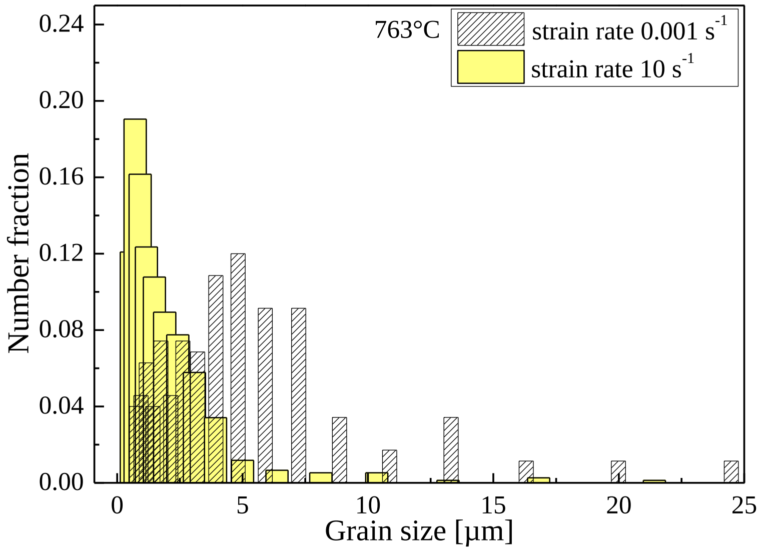

b) 843°C

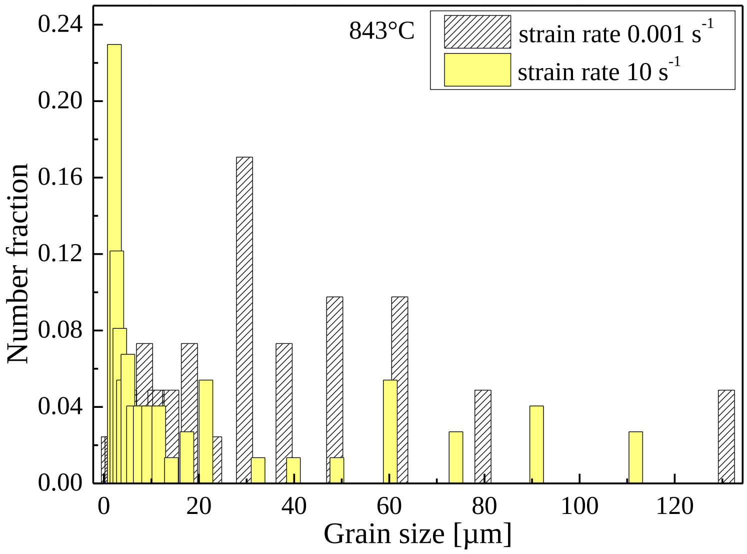

Figure 66. Determination of the β grain size after deformation at two strain rates and at a) 763°C and b) 843°C.

This result shows that at high strain rates small grains are formed during hot deformation.

4.2.4 Constitutive equations

Constitutive equations have been calculated for the stress values at a strain of 0.4 using two different approaches. Firstly, only one equation was developed in the whole temperature and strain rate ranges. Secondly, the calculation was developed for both deformation regions: α+β- and β-fields. It should be mentioned, that the constitutive equations for the two phase range were developed as if it were a single phase. This simplification results in phenomenological constitutive equations which are empirically used.

The stress multiplier *c* was found to be 0.008 MPa^{-1} and a stress exponent *n* of 3.45 was calculated. The calculation of the apparent activation energy is obtained from the slope of the linear regression for each strain rate as shown in Figure 67 a). For the first approach the calculated value of the activation energy was 212 kJ mol^{-1}. The constitutive equation can be written as:

$$\dot{\varepsilon} = 7.33 \cdot 10^{8}[\sinh(0.008\sigma_{0.4})]^{3.45}\exp\left(\frac{-211673}{RT}\right) \quad \textbf{Equation 50}$$

The activation energy for the second approach gave a *Q* value in the α+β-field of 226 kJ mol^{-1} and 204 kJ mol^{-1} for the β-field. The constitutive equations are shown in Equation 51 and Equation 52 for the α+β-, and β-fields, respectively.

$$\dot{\varepsilon} = 3.93 \cdot 10^{9}[\sinh(0.008\sigma_{0.4})]^{3.47}\exp\left(\frac{-226161}{RT}\right) \quad \textbf{Equation 51}$$

$$\dot{\varepsilon} = 4.80 \cdot 10^{8}[\sinh(0.008\sigma_{0.4})]^{3.44}\exp\left(\frac{-203806}{RT}\right) \quad \textbf{Equation 52}$$

In Figure 67 b) the correlation of *Z* versus the flow stress is shown for the first and in Figure 67 c) for the second approach, both results show a good correlation as seen in the R^2 which is close to 1.

a) Determination of *Q*

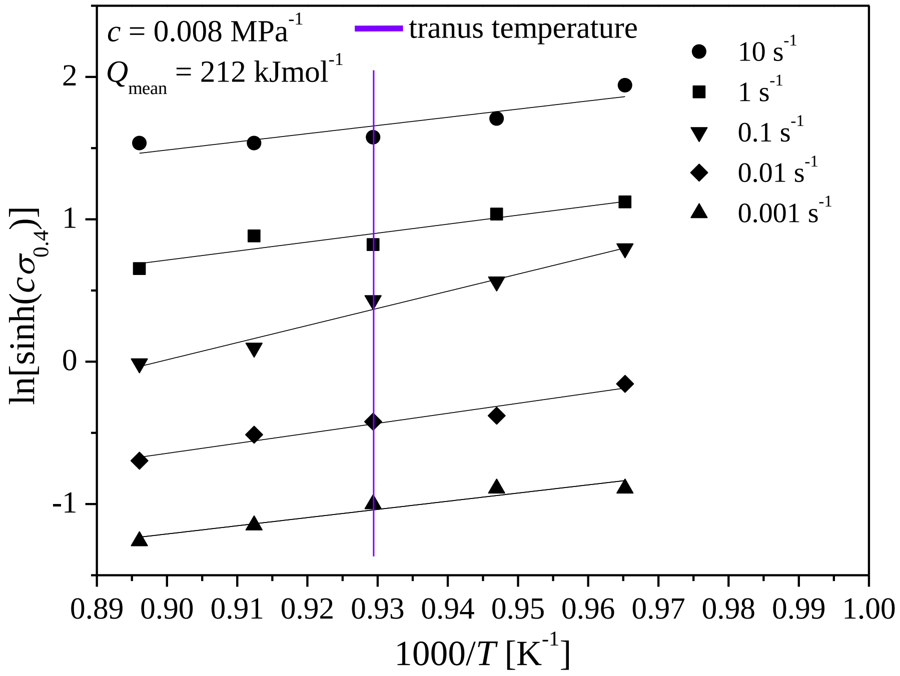

b) Zener-Hollomon vs. flow stress using one equation

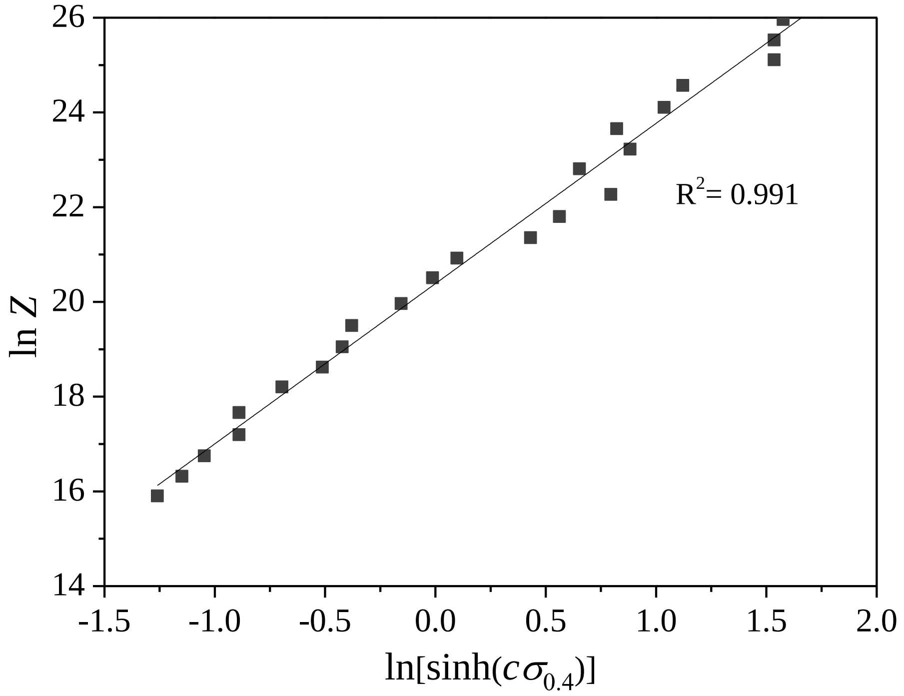

c) Zener-Hollomon vs. flow stress using two equations (α+β-, and β-field)

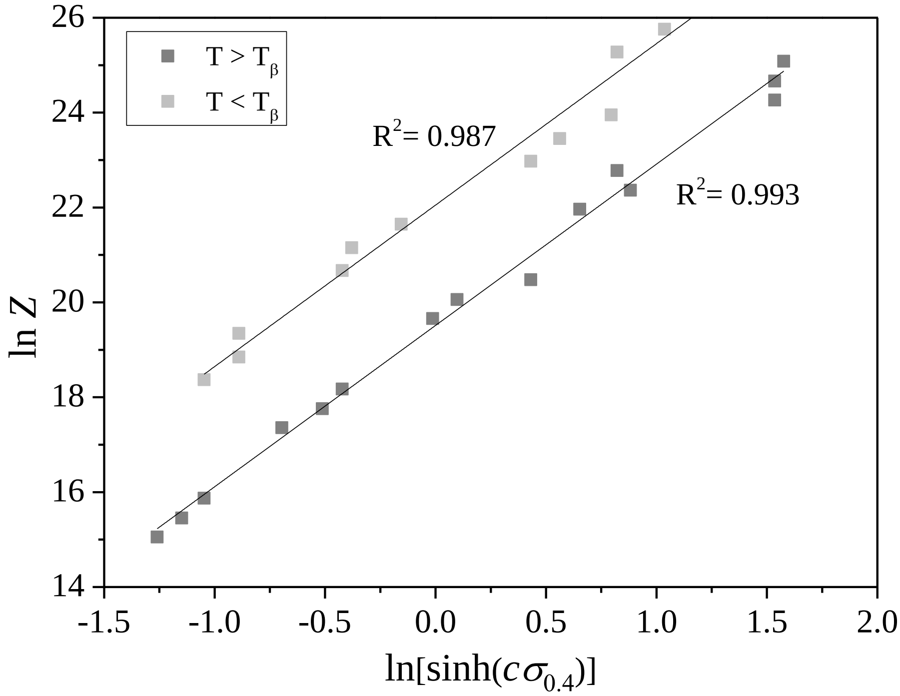

Figure 67. Constitutive equations plots: a) showing the determination of the activation energy *Q* and b,c) relationship Zener-Hollomon versus flow stress.

Furthermore the β subgrain size was measured and plotted as a function of the Zener-Hollomon parameter as observed in Figure 68. The ln β subgrain size depends on *Z* as follows (Equation 53):

$\ln \delta_{SS} = -\ 0.206 \ln Z + 5.89$ **Equation 53**

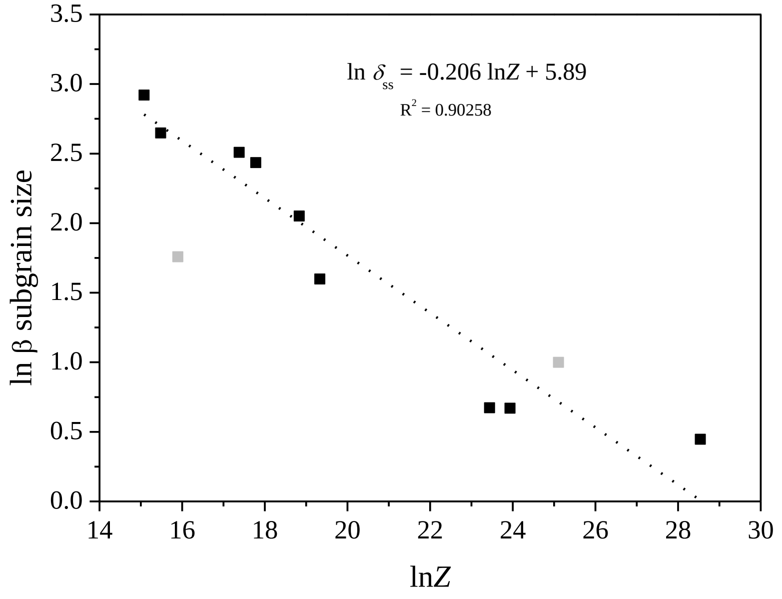

Figure 68. ln β subgrain size as a function of the Zener-Hollomon parameter, calculated at a strain of 0.4. The grey symbols represent the subgrain size at a temperature of 803°C.

4.2.5 Processing maps

Processing maps were calculated for stress values at constant strains of 0.3 (Figure 69), 0.4 (Figure 70), 0.5 (Figure 71) and 0.6 (Figure 72). First, processing maps based on the DMM by Prasad, then the ones based on the mDMM by Murty and Rao and finally, the *m* map were calculated. The instability parameter κ_j was plotted and overlapped to the dissipation efficiency model by Murty and Rao using Equation 27. Furthermore the instability parameter α_{SJ} was calculated and plotted using Equation 37.

For a strain of 0.3 it can be seen that the values of the efficiency of power dissipation plotted as isolines shown in the Prasad's model have the same tendency compared to the isolines in the *m* map. The dissipation efficiency values of Murty and Rao are showing the highest values at moderate strain rates, being this the largest difference compared to the model of Prasad. The second difference is that all $\eta_{M\&R}$ values are in general higher than the η_P ones. Another interesting point in the model of Murty and Rao is, that a difference in the values between the α+β- and the β-field can be realised. Below the T_β a wider range of values can be observed.

The behaviour of the instability parameters for all the models is significantly different. Prasad's ξ shows instability at high strain rates, nearly independent of the temperature. Murty and Rao's κ brings instability independent of the temperature for strain rates higher than 0.01 s^{-1}. In the *m* map no instability can be seen, although very low positive values appear at very high strain rates. The parameter κ_j is negative at high strain rates and moderate temperatures. The calculation of the instability parameter α_{SJ} was carried out using two approaches. In the first one, shown on the left hand side, the temperature term was taken into account and on the right hand side the α_{SJ} value was calculated without this term. Only if the temperature term is taken into account, instability is predicted in the low temperatures and high strain rates window.

With increasing the strain to 0.4 the values of efficiency and instability did not change significantly.

The efficiency values decreased a little bit by increasing the strain to 0.5 but the trend is still the same. The instability areas have been increased at 0.5 of strain for the model of Prasad. Interesting is that in the case of α_{SJ} no instability is predicted for 0.5 of strain at high strain rates.

The maps plotted using stress values at a strain of 0.6 show that the efficiency values have again decreased with respect to lower strains. In the instability map of Prasad no big difference to the strain of 0.5 could be seen. Additionally, no change is visible in the map of κ_j. For the instability of Semiatin and Jonas α_{SJ}, there prediction of instability appears again at high strain rates and moderate temperatures.

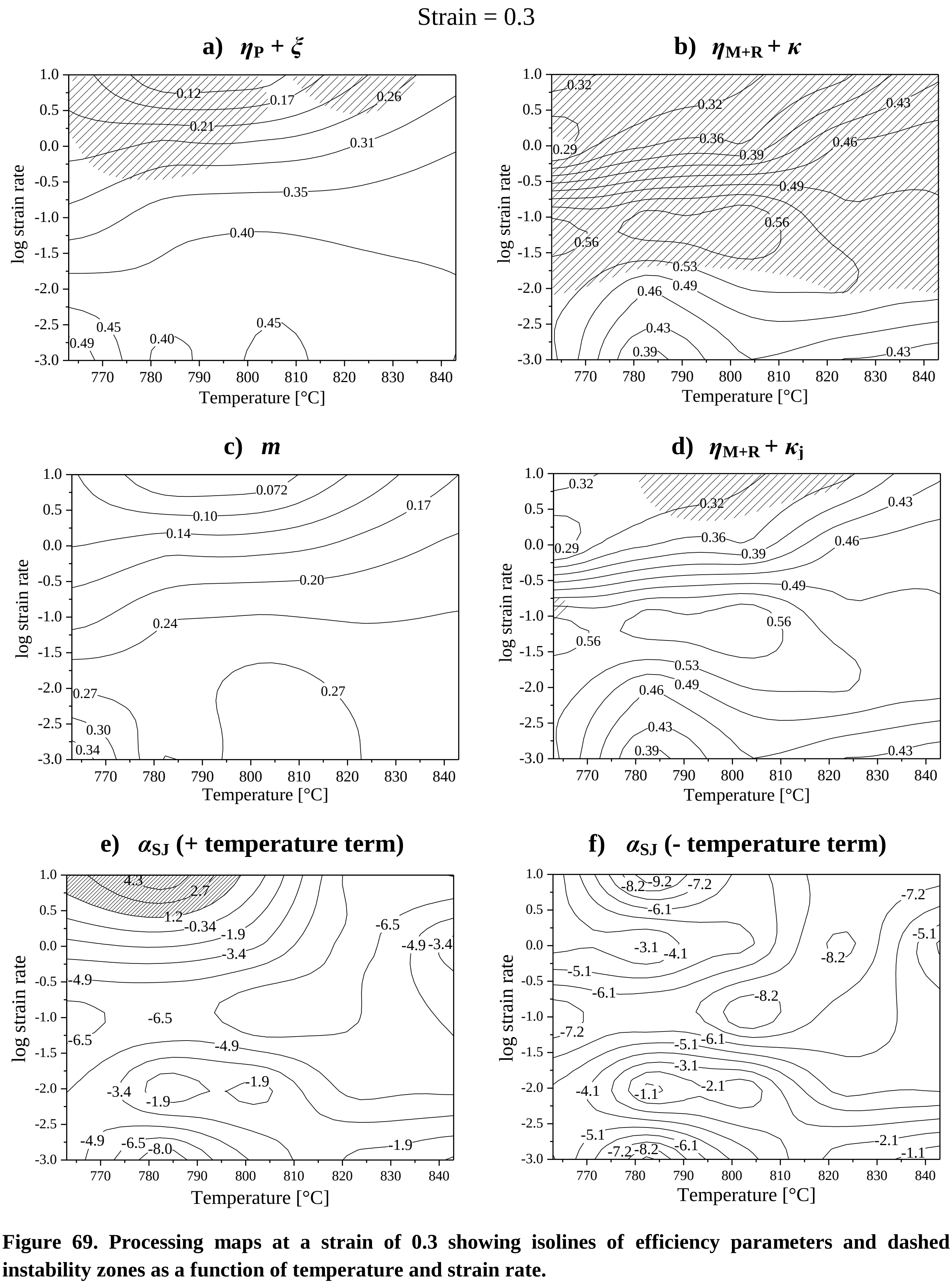

Figure 69. Processing maps at a strain of 0.3 showing isolines of efficiency parameters and dashed instability zones as a function of temperature and strain rate.

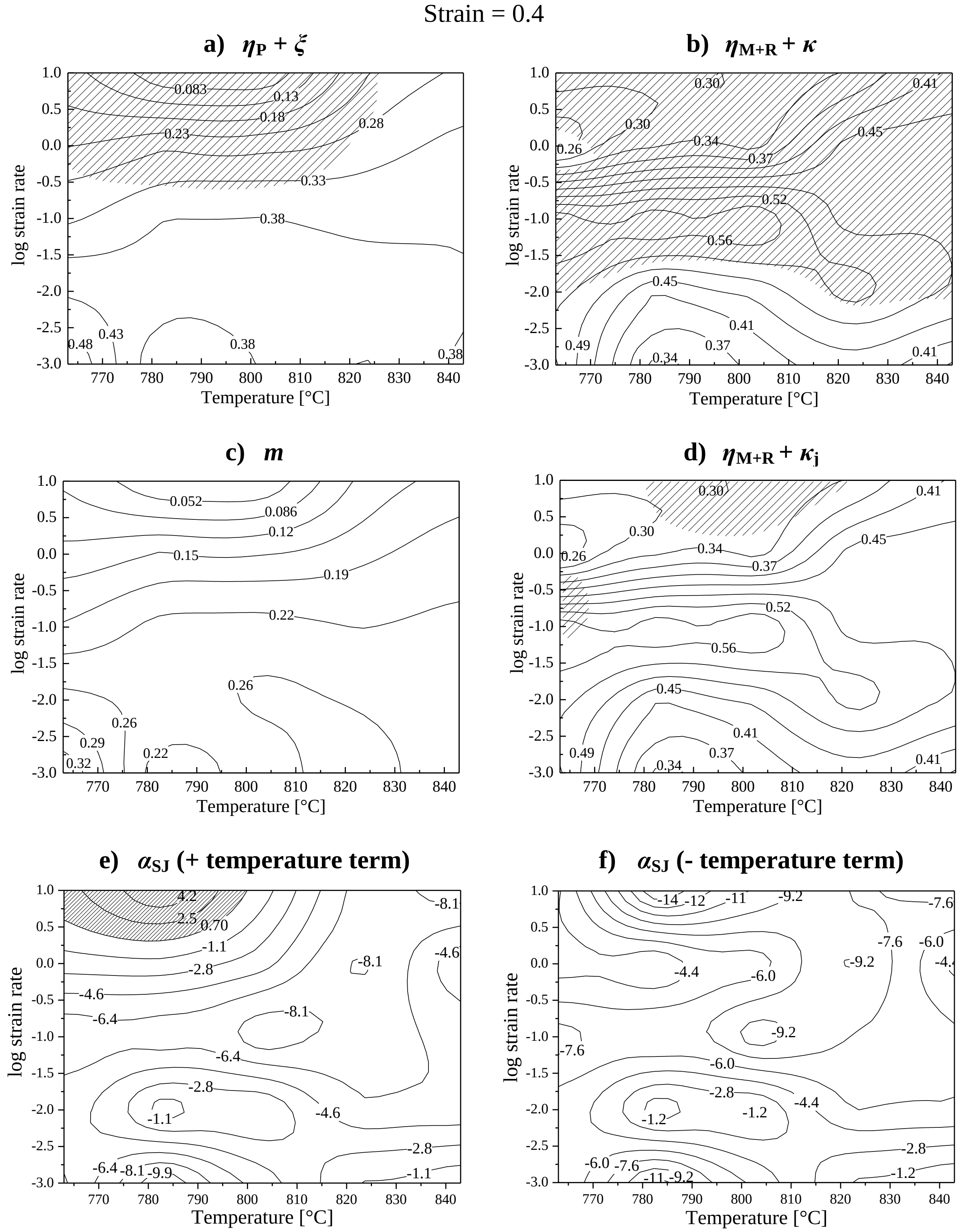

Figure 70. Processing maps at a strain of 0.4 showing isolines of efficiency parameters and dashed instability zones as a function of temperature and strain rate.

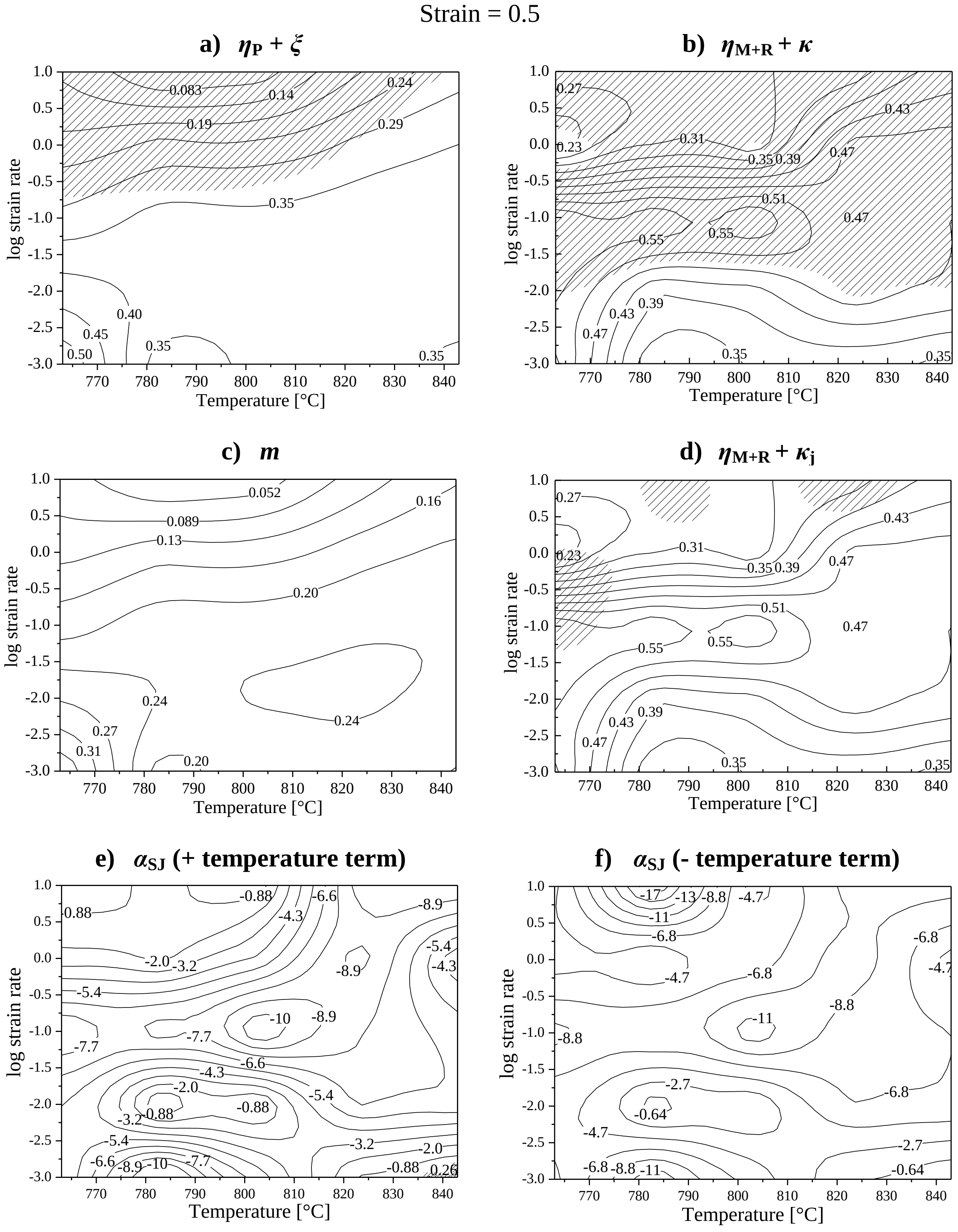

Figure 71. Processing maps at a strain of 0.5 showing isolines of efficiency parameters and dashed instability zones as a function of temperature and strain rate.

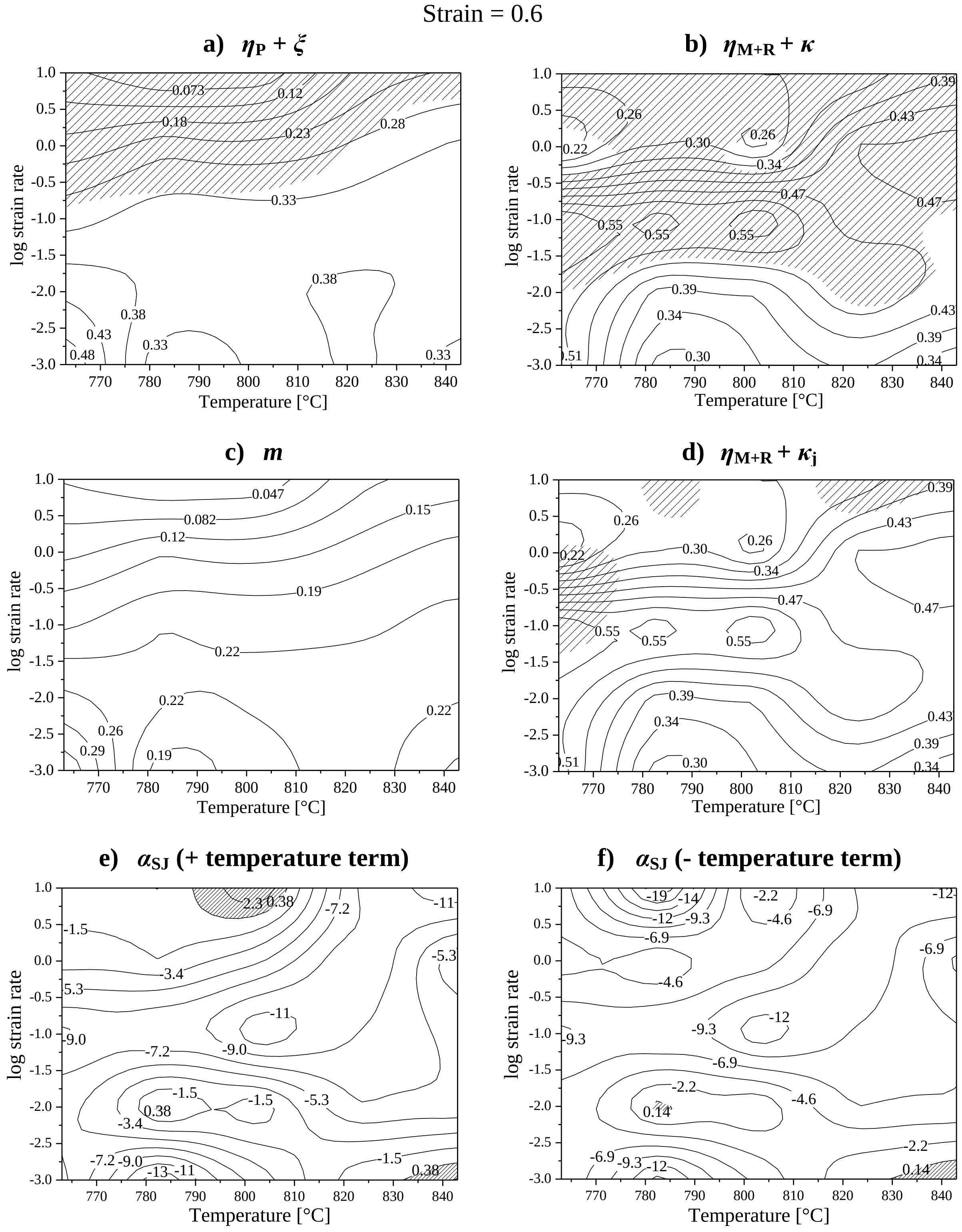

Figure 72. Processing maps at a strain of 0.6 showing isolines of efficiency parameters and dashed instability zones as a function of temperature and strain rate.

4.3 Steel containing nitrogen

4.3.1 Microstructure of the as-received material and dilatometry investigations

The microstructure before deformation and after austenitization at 1000°C and water quenching can be seen in Figure 73 for two different magnifications.

The material consists mainly of bainite and furthermore, a little amount of “Widmanstätten” ferrite is present at the grain boundaries, as shown by the grey arrow.

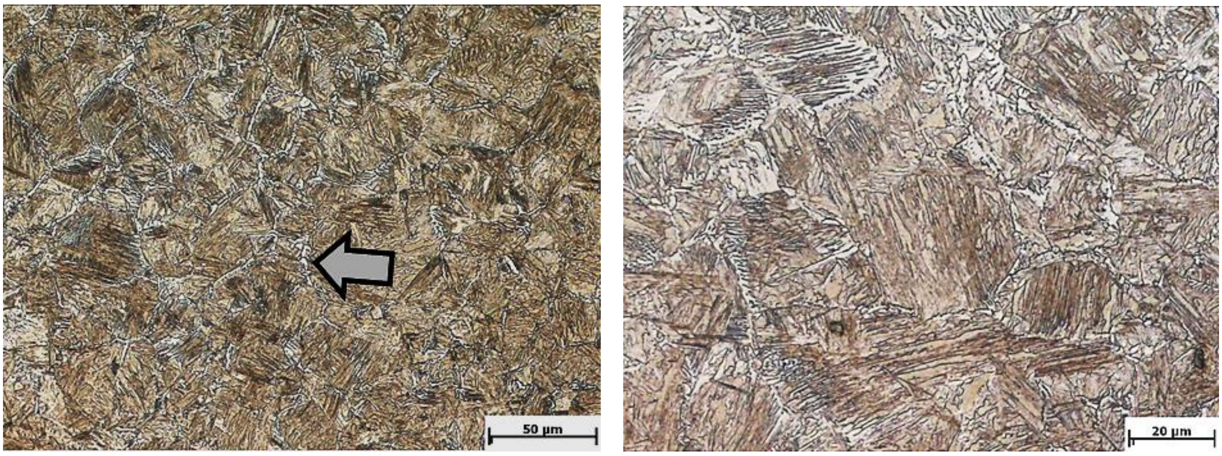

Figure 73. LOM investigations of the material after austenitization and water quenching for two different magnifications. The grey arrow indicates “Widmanstätten” ferrite at the grain boundaries.

The results of the dilatometry tests, i.e. the elongation as a function of temperature, are plotted in Figure 74 a) for a cooling rate of 1K s^{-1} and for helium quenching in Figure 74 b).

a) Cooling rate: 1K s^{-1}

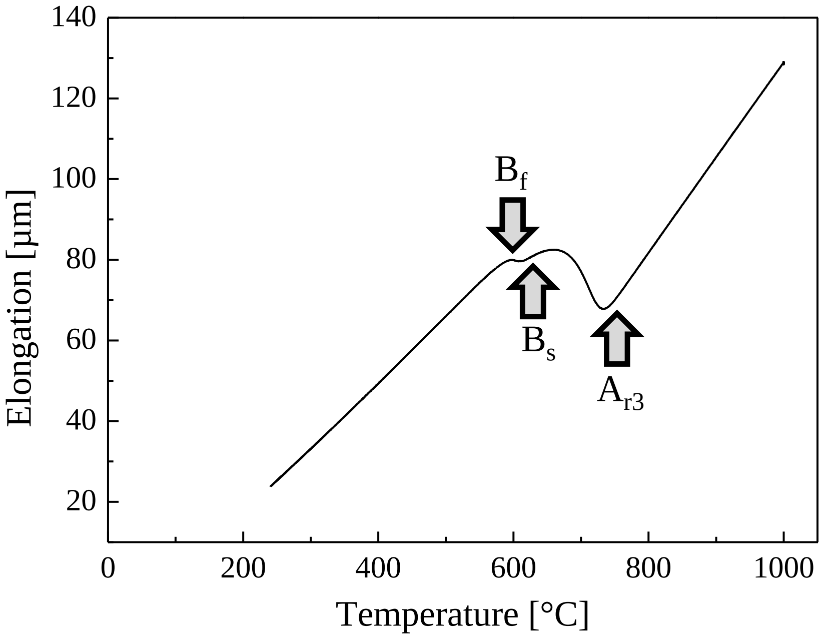

b) Cooling rate: Helium

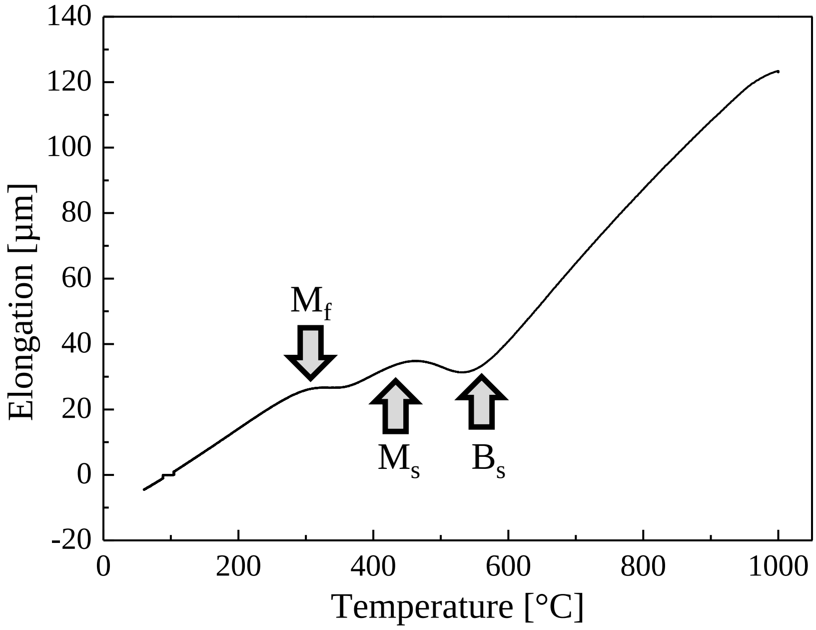

Figure 74. Dilatometry curves for two different cooling rates a) 1K s^{-1} and b) He-quench.

The phase transformation temperature values obtained using the tangent method are the A_{r3} = 744°C, B_s = 618°C and B_f = 581°C for 1K s^{-1} cooling rate. Martensite start and finish temperatures obtained for the He quenched sample are M_s = 437°C and M_f = 268°C, respectively. Bainite starts forming at 568°C for the fast cooled sample.

4.3.2 Flow curves

The flow curves are presented in Figure 75 for a temperature range of 750–1000°C and for a strain rate range of 0.01–100 s^{-1}. The deformation tests at the highest strain rate show a ringing effect in the flow curves. In [99] this phenomenon of ringing for high speed deformation is explained. During a deformation a transducer picks up the vibration of a system. This vibration will be added to its signal and therefore shows a ringing effect. This signal could be misunderstood as a signal of dynamic recrystallization. Therefore the curves are smoothed using the Adjacent-Averaging filter technique to avoid this, however still some small oscillation waves can be seen. The flow curves obtained at low strain rates 0.01–0.1 s^{-1} exhibit softening for all temperatures. In the higher strain rate range between 1–10 s^{-1}, steady state is observed at temperatures larger than 800°C. No steady state is achieved up to a strain of 0.6 for the highest strain rate 100 s^{-1} for all temperatures, and for 1–10 s^{-1} for the low temperatures.

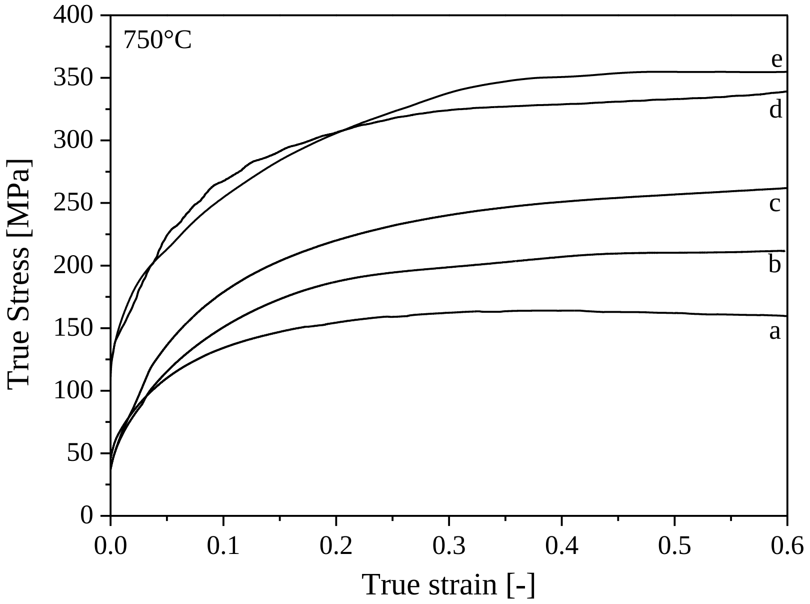
750°C
True Stress [MPa]
0
50
100
150
200
250
300
350
400
True strain [-]
0.0
0.1
0.2
0.3
0.4
0.5
0.6
e
d
c
b
a

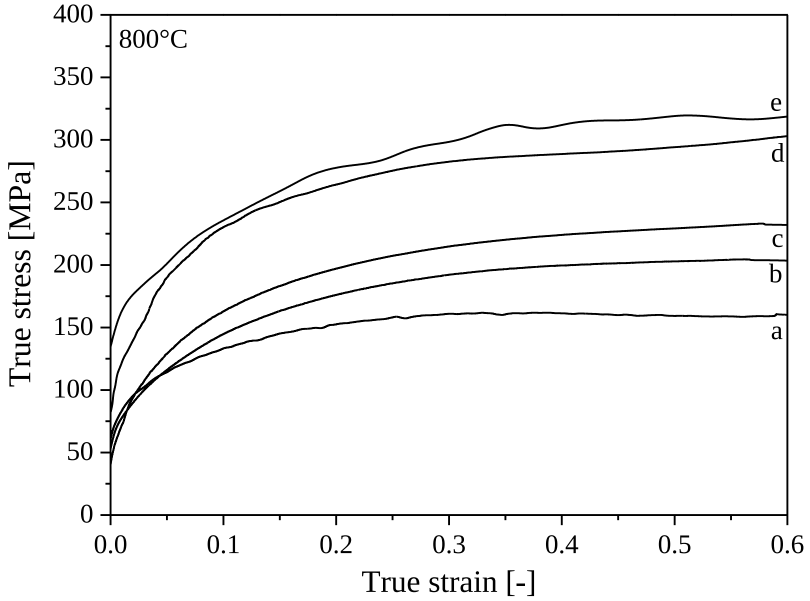
800°C
True stress [MPa]
0
50
100
150
200
250
300
350
400
True strain [-]
0.0
0.1
0.2
0.3
0.4
0.5
0.6
e
d
c
b
a

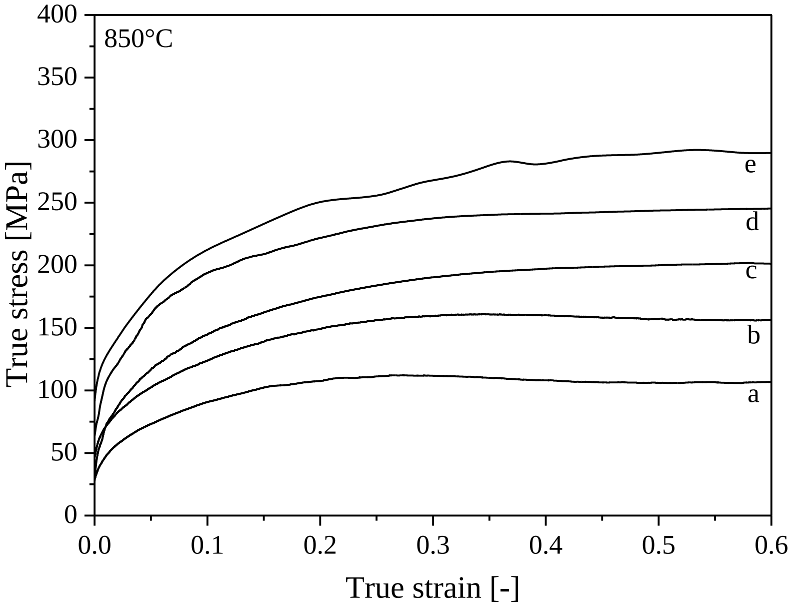
850°C
True stress [MPa]
0
50
100
150
200
250
300
350
400
True strain [-]
0.0
0.1
0.2
0.3
0.4
0.5
0.6
e
d
c
b
a

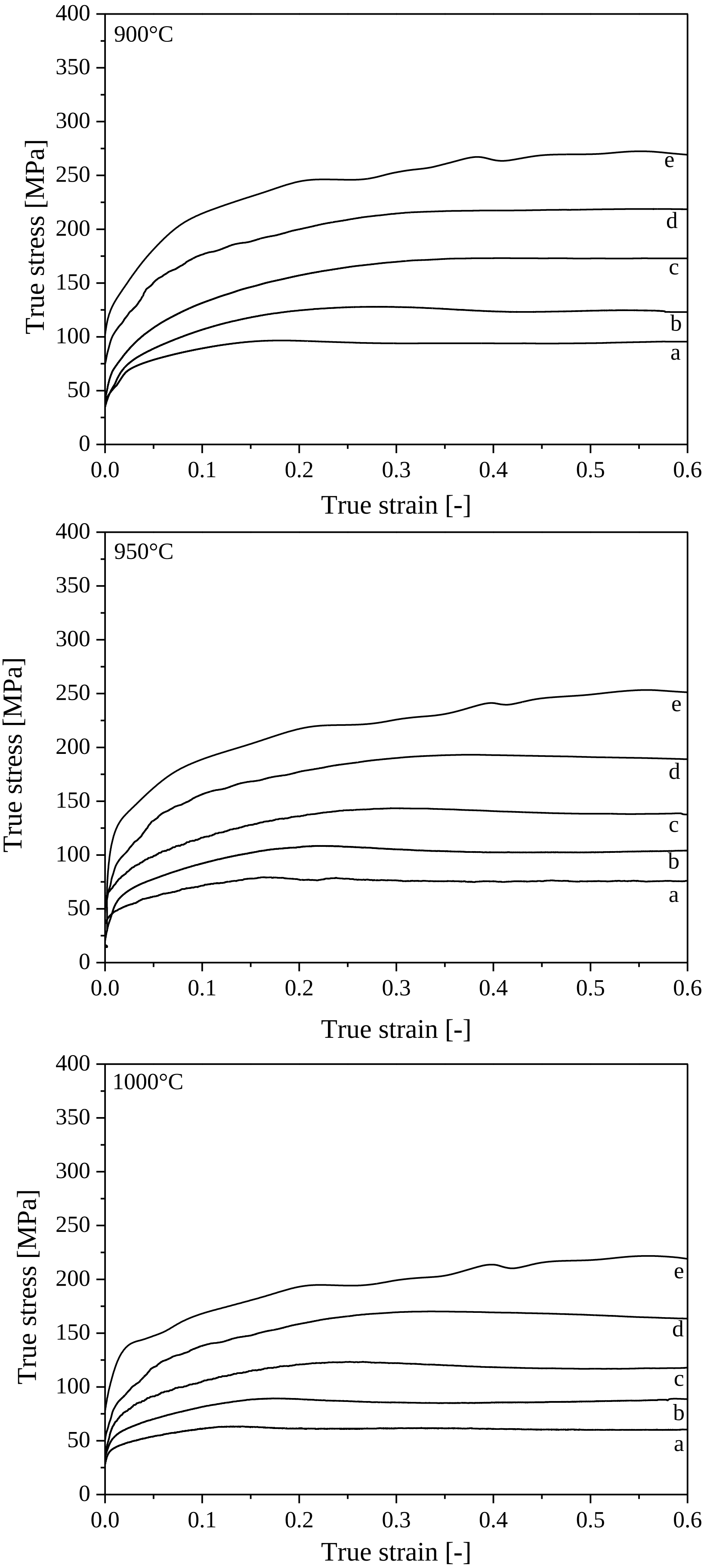

Figure 75. Flow curves obtained after deformation at 750°C–1000°C for strain rates: a) 0.01 s^{-1}, b) 0.1 s^{-1}, c) 1 s^{-1}, d) 10 s^{-1} and e) 100 s^{-1}.

The measured increment of temperature due to self-heating occurring during the deformation is tabulated in Table 10 as a function of deformation temperature and strain rate for the lowest and highest temperatures of 750°C and 1000°C and lowest and highest strain rates of 0.01 s^{-1} and 100 s^{-1}.

Table 10. Temperature increment measured during deformation as a function of strain rate and temperature.

$\dot{\varepsilon}$ [s^{-1}]	T [°C]	ΔT [°C]
0.01	750	2
0.01	1000	1
100	750	18
100	1000	20

Additionally, the self-heating can be appraised using Equation 54 [100]:

$$\Delta T = \frac{\eta \int_0^{\varepsilon} \sigma d\varepsilon}{\rho\, C_p} \qquad \textbf{Equation 54}$$

in which η is the adiabatic correction factor, the integral is the area under the uncorrected stress-strain curve, ρ is the density and C_p is the specific heat. The η parameter is 0.95 for strain rates > 1 s^{-1} and η is (0.316) lg $\dot{\varepsilon}$ + 0.95 for strain rates between 10^{-3} s^{-1} and 1 s^{-1} [101]. Hence, for a $\dot{\varepsilon}$ of 0.01 s^{-1} a η value of 0.318 is calculated.

The data used was a low alloyed steel with a C amount of 0.13 % from DEFORM database. The specific heat times density at 750°C is 4.60 $N/mm^2/C$, whereas the heat capacity at 1000°C is 5.26 $N/mm^2/C$. Table 11 shows the temperature increment based on Equation 54.

Table 11. Temperature increment calculated based on Equation 54.

$\dot{\varepsilon}$ [s^{-1}]	T [°C]	ΔT [°C]
0.01	750	6
0.01	1000	2
100	750	44
100	1000	25

Generally, the calculated values are higher as the measured ones. The reason therefore may be due to a heat exchange of the sample with the surrounding area during the deformation.

4.3.3 Microstructure after hot deformation

4.3.3.1 Light optical microscope investigations

Light optical microscope investigations done after hot deformation are shown in Figure 76. It can be observed that the amount of ferrite is larger after deformation at 100 s^{-1} than at 0.01 s^{-1} for a deformation temperature of 750°C. This trend is also observed for deformation at higher temperatures. The micrographs of samples deformed at 900°C and 1000°C show that austenite grain size decreases with increasing strain rate and decreasing temperature. Finally, no defects like pores or deformation bands were detected in the deformed samples.

750°C, 0.01 s^{-1} **750°C, 100 s^{-1}**

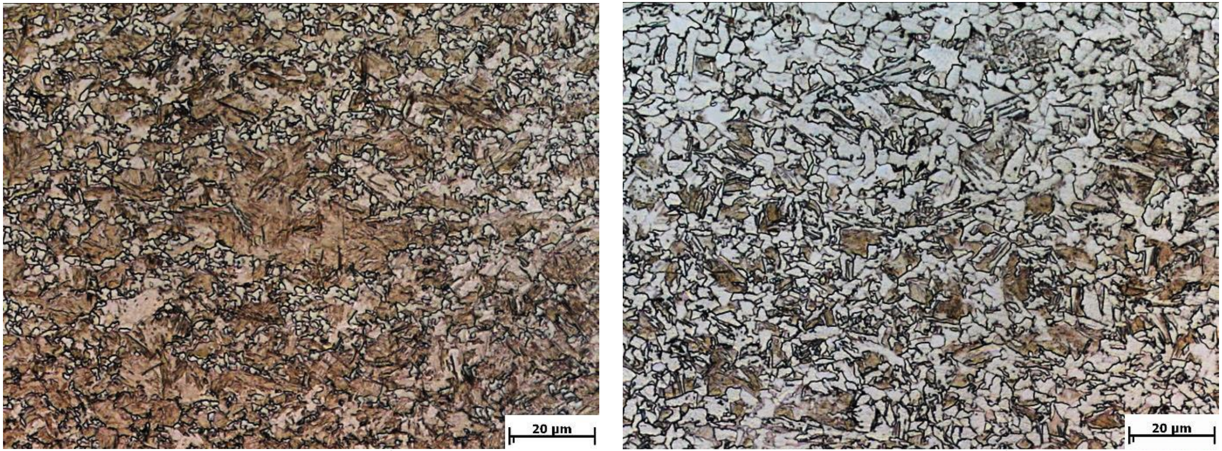

900°C, 0.01 s^{-1} **900°C, 100 s^{-1}**

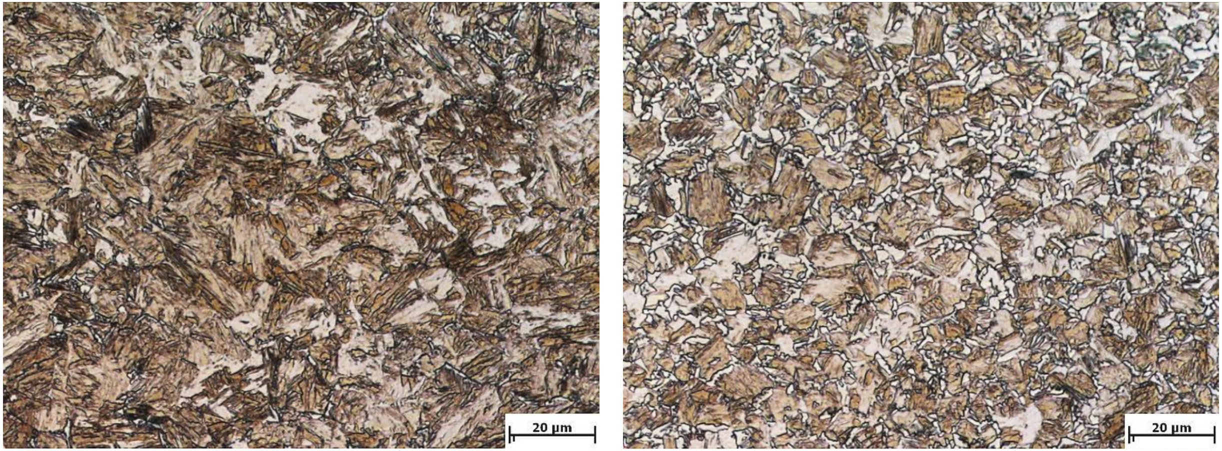

1000°C, 0.01 s^{-1} **1000°C, 100 s^{-1}**

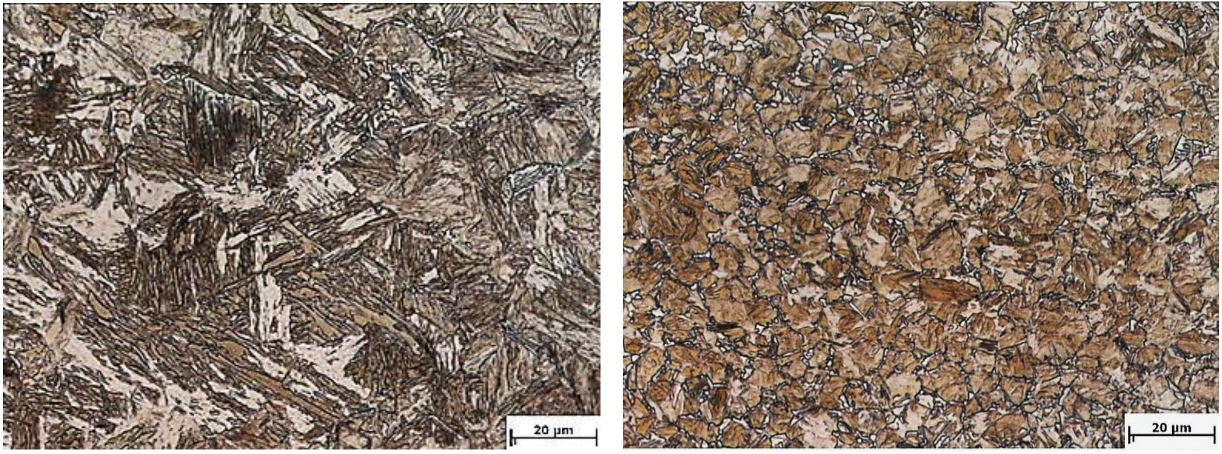

Figure 76. LOM pictures of samples after deformation at temperatures of 750°C, 900°C and 1000°C for strain rates of 0.01 s^{-1} and 100 s^{-1}. Local strain of 1, load direction is vertical.

4.3.3.2 EBSD measurements

EBSD measurements were performed for samples after deformation at 750°C and strain rates of 0.01 s^{-1} and 100 s^{-1}, and at 1000°C for strain rates of 0.01 s^{-1} and 100 s^{-1}. The unit triangle in Figure 77 represents the crystal orientation of ferrite, whereas the 001 plane is shown in red, the 101 plane in green and the 111 plane in blue.

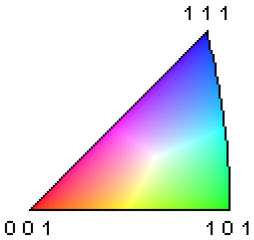

Figure 77. Unit triangle of ferrite for the EBSD orientation maps.

Figure 78 shows the IPF maps of samples deformed at 750°C and strain rates of 0.01 s^{-1} and 100 s^{-1}, as well as samples deformed at 1000°C for strain rates of 0.01 s^{-1} and 100 s^{-1}. The microstructure after deformation at 750°C consists mainly of globular grains, whereas the grains received after the deformation at 1000°C and a strain rate of 0.01 s^{-1} have a lamellar shape. Lamellar ferrite appears after hot working as a transformation of austenite into ferrite, especially at the high strain rate.

a) IPF map, 750°C, 0.01 s^{-1}　**b) IPF map, 750°C, 100 s^{-1}**

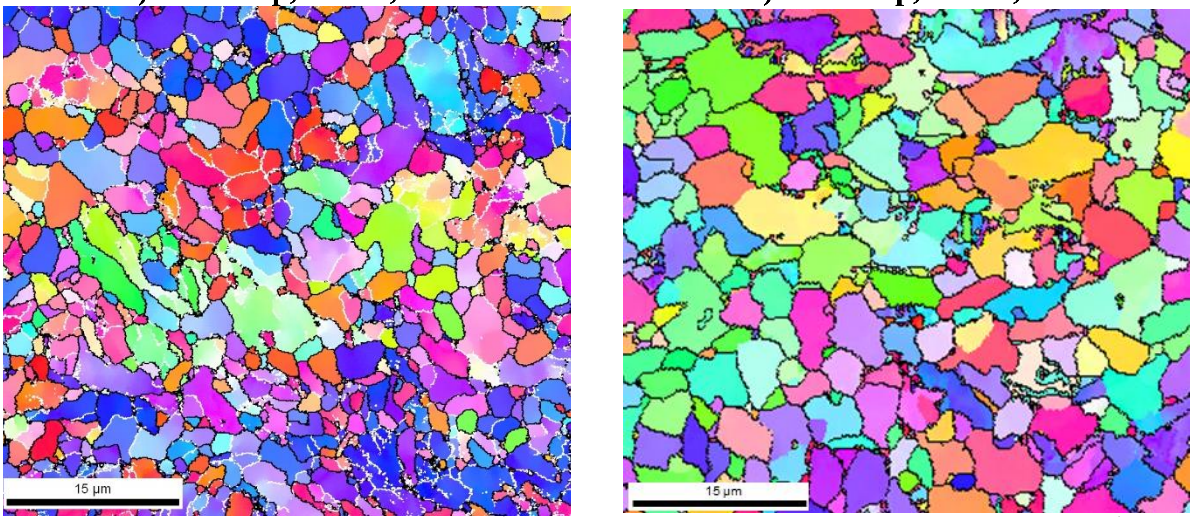

c) IPF map, 1000°C, 0.01 s^{-1}　**d) IPF map, 1000°C, 100 s^{-1}**

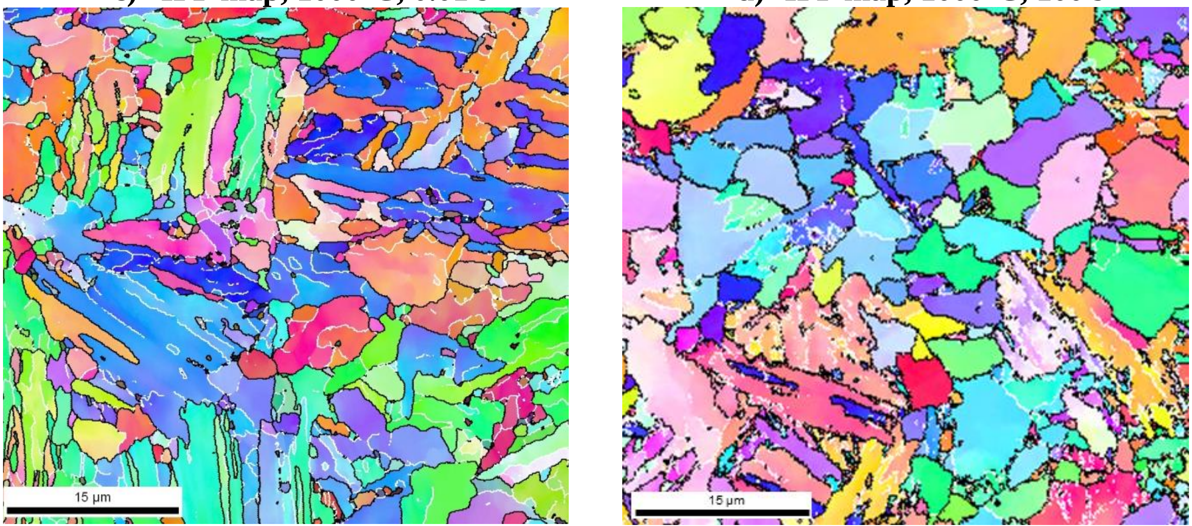

Figure 78. EBSD investigations: a) 750°C, 0.01 s^{-1}; b) 750°C, 100 s^{-1}; c) 1000°C, 0.01 s^{-1}, d) 1000°C, 100 s^{-1}. Measurements carried out in the middle of the sample (local strain of 1.1). Load direction is vertical.

4.3.4 Constitutive equations

The constitutive equations were built using the stress values at a strain of 0.4. The results are given within Figure 79 and Equation 55. Figure 79 a) shows the graphs used to obtain the activation energy *Q* and Figure 79 b) presents the correlation of Zener-Hollomon versus the flow stress.

The stress multiplier obtained was 0.009 MPa^{-1}, and the apparent activation energy value out of Figure 79 a) was calculated as 323 kJ mol^{-1}. The stress exponent *n* was calculated to be 5.41.

a) Determination of *Q*

b) Zener-Hollomon versus flow stress

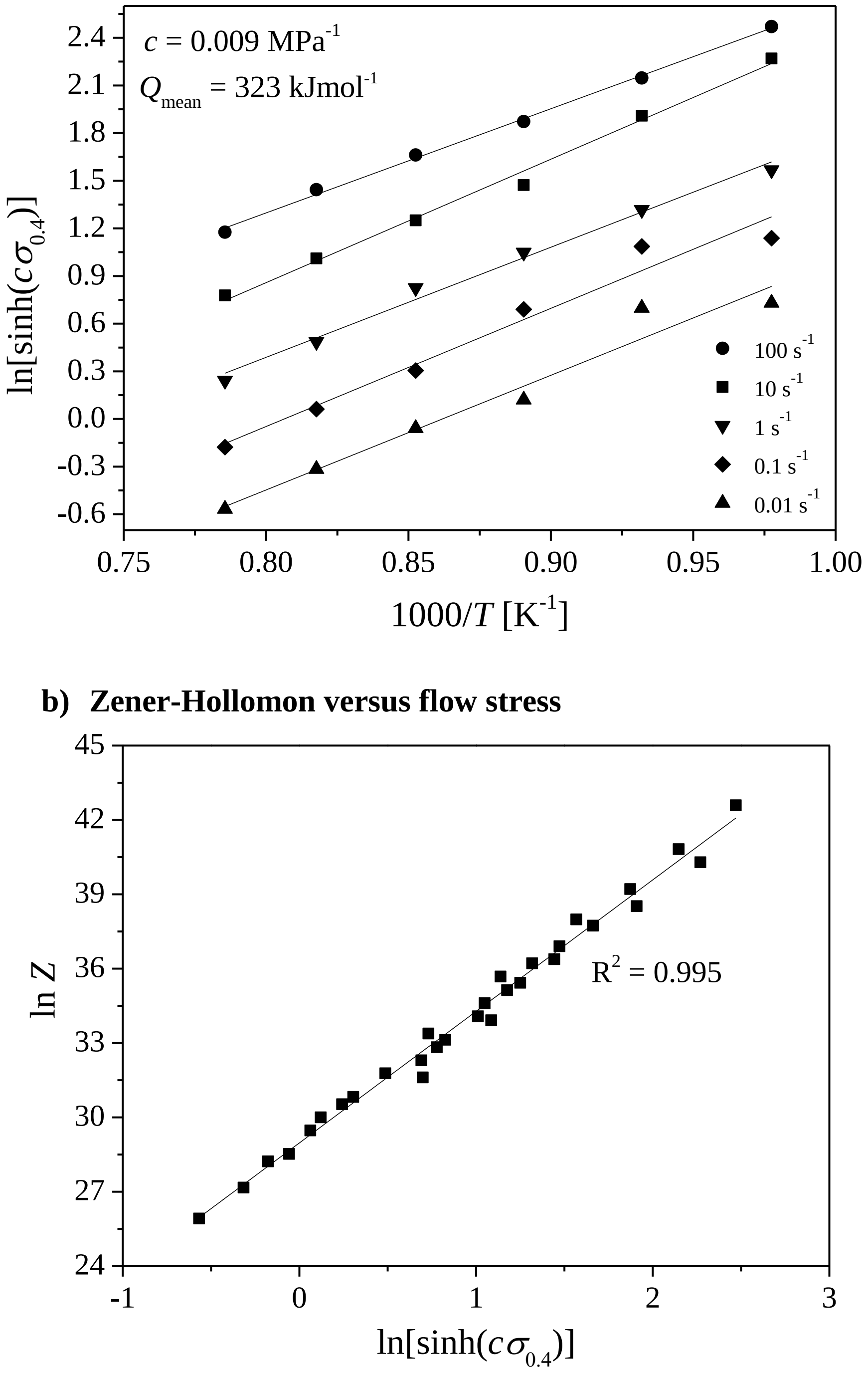

Figure 79. Determination of parameters of the constitutive equations: a) activation energy *Q* and b) relationship between Zener-Hollomon and flow stress.

The constitutive equation for the studied range of temperatures and strain rates can be expressed as:

$$\dot{\varepsilon} = 3.75 \cdot 10^{12}[\sinh(0.009\sigma_{0.4})]^{5.41}\exp\left(\frac{-323077}{RT}\right) \quad \textbf{Equation 55}$$

4.3.5 Processing maps

Processing maps were calculated for a strain of 0.2 (Figure 80), 0.3 (Figure 81), 0.4 (Figure 82) and 0.5 (Figure 83). The isolines in the maps a - d) show the dissipation efficiency values and the dashed zones are showing negative values of instability parameters. For the α_{SJ} map e), the positive values on the isolines represent instability.

The model of Prasad shows increasing η_{P} values with increasing strain and the highest values are occurring at 850°C for a strain rate of 0.01 s^{-1} and at 1000°C for a strain rate of 0.01–1 s^{-1}. At the lowest strain, negative values of instability parameters are calculated for strain rates larger than 1 and for a temperature of 750°C. In the range of temperatures between 775°C and 850°C, instability appears between strain rates of 1–10 s^{-1}. Between 850°C and 860°C, instability is predicted independently of the strain rate. The instability area is shifted to higher strain rates and higher temperatures with increasing strain.

Murty’s and Rao’s model predicts the largest efficiency of power dissipation values around 850°C and 0.1 s^{-1}. It is also observed that the $\eta_{\mathrm{M+R}}$ values are increasing with increasing strain. Stability is predicted at a strain rate of 0.01 s^{-1} for all temperatures. For strain rates larger than 0.01 s^{-1}, instability is predicted for all temperatures and all strains. Only between 750°C and 850°C and between a strain rate of 0.1 s^{-1} and 3 s^{-1} stability is predicted.

The tendency of m isolines is similar to the isolines of the map proposed by Prasad. As explained in [9], flow instabilities are predicted for m values smaller than zero. For this steel investigation, this is the case for the lowest strain at low temperatures for high strain rates. With increasing the strain, m changes to positive but still has low values in this area.

The distribution of κ_{j} is similar to that of Prasad’s instability parameter, shown instability at strain rates higher than 1 s^{-1}, especially at temperatures below 850°C and for the highest strain also for temperatures above 900°C.

The instability map produced by using Equation 37 from Semiatin and Jonas shows negative values, meaning that no instability is predicted for hot deformation at the tested temperatures and strain rates.

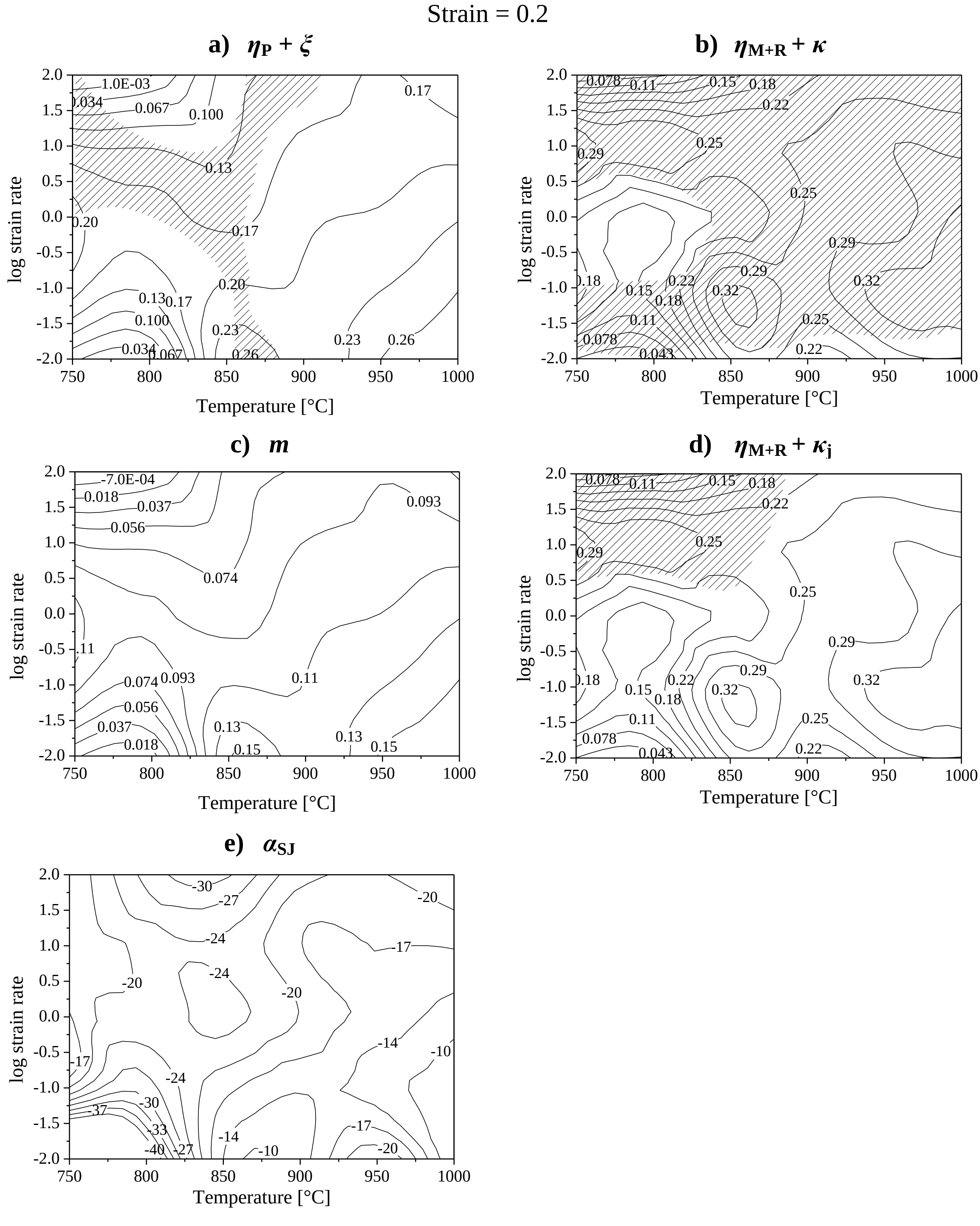

Figure 80. Processing maps for the steel alloyed with N at a strain of 0.2 showing isolines of efficiency parameters and dashed instability zones as a function of temperature and strain rate.

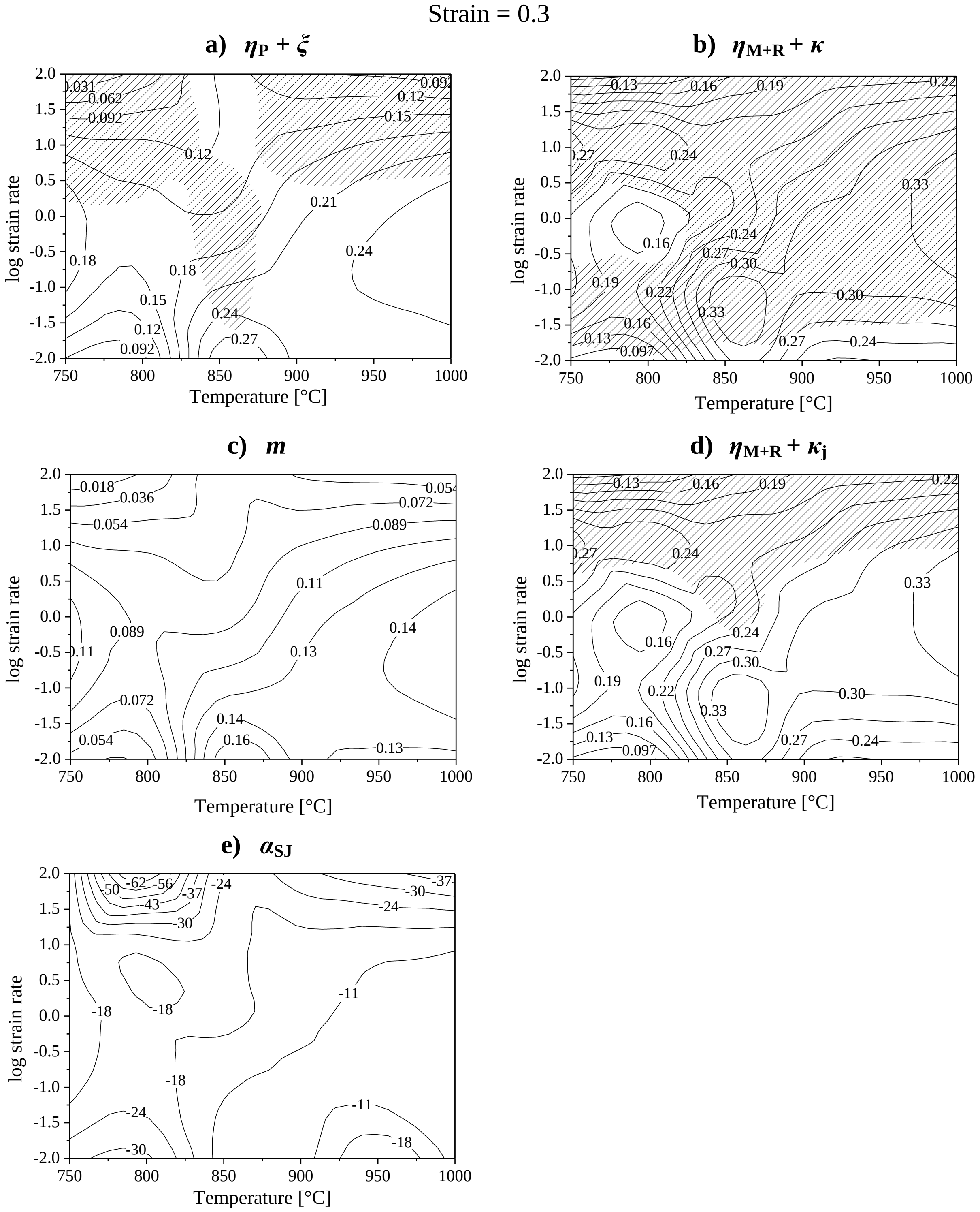

Figure 81. Processing maps for the steel alloyed with N at a strain of 0.3 showing isolines of efficiency parameters and dashed instability zones as a function of temperature and strain rate.

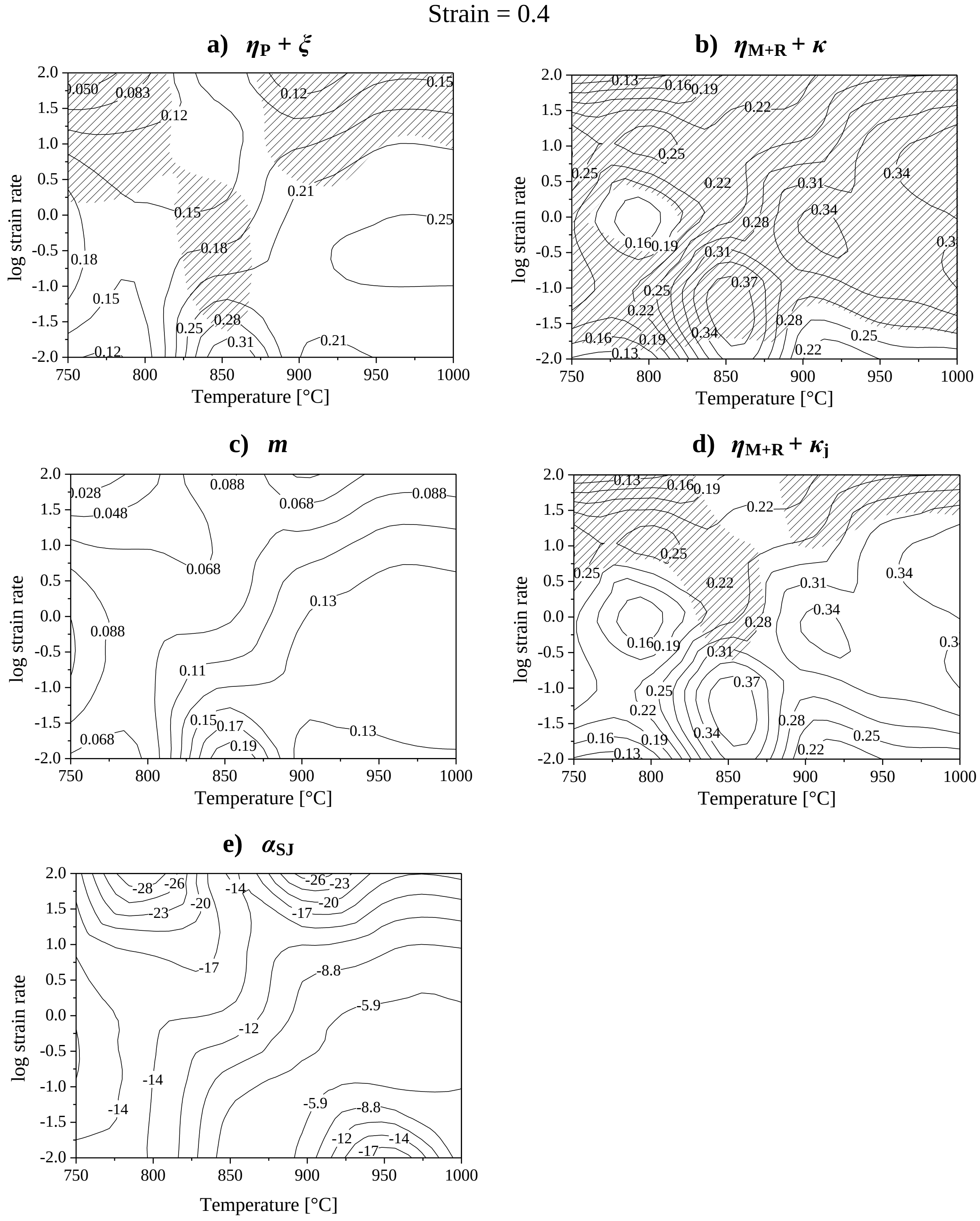

Strain = 0.4

a) $\eta_P + \xi$

b) $\eta_{M+R} + \kappa$

c) m

d) $\eta_{M+R} + \kappa_j$

e) α_{SJ}

Figure 82. Processing maps for the steel alloyed with N at a strain of 0.4 showing isolines of efficiency parameters and dashed instability zones as a function of temperature and strain rate.

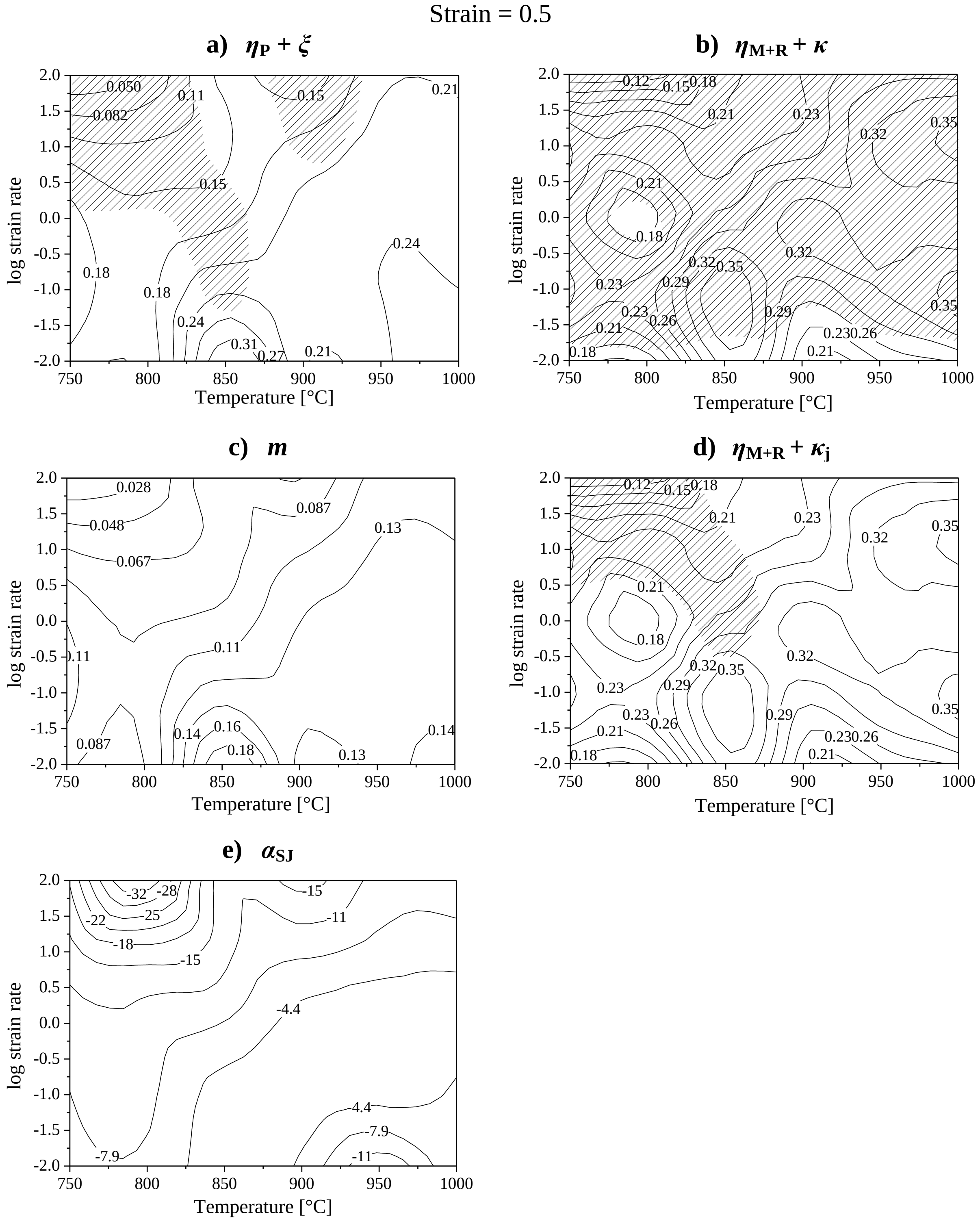

Figure 83. Processing maps for the steel alloyed with N at a strain of 0.5 showing isolines of efficiency parameters and dashed instability zones as a function of temperature and strain rate.

4.4 Steel containing vanadium

4.4.1 Microstructure of the as-received material and dilatometry investigations

Different investigations for the as-received material were made to obtain a starting microstructure with large austenite grains. Therefore, dilatometry and LOM investigations were performed for three different conditions. Figure 84 summarizes the different applied heating and cooling treatments.

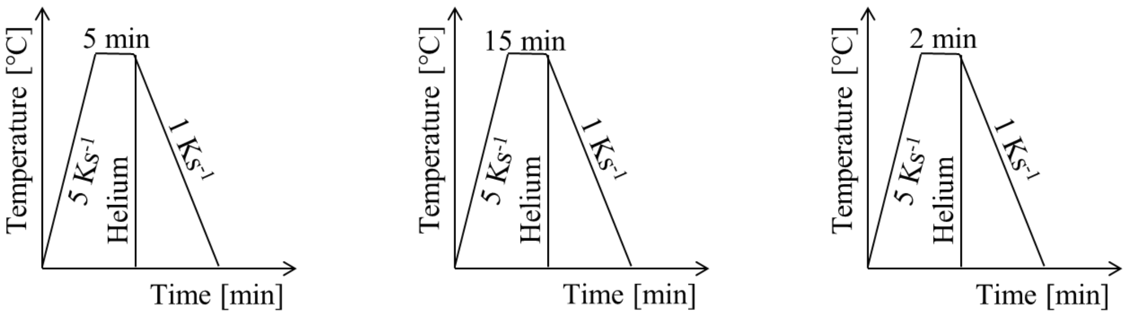

a) 1000°C, 5 minutes **b) 1000°C, 15 minutes** **c) 1150°C, 2 minutes**

Figure 84. Schemas for the three different heating and cooling treatments for: 1) 1000°C, 5 minutes 2) 1000°C, 15 minutes and 3) 1150°C, 2 minutes.

The dilatometer curves in Figure 85 show that for the slow cooling, mainly ferrite, perlite and bainite was obtained while for the fast quenching in Figure 86 only martensite and a few amount of bainite was obtained. Additionally in the LOM pictures, some ferrite at the grain boundaries was observed, especially at the sample austenitized at 1000°C and 5 minutes.

The determined temperatures in Figure 85 a) are A_{r3} = 722°C, B_s = 613°C and B_f = 570°C and in Figure 85 b) the obtained values are similar: A_{r3} = 722°C, B_s = 611°C and B_f = 570°C. For the later on used condition the following values were measured using Figure 85 c) A_{r3} = 709°C, B_s = 608°C and B_f = 565°C. These temperatures correspond to the non-isothermal decomposition of austenite into ferrite, of austenite into ferrite and pearlite and of remaining austenite into bainite. Using Figure 86 a-c) the following martensitic transformation temperatures were obtained a) M_s = 469°C and M_f = 285°C, b) M_s = 474°C and M_f = 285°C and for condition c) M_s = 469°C and M_f = 289°C.

a) 1000°C, 5 minutes; Cooling rate: 1K s^{-1}

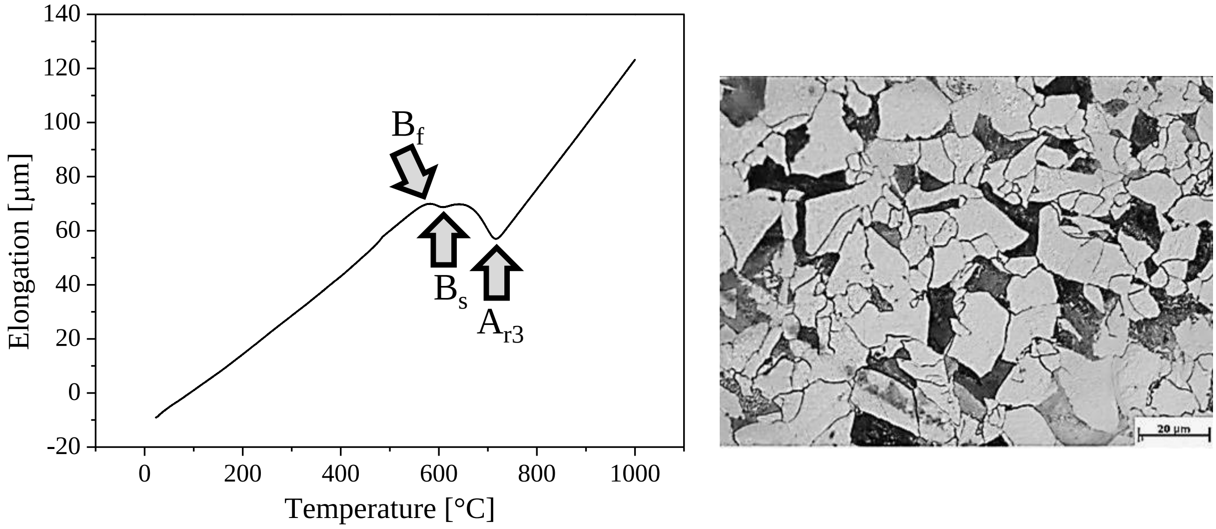

b) 1000°C, 15 minutes; Cooling rate: 1K s^{-1}

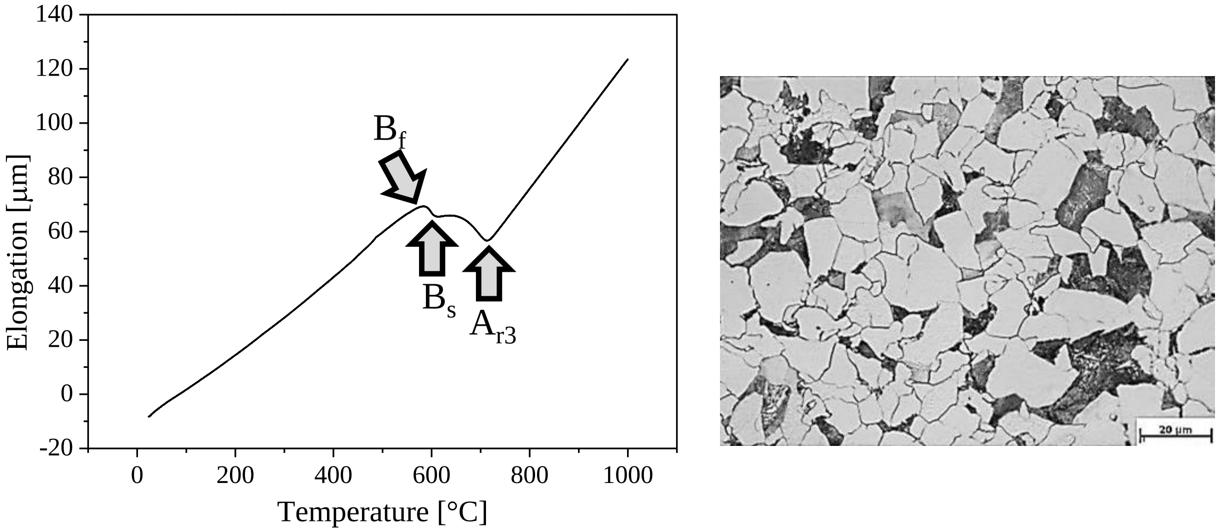

c) 1150°C, 2 minutes; Cooling rate: 1K s^{-1}

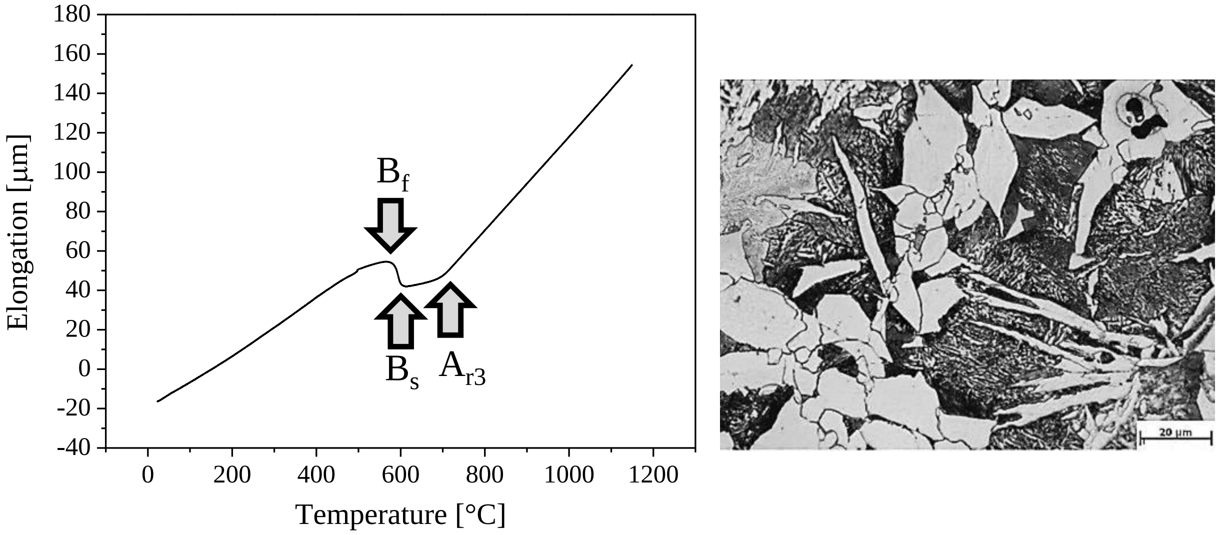

Figure 85. Dilatometric curves showing the change in length as a function of the temperature during cooling with 1 K s^{-1} after austenitization. A_{r3}, B_s, and B_f temperatures were obtained.

a) 1000°C, 5 minutes; Cooling rate: He

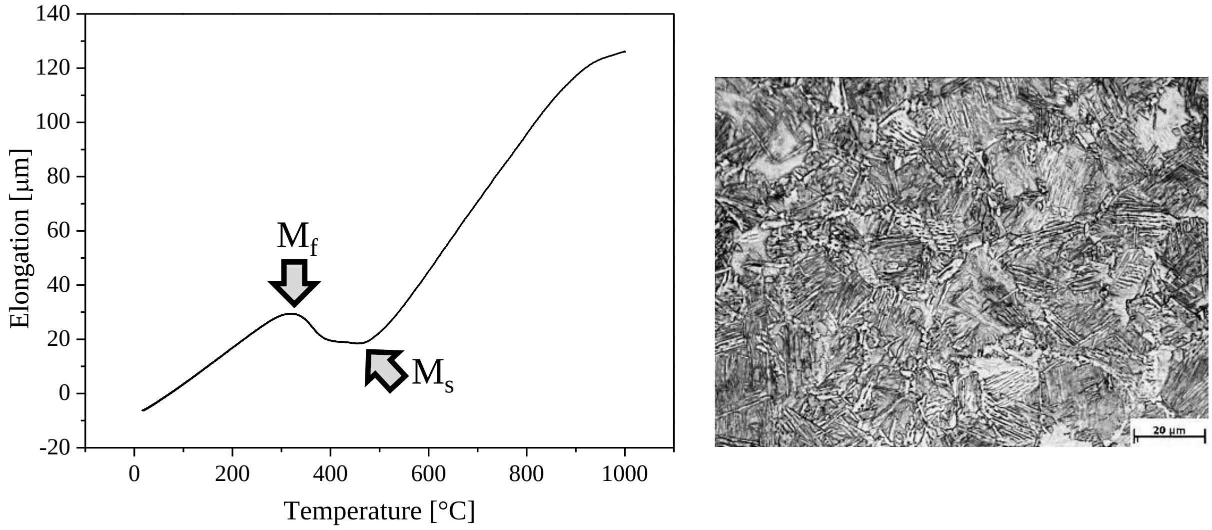

b) 1000°C, 15 minutes; Cooling rate: He

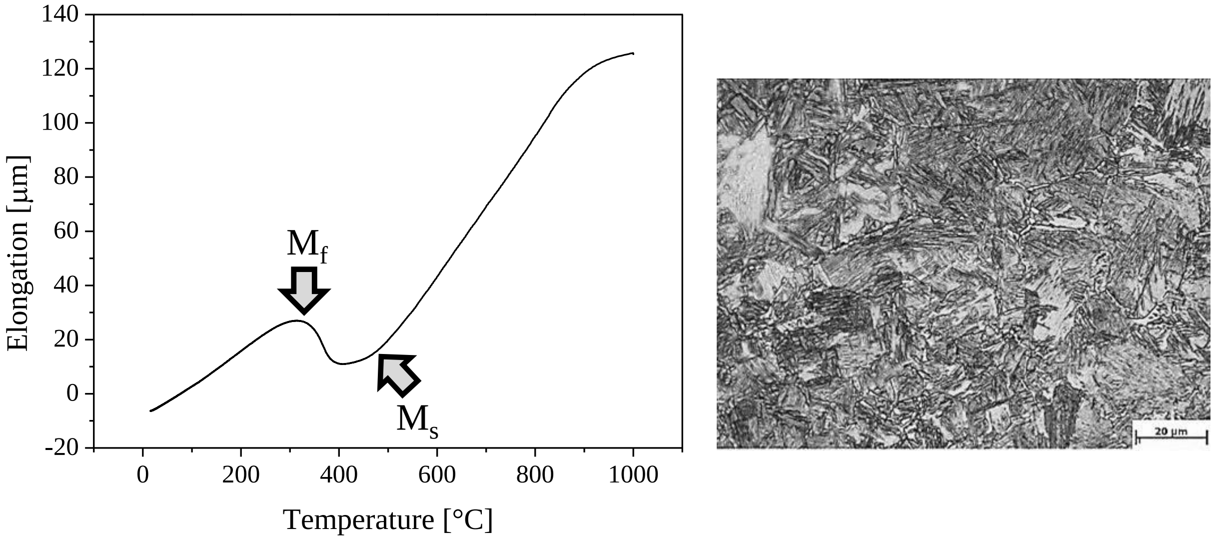

c) 1150°C, 2 minutes; Cooling rate: He

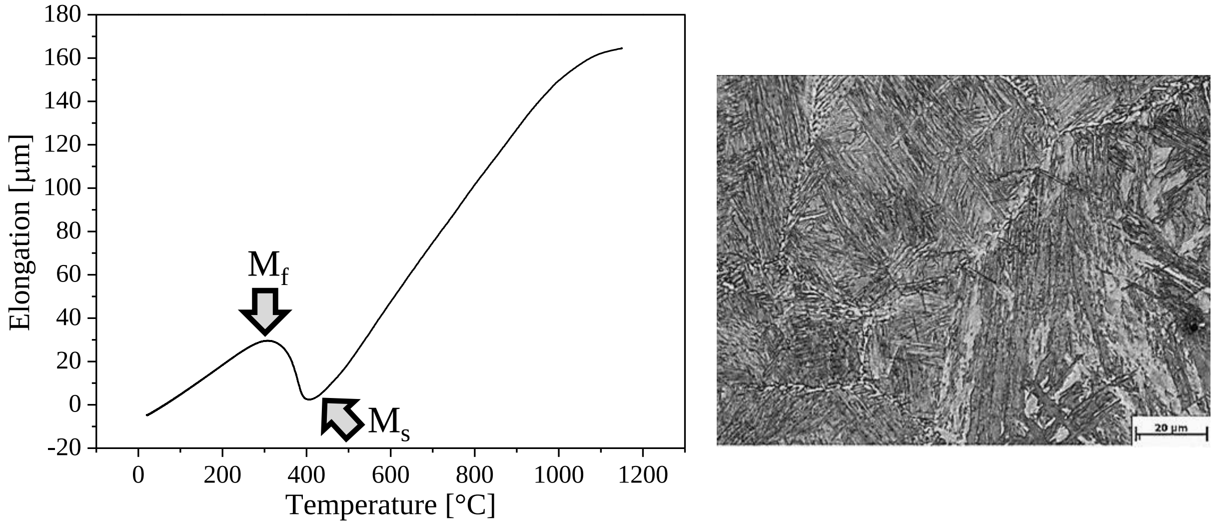

Figure 86. Dilatometric curves showing the change in length as a function of the temperature during cooling with He after austenitization. M_s and M_f temperatures were obtained.

4.4.2 Flow curves

The flow curves obtained for this steel are shown in Figure 87 as a function of the strain rate 0.001–80 s^{-1} and the temperature in a range of 750–1150°C. Generally, it can be seen that the flow stress increases with increasing strain rate and is decreasing with increasing temperature. For the lowest temperature strain hardening is the dominant mechanism and no steady state is reached. With increasing the temperature, steady state is reached after reaching one or multi-peak stresses. As mentioned before, these peaks at high strain rates may occur due to a ringing effect explained in [99] and/or self-heating.

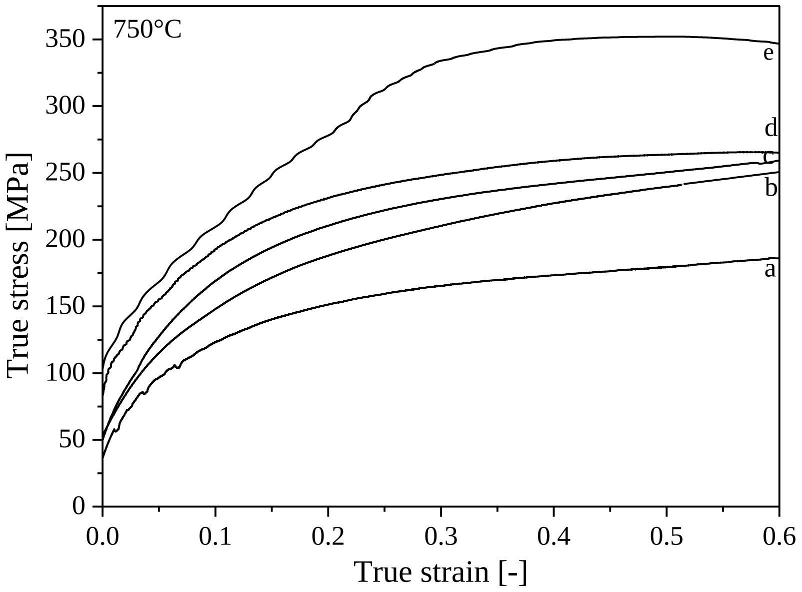

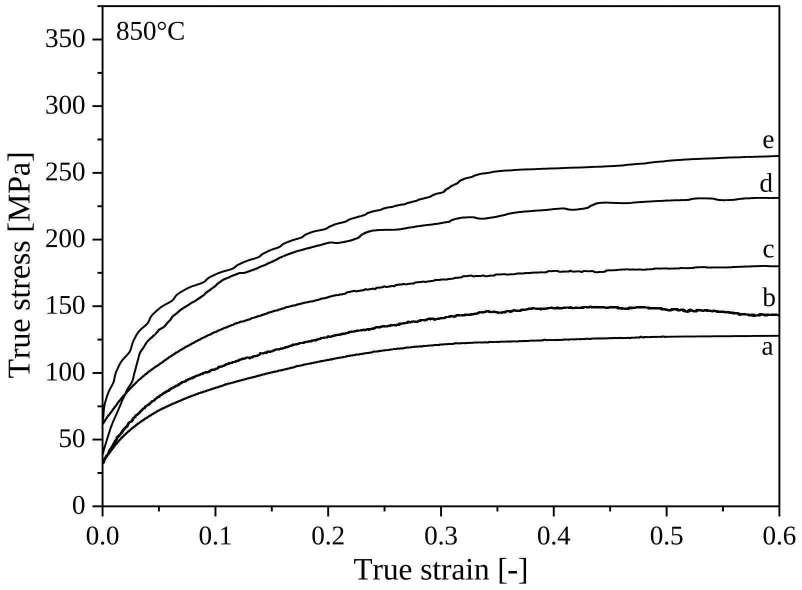

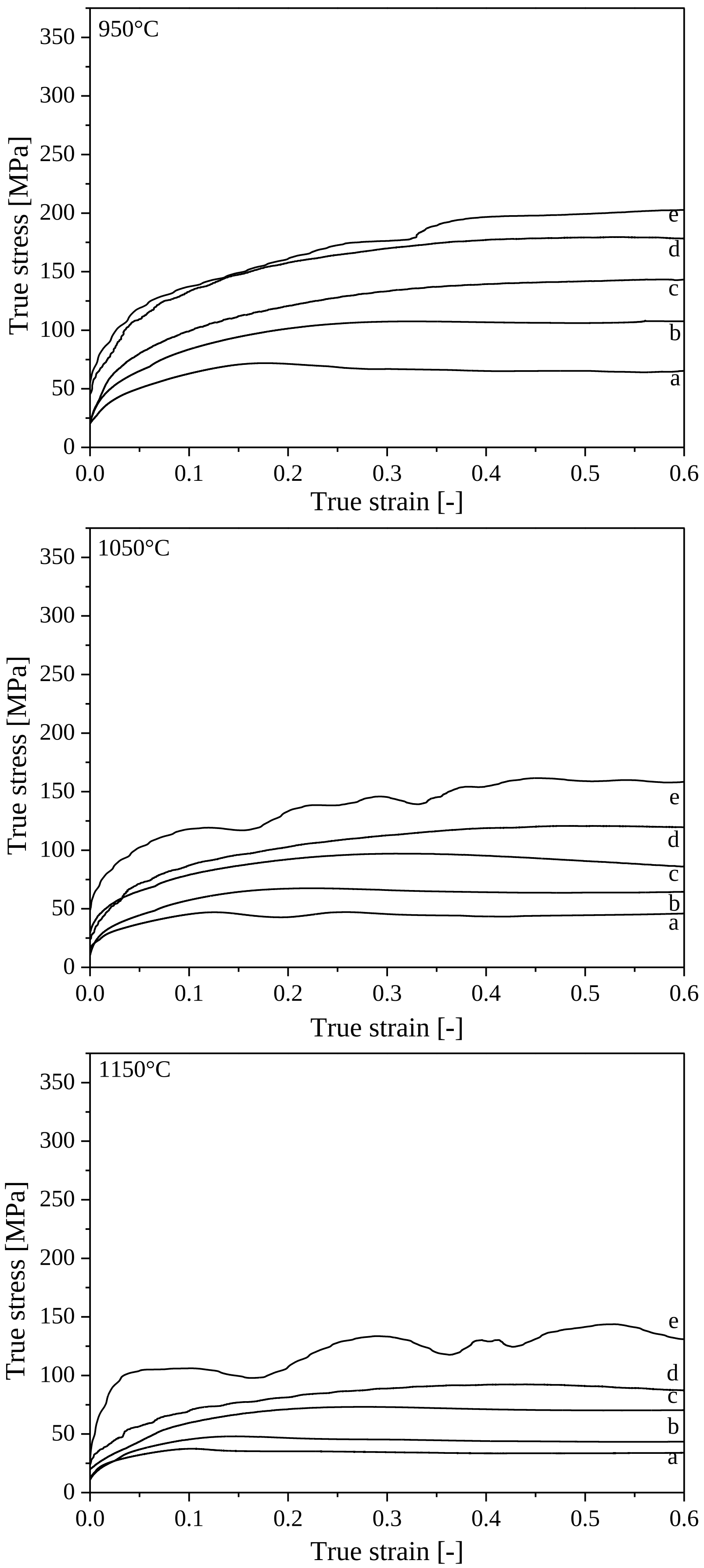

Figure 87. Flow curves obtained from compression tests at strain rates of a) 0.01 s^{-1}, b) 0.1 s^{-1}, c) 1 s^{-1}, d) 10 s^{-1} and e) 80 s^{-1}.

4.4.3 Microstructure after hot deformation

Micrographs taken from the middle of the samples are shown in Figure 88 for low, moderate and high temperatures for the lowest and the highest applied strain rate.

Elongation of the austenite grain normal to the deformation direction is observed for temperatures lower than 850°C, in agreement with [102]. Deformation bands are detected at the deformation temperature of 750°C for all the strain rates and for 850°C at strain rates higher than 0.1 s^{-1}. Furthermore some equiaxed grains were formed at 850°C and a strain rate of 0.1 s^{-1}. Fine ferrite grains can be seen on the grain boundaries for 750°C which is in agreement with [69].

On the other hand, refinement of the austenite takes place for all the strain rates at temperatures higher than 950°C. In the middle of the sample where the local strain is around 1.1 a full equiaxed microstructure can be observed for all samples except for the highest strain rate.

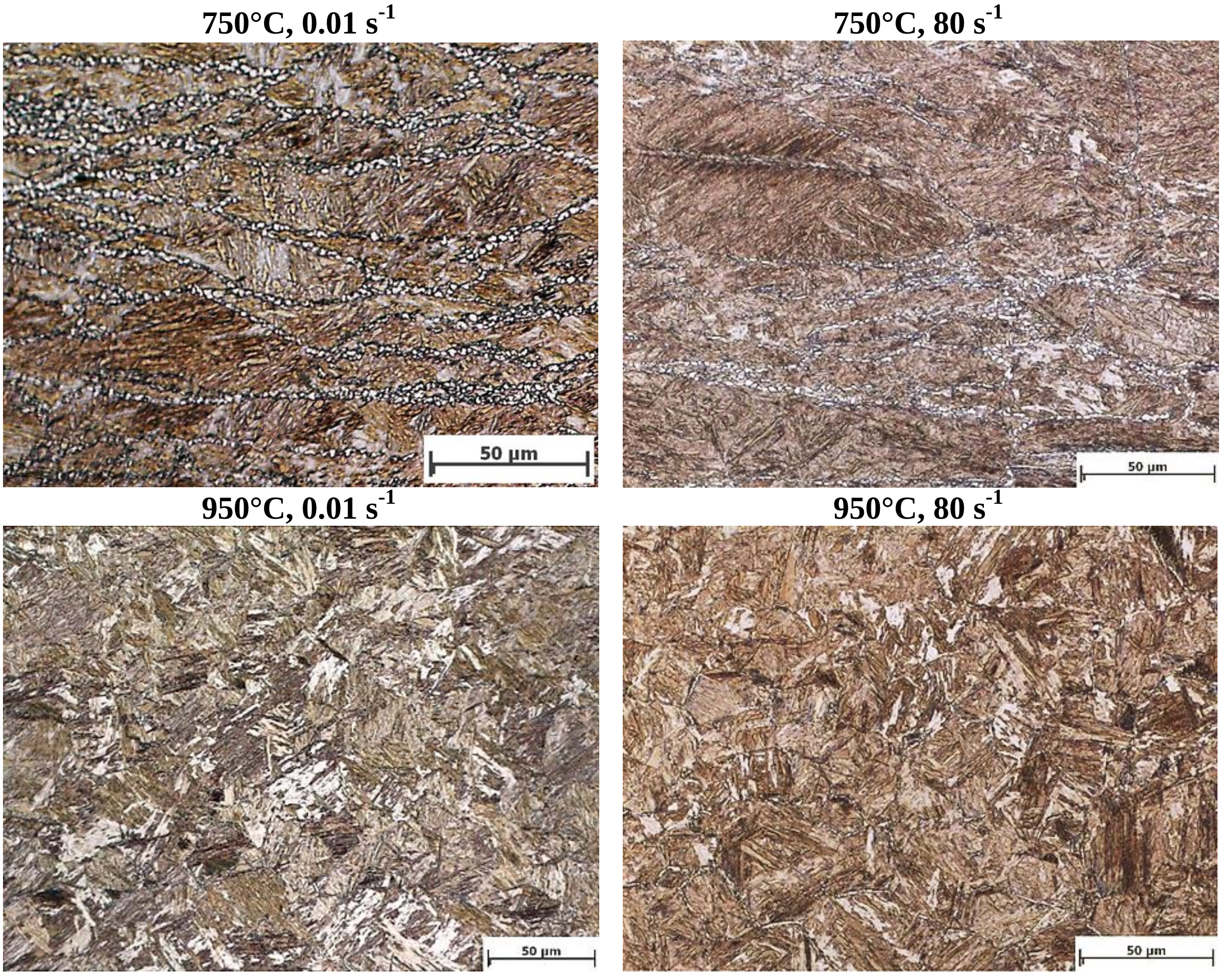

750°C, 0.01 s^{-1}

750°C, 80 s^{-1}

950°C, 0.01 s^{-1}

950°C, 80 s^{-1}

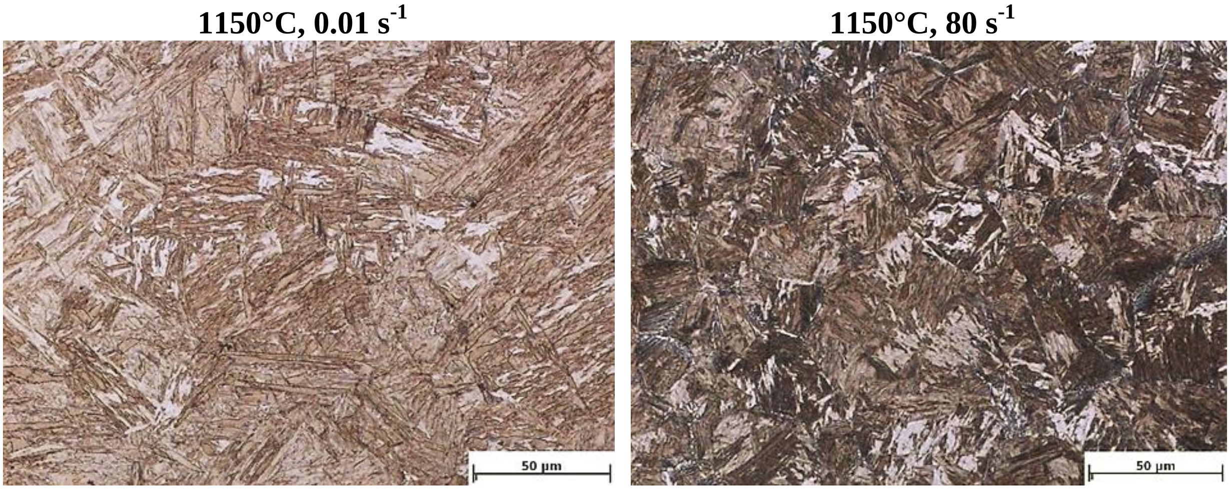

1150°C, 0.01 s^{-1}

1150°C, 80 s^{-1}

Figure 88. Microstructure of the steel samples deformed at 750°C, 950°C and 1150°C at a strain rate of 0.01 s^{-1} and 80 s^{-1}. Local strain of 1.1, load direction is vertical.

Some details of the observations mentioned before are shown in Figure 89. The grey arrows show deformation bands, the blue one deformed austenite, the orange one equiaxed austenite and the green arrow shows ferrite.

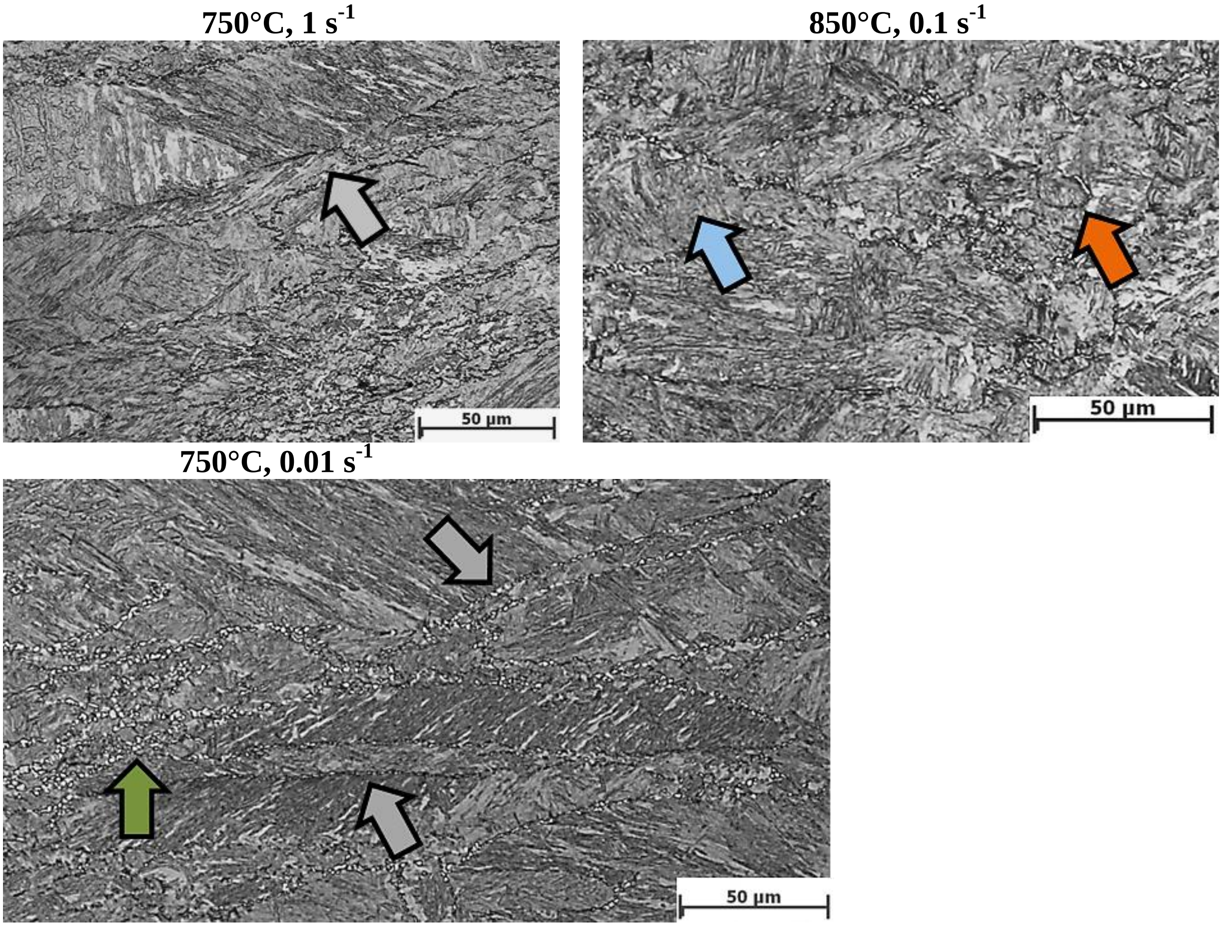

750°C, 1 s^{-1}

850°C, 0.1 s^{-1}

750°C, 0.01 s^{-1}

Figure 89. LOM pictures of samples deformed at different temperatures and strain rates. Grey arrows: deformation bands, blue arrow: deformed austenite, orange arrow: equiaxed austenite and green arrow: ferrite. Local strain of 1.1, load direction is vertical.

4.4.4 Constitutive equations

Constitutive equations using the stress at a strain of 0.4 were calculated and are shown in Figure 90 and Equation 56. The results are different compared to the results obtained for the steel alloyed with N. The *c* value is 0.015 MPa^{-1} compared to 0.009 MPa^{-1} for the previous steel. The apparent activation energy is 388 kJ mol^{-1} and higher than the 323 kJ mol^{-1}, and the stress exponent *n* with a value of 4.43 is smaller than the one observed for the previous alloy. Figure 90 a) shows the slopes used for the calculation of *Q* and in Figure 90 b) a good correlation between the *Z* parameter and the flow stress is visible.

a) Determination of *Q*

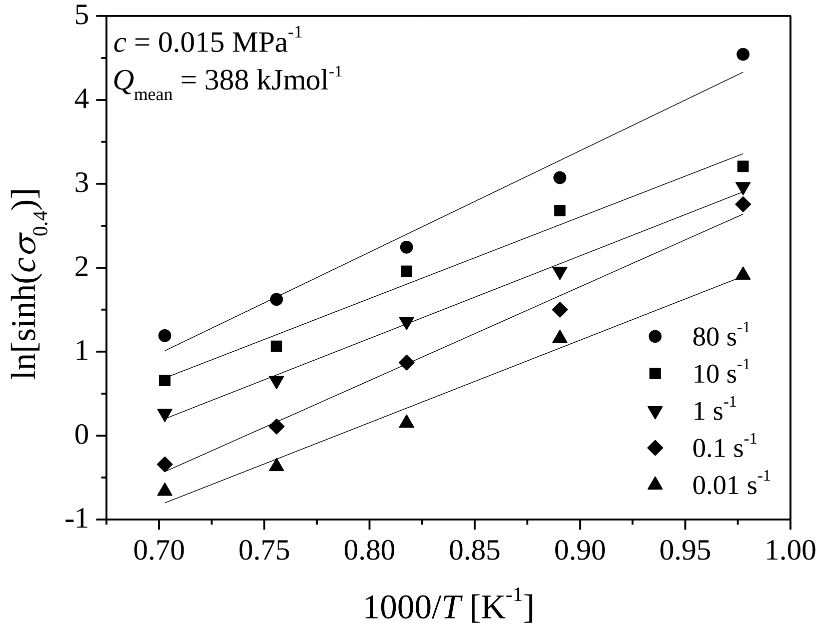

b) Zener-Hollomon versus flow stress

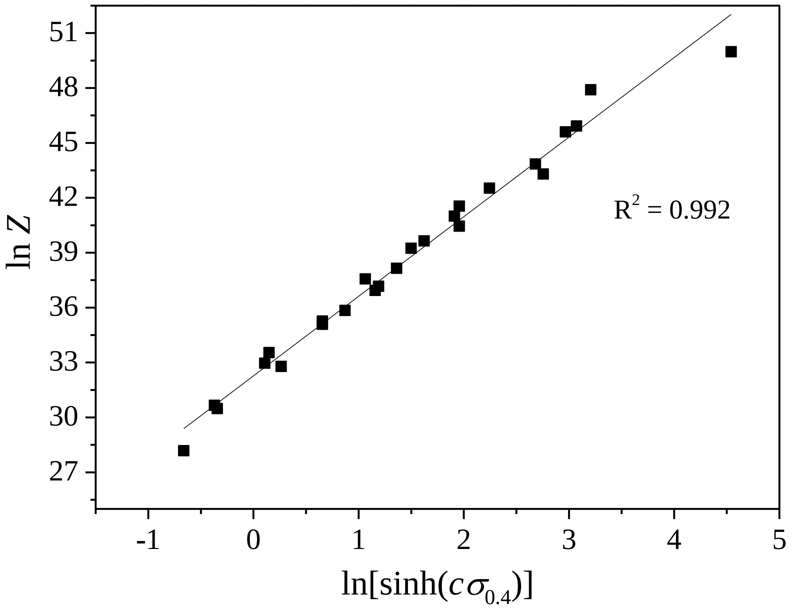

Figure 90. Determination of parameters for the constitutive equations: a) activation energy *Q* and b) relationship of the Zener-Hollomon parameter versus the flow stress.

The constitutive equation is expressed as in Equation 56:

$$\dot{\varepsilon} = 1.15 \cdot 10^{14} [\sinh(0.015\sigma_{0.4})]^{4.43} \exp\left(\frac{-387850}{RT}\right) \qquad \textbf{Equation 56}$$

4.4.5 Processing maps

Processing maps were calculated at constant strains of 0.2 (Figure 91), 0.3 (Figure 92), 0.4 (Figure 93) and 0.5 (Figure 94).

The first investigated model is based on DMM of Prasad. The area with the highest η_P value is found at the lowest strain rate and for temperatures around 1050°C and is shifted to lower temperatures by increasing strain. The second area of high η_P values appears at the highest temperature and highest strain rate. Negative instability parameter ξ is calculated at low temperatures and at moderate temperatures.

The mDMM by Murty and Rao shows the area of highest η_{M+R} values at low strain rates at temperatures between 950°C and 1125°C. This area is shifted to lower temperatures by increasing strain. A further area of large η_{M+R} appears at temperatures higher than 1125°C, for all strain rates. Large areas of flow instability are predicted. Generally, there is only a small area of stability at the lowest strain rate for all temperatures and strains.

The m map used for describing the formability shows the same trend as the model of Prasad. The maps show negative m values at a strain of 0.3 and of 0.5 for moderate temperatures and high strain rates. Additionally, negative m values are observed at 0.5 of strain for low temperatures and moderate strain rates.

The instability parameter κ_j shows a similar trend as the Prasad instability parameter.

The model of Semiatin and Jonas predicts stable flow in the whole range of temperatures and strain rates. The values which indicate in which direction instability will start are present at low temperatures and high strain rates and high temperatures and low strain rates.

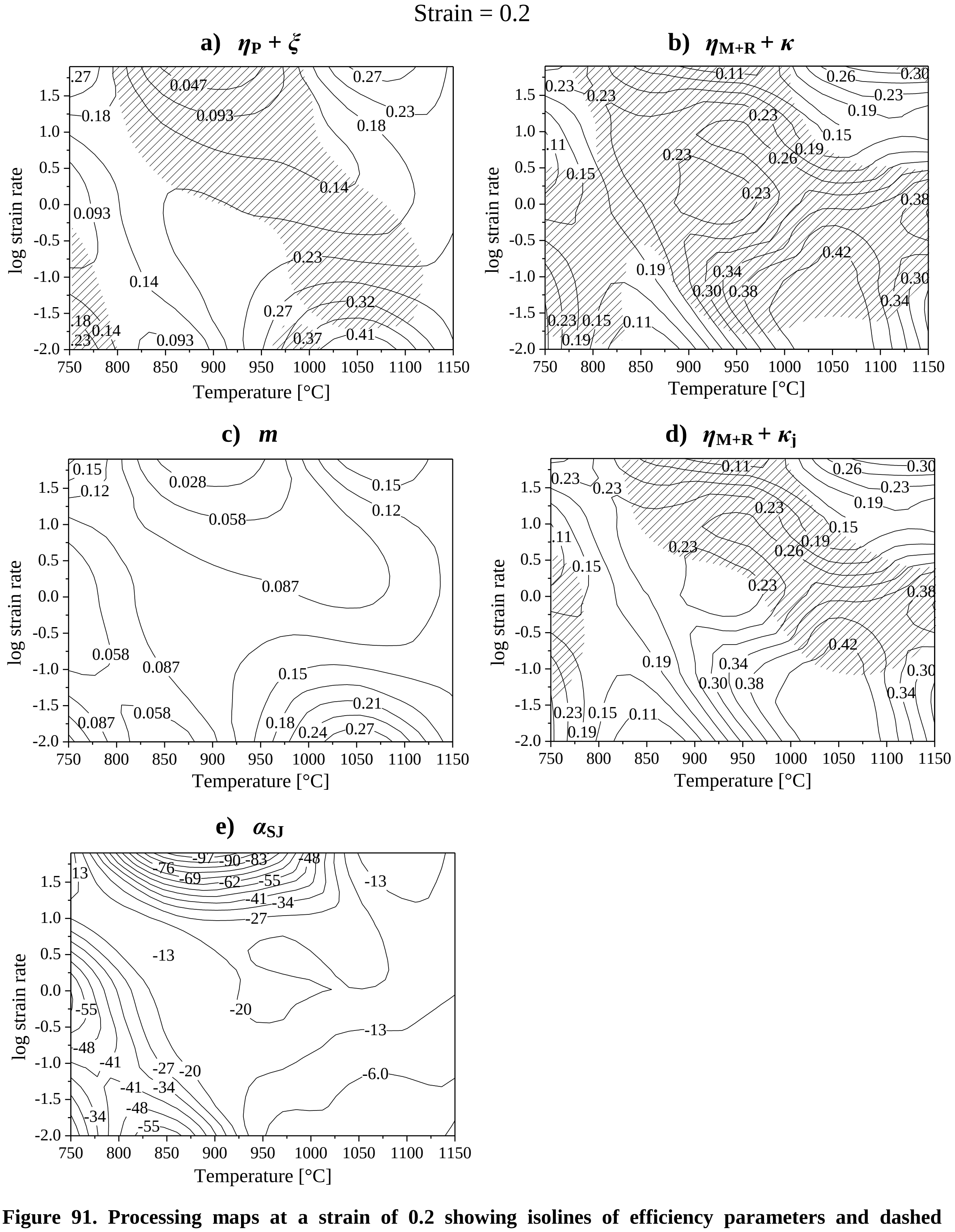

Figure 91. Processing maps at a strain of 0.2 showing isolines of efficiency parameters and dashed instability zones as a function of temperature and strain rate.

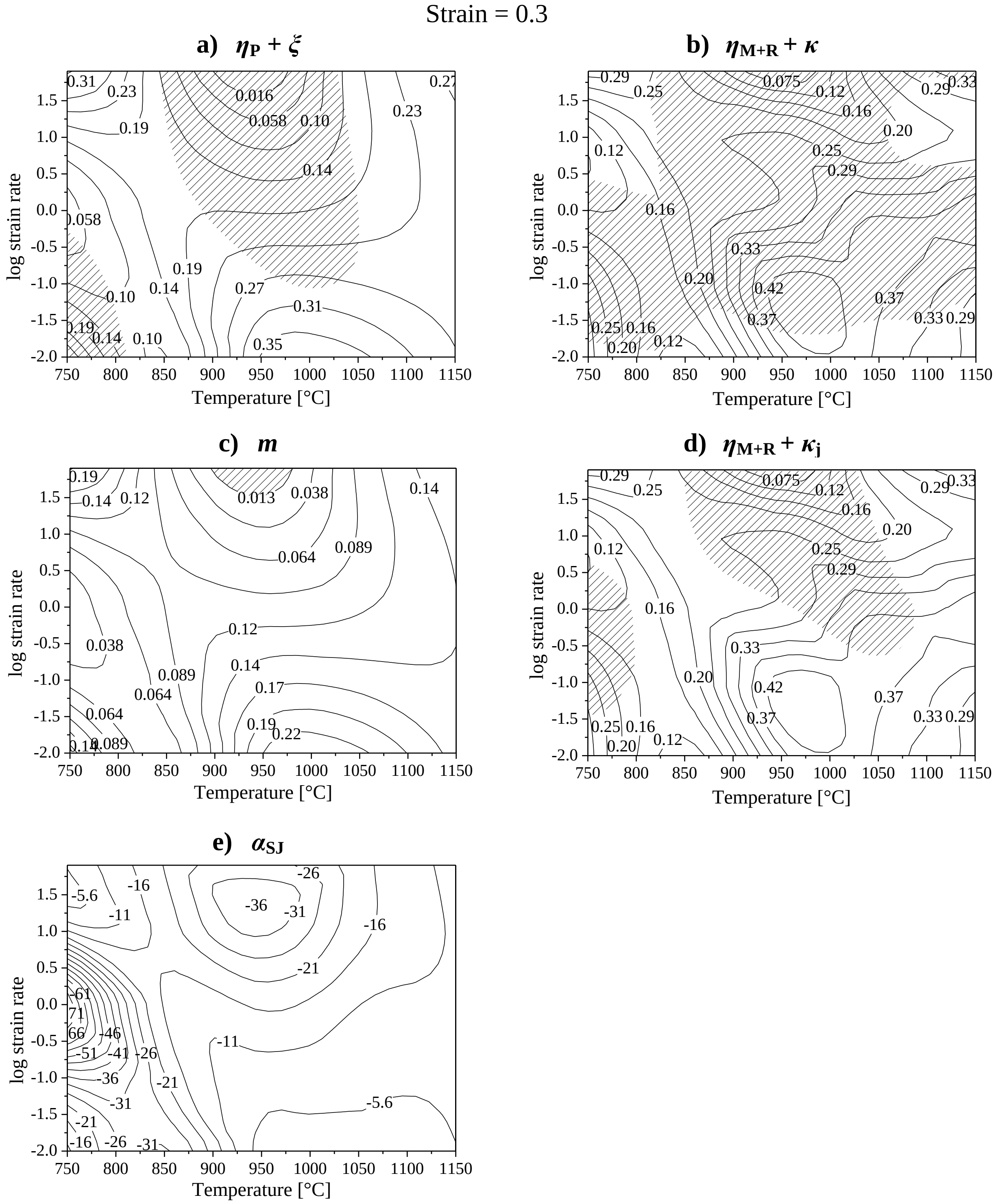

Figure 92. Processing maps at a strain of 0.3 showing isolines of efficiency parameters and dashed instability zones as a function of temperature and strain rate.

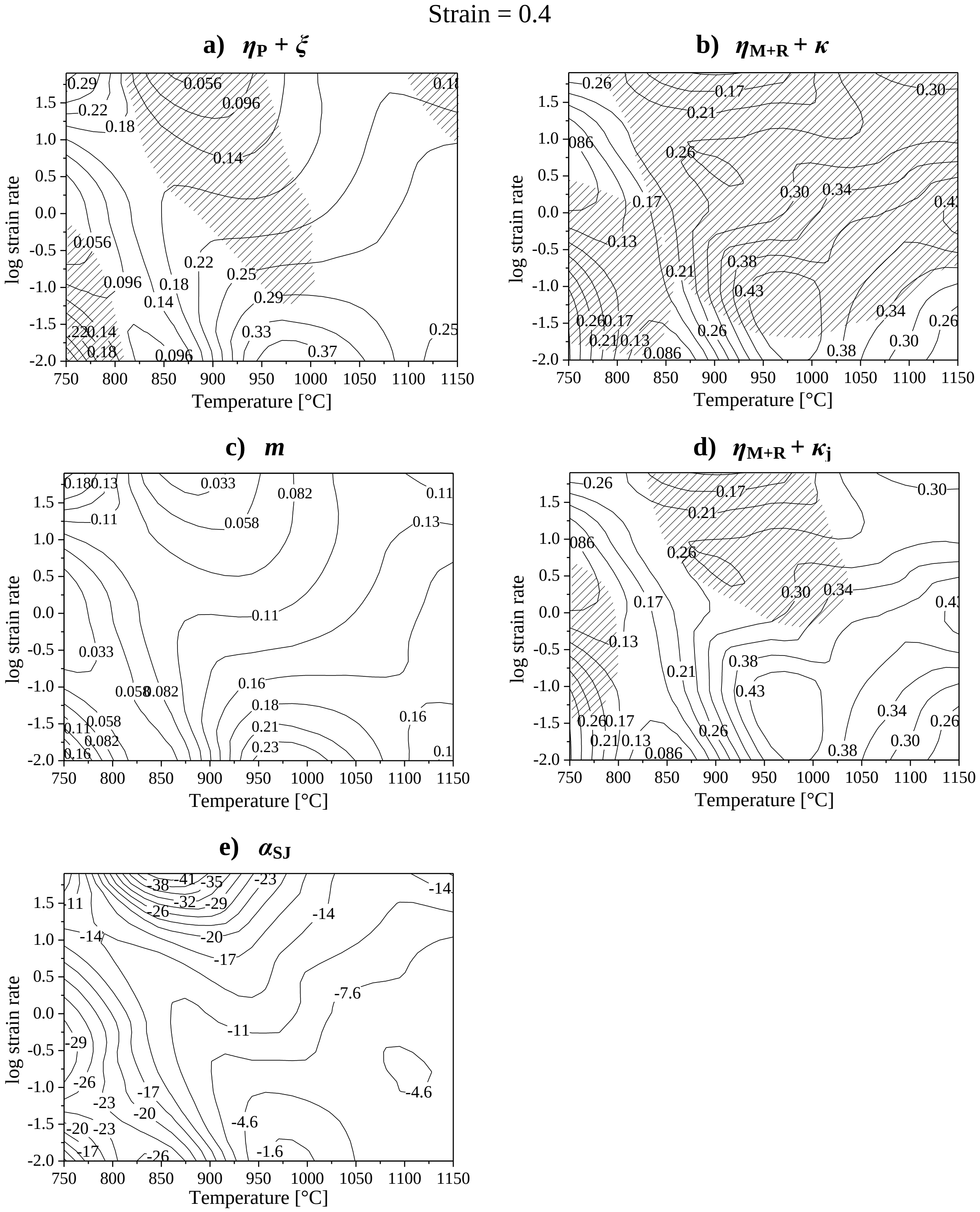

Figure 93. Processing maps at a strain of 0.4 showing isolines of efficiency parameters and dashed instability zones as a function of temperature and strain rate.

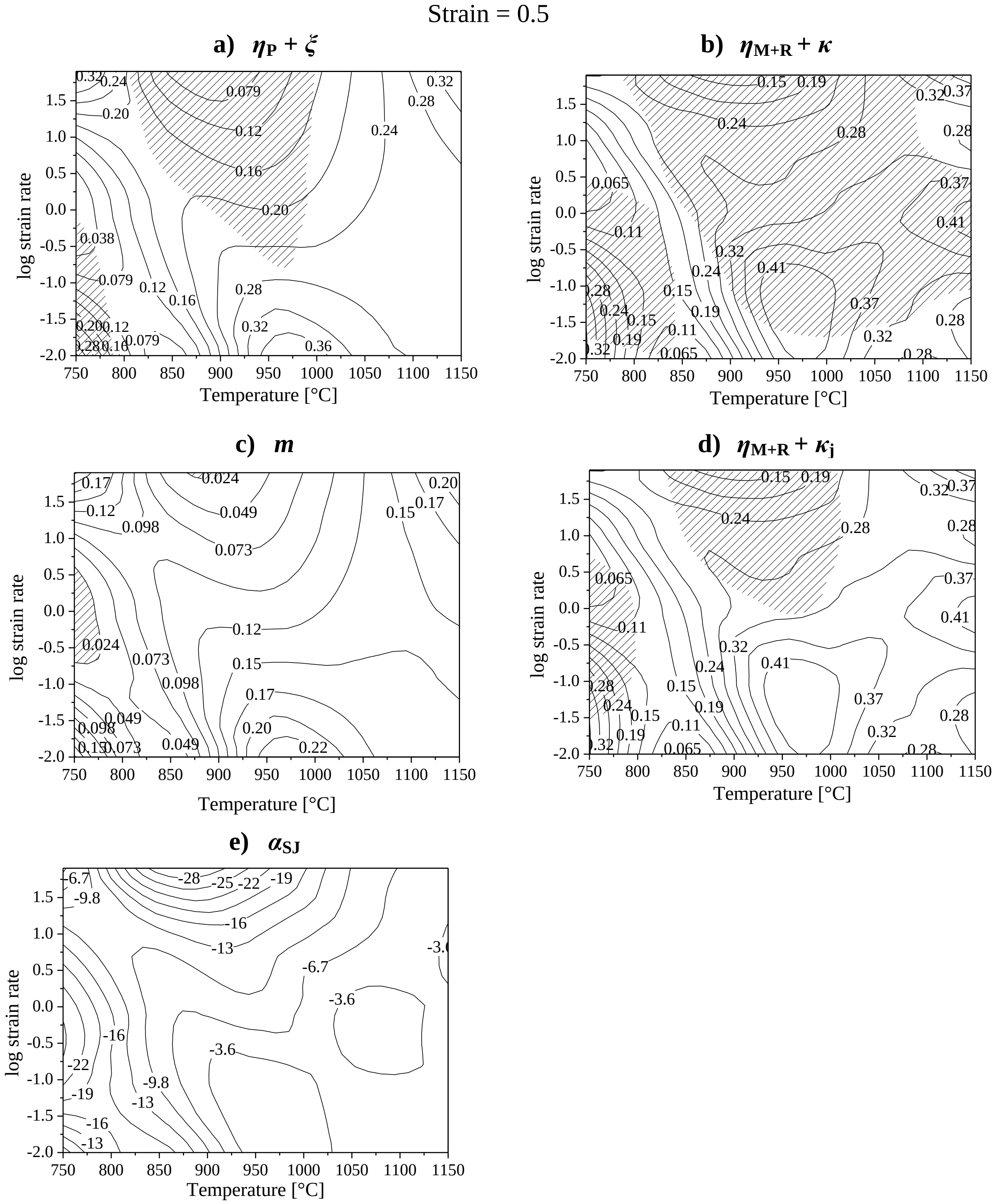

a) $\eta_P + \xi$

b) $\eta_{M+R} + \kappa$

c) m

d) $\eta_{M+R} + \kappa_j$

e) α_{SJ}

Figure 94. Processing maps at a strain of 0.5 showing isolines of efficiency parameters and dashed instability zones as a function of temperature and strain rate.

5 Discussion

The discussion chapter is divided into: hot deformation mechanisms of the studied materials, data treatment for calculating processing maps and the usage and validity of processing maps. The hot deformation behaviour of the Mg-alloy, the Ti-alloy and the two investigated steels is discussed first separately. Then the data treatment to obtain the maps is discussed. Finally, the usage and validity of DMM and non DMM models is discussed in general.

5.1 Magnesium

The analysis of the hot deformation mechanisms of magnesium is divided into low strain rate- and high strain rate ranges.

5.1.1 Low strain rate (0.001–0.1 s^{-1}) range

The flow curves give a first idea of the mechanisms which can occur during the hot deformation as a function of the strain rate, the temperature, the strain and the initial condition of the material. For Figure 31 it can be seen that with increasing temperature larger strains are accommodated without the onset of fracture. The flow curves for low temperatures (300–350°C) show a peak at higher strain rates (0.01–0.1 s^{-1}), whereas for the lowest strain rate of 0.001 s^{-1} softening for a deformation temperature of 300°C but steady state for the samples deformed at 350°C occurred. Furthermore, after deformation at 300°C twins were detected by microscopy for all strain rates. LOM investigations after deformation at 300°C and a strain rate of 0.1 s^{-1} are shown in Figure 95. The blue arrow in the picture marks a crack, whereas the green arrows indicate twins or new grains at former twins. These pictures were taken at different positions on the sample, meaning at different local strains. For the sample deformed at 300°C, pictures were taken at ~ 0.7, ~ 1 and ~ 1.1 of local strain. Due to this strain distribution in the sample, different amounts of recrystallized grains at the twins are observed. For low strains the boundaries are smooth, showing the typical shape of deformation twins which are lens shaped, while with increasing strain the boundaries start to serrate and become wavy (picture a)). In the second picture b) the twin already started to split into separate grains and finally in picture c), only new grains are visible. DRX starts preferably on twin domains, as well as on phase- and grain boundaries, because these areas have a much higher stored deformation energy than the surrounding matrix [103], [104]. Furthermore, twin boundaries behave as barriers for dislocations.

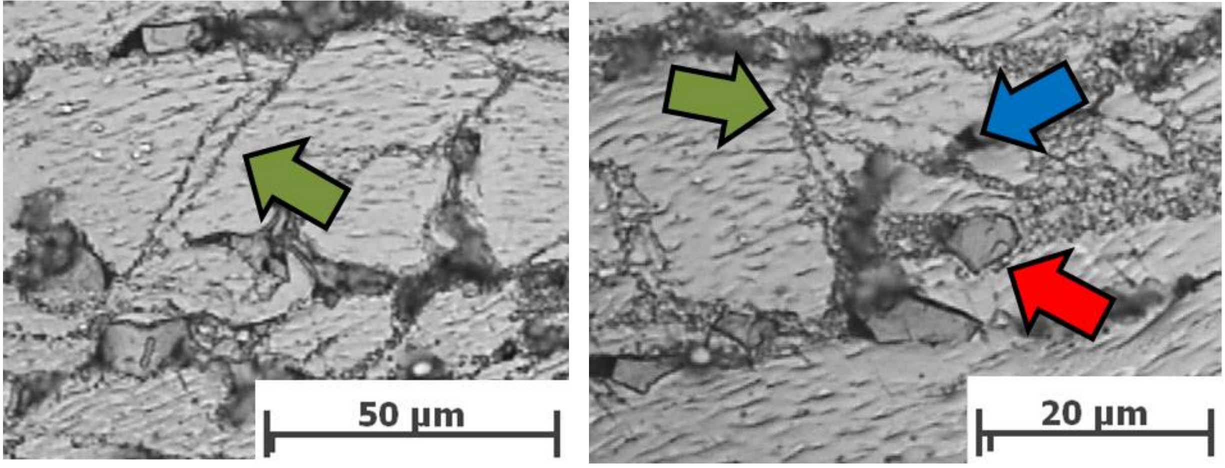
a) local strain of ~ 0.7

b) local strain of ~ 1

c) local strain of ~ 1.1

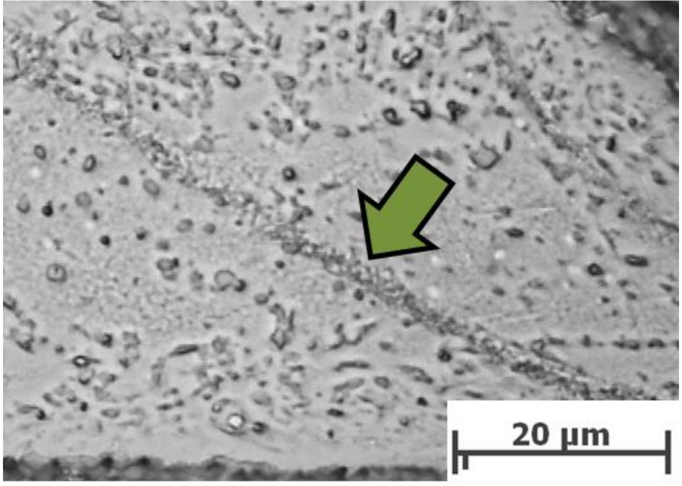

Figure 95. LOM investigations for a sample deformed at 300°C and at a strain rate of 0.1 s^{-1}. Green arrows indicate twins and new grains at former twins. The red arrow shows evidence for PSN and the blue arrow marks a crack.

Furthermore, intermetallic phases as well as fine spread precipitates are still present at these deformation conditions (Figure 34). DRV as well as DRX are possible, however the DRV mechanism is hindered due to many precipitates in the material. Precipitates hinder the movement of dislocations and boundaries. In the works of Robson et al. [105] and [106] the effect of particles on the recrystallization behaviour in Mg alloys was investigated. He mentions in the case of large particles, meaning a size > 1 µm, particle stimulated nucleation (PSN) may promote recrystallization which was indicated with a red arrow in Figure 95 b). Additionally, some small new grains are present around this large particle in the LOM investigations. EBSD measurements could be carried out to prove if this new grains are a result of PSN due to different produced orientations. However, these coarse particles only have a minor effect on DRX due to the fact that DRX occurs preferred along the prior grain boundaries and not so much at particles. To go into detail, the reason for DRX occurring preferably at prior grain boundaries is that the lattice rotations at particles are not as effective as the lattice rotations generated at prior grain boundaries. Additionally, Robson et al. [105] mention in their work that clusters of large particles are more preferred sites for initiating PSN than single particles, due to the fact that the accumulated misorientation toward single particles is less than 5°, whereas the misorientation in clusters of particles reaches values of about 30°.

With increasing the temperature to 400°C the flow curves show slightly softening and steady state. In the LOM pictures larger amounts of new grains compared to the lower temperatures can be seen and precipitates are still present. Still DRV is hindered, so DRX occurs. In Figure 96 two deformed samples at a) 400°C and 0.001 s^{-1} and b) 400°C and 0.1 s^{-1} are presented. New grains are formed mainly around the prior grain boundaries and the intermetallic phases and the shape of the grains and their sizes are different. The reason therefore may be that not only DRX but also mDRX occurred for Figure 96 a) in which the grains are larger compared to the grains in Figure 96 b). In the work of Beer et al. [107] is mentioned that post-dynamic recrystallization can occur during subsequent annealing or if the cooling rate is too slow, which leads to an increase in the grain size. Additionally, the cooling rate for this two deformed samples is different. It took 0.89 s to quench sample a) below 200°C and 0.52 s to quench sample b) below 200°C.

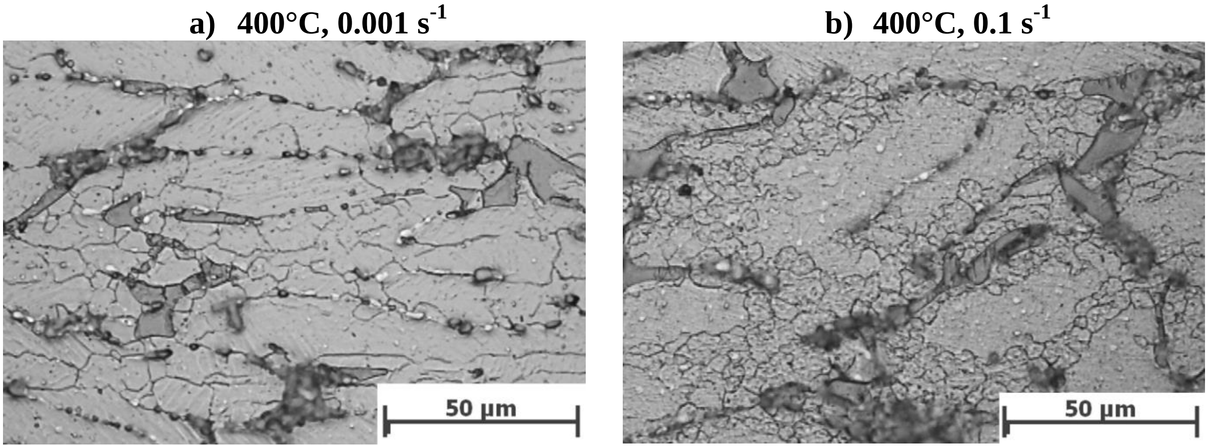

Figure 96. Microstructure obtained after deformation at a) 400°C and 0.001 s^{-1} and b) 400°C and 0.1 s^{-1}. Pictures taken at a local strain of 1, load direction is vertical.

Authors of several studies on hot deformation of magnesium [58], [59], [105] have mentioned that DRX occurs during deformation tests with water quenching. However, the quenching rate is not mentioned in detail. Thus, mDRX or even SRX could occur if the cooling rate is too slow [77]. Therefore, the word “immediately”, related to the time of water quenching, is sometimes not significant enough.

In addition, the grain sizes of the recrystallized grains are shown in Table 8, Figure 36 and Figure 44. Figure 44 which shows the influence of Z on the dynamically recrystallized grain size depicts large scattering of the data, especially for high temperatures and the highest strain rate. Therefore, the value of 500°C and a strain rate of 10 s^{-1} which is related to mDRX was deleted. However, the result was not good enough and in addition the value of 400°C and a strain rate of 10 s^{-1} was deleted as well and the obtained result is present in Figure 99. The obtained standard error was closer to 1 compared to the standard error obtained using all values.

The microstructure of the samples deformed at 500°C shows for the lowest strain rates no new grains. With increasing the strain rate up to 0.1 s^{-1} the microstructure changes and new grains are present. However, these DRX grains are large (21 µm) if compared to other DRX grain sizes (< 10 µm) below 500°C.

Moreover, the precipitates that appear up to 450°C have changed their shape at 500°C from a lamellar shape to a more circular one. At 500°C two things occur: 1) due to coarsening and dissolution of fine precipitates, dislocation movement is easier and 2) due to diffusion of Al in Mg, the SFE increases. These two phenomena are favourable for dynamic recovery, thus no formation of new grains could be observed.

5.1.2 High strain rate (0.1–10 s^{-1}) range

The flow curves obtained at high strain rates and for a temperature range between 300–350°C show softening for all strain rates. The LOM micrographs show a high amount of intermetallic phases and precipitates. Additionally, twins are detected for all deformation rates at 300°C, which is also indicated in the flow curves in the change of the slope at low strains. No new small grains can be seen for a strain rate of 10 s^{-1} at a deformation temperature of 300°C. With the increase of the temperature to 350°C, some small grains are present. The new grains are formed at former twins (indicated by green arrow in Figure 97) at a local strain of 1 and a strain rate of 10 s^{-1}, or at prior grain boundaries.

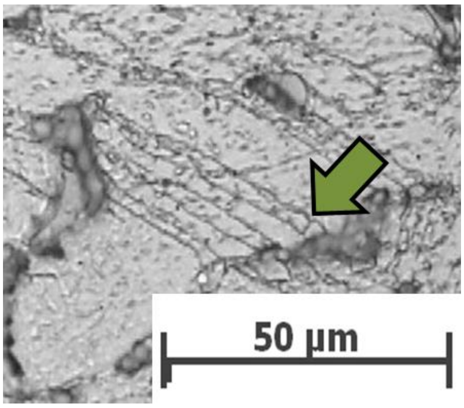

Figure 97. New grains formed at former twins (indicated with a green arrow).

If increasing the temperature to a range of 400°C–450°C a fully recrystallized structure for a strain rate of 10 s^{-1} is given. The flow curves present considerable softening for the 400°C and a strain rate of 10 s^{-1}, and for 450°C and 10 s^{-1}. For lower strain rates a partially recrystallized structure is present. A comparison between the partially and fully recrystallized structures is shown in Figure 34.

For the flow curves obtained at a deformation temperature of 400°C (Figure 31), the peak stresses are shifted to larger strains with decreasing strain rate, in agreement with the recrystallization grade. Generally, with increasing the strain rate less time is available for recrystallization mechanisms and therefore the peak is usually shifted to lower strain values. The reason for an inverse response can be explained by the nucleation sites, increased at higher strain rates by the formation of twins.

At the highest temperature of 500°C, softening is present for all strain rates and additionally for the highest strain rate of 10 s^{-1} recrystallization peaks are visible.

The micrographs show again a fully recrystallized structure as obtained for the 400°C as well. In addition can be seen, that the grain size for this highest temperature is large compared to the grain size obtained at a deformation temperature of 400°C in the micrographs of Figure 34. Furthermore, at 500°C a few precipitates in globular shape can be seen. Finally, and due to large deformation temperatures and due to a not large enough cooling rate, not only DRX but also mDRX or even static growth could take place.

In the paper of Srinivasan et al. [58] DRX is mentioned for a deformation temperature of 425°C and a strain rate of 100 s^{-1}. The grain size was not investigated in the work of Srinivasan et al. However, as can be seen in Figure 98, the size of the grains is large and therefore, the question that arises is if it is really only DRX that occurred.

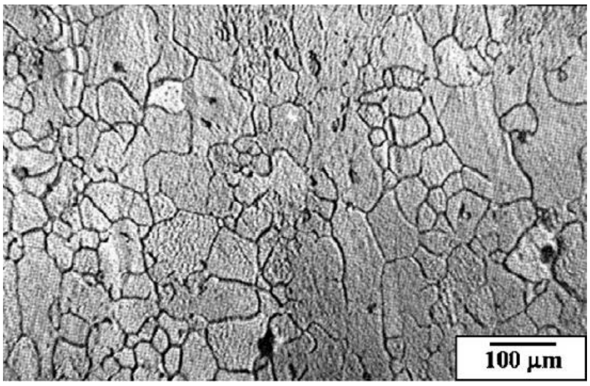

Figure 98. Microstructure of a Mg-alloy deformed at 425°C at a strain rate of 100 s^{-1} [58].

Therefore, the grain size and *Z* were calculated and added as a blue point in the diagram shown in Figure 99. It is recognizable that the point of 425°C and 100 s^{-1} as well as the point at 500°C and 10 s^{-1} are scattering too much.

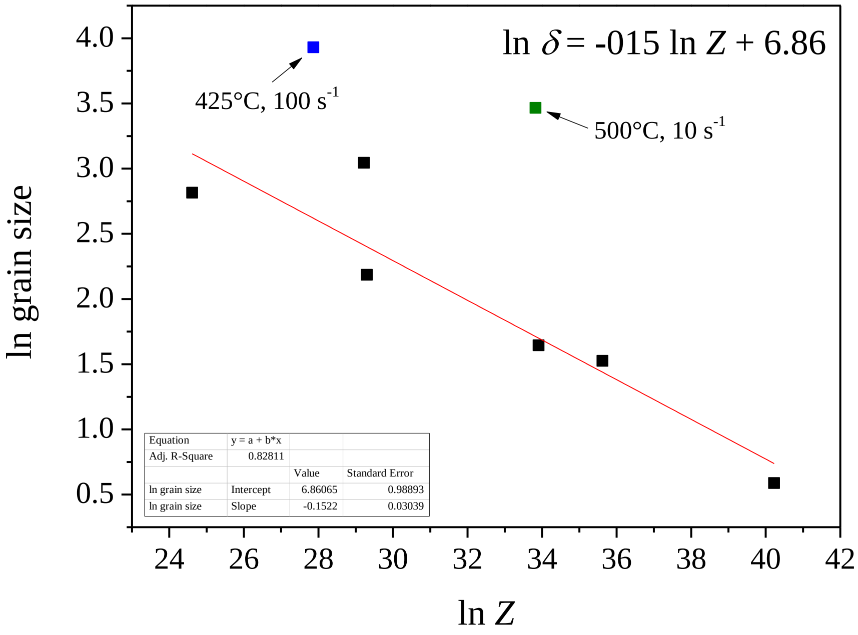

Equation	y = a + b*x		
Adj. R-Square	0.82811		
		Value	Standard Error
ln grain size	Intercept	6.86065	0.98893
ln grain size	Slope	-0.1522	0.03039

Figure 99. Influence of *Z* on the dynamically recrystallized grain size.

To conclude a summary or microstructural map of the deformation behaviour of DieMag422 is given in Figure 100. This summary map shows in which area restoration mechanisms and instability occurs. The map is supported and confirmed by LOM pictures, EBSD measurements and the analysis done before. At very low temperature independently of the strain rate, voids can be seen in the samples and are indicated with a pink arrow in Figure 100. Twins can be detected for low temperatures for all strain rates and for increasing the temperature, twins can be only found at the highest strain rate. This is also proven with the slope in the flow curves. DRX is the most present restoration mechanism for the deformation of the DieMag422 alloy. However, a small area of DRV is present at higher temperatures and low strain rates due to the fact of diffusion of Al in Mg which leads to an increase in the SFE.

Finally, it has to be mentioned, that care with the applied cooling method has to be taken. If the quenching takes around 1 second, this can be too long for this Mg-alloy and leads to mDRX.

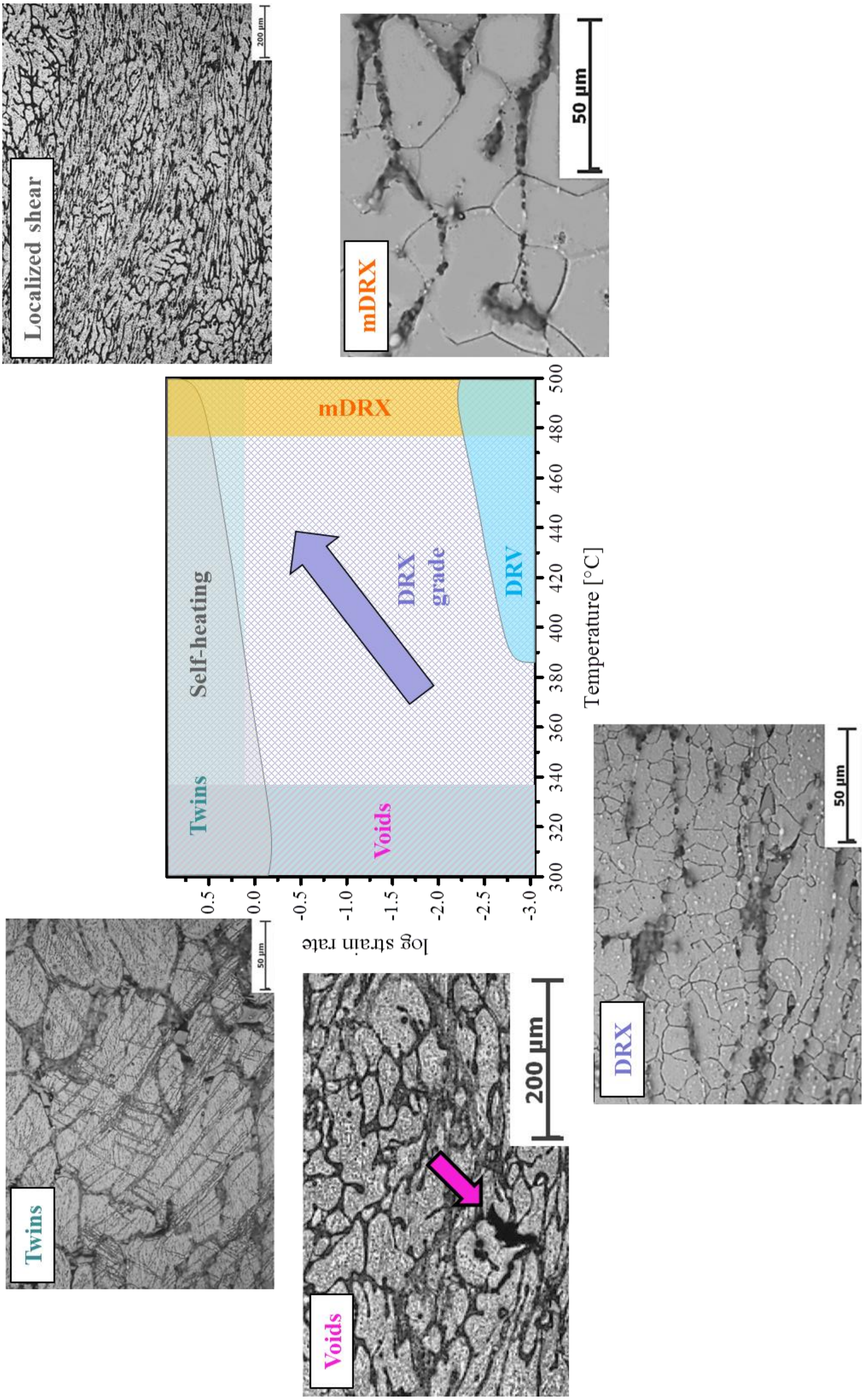

Figure 100. Microstructural map of the deformation behaviour occurring in DieMag422.

5.2 Titanium

The as received microstructure of the alloy consists of a large amount of β-phase (70 vol%), as seen in the light optical micrographs and in the maps obtained from EBSD measurements. Due to this large amount of β-phase ranging from 85 vol% at 763°C to 100 vol% above T_β , it is expected that most of the restoration mechanisms during hot deformation take place in this soft phase. On the other hand, the α-grains behave as hard particles and therefore pin the dislocation and the HAGB movements and thus, the β subgrains cannot grow beyond the α-grains.

The deformation mechanisms of this alloy is analysed according to strain rate ranges.

5.2.1 Low strain rate (0.001–0.1 s^{-1}) range

At low strain rates, the flow curves show a sharp peak stress at a relatively low strain (< 0.03) for all temperatures. Discontinuous yielding is visible for all the strain rates. This phenomenon was also observed in Ti55531 [83] and in similar alloys [108]. The yielding is attributable to the interaction between the solutes and mobile dislocations. In this work, small solutes are Fe and O.

The analysed microstructures show that the grain boundaries are serrated with the amplitude of the waves decreasing by increasing the strain rate. Furthermore, it is observed from the EBSD measurements that new grains and subgrains have the size of the amplitude of the serrated boundaries. The obtained EBSD measurements shown in Figure 58 a), Figure 59 a), Figure 60 a) and Figure 61 a), b) confirm that subgrains are formed at low strain rates for all the temperatures. The LOM picture in Figure 55 shows that the original β grains are elongated due to the compression for a strain rate of 0.001 s^{-1} and a temperature of 803°C. Furthermore, the fine dispersed α-phase can hinder the migration of β grains. The α-grains at the grain boundary are indicated with a white arrow in Figure 101.

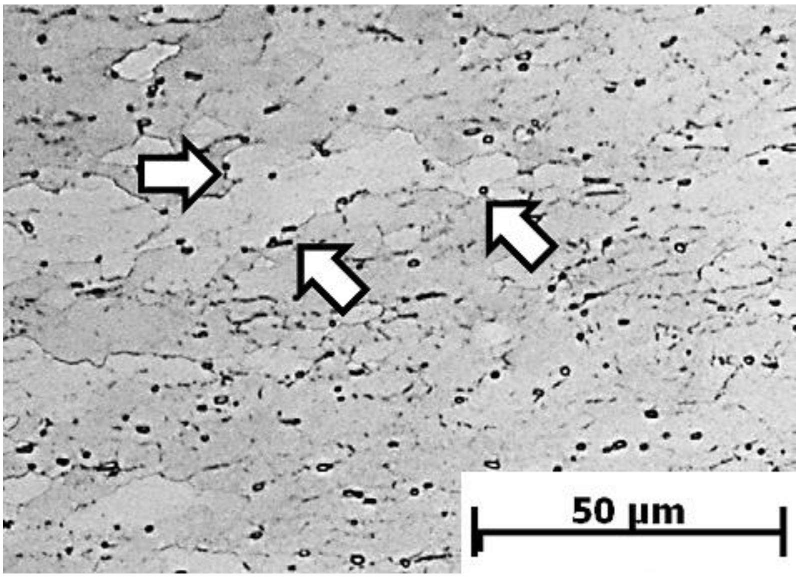

Figure 101. α-grains depicted in black, in a sample deformed at a strain rate of 0.001 s^{-1} and at a deformation temperature of 803°C. The white arrows indicate α-grains at the prior β grain boundaries. Pictures taken at a local strain of 1, load direction is vertical (LOM).

Another restoration mechanism which occurs during low strain rate deformation, although in a lower amount, is gDRX. The results are new small grains of subgrain size or smaller, formed along the prior β grain boundary after large strain. This phenomenon was especially observed in the presence of α-phase. White circles in Figure 102 indicate some of these new grains built by gDRX, as described in [22]. The recrystallized grains are formed surrounded by high angle grain boundaries provided by prior β grain boundaries and phase boundaries.

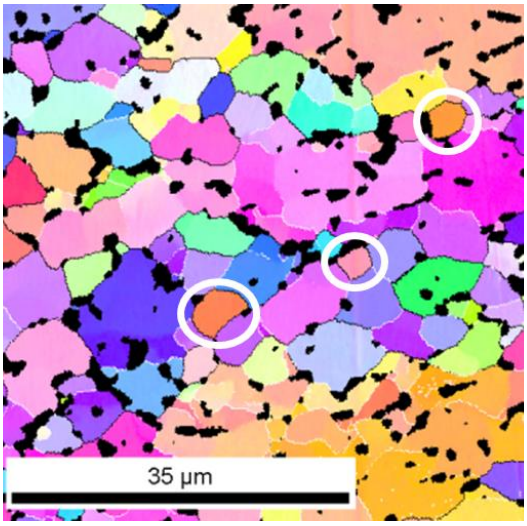

Figure 102. EBSD measurement at 763°C, 0.001 s^{-1}; white circles indicate gDRX and α-phase is depicted black.

Below the T_β, the *m* values are larger compared to the β-field. Finally, it was observed that at low strain rates α-phase dissolves during the deformation as reported in [109]. A lower content of α-phase at low strain rates compared to higher strain rates can be related to: 1) a modification of the equilibrium conditions due to the deformation and to 2) an acceleration of the dissolution of α if the material is not in equilibrium before deformation. The slow diffusion process of large and slow elements like molybdenum can still produce a transformation of α into β if the time of the pre-heating is not long enough [110]. This phenomenon is furthermore presented in the work of Jones et al. [84]. A reduction in the α-phase was seen for a temperature of 835°C due to an increase of soaking time. In addition the work of Cotton et al. [111] is referred, in which it is mentioned that Ti5553 contains slow diffusion elements, as Ti55531 in this work, and that this elements postpone the onset of precipitation and inhibit coarsening.

5.2.2 High strain rate (0.1–10 s^{-1}) range

The flow curves for the high strain rate range show more intense softening than for the low strain rate range. Discontinuous yielding is present in the flow curves of Figure 53, similar to the yielding observed at low strain rates.

The deformation mechanisms observed at high strain rates take place mainly in the β-field. Figure 56 shows serrated prior β HAGB. The waves at these high strain rates show smaller amplitudes compared to them at low strain rates. Furthermore, a large misorientation gradient is measured from the middle of the grain toward the boundary.

It can be stated that DRV and cDRX mechanisms are occurring both at high strain rates. On the one hand, the developed subgrain structure can be seen only close to prior grain boundaries. On the other hand, new recrystallized grains can be found along the prior β HAGB, which indicates cDRX by progressive lattice rotation. Figure 103 shows a detail of the HAGB, in which small new grains are formed. The formation of new grains due to cDRX increases with increasing strain rate, what was investigated in Figure 61.

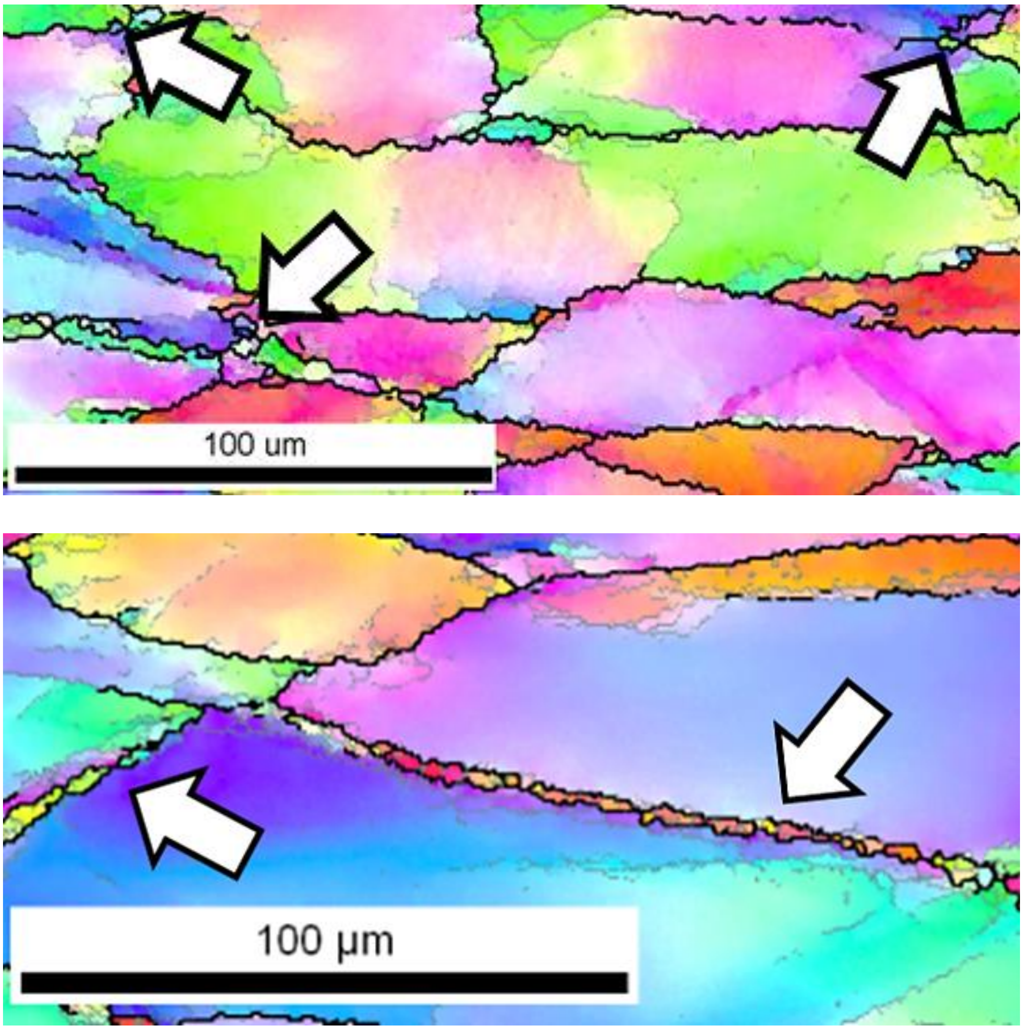

Figure 103. White arrows indicating small grains at the β HAGB.

A microstructural map of the mechanisms which occur during the hot deformation of Ti55531 is shown in Figure 104. Areas are showing restoration mechanisms like DRV, DRX, and instability parameters related to the temperature and strain rate.

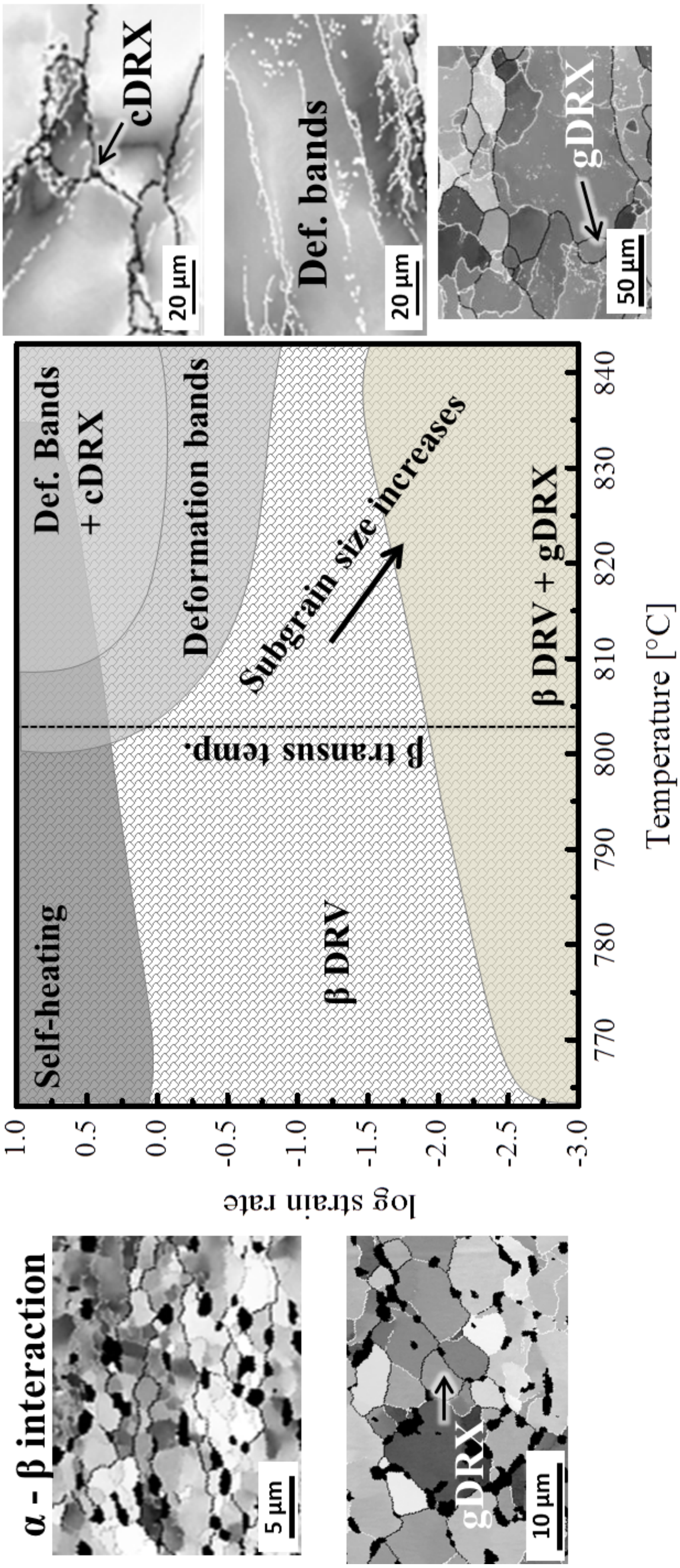

Figure 104. Microstructural map of mechanisms during hot deformation depending on temperature and strain rate.

5.3 Steel containing nitrogen

The flow curves show softening at all temperatures for strain rates below 1 s^{-1}, whereas the flow curves obtained after deformation at a strain rate of 100 s^{-1} and for all temperatures show that no steady state is reached. The same trend is observed for deformation carried out below a temperature of 850°C for 10 s^{-1} as well. A similar trend is observed in the work of Rao et al. [112] for a low-carbon steel for a temperature of 900°C and 1000°C and a strain rate of 8 s^{-1}. Additionally, a peak can be identified for the lowest strain rate for all temperatures although it is more visible at temperatures higher than 850°C. The peaks are broad and indicate DRX. As recovery is slow in austenite, DRX will occur once a critical strain and temperature is achieved [44]. However, DRX occurs only at temperatures ≥ 850°C and therefore, the little softening effect seen for temperatures below, can be explained by the formation of the soft ferrite phase.

The microstructure observed for the highest temperature (1000°C) and lowest strain rate (0.01 s^{-1}) shows coarser grains than at lower temperatures and additionally no ferrite is present. The micrograph obtained for the lowest temperature of 750°C and a strain rate of 0.01 s^{-1} shows finer, more globular grains and ferrite is present. The ferrite appears in a globular shape for this low deformation rate and it is built during the deformation.

At high strain rates the obtained micrographs show a large amount of ferrite even at high temperatures, showing a discrepancy to what is expected high above A_{r3}. On the one hand, for the deformation at the highest strain rate (100 s^{-1}) and the lowest temperature (750°C) a large amount of ferrite is present. For the other conditions (1000°C and 100 s^{-1}) still ferrite is present, although the amount is less and the shape is different. The formation of ferrite during cooling can be explained using Figure 105.

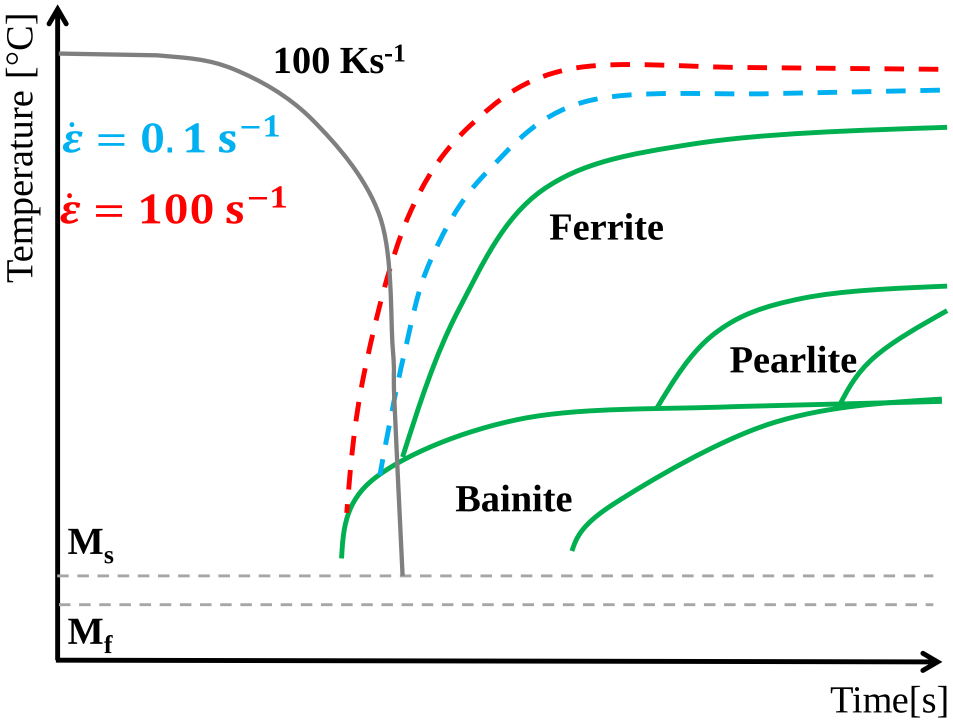

Figure 105. Schema of a CCT diagram to show the shift of the ferrite nose.

In this schematic continuous cooling transformation (CCT) diagram the transformation temperature lines are shown of a sample without deformation (green) and of a sample deformed at a T > A_{r3} for low and high strain rates. Due to both a grain refinement of austenite by DRX and stored energy due to plastic deformation, the transformation temperatures are shifted to shorter times. If the cooling rate is the grey line, for a non-deformed condition no ferrite is formed, whereas for the high strain rate ferrite is present due to a shift of the ferrite nose to the left side in the CCT diagram. Therefore, the higher amount of ferrite will be formed at the higher strain rate during cooling, even at 1000°C of deformation.

5.4 Steel containing vanadium

A peak can be seen in the flow curves deformed between 0.01 and 1 s^{-1} which is shifted to lower strain values with increasing temperature due to the mechanism of DRX occurring at high temperatures. An example is given in Figure 106 for a strain rate of 0.01 s^{-1} in a temperature range of 750–1150°C. The blue circles indicate the peak and the red arrow the shift to low strain values.

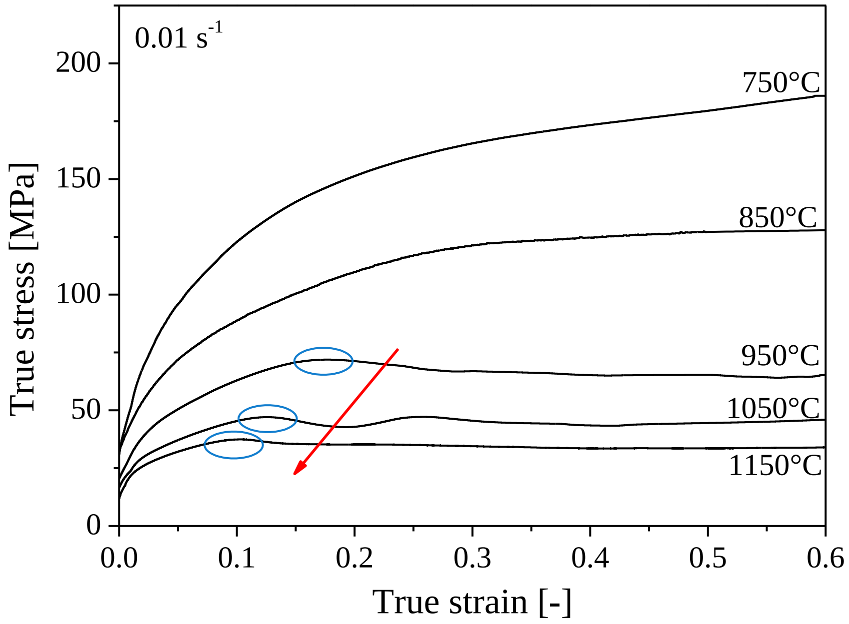

Figure 106. Flow curves for a strain rate of 0.01 s^{-1} as a function of the temperature.

The reason therefore is that the rate of the work hardening, which is higher at high strain rates and low temperatures, slows down the rate of work softening and therefore the peak and the onset of steady state flow is shifted to higher strain values [78].

This trend observed in the flow curve, is confirmed if looking to the LOM investigations. With a temperature > 950°C refinement of the austenite due to DRX takes place. In Figure 107 a correlation between the grain sizes with the *Z* parameter is given. However, it is difficult to obtain the correct grain size using LOM pictures due to phase transformation occurring during the deformation. For determining the equation showing the relationship between DRX grain size and *Z*, the points of 750°C and 850°C were not taken into account. At 750°C no DRX occurs and therefore, the data points are on different position than the values obtained for deformation at higher temperatures.

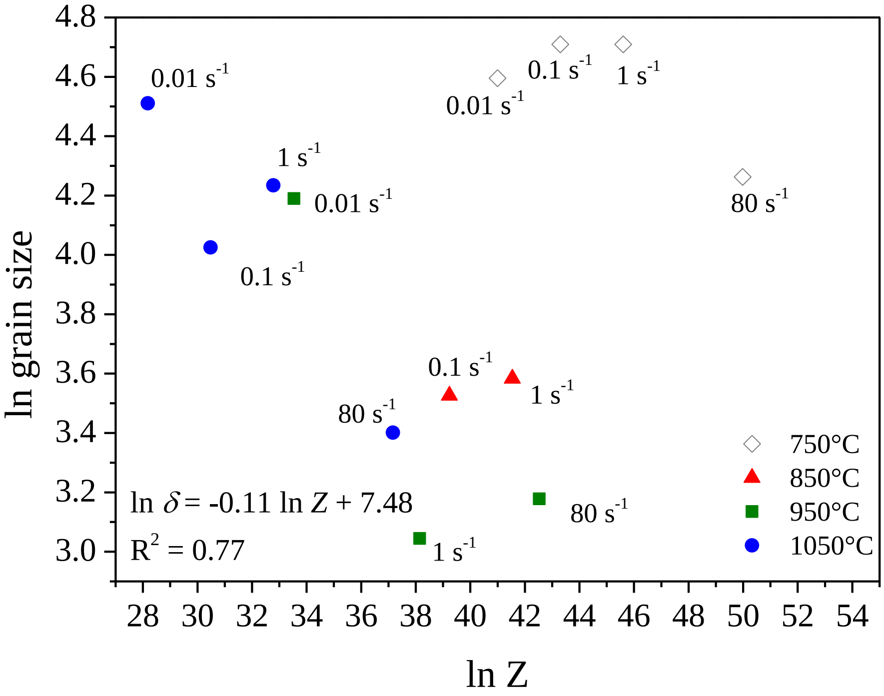

Figure 107. Correlation of the grain size with *Z* for all measured points.

The flow curves in the high strain rate range are dominated by strain hardening and some oscillations in the flow curves. The obtained micrographs show deformation bands for all strain rates at 750°C and for strain rates > 0.1 s^{-1} at 850°C and elongated austenite appears for temperatures below 850°C. Furthermore DRX of austenite takes place above 950°C. For low temperature deformation at 750°C fine ferrite is present at the grain boundaries. As mentioned in [102], the formation of ferrite occurs during the deformation.

Figure 108 shows the dependency of *m* on the strain, the strain rate and the temperature. For a temperature of 950°C a large difference in the *m* value for a low and a high strain rate can be seen, whereas the difference for the 850°C is not that large. Furthermore, the *m* values of 950°C are higher for the lower strain rate. The reason for the high values at high temperatures and low strain rates can be correlated to the slow strain rate, which gives the material time for diffusion and on the other hand another reason is the DRX which is occurring.

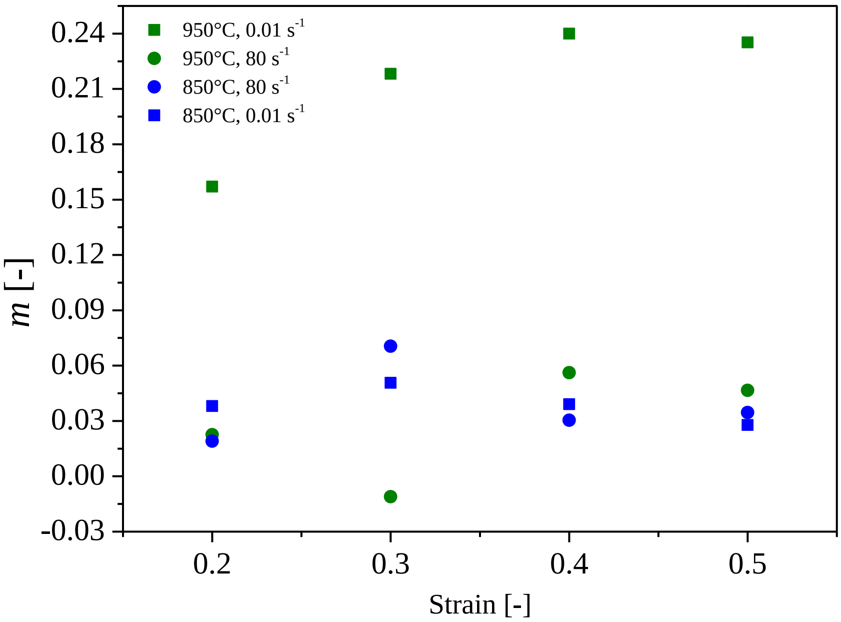

Figure 108. ***m*** **as a function of the strain, the strain rate and the temperature.**

Finally, Figure 109 shows a microstructural map of the mechanisms which can occur during the hot deformation related to the temperature and strain rate. Ferrite formation appears at lowest temperature seen in blue. Deformation bands in austenite are present between 750–850°C (in green). DRX of austenite occurs above 850°C and the grain size is increasing in direction of higher temperatures and lower strain rates. A temperature increase due to self-heating was measured at high strain rates.

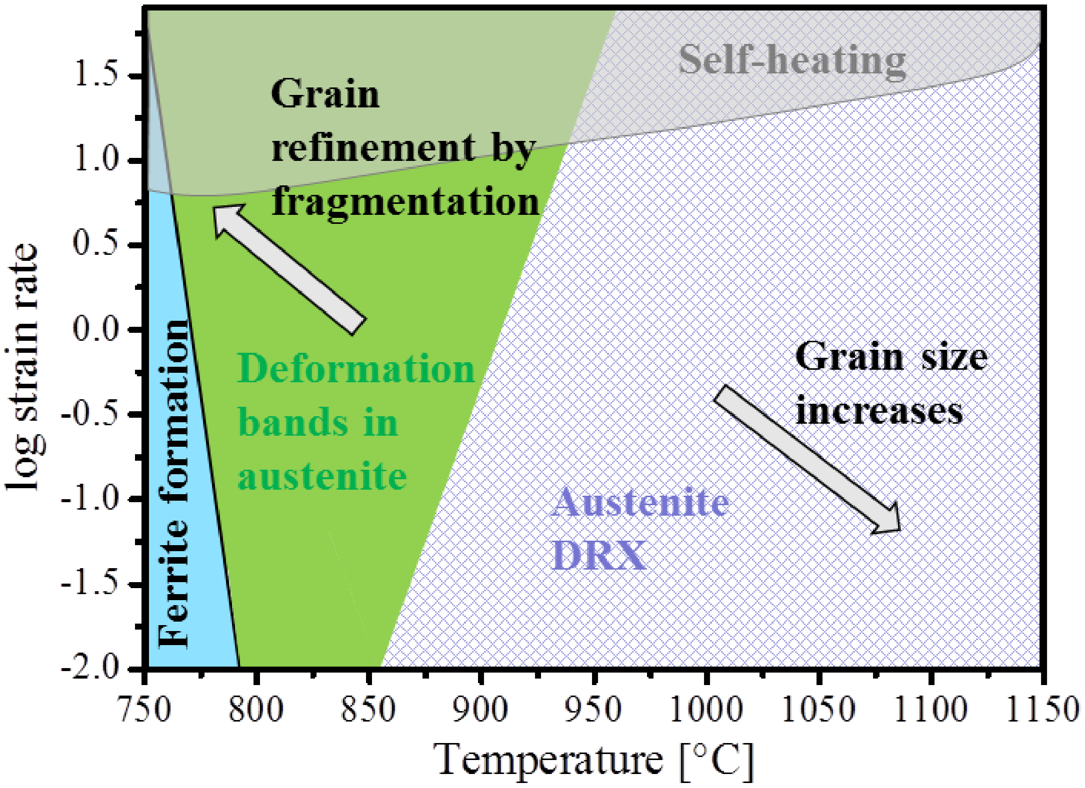

Figure 109. Microstructural map of the mechanisms occuring during the hot deformation related to the temperature and the strain rate.

5.5 Processing maps

This chapter discusses the processing maps and is separated into two sub chapters. The first one refers to the data treatment done to build the processing maps, while the second part deals with the usability and validity of the processing maps.

5.5.1 Data treatment

In this section, different approaches of data treatment used in the calculation of processing maps and instability parameters are discussed.

The instability parameter α_{SJ} developed by Semiatin and Jonas contains the derivative of the stress with respect to the strain for the calculation of the strain hardening term. The method used here was to fit the stress vs. strain curve with a polynomial followed by the derivation of the fitted curve. Figure 110 shows the sensitivity of the fitting method using polynomial fits of 2nd, 3rd or 4th order, and a partially fitting of the stress strain curve on the final result, meaning on the instability map.

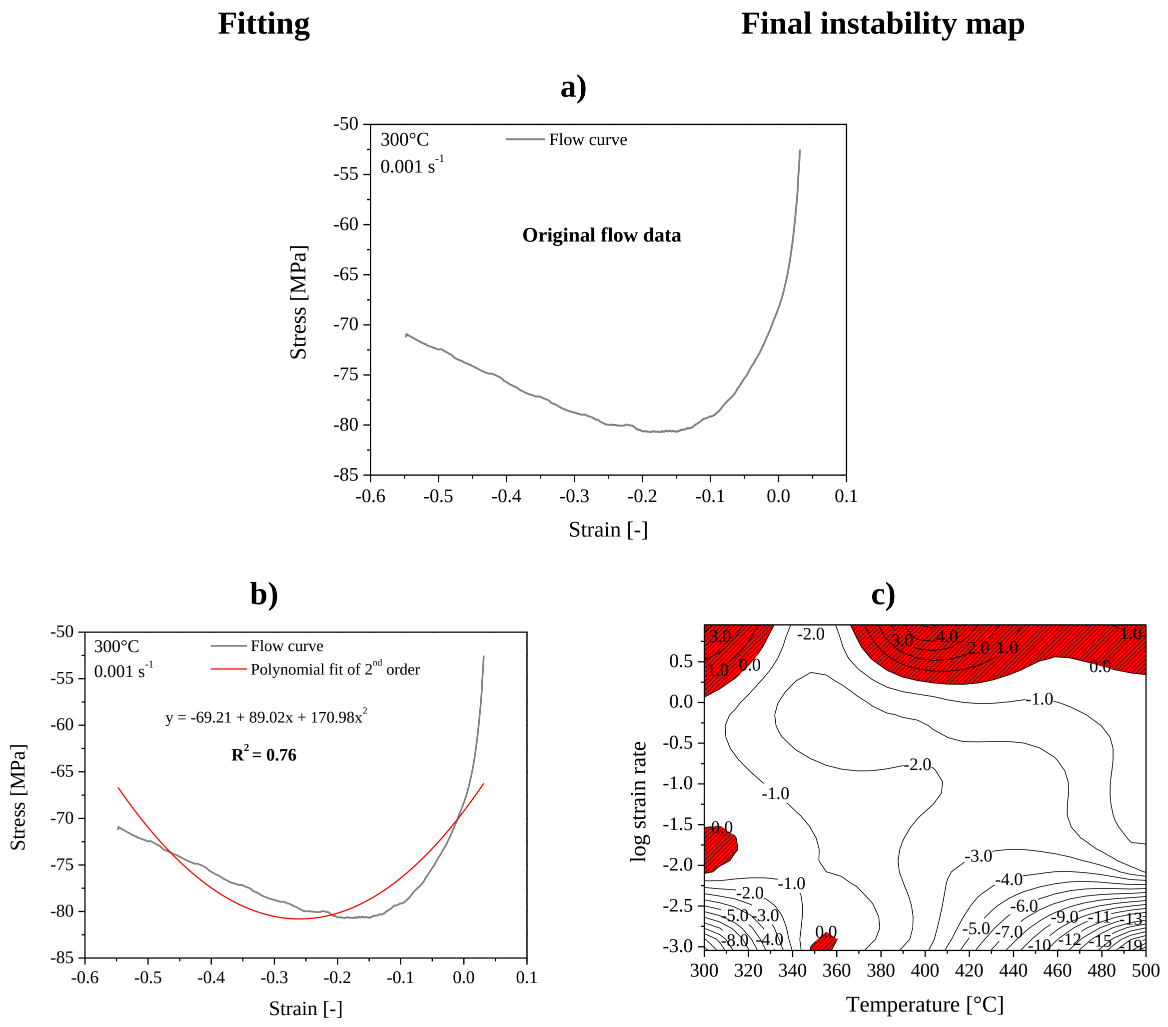

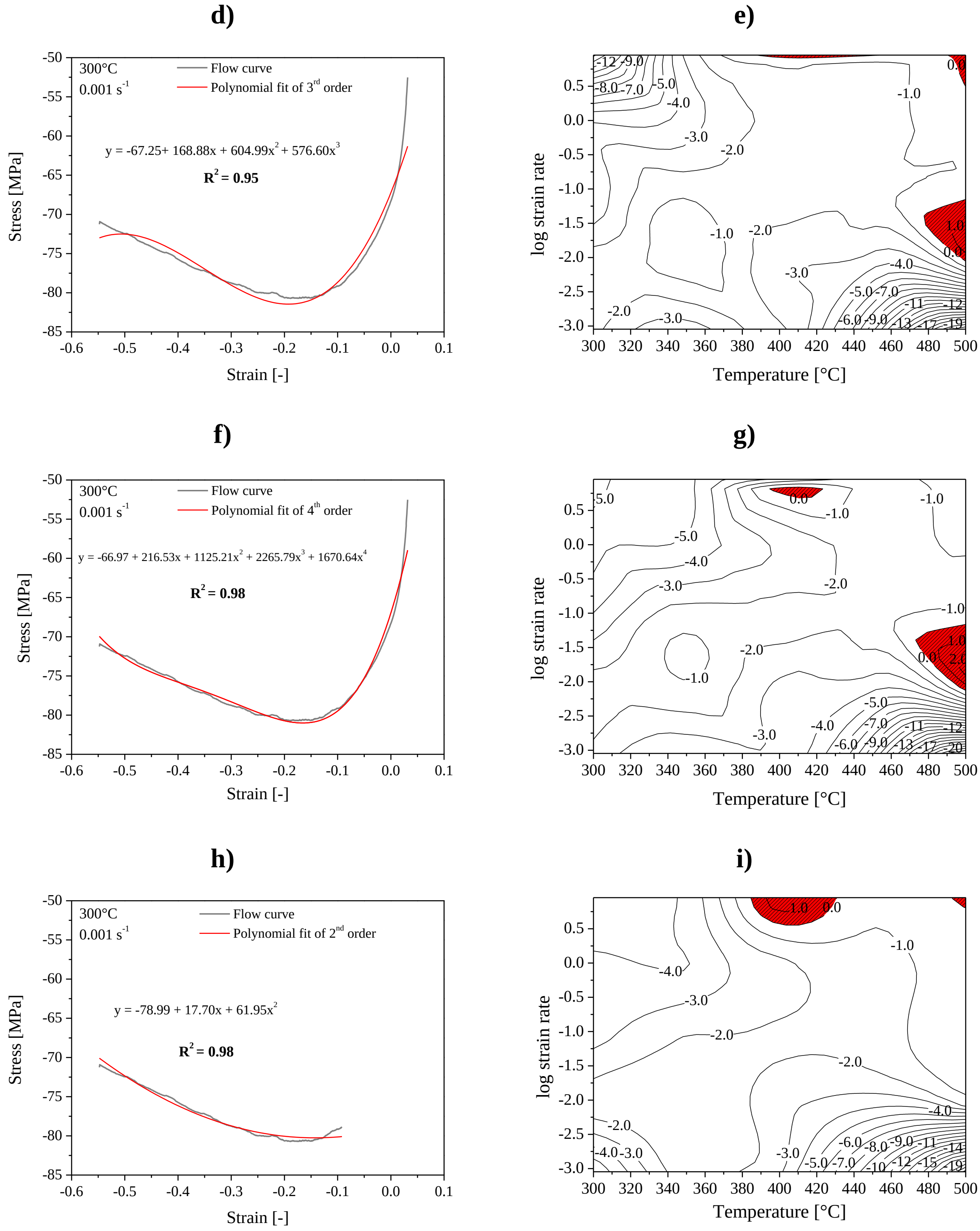

Figure 110. Optimizing the fitting operation to calculate the strain hardening term. Red zones represent $\alpha_{SJ} > 0$ meaning instability of the flow. The example is using the flow data of the Mg-alloy deformed at 300°C, a strain rate of 0.001 s^{-1} and a strain of 0.4.

For a polynomial fit of second order the lowest R^2 of 0.76 was obtained in Figure 110 b). Therefore, the resulting instability areas (Figure 110 c)) are at high strain rates for low as well as for high temperatures, at moderate strain rates and low temperature, and at low strain rates and moderate temperatures. The second approach using a polynomial fit of third order (Figure 110 d)) gives a much higher R^2 than before, with a value of 0.95. However, the slope in the fitted curve reproduces hardening at high strains. Thus, instability areas are predicted, such as at high temperatures from moderate to high strain rates, which cannot be explained using microstructure observations. The fit of 4th polynomial order results in a good description of the flow curve with a R^2 of 0.98 (Figure 110 f)) and a similar tendency in the region of instabilities as in the polynomial fit of 3rd order. For the investigations in Figure 110 h) a R^2 of 0.98 and instabilities only at high strain rates were obtained.

Finally, it has to be mentioned that at high temperatures and high strain rates, wedge cracking was observed close to the intermetallic phases.

5.5.2 Usability and validity of maps

To discuss the usability of the processing maps, we should ask first what is the physical meaning of the values of dissipation efficiency η and of the strain rate sensitivity m?

The strain rate sensitivity m measures the influence of thermal activation, and is related to the grade of dependency of the flow stress with the strain rate. Furthermore, the strain rate is directly correlated to the time. Therefore, diffusion controlled processes which occur during the deformation such as dynamic recovery, dynamic recrystallization and dynamic phase transformation need time, meaning that they are strongly influenced by the strain rate, meaning that m is large. On the other hand, if m is small, the process taking part during the deformation should be less dependent on the strain rate, meaning less dependent on time, meaning that it is less controlled or not controlled at all by diffusion. Some examples of these last processes are twinning, deformation bands and brittle cracking.

In this work an apparent m value was used, unless it is explicitly mentioned. This means, that uncorrected values of the stresses with respect to the temperature were used to calculate m. As consequence of self-heating, it could happen for example, that two flow curves are crossing, as shown in Figure 31 for 400°C, and then negative m values are the result. This can be used to follow the tendency of adiabatic flow and to interpret correctly the developed microstructure.

To compare apparent with non-apparent m values, a temperature correction of the flow stress was carried out using Equation 57 [113]. The actual temperature was measured during the compression tests using thermocouples welded on the sample. Thus, the ΔT as a function of the strain was obtained as the difference between the actual and the target temperature.

$$\sigma^I(\varepsilon,\dot{\varepsilon},T) = \sigma(\varepsilon,\dot{\varepsilon},T) - \left.\frac{\partial\sigma(T)}{\partial T}\right|_{\varepsilon,\dot{\varepsilon}} \Delta T \qquad \textbf{Equation 57}$$

Figure 111 shows the comparison of the flow curves for 400°C for uncorrected and corrected stress values.

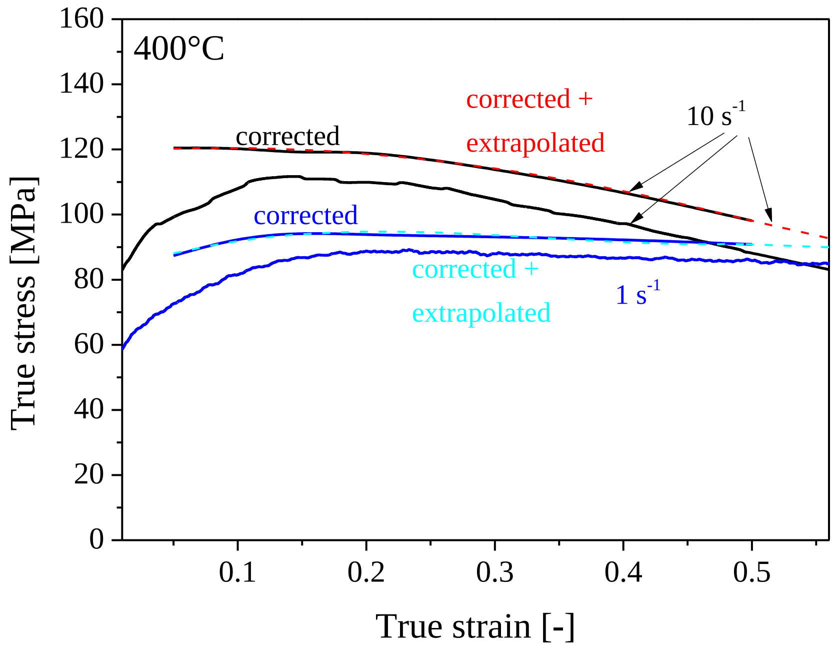

Figure 111. Comparison of uncorrected and corrected stress values for Mg deformed at 400°C and at strain rates of 10 s^{-1} and 1 s^{-1}.

It can be seen, that the corrected and extrapolated flow curve is not crossing the flow curve for the lower strain rate anymore. Furthermore, the *m* values calculated using the flow curves with the corrected stress values are shown in Figure 112 for a strain of 0.5.

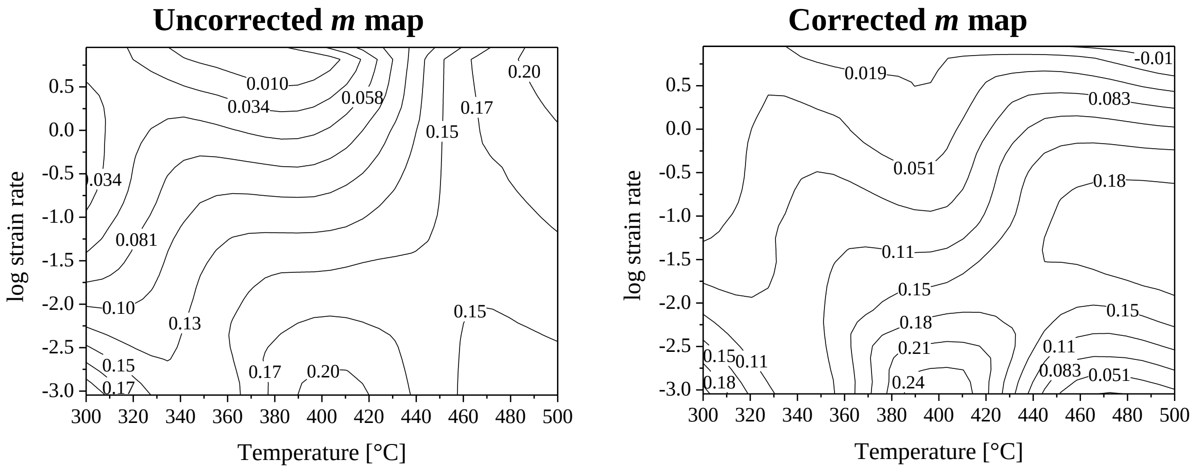
Uncorrected *m* map

Corrected *m* map

Figure 112. *m* maps for a strain of 0.5 for uncorrected and corrected values.

The direct microstructural interpretation of the *m* values, as already described is:

- high *m* value is correlated to diffusional mechanisms as there are for example DRX or also the transformation of austenite into ferrite phase. Therefore, it has to be considered in the usage of processing maps, that if there is a high *m* value it is not always DRX which is represented. Additionally, it is not possible to make a separation of cDRX and gDRX based on the obtained *m* values.
- Small *m* value and *m* = 0 means that the process taking place during the hot deformation is less or not controlled by diffusion.

Furthermore, *m* can be consulted for comparing the flow behaviour of different materials. Figure 113 shows a sketch of flow curves for 2 materials, material 1 in green and material 2 in blue, for a given strain. The values can be plotted as in the diagram on the right hand side and *m* can be calculated out of the slope, in this example a constant value.

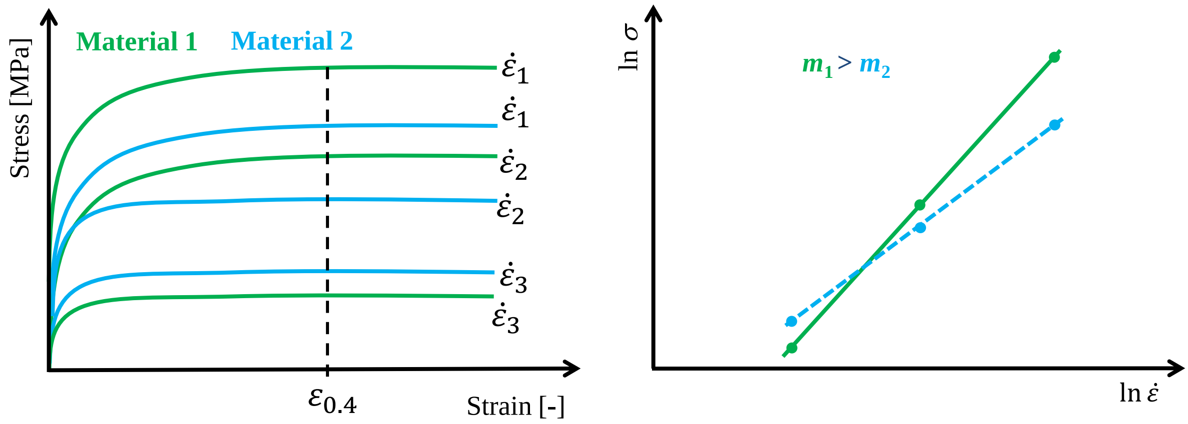

Figure 113. Determination of the strain rate sensitivity *m*.

In the case of using η_P, the discussion is the same as for *m*, because η_P is calculated directly using *m* (Equation 13).

The last value used to describe the microstructural changes η_{M+R} in Equation 16 is not that directly related to the strain rate sensitivity at the first sight, however it follows the same tendency as *m* since it is the integral of stress as a function of strain rate, as seen in Equation 15.

Consequently, it would be enough if using only the *m* maps for the prediction and explanation of microstructural changes during hot deformation.

In addition, it has to be noted that the prediction "low or high" η or *m* values is relative, since if a processing map is taken into account, the highest occurring value is a high value which can be a moderate value in another map.

Additionally, the α_{SJ} map was also calculated using the corrected flow curves. Figure 114 shows the comparison between the usage of the uncorrected and the corrected flow data. However, the calculation of the strain dependent term for the α_{SJ} map is not accurate enough because only a few points were used to rebuild the flow curve.

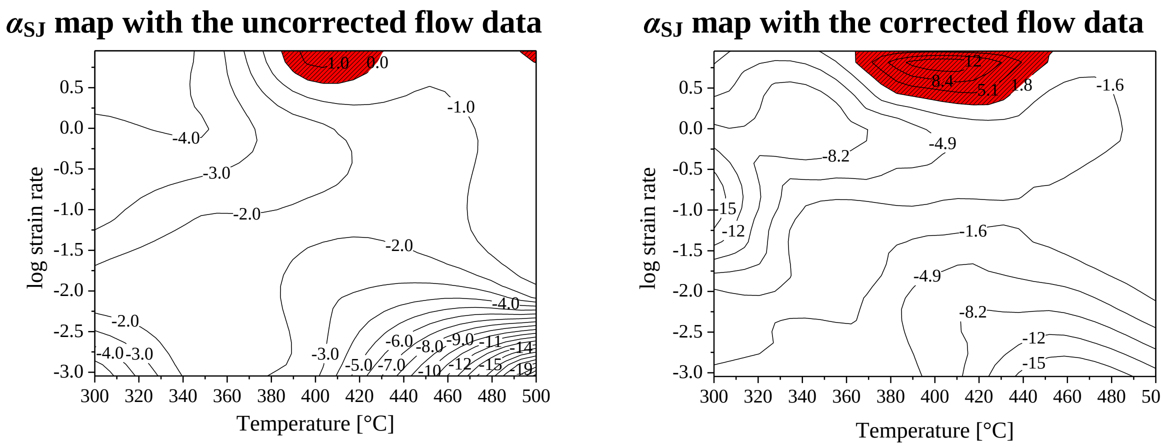
α_{SJ} map with the uncorrected flow data

α_{SJ} map with the corrected flow data

Figure 114. Comparison between two α_{SJ} maps for using uncorrected and corrected flow data.

Three instability parameters based on the DMM (ξ, κ, κ_j) and one not based on DMM (α_{SJ}) were used in this work. The parameters used by DMM are based on the continuum principles as applied to large plastic strain, which was proposed by Ziegler. However, this approach is only guilty for a constant temperature and strain and furthermore, the material has to be homogeneous. This means, if for example there are particles in the material the approach is not applicable. Finally, Ziegler can be only used for one point in the material, where strain and temperature is constant.

To use the inequality equation (Equation 17) for the DMM, the D is equal to J. The J is derived from Equation 7 in which $P = G + J$, and G is correlated to the heat and J is related to the microstructural changes. The equation can be explained as a maximum dissipation, which is possible depending on the strain rate and if this term $\frac{D}{\dot{\varepsilon}}$ is higher than $\frac{\partial D}{\partial \dot{\varepsilon}}$ instability occurs. However, as explained in the state of the art, if the separation of G and J is not correct, not only η but also the instability parameters will be erroneous.

The parameters ξ and κ are a function of the strain rate sensitivity m, which is dependent on the strain rate, although taken as a constant for the calculation of ξ. κ_j is directly derived from the DMM definition and therefore, avoids the usage of m.

The further instability parameter α_{SJ} has two parts. On the one hand the constant strain rate strain hardening rate γ' and on the other hand again the strain rate sensitivity parameter is considered to calculate α_{SJ}. The constant strain rate strain hardening rate γ' has two main influences: a strain dependent term which is negative in the case of flow softening, and a temperature dependent one, which is negative due to thermal softening. Instabilities are predicted in the theory if α_{SJ} is positive, and for titanium proved to predict instabilities if $\alpha_{SJ} > 5$. Although it is not defined, what happens in the case of m negative? Table 12 shows the influence of the separated parameters on the final α_{SJ}. From this table it can be observed that the last row is inconsistent and cannot be used as a stability criterion.

Table 12. Influence of the γ' and the m parameter on α_{SJ}.

γ'-1	m	α_{SJ}	Stability/Instability
<0	>0	negative	stability
<0	<0	positive	instability
>0	>0	positive	instability
>0	<0	negative	stability

A further point which has to be considered is the dependency on the strain. Instability occurs at a certain strain, and therefore, if once instability occurred, it has to be seen in the maps as well at higher strains. There should be no physical reason why at higher strains instabilities disappear.

The usability and the validity of processing maps based on DMM and different instability parameters are investigated separately for the four different used alloys. Based on the discussion of m values and diffusion controlled mechanisms, and of the instabilities, “good results” will mean that the calculated values out of the processing maps are in agreement with the obtained LOM or EBSD measurements.

However, the usage of *m* would be the one with the best physical foundation and the reason, why some results are not as good is because the usage of “moderate” and “high” value is subjective.

For the following summaries given in Table 13, Table 15, Table 17, and Table 19 it has to be mentioned that the fact that identical results are reported for η_P and *m* is a triviality due to their direct relationship in Equation 13.

5.5.2.1 Magnesium

Table 13 shows a summary and the results of the used models related to dissipation efficiency values and the strain rate sensitivity *m*. Therefore, the processing maps are separated into 6 areas, regarding low and high strain rate ranges as well as low, moderate, and high temperature ranges. Low temperature means up to 360°C, moderate between 360°C and 440°C, and high temperature is higher than 440°C. Furthermore, the obtained microstructure is mentioned shortly. The trend observed in the processing maps and described in the table is similar for different strains, however the values are decreasing with increasing strain.

Table 13. Summary of the Mg results.

Range	Microstructure	η_P	η_{M+R}	m
Low $\dot{\varepsilon}$ and low T.	Some DRX grains	High–mod. (with increasing $\dot{\varepsilon}$)	High–mod. (with increasing $\dot{\varepsilon}$)	High–mod. (with increasing $\dot{\varepsilon}$)
Low $\dot{\varepsilon}$ and mod T.	0.001 s^{-1}: some big new DRX grains 0.1 s^{-1}: some small new DRX grains	High–mod. (with increasing $\dot{\varepsilon}$)	High and mod.	High–mod. (with increasing $\dot{\varepsilon}$)
Low $\dot{\varepsilon}$ and high T.	0.001 s^{-1}: no DRX grains 0.1 s^{-1}: big new grains	Low–mod. (with increasing $\dot{\varepsilon}$)	Low–mod. (with increasing $\dot{\varepsilon}$)	Low–mod. (with increasing $\dot{\varepsilon}$)
High $\dot{\varepsilon}$ and low T.	Twins, no DRX grains	Low	Mod–low (with increasing $\dot{\varepsilon}$)	Low
High $\dot{\varepsilon}$ and mod T.	Full DRX	Mod.	High–mod. (with increasing $\dot{\varepsilon}$)	Mod.
High $\dot{\varepsilon}$ and high T.	Full DRX or mDRX	High–mod. (with increasing $\dot{\varepsilon}$)	High	High–mod. (with increasing $\dot{\varepsilon}$)

In general it can be stated that the prediction of the three different approaches is good and follows the same tendency. If the microstructure shows DRX grains, as for high strain rate and moderate temperature, high η and *m* values are the result. On the other hand, twinning is correlated to low values of η and *m*. Special care should be taken for mechanisms which occur after the deformation, such as mDRX, since this is not visible in the flow curves. The obtained micrographs however, show the mDRX grains and therefore, processing maps cannot predict correctly.

The instability correlation of models and micrographs for Mg is shown in Table 14. The main instabilities which are occurring are voids, which can be seen in Figure 95. Two different types of voids are present. If the temperature is low particles themselves crack, and for higher temperature the surrounding area, the matrix cracks. Furthermore, self-heating occurs at the high strain rates that can lead to shear bands.

The different instability models vary significantly. Prasad and κ_j are showing the best results. α_{SJ} is showing instability at high strain rates and moderate temperatures and m is showing mostly no instability although in some regions damage was seen in the material.

Table 14. Comparison of different instability parameters for Mg.

Range	**Microstructural instabilities**	$\xi < 0$	$\kappa < 0$	$m < 0$	$\kappa_j < 0$	$\alpha_{SJ} > 0$
Low $\dot{\varepsilon}$ and low T	Voids, deformation bands	$\dot{\varepsilon} > 0.01\ s^{-1}$	$\dot{\varepsilon} > 0.003\ s^{-1}$	-	$\dot{\varepsilon} > 0.006\ s^{-1}$	-
Low $\dot{\varepsilon}$ and mod. T	-	-	$\dot{\varepsilon} > 0.003\ s^{-1}$	-	-	-
Low $\dot{\varepsilon}$ and high T	-	-	-	-	-	-
High $\dot{\varepsilon}$ and low T	Voids (very few)	$\dot{\varepsilon} > 0.1\ s^{-1}$	$\dot{\varepsilon} > 0.1\ s^{-1}$	-	$\dot{\varepsilon} > 0.1\ s^{-1}$	-
High $\dot{\varepsilon}$ and mod. T	Voids (very few)	$\dot{\varepsilon} > 0.1\ s^{-1}$	$\dot{\varepsilon} > 0.1\ s^{-1}$	-	$\dot{\varepsilon} > 0.1\ s^{-1}$	$\dot{\varepsilon} > 1\ s^{-1}$
High $\dot{\varepsilon}$ and high T	Voids (very few)	$\dot{\varepsilon} > 1\ s^{-1}$	$\dot{\varepsilon} > 0.1\ s^{-1}$	-	$\dot{\varepsilon} > 1\ s^{-1}$	-

5.5.2.2 Titanium

For the Ti-alloy, Table 15 will summarize the obtained results. At low strain rates and low temperatures, as well as at high strain rates and high temperatures DRX occurs and high values should be seen in the processing maps. Low temperature means a range of 763–790°C, a moderate temperature is between 790°C and 815°C and high temperature is above 815°C.

Table 15. Summary of the Ti results.

Range	**Microstructure**	η_P	η_{M+R}	m
Low $\dot{\varepsilon}$ and low T.	Subgrains: DRV low amount of new grains: gDRX;	Highest	High (with increasing $\dot{\varepsilon}$: highest)	Highest
Low $\dot{\varepsilon}$ and mod T.	Subgrains: DRV	High	Mod–high (with increasing $\dot{\varepsilon}$: highest)	High
Low $\dot{\varepsilon}$ and high T.	Subgrains: DRV	High	Mod–high (with increasing $\dot{\varepsilon}$)	High
High $\dot{\varepsilon}$ and low T.	Subgrains: DRV	Mod–low	High for 0.1 s^{-1}; High–mod. (with	Mod–low

			increasing $\dot{\varepsilon}$)	
High $\dot{\varepsilon}$ and mod T.	Subgrains: DRV	Mod–low (with increasing $\dot{\varepsilon}$)	High for 0.1 s^{-1}; mod. > 0.15 s^{-1}	Mod–low (with increasing $\dot{\varepsilon}$)
High $\dot{\varepsilon}$ and high T.	Deformation bands, some subgrain boundaries, small cDRX grains at boundaries	Moderate	High	Moderate

The model which gives the best agreement for the Ti-alloy is the one of Murty and Rao based on Table 15.

In Table 16 the obtained instability parameters are given for the Ti-alloy.

Table 16. Comparison of different instability parameters for Ti.

Range	**Microstructural instabilities**	$\xi < 0$	$\kappa < 0$	$m < 0$	$\kappa_j < 0$	$\alpha_{SJ} > 0$
Low $\dot{\varepsilon}$ and low T	-	-	$\dot{\varepsilon} > 0.01\ s^{-1}$	-	Around 0.1 s^{-1}	-
Low $\dot{\varepsilon}$ and mod. T	-	-	$\dot{\varepsilon} > 0.01\ s^{-1}$	-	-	-
Low $\dot{\varepsilon}$ and high T	-	-	$\dot{\varepsilon} > 0.01\ s^{-1}$	-	-	ε of 0.5 + 0.6
High $\dot{\varepsilon}$ and low T	-	$\dot{\varepsilon} > 0.1\ s^{-1}$	$\dot{\varepsilon} > 0.1\ s^{-1}$	-	$\dot{\varepsilon}$: 0.1 - 1 s^{-1} + < 775°C; 785°C + 10 s^{-1}	$\dot{\varepsilon} > 5\ s^{-1}$ at low ε
High $\dot{\varepsilon}$ and mod. T	Micro-deformation bands	$\dot{\varepsilon} > 0.1\ s^{-1}$	$\dot{\varepsilon} > 0.1\ s^{-1}$	-	-	$\dot{\varepsilon} > 5\ s^{-1}$ at high ε
High $\dot{\varepsilon}$ and high T	Micro-deformation bands	< 825°C and > 3 s^{-1}	$\dot{\varepsilon} > 0.1\ s^{-1}$	-	$\dot{\varepsilon}$: 3 s^{-1} + T: 815–835°C	-

The best result is given for the instability model proposed by Prasad. The model of Murty and Rao is showing wrong results and the *m* map is showing stability everywhere although micro-deformation (inter-granular) bands were observed for high strain rates. The instability values of κ_j are working well, but at the lowest strain rate and temperature it is showing instability where no instability was found in the micrographs. The parameter α_{SJ} is working in most of the cases. However, it is showing no instability for the highest strain rate and the highest temperature, although deformation bands are visible.

5.5.2.3 Steel containing nitrogen

For the steel alloyed with nitrogen a summary is given in Table 17. At low temperatures and low strain rates ferrite formation is obtained using LOM. Therefore, low to moderate values are presented in all three different approaches. DRX starts to occur at temperatures higher than 850°C. Low temperature is below 825°C, moderate temperature between 825–925°C and high temperature above 925°C.

Table 17. Summary of the steel alloyed with N.

Range	Microstructure	η_P	η_{M+R}	m
Low $\dot{\varepsilon}$ and low T.	no DRX/ferrite formation	Moderate	Low–mod. (with increasing T)	Moderate
Low $\dot{\varepsilon}$ and mod T.	DRX	Highest–mod. (with increasing $\dot{\varepsilon}$)	Highest–mod. (with increasing T)	Highest–mod. (with increasing $\dot{\varepsilon}$)
Low $\dot{\varepsilon}$ and high T.	DRX	High	High	High
High $\dot{\varepsilon}$ and low T.	no DRX	Low	Mod–low (with increasing $\dot{\varepsilon}$)	Low
High $\dot{\varepsilon}$ and mod T.	DRX	Moderate	High–mod. (with increasing $\dot{\varepsilon}$)	Moderate
High $\dot{\varepsilon}$ and high T.	DRX	Moderate	High	Moderate

The instability parameters calculated for the steel alloyed with nitrogen are given in Table 18.

Table 18. Comparison of different instability parameters for the steel alloyed with N.

Range	Microstructural instabilities	$\xi < 0$	$\kappa < 0$	$m < 0$	$\kappa_j < 0$	$\alpha_{SJ} > 0$
Low $\dot{\varepsilon}$ and low T	-	-	> 0.02 s^{-1}	-	-	-
Low $\dot{\varepsilon}$ and mod. T	-	< 875°C + > 0.06 s^{-1}	> 0.02 s^{-1}	-	< 875°C + > 0.3 s^{-1}	-
Low $\dot{\varepsilon}$ and high T	-	-	> 0.02 s^{-1}	-	-	-
High $\dot{\varepsilon}$ and low T	-	> 1 s^{-1}	> 1 s^{-1}	ε of 0.2	> 3 s^{-1}	-
High $\dot{\varepsilon}$ and mod. T	Deformation bands	> 875°C + > 5 s^{-1}; < 875°C + < 10 s^{-1}	> 1 s^{-1}	-	< 875°C + < 10 s^{-1}; > 875°C + > 5 s^{-1}	-
High $\dot{\varepsilon}$ and high T	Deformation bands	> 10 s^{-1} + < 940°C	> 1 s^{-1}	-	> 30 s^{-1}	-

For the first investigated steel none of the used models is fitting completely with the obtained micrographs.

5.5.2.4 Steel containing vanadium

For the steel alloyed with vanadium the results are shown in Table 19. At low temperatures ferrite was formed and additionally a critical temperature is necessary for DRX to start. In the low strain rate ranges the three approaches correlate with the microstructure, whereas at the high strain rate range, only one model is in good agreement. Low temperature is below 875°C, moderate temperature between 875–1025°C and high temperature above 1025°C.

Table 19. Summary of the steel alloyed with V.

Range	**Microstructure**	η_P	η_{M+R}	m
Low $\dot{\varepsilon}$ and low T.	DRV/ferrite formation	Mod–lowest (with increasing $\dot{\varepsilon}$)	Mod–low (with increasing T)	Mod–lowest (with increasing $\dot{\varepsilon}$)
Low $\dot{\varepsilon}$ and mod T.	DRX	Mod–highest (with increasing T)	Mod–highest (with increasing T)	Mod–highest (with increasing T)
Low $\dot{\varepsilon}$ and high T.	DRX	High–mod. (with increasing T)	High–mod. (with increasing T)	High–mod. (with increasing T)
High $\dot{\varepsilon}$ and low T.	DRV	Low–mod. (with increasing $\dot{\varepsilon}$)	Low–mod. (with increasing T)	Low–mod. (with increasing $\dot{\varepsilon}$)
High $\dot{\varepsilon}$ and mod T.	DRX	Mod–lowest (with increasing $\dot{\varepsilon}$)	High–mod. (with increasing $\dot{\varepsilon}$)	Mod–lowest (with increasing $\dot{\varepsilon}$)
High $\dot{\varepsilon}$ and high T.	DRX	Moderate	High	Moderate

In Table 20 the results for the different instability parameters of the steel alloyed with V are shown. The parameters ξ, κ and κ_j are showing the best results.

Table 20. Comparison of different instability parameters for the steel alloyed with V.

Range	**Microstructural instabilities**	$\xi < 0$	$\kappa < 0$	$m < 0$	$\kappa_j < 0$	$\alpha_{SJ} > 0$
Low $\dot{\varepsilon}$ and low T	Deformation bands	< 800°C	> 0.01 s^{-1}	< 800°C, around 1 s^{-1} for $\varepsilon = 0.5$	> 0.03 s^{-1} < 800°C	-
Low $\dot{\varepsilon}$ and mod. T	Deformation bands	> 900°C+ < 975°C + > 0.2 s^{-1}	> 0.03 s^{-1}	-	-	-
Low $\dot{\varepsilon}$ and high T	-	-	> 0.03 s^{-1}	-	-	-
High $\dot{\varepsilon}$ and low T	Deformation bands	> 825°C + > 3 s^{-1}	> 800°C	> 30 s^{-1} for $\varepsilon = 0.3$	< 5 s^{-1} + < 800°C; > 825°C + > 5 s^{-1}	-
High $\dot{\varepsilon}$ and mod. T	Deformation bands	< 980°C	> 1 s^{-1}	-	> 1 s^{-1}	-
High $\dot{\varepsilon}$ and high T	-	-	> 1 s^{-1}	-	-	-

6 Summary and conclusions

Thermomechanical processes play an important role in the production of metallic goods and have a large influence on the microstructure and hence on the final properties of materials. In the last years many different methods and approaches were tried to predict these final properties to avoid too many pre-trials in laboratories. One method intense used in the last decade is the so-called processing map based on the DMM developed by Prasad et al. [6]. This approach of processing maps is widely used by engineers and scientists due to its simplicity. The goal is to predict and describe formability to allow choosing the optimal process parameters such as strain rate, strain and temperature. However, many controversies [8], [9], [10], [11] were generated concerning to their thermodynamically foundation and their applications. Therefore, a request for a detailed consideration appeared and resulted in this thesis.

This work was focused on the hot deformation behaviour of four different alloys as they are Ti- and Mg-alloys, and two different steels microalloyed with N or V. Many different materials were chosen to ensure a wide range of behaviours due to differences in the stacking fault energies, crystal structures and phase conditions.

Hot compression tests were carried out using a Gleeble® 3800 to study the hot deformation behaviour and to obtain flow curves which are used for the calculation of processing maps. Not only processing maps based on the DMM by Prasad were calculated but also further DMM approaches of Murty and Rao [7] and Poletti [69] as well as a parameter developed by Semiatin and Jonas [17] were compared. Finally, the calculated maps were correlated with the microstructure using microscopy and EBSD measurements.

Processing maps based on DMM consist of two superimposed maps, the dissipation efficiency map η and the instability map ξ. The dissipation efficiency map was assumed to the microstructural changes in the material, whereas the instability map is correlated to flow localization, non-adiabatic and adiabatic shear bands, cracks and the formation of voids. The calculation of η and ξ is based on a partition of the input power P into J (metallurgical) and G (thermal), which however cannot be explained from the thermodynamic point of view. Murty and Rao modified the DMM by Prasad because the strain rate sensitivity m varies with the strain rate and the temperature. Therefore the calculation in the DMM of J and finally the calculation of η will be erroneous if using m as a constant.

Furthermore, it was shown in this work that because $\eta = \frac{2m}{m+1}$ in the processing maps of Prasad, and in the processing maps of Murty and Rao a correlation of η with m exists as well, the usage of m for describing microstructural changes should be favored, since its physical interpretation is clear and widely accepted. The predication of a high m value can be seen as diffusional mechanisms as DRX or also the transformation of austenite into ferrite phase. Small m values predicate that the occurring process is not or only less controlled by diffusion.

From this work it was found that the m map shows a good correlation between the calculated values and the observed microstructure. Good correlation means, if high m values are calculated, DRX grains or phase transformation were detected using microscopy.

However, processing maps consist of two superimposed maps and although the dissipation efficiency maps as well as the *m* maps can be interpreted from the microstructural point of view, this is not the case of the instability parameter. No consensus could be found using the different instability approaches. In most of the cases all the parameters predict instabilities although no damage was observed in the micrographs at the local deformation conditions. Finally, all instability parameters of the DMM based on continuum principles by Ziegler are not proven. For the development, *J* is taken as dissipative function, although the separation of *P* into *G* and *J* is thermodynamically not founded.
Additionally, another instability parameter (α_{SJ}) [17] not based on the DMM was adopted and interpreted within this work. This approach is founded with the consideration of two separated influences of strain softening and temperature softening. Although the tendency of this approach shows better results with respect to the microstructure as the DMM parameters, the results were not satisfactory.

In addition to the processing maps based on the DMM and the *m* map, a further map called microstructural map was developed as a function of temperature and strain rate. These maps are shown in Figure 100, Figure 104, and Figure 109 and gave an overview of the deformation mechanisms by experimental observations of the microstructure and the flow curves. Experiments for a broad temperature and strain rate range have to be carried out and additionally, LOM and EBSD measurements have to be done to describe the mechanisms which occur. Lastly, this map is easy to interpret, is based on experimental results and can be combined with, for example, the *m* map.

The conclusions of this thesis can be summarized as follows:

- The dissipation efficiency maps based on the model of Murty and Rao and the *m* maps are in good agreement with the LOM and EBSD investigations. If microstructural changes as DRX occur, a trend to higher η and *m* values can be seen. However, it is recommendable to confirm the obtained values in the processing maps using microscopy, since there is no distinction of which softening mechanism took place.

- The different instability parameters (ξ, κ, κ_j and α_{SJ}) used in this work were non-satisfying with respect to the prediction of total damage. This could be due to parameters based on its derivation from *J* as the dissipation function which is not thermodynamically founded.

and finally:

- **Processing maps** meaning the parameter η based on the DMM and especially the variation of *m* as a function of temperature and strain rate **are useful tools** to describe formability, however many experiments (deformation tests and microscopy) should be made to elucidate the deformation mechanisms.

- Nevertheless, with **effort** to develop an instability model based on thermodynamics, **processing maps can be a useful tool**.

- The **microstructural-maps** as presented e. g. in Figure 100 give an **overview** of occurring deformation mechanisms and can be combined with *m* and a damage parameter.

7 Outlook

Scientists as well as industrial partners are interested in the usage of deformation maps to choose the optimal forming parameters as strain rate, strain and temperature. Many papers were published in the last year which depicts the interest in this topic. However, the maps are calculated without taking into account the physical and thermo-dynamical meaning of the parameters.

Consequently, further investigations and the developing of new models based on thermodynamics, would give a large scientific impact.

To define and calculate a new efficient theory under the DMM ideas, the following points should be considered and carried out:

- A model should be developed to describe and predict: damage, flow localization and microstructural changes as a function of the temperature, the strain and the strain rate.

- The model should be based on irreversible thermodynamics to describe plastic deformation as introduced by Ziegler [65].

- Transient state flow instead of steady state flow should be considered to take into account the storage and release of energy as a consequence of microstructural changes during hot deformation.

List of Figures

List of Tables

Bibliography

[1] B. Verlinden, J. Driver, I. Samajdar and R. D. Doherty, Thermo-Mechanical Processing of Metallic Materials, Oxford, UK: Elsevier, 2007.

[2] C. M. Sellars and W. J. McTegart, “On the mechanism of hot deformation,” *Acta Metallurgica,* vol. 14, pp. 1136-1138, 1966.

[3] H. J. McQueen and N. D. Ryan, “Constitutive analysis in hot working,” *Materials Science and Engineering A*, vol. 322, no. 1-2, pp. 43-63, 2002.

[4] H. J. Frost and M. F. Ashby, Deformation - mechanism maps, Pergamon Press, 1982.

[5] R. Raj, “Development of a Processing Map for Use in Warm-Forming and Hot-Forming Processes,” *Metallurgical Transactions A,* vol. 12, pp. 1089 - 1097, June 1981.

[6] Y. V. R. K. Prasad, H. L. Gegel, S. M. Doraivelu, J. C. Malas, J. T. Morgan, K. A. Lark and D. R. Barker, “Modeling of Dynamic Material Behavior in Hot Deformation: Forging of Ti-6242,” *Metallurgical Transactions A,* vol. 15, pp. 1883 - 1892, 1984.

[7] S. V. S. N. Murty and B. N. Rao, “Ziegler's criterion on the instability regions in processing maps,” *Journal of materials science letters,* vol. 17, pp. 1203-1205, 1998.

[8] S. Ghosh, “Interpretation of Microstructural Evolution Using Dynamic Materials Modeling,” *Metallurgical and Materials Transactions A,* vol. 31, no. 11, pp. 2973-2974, 2000.

[9] F. Montheillet, J. J. Jonas and K. W. Neale, “Modeling of Dynamic Material Behavior: A Critical Evaluation of the Dissipator Power Co-content Approach,” *Metallurgical and Materials Transactions A,* vol. 27, pp. 232-235, 1996.

[10] S. Ghosh, “Interpretation of Flow Instability Using Dynamic Material Modeling,” *Metallurgical and Materials Transactions A,* vol. 33A, pp. 1569-1572, 2001.

[11] E. Bozzini and E. Cerri, “Numerical reliability of hot working processing maps,” *Materials Science and Engineering A,* vol. 328, no. 1-2, pp. 344-347, 2002.

[12] ASM, Forming and Forging, Volume 14, ASM International, 1993.

[13] R. H. Wagoner and J. L. Chenot, “The Tensile Test and Basic Material Behavior,” in *Fundamentals of metal forming,* John Wiley & Sons, Inc., 1996, pp. 1-11.

[14] W. F. Hosford, Mechanical Behavior of Materials, Cambridge University Press, 2010.

[15] A. Considère, “L'Emploi du fer et de l'acier dans les cunstructions.,” *Annales de Ponts et Chaussées 9,* pp. 574-775, 1885.

[16] E. W. Hart, “Theory of the tensile test,” *Acta Metallurgica,* vol. 15, no. 2, pp. 351-355, 1967.

[17] S. L. Semiatin and J. J. Jonas, “Flow Localization Due to Flow Softening: Axisymmetric Deformation,” in *Formability & Workability of Metals - Plastic instability & flow localization*, Metals Park, Ohio, American Society for Metals, 1984, pp. 51-55.

[18] D. Walgraef and E. C. Aifantis, “On certain problems of deformation-induced material instabilities,” *International Journal of Engineering Science*, vol. 59, pp. 140-155, 2012.

[19] J. R. Rice, “The localization of plastic deformation,” *Theoretical and Applied*

Mechanics (Proceedings of the 14th International Congress on Theoretical and Applied Mechanics), pp. 207-220, 1976.

[20] S. Boakye-Yiadom and M. Nabil Bassim, "Effect of prior heat treatment on the dynamic impact behavior of 4340 steel and formation of adiabatic shear bands," *Materials Science and Engineering A,* vol. 528, no. 29-30, pp. 8700-8708, 2011.

[21] T. Sakai and J. J. Jonas, "Plastic Deformation: Role of Recovery and Recrystallization," in *Encyclopedia of Materials: Science and Technology (Second Edition),* 2001, pp. 7079-7084.

[22] F. Humphreys and M. Hatherly, Recrystallization and Related Annealing Phenomena, Elsevier, 2004.

[23] S. H. Zahiri and P. D. Hodgson, "The static, dynamic and metadynamic recrystallization of a medium carbon steel," *Materials Science and Technology* , vol. 20, no. 4, pp. 458-464, 2004.

[24] T. Sakai and J. J. Jonas, "Dynamic recrystallization: Mechanical and microstructural considerations," *Acta Metallurgica,* vol. 32, no. 2, pp. 189-209, 1984.

[25] S. E. Ion, F. J. Humphreys and S. H. White, "Dynamic recrystallization and the development of microstructure during the high temperature deformation of magnesium," *Acta Metallurgica,* vol. 30, no. 10, pp. 1909-1919, 1982.

[26] Gottstein, "Erholung, Rekristallisation, Kornvergrößerung," in *Physikalische Grundlagen der Materialkunde,* Berlin Heidelberg, Springer, 2007, pp. 303-357.

[27] M. J. Luton and C. M. Sellars, "Dynamic recrystallization in Nickel and Nickel-Iron alloys during high temperature deformation," *Acta Metallurgica,* vol. 17, no. 8, pp. 1033-1043, 1969.

[28] S. Gourdet and F. Montheillet, "An experimental study of the recrystallization mechanism during hot deformation of aluminium," *Materials Science and Engineering A,* vol. 283, no. 1-2, pp. 274-288, 2000.

[29] A. Beck, "Physikalische Eigenschaften des Magnesium-Einkristalls und ihre Bedeutung für den Vielkristall," in *Magnesium und seine Legierungen,* Springer, 2001, pp. 18-36.

[30] S. Kleiner, "Magnesium und seine Legierungen," in *Feinstbearbeitung technischer Oberflächen - 6. Internationales IWF-Kolloquium,* Egerkingen, Schweiz, 2002.

[31] A. Beer, "The evolution of hot working stress and microstructure in Mg-3Al-1Zn," Deakin University, Australia, 2004.

[32] J. W. Christian and S. Mahajan, "Deformation twinning," *Progress in Materials Science,* vol. 39, no. 1-5, pp. 1-157, 1995.

[33] Q. Ma, S. J. Horstemeyer, B. Li, Z. McClelland, P. T. Wang and M. F. Horstemeyer, "Microstructure and texture evolution in a magnesium alloy during extrusion at various extrusion speeds," *Magnesium Technology 2013 (eds N. Hort, S. N. Mathaudhu, N. R. Neelameggham and M. Alderman),* pp. 95-99, 2013.

[34] A. Mwembela, E. B. Konopleva and H. J. McQueen, "Microstructural development in Mg alloy AZ31 during hot working," *Scripta Materialia,* vol. 37, no. 11, pp. 1789-1795, 1997.

[35] M. R. Barnett, “Influence of deformation conditions and texture on the high temperature flow stress of magnesium AZ31,” *Journal of Light Metals,* vol. 1, no. 3, pp. 167 - 177, 2001.

[36] M. M. Myshlyaev, H. J. McQueen, A. Mwembela and E. Konopleva, “Twinning, dynamic recovery and recrystallization in hot worked Mg-Al-Zn alloy,” *Materials Science and Engineering A,* vol. 337, no. 1-2, pp. 121-133, 2002.

[37] A. G. Beer and M. R. Barnett, “Influence of initial microstructure on the hot working flow stress of Mg-3Al-1Zn,” *Materials Science and Engineering A,* vol. 423, no. 1-2, pp. 292-299, 2006.

[38] S. Spigarelli, M. E. Mehtedi, M. Cabibbo, E. Evangelista, J. Kaneko, A. Jäger and V. Gartnerova, “Analysis of high-temperature deformation and microstructure of AZ31 magnesium alloy,” *Materials Science and Engineering A,* vol. 462, no. 1-2, pp. 197-201, 2007.

[39] J. C. Tan and M. J. Tan, “Dynamic continuous recrystallization characteristics in two stage deformation on Mg-3Al-1Zn alloy sheet,” *Materials Science and Engineering A,* vol. 339, no. 1-2, pp. 124-132, 2003.

[40] H. J. McQueen and E. V. Konopleva, “Creep and hot working of Mg alloy AZ91,” in *Magnesium Technology 2001 (ed J. N. Hryn),* TMS (The Minerals, Metals & Materials Society), 2001, pp. 227-233.

[41] W. P. Peng, P. J. Li, P. Zeng and L. P. Lei, “Hot deformation behavior and microstructure evolution of twin-roll-cast Mg-2.9Al-0.9Zn alloy: A study with processing maps,” *Materials Science and Engineering A,* vol. 494, no. 1-2, pp. 173-178, 2008.

[42] G. Lütjering and J. C. Williams, Titanium, Springer, 2007.

[43] W. Bergmann, Werkstofftechnik 1, Hanser, 2005.

[44] R. Colás, “A model for the hot deformation of low carbon steel,” *Journal of Materials Processing Technology,* vol. 62, no. 1-3, pp. 180-184, 1996.

[45] S. V. S. N. Murty, S. Torizuka, K. Nagai, T. Kitai and Y. Kogo, “Dynamic recrystallization of ferrite during warm deformation of ultrafine grained ultra-low carbon steel,” *Scripta Materiala 53,* vol. 53, no. 6, pp. 763-768, 2005.

[46] B. Eghbali, A. Abdollah-Zadeh, H. Beladi and P. D. Hodgson, “Characterization on ferrite microstructure evolution during large strain warm torsion testing of plain low carbon steel,” *Materials Science and Engineering A,* Vols. 435-436, pp. 499-503, 2006.

[47] A. Momeni, H. Arabi, A. Rezaei, H. Badri and S. M. Abbasi, “Hot deformation behavior of austenite in HSLA-100 microalloyed steel,” *Materials Science and Engineering A,* vol. 528, no. 4-5, pp. 2158-2163, 2011.

[48] B. Eghbali and A. Abdollah-Zadeh, “Influence of deformation temperature on the ferrite grain refinement in a low carbon Nb-Ti microalloyed steel,” *Journal of Materials Processing Technology,* vol. 180, no. 1-3, pp. 44-48, 2006.

[49] B. Heine, “Mechanische Eigenschaften rissfreier Proben bei steigender Beanspruchung,” in *Werkstoffprüfung - Ermittlung von Werkstoffeigenschaften,* Carl Hanser Verlag München, 2011, pp. 150-209.

[50] D. G. Robertson and H. B. McShane, “Isothermal hot deformation behaviour of metastable beta titanium alloy Ti-10V-2Fe-3Al,” *Materials Science and Technology,* vol. 13, pp. 575-583, 1997.

[51] DSI, “Operation of Gleeble Systems,” in *Gleeble Users Training 2013 - Gleeble Systems and Applications,* 2013, pp. 15-52.

[52] „Institute for Frontier Materials - Equipment,“ [Online]. Available: http://www.deakin.edu.au/research/ifm/facilities/hsr.php.

[53] „Dilatometry - TA Instruments,“ 2013.

[54] Y. V. R. K. Prasad and S. Sasidhara, Hot Working Guide: Compendium of Processing Maps, Materials Park, Ohio: ASM International, 1997, pp. 1 - 24.

[55] L. E. Malvern, Introduction to the mechanics of a continuous medium, Prentice Hall, 1969.

[56] Y. V. R. K. Prasad and T. Seshacharyulu, “Processing maps for hot working of titanium alloys,” *Materials Science and Engineering A,* vol. 243, no. 1-2, pp. 82-88, 1998.

[57] Y. V. R. K. Prasad and K. P. Rao, “Processing maps for hot deformation of rolled AZ31 magnesium alloy plate: Anisotropy of hot working,” *Materials Science and Engineering A,* vol. 487, no. 1-2, pp. 316-327, 2008.

[58] N. Srinivasan, Y. V. R. K. Prasad and P. R. Rao, “Hot deformation behaviour of Mg-3Al alloy - A study using processing maps,” *Materials Science and Engineering A,* vol. 476, no. 1-2, pp. 146-156, 2008.

[59] S. Anbuselvan and S. Ramanathan, “Hot deformation and processing maps of extruded ZE41A magnesium alloy,” *Materials and Design,* vol. 31, no. 5, pp. 2319-2323, 2010.

[60] Y. Xu, L. Hu, T. Deng and L. Ye, “Hot deformation behavior and processing maps of as-cast AZ61 magnesium alloy,” *Materials Science and Engineering A* , vol. 559, pp. 528-533, 2013.

[61] S. V. S. N. Murty and B. N. Rao, “On the flow localization concepts in the processing maps of titanium alloy Ti-24Al-20Nb,” *Journal of Materials Processing Technology 104,* vol. 104, no. 1-2, pp. 103-109, 2000.

[62] S. V. S. N. Murty, B. N. Rao and B. P. Kashyap, “On the hot working characteristics of 2014 Al-20vol% Al2O3 metal matrix composite,” *Journal of Materials Processing Technology 166,* vol. 166, no. 2, pp. 279-285, 2005.

[63] C. Poletti, F. Warchomicka and H. P. Degischer, “Local deformation of Ti6Al4V modified 1 wt% B and 0.1 wt% C,” *Materials Science and Engineering A,* vol. 527, no. 4-5, pp. 1109-1116, 2010.

[64] C. Poletti, H. P. Degischer, S. Kremmer and W. Marketz, “Processing maps of Ti662 unreinforced and reinforced with TiC particles according to dynamic models,” *Materials Science and Engineering A,* vol. 486, no. 1-2, pp. 127-137, 2008.

[65] H. Ziegler, An Introduction to thermomechanics., North-Holland Pubslishing Company, 1983.

[66] S. V. S. N. Murty, B. N. Rao and B. P. Kashyap, “Instability criteria for hot deformation of materials,” *International Materials Reviews 45,* vol. 45, no. 1, pp. 15-26,

2000.

[67] Y. V. R. K. Prasad, “Author's Reply: Dynamic Materials Model: Basis and Principles,” *Metallurgical and Materials Transactions A,* vol. 27, no. 1, pp. 235-236, 1996.

[68] S. V. S. N. Murty and B. N. Rao, “On the development of instability criteria during hotworking with reference to IN 718,” *Materials Science and Engineering A,* vol. 254, no. 1-2, pp. 76-82, 1998.

[69] C. Poletti, J. Six, M. Hochegger, H. P. Degischer and S. Ilie, “Hot Deformation Behaviour of Low Alloy Steel,” *steel research int.,* vol. 82, no. 6, pp. 710-718, 2011.

[70] M. Xiong, Z. Weidong, S. Yu, Z. Yongqing, W. Shaoli and Z. Yigang, “A Comparative Study of Various Flow Instability Criteria in Processing Map,” *Rare Metal Materials and Engineering ,* vol. 39, no. 5, pp. 756-761, 2010.

[71] G. Gottstein, “Die Fließkurve,” in *Physikalische Grundlagen der Materialkunde,* Berlin Heidelberg, Springer, 2001, pp. 190-197.

[72] J. Rösler, H. Harders and M. Bäker, “Kriechen,” in *Mechanisches Verhalten der Werkstoffe,* Springer DE, 2008, pp. 383-407.

[73] N. E. Dowling, Mechanical Behaviour of Materials: Engineering Methods for Deformation, Fractura and Fatigue., Pearsons Prentice Hall, 3rd edition 2007.

[74] C. Poletti, Habilitation: Hot deformation of metal based materials: experimental and modelling, Graz, 2011.

[75] T. Furu, K. Marthinsen and E. Nes, “Particle Effects on Recrystallization of Metals,” in *Recrystallization’92,* Spain, 1992.

[76] Y. V. R. K. Prasad, K. P. Rao and M. Gupta, “Hot workability and deformation mechanisms in Mg/nano-Al2O3 composite,” *Composites Science and Technology ,* vol. 69, no. 7-8, pp. 1070-1076, 2009.

[77] A. G. Beer and M. R. Barnett, “Microstructure evolution in hot worked and annealed magnesium alloy AZ31,” *Materials Science and Engineering A,* vol. 485, no. 1-2, pp. 318-324, 2008.

[78] A. Momeni and K. Dehghani, “Characterization of hot deformation behavior of 410 martensitic stainless steel using constitutive equations and processing maps,” *Materials Science and Engineering A527,* vol. 527, no. 21-22, pp. 5467-5473, 2010.

[79] Z. Zeng, S. Jonsson and Y. Zhang, “Constitutive equations for pure titanium at elevated temperatures,” *Materials Science and Engineering A ,* vol. 505, no. 1-2, pp. 116-119, 2009.

[80] H. Dieringa, Y. Huang, P. Wittke, M. Klein, F. Walther, M. Dikovits and C. Poletti, “Compression-creep response of magnesium alloy DieMag422 containing barium compared with commercial creep-resistant alloys AE42 and MRI230D,” *Materials Science and Engineering A*, vol. 585, pp. 430-438, 2013.

[81] „Ti 5Al-5Mo-5V-3Cr-1Zr. Materials supplier receiving inspection Report, VSMPO“.

[82] F. Warchomicka, “Microstructural behaviour of near beta-titanium alloys during thermomechanical processes,” Vienna, 2008.

[83] F. Warchomicka, C. Poletti and M. Stockinger, “Study of the hot deformation behaviour

in Ti-5Al-5Mo-5V-3Cr-1Zr," *Materials Science and Engineering A,* vol. 528, no. 28, pp. 8277-8285, 2011.

[84] N. G. Jones, R. J. Dashwood, D. Dye and M. Jackson, "Thermomechanical processing of Ti-5Al-5Mo-5V-3Cr," *Materials Science and Engineering A,* vol. 490, no. 1-2, pp. 369-377, 2008.

[85] R. R. Boyer and R. D. Briggs, "The Use of beta Titanium Alloys in the Aerospace Industry," *Journal of Materials Engineering and Performance,* vol. 14, no. 6, pp. 681-685, 2005.

[86] A. Samoilov, P. Stiaszny, A. Pichler, H. Spindler, B. Skandera, H. P. Degischer, B. Kriszt and M. Eigelsberger, "Development of V-based microalloyed high strength hot strip for production with reduced rolling forces," Linz, 2003.

[87] B. Skandera, A. Samoilov, P. Stiaszny and H. P. Degischer, "Development of vanadium microalloyed high strength hot rolled steel strip," London, 2004.

[88] F. A. Khalid and D. V. Edmonds, "On the properties and structure of micro-alloyed and copper-bearing hot-rolled steels," *Journal of Materials Processing Technology* , vol. 72, no. 3, pp. 434-436, 1997.

[89] C. Poletti, F. Warchomicka, R. Okruch and H. Knoblich, "Microstructural Features of AZ31 Deformed at High Temperatures," *Practical Metallography 47-9,* vol. 47, no. 9, pp. 517-529, 2010.

[90] F. J. Humphreys, "Review - Grain and subgrain characterisation by electron backscatter diffraction," *Journal of Materials Science,* vol. 36, pp. 3833 - 3854, 2001.

[91] „OIM Analysis 5 Manual".

[92] „ImageJ," 2013. [Online]. Available: http://rsb.info.nih.gov/ij/.

[93] A. E112-10, "Standard Test Methods for Determining Grain Size".

[94] H.-J. Bargel and G. Schulze, Werkstoffkunde, Berlin: Springer, 2005.

[95] „OriginLab - Data Analysis and Graphing Software," 2013. [Online]. Available: www.originlab.com.

[96] J. H. Kim, N. E. Kang, C. D. Yim and B. K. Kim, "Effect of calcium content on the microstructural evolution and mechanical properties of wrought Mg-3Al-1Zn alloy," *Materials Science and Engineering A,* vol. 525, no. 1-2, pp. 18-29, 2009.

[97] A. Grosvenor and C. H. J. Davies, "Microstructural Evolution during the Hot Deformation of Magnesium Alloy AZ31," *Materials Science Forum,* Vols. 426-432, pp. 4567-4572, 2003.

[98] S. V. S. N. Murty, B. N. Rao and B. P. Kashyap, "Identification of flow instabilities in the processing maps of AISI 304 stainless steel," *Journal of Materials Processing Technology 166,* vol. 166, no. 2, pp. 268-278, 2005.

[99] DSI - Dynamic Systems Inc., Application Notes.

[100] D. Rittel, A. A. Kidane, M. Alkhader, A. Venkert, P. Landau and G. Ravichandran, "On the dynamically stored energy of cold work in pure single crystal and polycrystalline copper," *Acta Materialia,* vol. 60, no. 9, pp. 3719-3728, 2012.

[101] R. L. Goetz and S. L. Semiatin, "The adiabatic correction factor for deformation heating

during the uniaxial compression test," *Journal of Materials and Engineering and Performance,* vol. 10, no. 6, pp. 710-717, 2001.

[102] C. Poletti, M. Dikovits and J. Ruete, "Hot deformation studies of a low carbon steel containing V," *Key Engineering Materials,* Vols. 554-557, pp. 1224-1231, 2013.

[103] M. R. Barnett, "Quenched and Annealed Microstructures of Hot Worked Magnesium AZ31," *Materials Transactions,* vol. 44, no. 4, pp. 571-577, 2003.

[104] M. Hradilová, F. Montheillet, A. Fraczkiewicz, C. Desrayaud and P. Lejcek, "Effect of Ca-addition on dynamic recrystallization of Mg-Zn alloy during hot deformation," *Materials Science and Engineering A,* vol. 580, pp. 217-226, 2013.

[105] J. D. Robson, D. T. Henry and B. Davis, "Particle effect on recrystallization in magnesium-manganese alloys: Particle-stimulated nucleation," *Acta Materiala,* vol. 57, no. 9, pp. 2739-2747, 2009.

[106] J. D. Robson, D. T. Henry and B. Davis, "Particle effects on recrystallization in magnesium-manganes alloys: Particle pinning," *Materials Science and Engineering A* , vol. 528, no. 12, pp. 4239-4247, 2011.

[107] A. G. Beer and M. R. Barnett, "The post-deformation recrystallization behaviour of magnesium alloy Mg-3Al-1Zn," *Scripta Materialia,* vol. 61, no. 12, pp. 1097-1100, 2009.

[108] X. Ma, W. Zeng, B. Xu, Y. Sun, C. Xue and Y. Han, "Characterization of the hot deformation behavior of a Ti-22Al-25Nb alloy using processing maps based on the Murty criterion," *Intermetallics 20,* vol. 20, no. 1, pp. 1-7, 2012.

[109] C. Poletti, F. Warchomicka, M. Dikovits and S. Großeiber, "Microstructure evolution of allotropic materials during thermomechanical processing," *Materials Science Forum,* vol. 710, pp. 93-100, 2012.

[110] A. Dehghan - Manshadi and R. J. Dippenaar, "Development of α-phase morphologies during low temperature isothermal heat treatment of a Ti-5Al-5Mo-5V-3Cr alloy," *Materials Science and Engineering A,* vol. 528, no. 3, pp. 1833-1839, 2011.

[111] J. D. Cotton, R. R. Boyer, R. D. Briggs, R. G. Baggerly, C. A. Meyer, M. D. Carter, W. Wood, G. Tewksbury, V. Li and X. Yao, "Phase Transformations in Ti-5Al-5Mo- 5V-3Cr-0.5Fe," *Titanium 2007: Science and Tchnology, 2, The Japanese Institute of Metals,* pp. 471-479, 2007.

[112] K. P. Rao, Y. K. D. V. Prasad and E. B. Hawbolt, "Hot deformation studies on a low-carbon steel: Part 1 - flow curves and the constitutive relationship," *Journal of Materials Processing Technology* , vol. 56, no. 1-4, pp. 897-907, 1996.

[113] J. Zhang, H. Di, X. Wang, Y. Cao, J. Zhang and T. Ma, "Constitutive analysis of the hot deformation behavior of Fe-23Mn-2Al-0.2C twinning induced plasticity steel in consideration of strain," *Materials and Design* , vol. 44, pp. 354-464, 2013.